Global stability of compressible flow about a swept parabolic body

Christoph Mack

To cite this version:

Christoph Mack. Global stability of compressible flow about a swept parabolic body. Engineering Sciences [physics]. Ecole Polytechnique X, 2009. English. NNT : . pastel-00005752

HAL Id: pastel-00005752

https://pastel.hal.science/pastel-00005752

École Polytechnique
Laboratoire d'Hydrodynamique (LadHyX)

Thèse présentée pour obtenir le grade de
DOCTEUR DE L'ÉCOLE POLYTECHNIQUE
spécialité: mécanique

par

CHRISTOPH MACK

Global stability of compressible flow about a swept parabolic body*

---

* Stabilité globale de l'écoulement compressible autour d'un cylindre de section parabolique

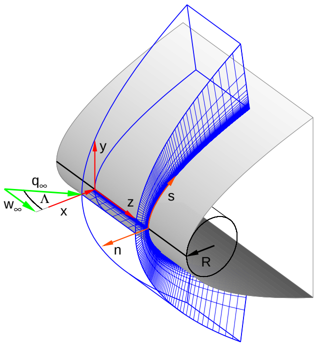

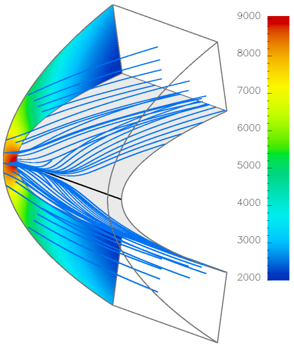

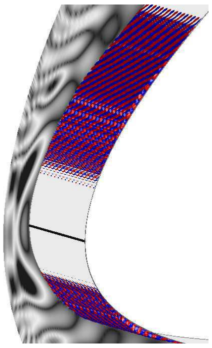

soutenue le 20 novembre 2009 devant le jury composé de:

J.-P. Bonnet	examinateur	Université de Poitiers, France
R. Friedrich	rapporteur	TU München, Germany
P. Huerre	président du jury	École Polytechnique, France
D. Obrist	examinateur	ETH Zürich, Switzerland
N. Peake	rapporteur	University of Cambridge, UK
P.J. Schmid	directeur de thèse	École Polytechnique, France
J. Sesterhenn	examinateur	TU Berlin, Germany

Christoph Mack

Global stability of compressible flow about a swept parabolic body

Doctoral thesis
École Polytechnique
2009

Contents

Part I

Global stability of compressible flow about a swept parabolic body

Chapter 1

Introduction

Flow about a blunt body is frequently encountered in aeronautical, vehicle or marine applications. The swept wings of civil aircraft, the spoilers on race cars and the control surfaces of submarines display only a few of many examples. They share the requirement that the flow near the stagnation or attachment line, the location where the fluid comes to rest, and its development farther downstream from the stagnation line have to be fully understood for an efficient design and a proper performance. It is the topic of the present thesis to investigate the stability behavior of compressible leading-edge flow with respect to small perturbations by performing a global stability analysis.

For this analysis, flow in the leading-edge region of a yawed blunt body is modeled by compressible flow about a swept parabolic body. This flow model treats the movement of air in the vicinity of the attachment line and the region farther downstream as one entity. This is in contrast to previous theoretical and numerical studies where both regions have been studied separately — a necessary approach to apply standard numerical algorithms — using distinct simplified local flow models. Results from these local investigations still constitute most of our current understanding of swept leading-edge flow despite a number of unanswered but practically relevant questions. In this sense, this thesis attempts to answer some of these questions by studying a flow model that represents a closer approximation to realistic flow situations.

Soon after the invention of aircraft in the beginning of the twentieth century it was realized that the aerodynamic design of high-performance aircraft crucially depends on a profound understanding of compressible flow around wings. In particular, the details of the transition process from laminar to turbulent fluid motion, yielding increased drag and a loss of flight performance, play a dominant role in the description of this flow. Two-dimensional hydrodynamic instabilities of the Tollmien–Schlichting type have been found to trigger this transition process and to initiate the breakdown into turbulence in a region rather far downstream of the attachment line for unswept wings, the standard design concept for low-speed aircraft in the early twentieth century. With the advent of *high-speed* aircraft in the 1940s, for instance, the jet-engined Messerschmitt ME 262, the introduction of *swept wings* became necessary in order to overcome serious design problems emanating from compressibility effects, notably the shock stall phenomenon. *Sweep*, however, considerably alters the stability properties and thus the transition process of the flow in the wing's leading-edge region, and "a truly optimum system can only be achieved through a complete understanding of the laminar to turbulent transition process" (Poll, 1984).

The present thesis is concerned with the stability behavior of compressible flow in the leading-edge region of yawed blunt bodies such as swept air- and spacecraft wings or blended wing-body configurations (see figure 1.1). In particular, we will focus on the flow near and downstream of the attachment line. Such an attachment line is formed on the windward surface of any convex-curved object — which will be modeled by a swept parabolic body — immersed in fluid flow. A sound understanding of the flow stability and the laminar-turbulent transition process

Figure 1.1. Typical examples of compressible flow about a yawed blunt body: subsonic flow about the swept wings of a civil aircraft (left), swept leading-edge flow about a blended wing-body (BWB) aircraft, a concept for future aircraft (top right), and hypersonic flow about the swept wings of a space shuttle (bottom right).

in this region is important from several points of view: (i) to improve the performance and fuel efficiency of current civil aircraft, (ii) to allow the optimal aerodynamic design of future high-performance aircraft such as blended wing-body configurations, and (iii) to predict and manipulate the thermal loads that exist for the swept wings (as well as the lower side) of spacecraft. In the latter application, a thermal protection system (TPS) is used to protect the space vehicle from temperatures up to 1650 ° C. Moreover, as pointed out in a review article by Reed et al. (1996), understanding the laminar to turbulent transition process is necessary for the accurate prediction of hydro- and aerodynamic forces and the temperature field on the surface of transport vehicles in general.

1.1 Flow situation

The flow situation in the leading-edge region of a swept blunt body is sketched in figure 1.2. In it, the flow impinges onto a convex-curved body — whose leading-edge curvature is given by the leading-edge radius R — with a freestream velocity q_∞ under a sweep angle Λ yielding a velocity component normal, u_∞, and a component parallel to the leading-edge, w_∞. The latter velocity component points along the spanwise z-direction and is denoted as the sweep velocity. The resulting flow forms a local stagnation-point flow near the attachment line, the point where the fluid comes to rest, which turns into a highly three-dimensional flow downstream of the attachment line. To indicate the three-dimensional character of the flow, the streamline pattern of the inviscid outer flow in the leading-edge region is depicted by curved lines in figure 1.2. Furthermore, as a result of viscous effects in the flow, a thin three-dimensional boundary layer exists between the body and the surface of the external streamlines. This boundary layer fully covers the surface of the body as it grows in the chordwise x-direction, and its thickness is denoted by δ_{99} (see figure 1.2). In summary, the flow situation displayed in figure 1.2 features a large number of independent variables which "produces a problem of great complexity" (Poll, 1978). The degree of complexity can be reduced by assuming a body of infinite span; practical experience with high aspect ratio untapered swept cylinders has shown that in those regions where the external flow is effectively independent of the spanwise coordinate, z, the boundary layer is also approximately independent of z (see Poll, 1978).

Boundary-layer flows such as swept leading-edge flow (see figure 1.2) feature velocity gradi-

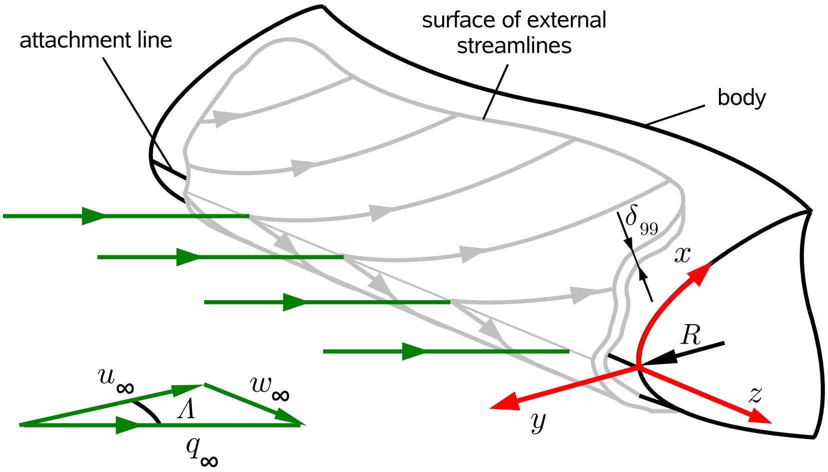

Figure 1.2. Sketch of viscous flow in the leading-edge region of a swept blunt body of infinite span (adapted from Poll, 1978).

ents inside the viscous boundary layer, and these gradients result in diffusive effects. For civil aircraft traveling at several hundreds of kilometer per hour, for instance, the velocity of the outer flow drops to zero at the surface of the wing, in the wing's leading-edge region, over vertical distances on the order of millimeters. The resulting diffusive effects are responsible for skin friction (drag) and heat transfer (thermal load), and they highly depend on the state of the boundary layer; if the boundary layer undergoes a transition from laminar to turbulent fluid motion, drastic increases in drag and thermal load result. The Reynolds number Re which describes the ratio of inertial to viscous forces governs this transition process and thus characterizes the stability of the boundary-layer flow.

1.1.1 Early experiments

The desire to suppress laminar-turbulent transition on swept wings and to maintain laminar flow over a whole aircraft wing dates back to the 1940s. At this time, experimental investigations on swept wings suggested that the presence of sweep does not affect the stability of the flow. However, in later flight tests on swept wing aircraft, Gray (1952) noticed that beyond a critical speed q_∞, the laminar-turbulent transition front moved toward the leading edge of the wing, and transition could occur at, or very close to, the attachment line. This feature could not be explained by existing two-dimensional arguments, i.e., by instabilities of the *Tollmien–Schlichting* type. Gray further observed that the critical speed q_∞ for early transition depends on the sweep angle Λ as well as the leading-edge radius R of the wing.

Crossflow instabilities

Theoretical and experimental investigations followed and revealed a new type of instability, the *crossflow instability*, which is due to a velocity component inside the boundary layer that is transverse to external streamlines. The presence of sweep (and curvature) gives rise to a highly three-dimensional boundary-layer flow in the leading-edge region of a swept wing — as sketched in figure 1.2 — and thus fundamentally alters its inherent stability properties; the initially two-dimensional boundary-layer flow along the attachment line gradually merges into a three-dimensional boundary-layer flow as it develops downstream of the attachment line. The crossflow instability exhibits coherent co-rotating vortices whose axes are almost aligned with the streamlines of the external flow (see, e.g., Bippes, 1999, for details). As an example, Poll

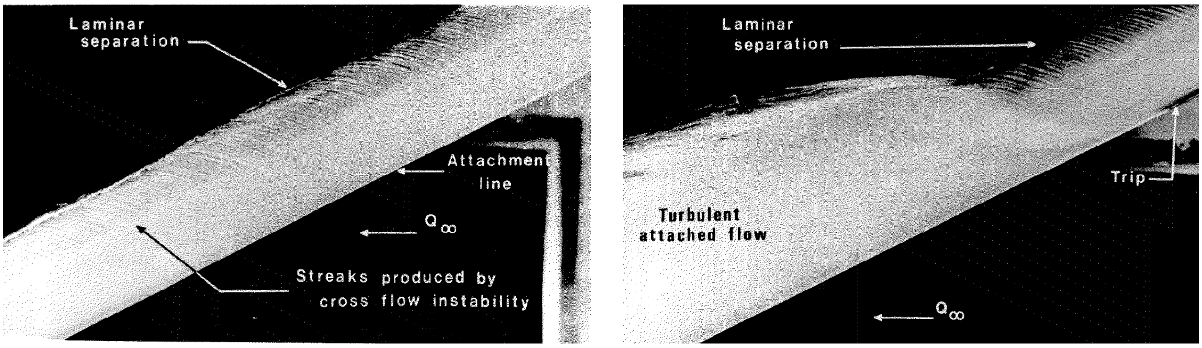

Figure 1.3. Results from wind-tunnel experiments on a swept wing configuration with a semi-circular leading edge for a sweep angle $\Lambda = 63\,^\circ$ and a freestream velocity $q_\infty = 28$ [m/s] (taken from Poll, 1978, 1979); the flow (in white) is visualized using oil: (left) streaky structures in form of co-rotating vortices produced by the crossflow instability; (right) phenomenon of leading-edge contamination as a result of large-scale perturbations caused by a trip wire of a diameter $d = 0.34$ [mm] mounted across the attachment line.

(1978, 1979) reported their presence in form of oil-film streaks in his wind-tunnel experiments (see figure 1.3 left); the same characteristic pattern had been observed in Gray's (1952) flight tests. The prevalence of crossflow vortices led, in the mid-1950s, to the hypothesis of a crossflow-vortex induced transition, and experiments had been designed to eliminate the vortices using suction systems and thus render the flow in the vicinity of the leading edge laminar.

Leading-edge (attachment-line) contamination

Contrary to the hypothesis of a crossflow-induced transition, tests in 1963 revealed that at design conditions laminar flow was restricted to small regions near the wing tips, and that the source of the transition problem was turbulent flow from the wing-fuselage junction traveling along the attachment line and contaminating the wing's leading edge. If the governing Reynolds number Re was sufficiently high, the large-scale perturbations produced and sustained a turbulent boundary layer not only along the attachment line but also at all chordwise locations of the swept wing (see figure 1.3 right).

In an early attempt to gather detailed information on *leading-edge contamination*, Pfenninger and Gaster independently conducted a number of wind-tunnel investigations in the 1963s. In his experiments on a swept X-21 wing, Pfenninger observed that unexpectedly high suction rates had to be applied to achieve laminar flow over the outer part of the wing (see Reed and Saric, 1989, for details). This strong suction was required particularly in the wing's leading-edge region which indicated that rather strong disturbances had to be present in the laminar boundary layer originating near the upstream part of the wing. Evaluating his database and summarizing his findings (in Pfenninger, 1965), he was able to establish a criterion for the existence of spanwise contamination in the presence of an initially turbulent attachment-line boundary layer emanating from the wing-fuselage junction. He further realized that maintaining a full-chord laminar flow on an X-21 wing critically depended on the existence of an undisturbed laminar attachment-line boundary layer, thus stressing the importance of flow instabilities in the vicinity of the attachment line. Pfenninger's criterion is expressed as a critical Reynolds number of $Re_\theta = w_\infty \theta / \nu \approx 100$ based on the momentum thickness θ (with the sweep velocity $w_\infty = q_\infty \sin \Lambda$ and the kinematic viscosity ν), and to this day this value still guides state-of-the-art design efforts for swept wings. A theoretical foundation for this critical value, however, is still missing. To avoid *leading-edge contamination* and create an undisturbed laminar boundary layer along the attachment line Gaster (1965) proposed a bump on the wing's leading edge.

These early flight tests initiated a great many experimental investigations on leading-edge (attachment-line) contamination and leading-edge instabilities. Analyzing the results from these in-flight tests as well as a number of wind-tunnel experiments, Joslin (1996) concluded that large roughness elements or trip wires mounted across the attachment line have an effect on the stability of the leading-edge boundary layer similar to that of contamination. His evaluation of previous data again yields Pfenninger's criterion, namely, disturbance decay for $Re_\theta < 100$ and unstable flow for $Re_\theta > 100$.

Attachment-line instabilities

Further attempts to better understand the stability of flow in the attachment-line region followed (e.g., Cumpsty and Head, 1969; Pfenninger and Bacon, 1969), and the flow was found to also be susceptible to instabilities close to the attachment line. However, it was Poll (1979) a decade later who established *attachment-line instabilities* as a viable alternative governing the stability of leading-edge flow. He conducted wind-tunnel experiments on a swept wing configuration with a semi-circular leading edge (the same swept wing model as used by Cumpsty and Head, 1969) and determined, in contrast to the above flight tests, a critical Reynolds number of $Re_{\theta,crit} \approx 230$ for infinitesimal perturbations. As a consequence of the findings for leading-edge contamination and attachment-line instabilities, Reed and Saric (1989) stated in their review article that, since the characteristic critical Reynolds number $Re_{\theta,crit} \approx 230$ for attachment-line instabilities is higher than the leading-edge contamination limit ($Re_\theta \approx 100$), "the contamination problem should be solved first".

The gathered experimental results as well as the need to fully understand the flow near the attachment line have fueled a substantial effort to investigate the flow behavior governed by the two identified and distinct instability mechanisms: while attachment-line instabilities are predominantly of a viscous nature, crossflow instabilities are based on an inflection point in the three-dimensional velocity profile and operate off the attachment line. For a recent overview of experiments and theory on the stability and transition of three-dimensional boundary layers the reader is referred to Bippes (1999) and Saric et al. (2003).

Experiments in compressible flow

The literature on studies of sub-, super- and hypersonic flow about blunt bodies such as swept wings and swept cylinders is relatively sparse. In Poll (1983), he extends his incompressible investigations (Poll, 1978, 1979) and discusses the influence of compressibility on the stability of swept leading-edge flow. Analyzing the available results from experiments with large-amplitude perturbations, he was able to determine a unique critical Reynolds number of 245 for sweep Mach numbers M_e up to 6.

A recent and comprehensive overview of existing studies for small-amplitude perturbations (for $1.53 \leq M_e \leq 8.06$) is given by Gaillard et al. (1999). In their article, they present a figure displaying the critical value of the Reynolds number for the onset of transition as a function of the sweep Mach number M_e. In the same figure, they mark a range of $0 \leq M_e \leq 5$, denoted as Creel's critical range (Creel et al., 1987), where the critical Reynolds number (650-700) for the onset of transition is nearly independent of the sweep Mach number; they further report that their results suggest a strong destabilizing influence of the sweep Mach number for values larger than approximately 5.

1.1.2 Laminar-turbulent transition on swept wings

Now, that we have revisited important literature about experimental studies on swept wings and swept wing models, we briefly summarize the instability mechanisms (and their governing parameters) that have been suggested to cause the transition from laminar to turbulent fluid motion on swept wings. In the past, it has been found that this laminar-turbulent transition

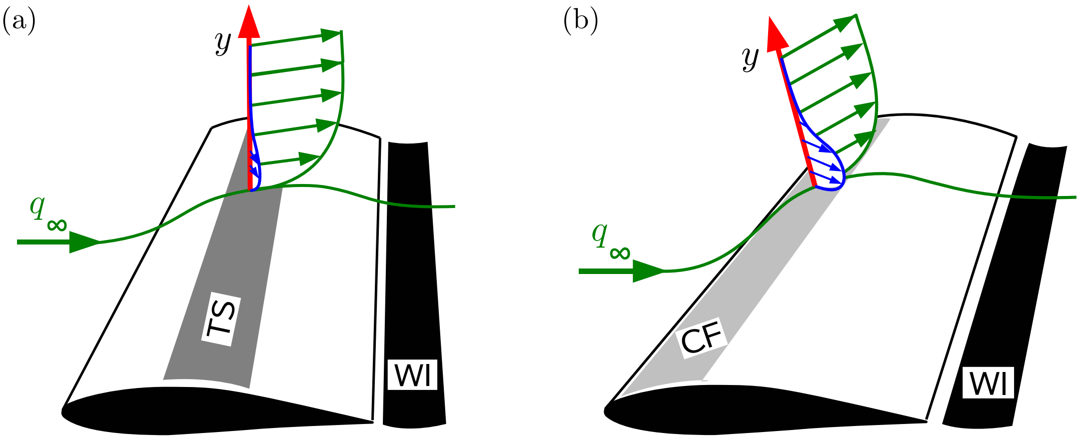

Figure 1.4. Sketch indicating the relevant instability mechanisms and the resulting transition regions on a swept wing depending on the sweep angle Λ (adapted from Oertel, Jr. and Stank, 1999): (a) transition in the mid-chord region of the wing due to Tollmien–Schlichting (TS) waves for rather small values of Λ and (b) crossflow-induced (CF) transition in the wing's leading-edge region for rather large Λ. The latter type of transition is caused by crossflow instabilities resulting from a sufficiently large crossflow velocity component (indicated in blue) inside the boundary layer. (WI stands for wake instabilities.)

process highly depends on the particular flow configuration: for rather small values of the sweep angle Λ, *streamwise instabilities* in form of Tollmien–Schlichting (TS) waves typically occur in the mid-chord region of a wing as sketched in figure 1.4(a). These instabilities are the consequence of an adverse pressure gradient in the downstream direction, and a favorable pressure gradient can be used to control them and thus delay transition considerably (see, e.g., Saric and Reed, 2003).

When changing the flow configuration, notably by increasing the sweep angle Λ, the laminar-turbulent transition process changes from a Tollmien–Schlichting (TS) to a crossflow-dominated (CF) transition due to *crossflow instabilities* as indicated in figure 1.4(b). As a consequence, the transition front moves toward the leading edge of the wing as, for instance, reported by Gray (1952). Furthermore, the favorable pressure gradient that stabilized the Tollmien–Schlichting waves now destabilize the crossflow vortices which leads to a laminar-turbulent transition farther upstream. Moreover, leading-edge curvature and sweep give rise to *leading-edge contamination* and *attachment-line instabilities* for large values of the leading-edge radius R and/or the sweep angle Λ. In summary, these features clearly demonstrate the delicate balancing act for the design of, for instance, advanced swept wings for high-performance aircraft. Since a profound understanding of compressible flow about swept wings in general, and of flow in the wing's leading-edge region in particular, is crucial for their optimal aerodynamic design, we focus our studies on attachment-line and crossflow instabilities.

In low-disturbance environments such as flight, boundary-layer transition to turbulence generally occurs through the growth of linear instabilities. As guidance for our investigation we rely on the roadmap suggested by Morkovin et al. (1994) (see figure 1.5) which has been deduced from an abundance of experiments and numerical simulations (see Reshotko, 1994, and references therein). It consists of a conceptual link between environmental disturbances and the onset of breakdown to turbulent fluid motion via five distinct paths. Even though for compressible flow about a swept blunt body multiple instability scenarios or a combination thereof are conceivable, we will concentrate on the low disturbance environment case given by path A (see figure 1.5 in grey). This path is characterized by (i) receptivity of the laminar flow to external perturbations, (ii) linear modal growth of boundary-layer-type instabilities, followed by (iii) non-linear breakdown into turbulence.

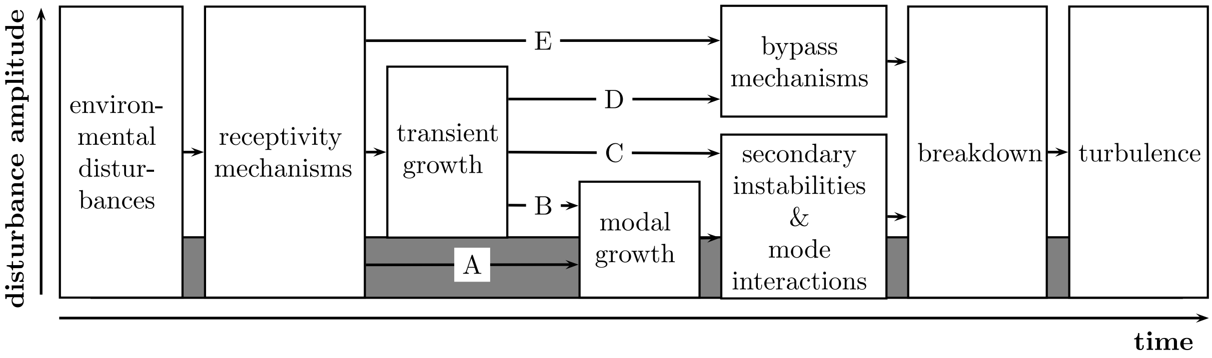

Figure 1.5. Roadmap to transition as suggested by Morkovin et al. (1994) (see Reshotko, 1994).

1.1.3 The sweep Reynolds number Re_θ

Experimentalists introduced the sweep Reynolds number Re_θ (based on the momentum thickness θ of the boundary layer) as the governing non-dimensional parameter for attachment-line flow. As we have seen in section §1.1.1, a critical value of $Re_\theta \approx 100$ has been found in several experimental investigations, and, to this day, it is still common practice in aircraft design to keep $Re_\theta < 100$ to ensure laminar flow along the attachment line of a swept wing (see, e.g., Joslin, 1996). Following Pfenninger (1977) and Poll (1985), an approximate relationship for Re_θ is given as (see Saric and Reed, 2003)

$$Re_\theta = 0.404 \left(\frac{q_\infty R \sin^2 \Lambda}{(1+\epsilon)\nu \cos \Lambda} \right)^{1/2} = 0.404 \left(\frac{u_\infty R}{(1+\epsilon)\nu} \right)^{1/2} \tan \Lambda, \tag{1.1}$$

where $u_\infty = q_\infty \cos \Lambda$ denotes the normal velocity, ν represents the kinematic viscosity of the fluid, and ϵ is the ellipticity of an equivalent ellipse[1]. Note that the factor of 0.404 in (1.1) was evaluated for incompressible flow (see, e.g., Poll, 1979).

As we can see, the leading-edge geometry described by the radius R as well as the sweep angle Λ has a strong influence on the stability behavior of leading-edge flow. Equation (1.1) further demonstrates that in order to ensure low values of Re_θ for certain flight conditions, defined by q_∞ and ν, it is necessary to have small values of R and/or Λ, as already discussed in section §1.1.2, to prevent unstable flow in the vicinity of the attachment line.

1.2 Linear stability theory

In its most general definition, linear stability theory is concerned with quantifying the behavior of infinitesimal perturbations about a finite-amplitude base state. If the small perturbations diverge from the finite-amplitude state, the flow is considered unstable; if the perturbed flow returns back to the base state, the flow is called stable. The stability property, of course, depends on the governing flow parameters such as, in our case, the sweep Reynolds number and the sweep Mach number, and their values at which the flow changes from stable to unstable are referred to as the critical parameters. The decomposition (A), see figure 1.6, into a base state $\phi_0(x,y,z,t)$ and a perturbation $\epsilon\phi'(x,y,z,t)$ is rather impractical in all its generality.

A further simplifying, but reasonable assumption is given by considering a steady base flow $\phi_0(x,y,z)$. As a consequence, the coefficients in the linearized[2] governing equations do no

---

[1] Increasing ϵ and thus changing the shape of the blunt body in the leading-edge region from cylindrical to increasingly elliptical has essentially the same effect as decreasing R.

[2] As a consequence of the linearization step, any information about the amplitude of the (modal) structures is lost.

$$\begin{array}{llcrrl}
\text{(A)} & \phi(x,y,z,t) & = & \phi_0(x,y,z,t) + \epsilon\phi'(x,y,z,t) & & \text{(general decomposition)} \\
\text{(B)} & \phi(x,y,z,t) & = & \phi_0(x,y,z) + \epsilon\widetilde{\phi}(x,y,z) & \mathrm{e}^{-\mathrm{i}\omega t} & \text{(steady base flow)} \\
\text{(C)} & \phi(x,y,z,t) & = & \phi_0(x,y) + \epsilon\widetilde{\phi}(x,y) & \mathrm{e}^{\mathrm{i}\beta z}\mathrm{e}^{-\mathrm{i}\omega t} & \text{(global approach)} \\
\text{(D)} & \phi(x,y,z,t) & = & f(x)\phi_0(y) + \epsilon\widetilde{\phi}(y) & g(x)\mathrm{e}^{\mathrm{i}\beta z}\mathrm{e}^{-\mathrm{i}\omega t} & \text{(semi-local approach)} \\
\text{(E)} & \phi(x,y,z,t) & = & \phi_0(y) + \epsilon\widetilde{\phi}(y) & \mathrm{e}^{\mathrm{i}\alpha x}\mathrm{e}^{\mathrm{i}\beta z}\mathrm{e}^{-\mathrm{i}\omega t} & \text{(local approach)}
\end{array}$$

Figure 1.6. Hierarchy of decompositions for linear stability theory: (A) general decomposition of the flow into a base state and a small-amplitude perturbation; (B) assumption of a steady base flow leading to a three-dimensional global stability problem (see, e.g., Bagheri et al., 2009); (C) global temporal stability problem with one homogeneous direction (our case); (D) semi-local approach taking advantage of the separability of the base flow; the x-dependence of the base flow, $f(x)$, yields an x-dependence of the perturbation $g(x)$ (e.g., $f(x) = x$ and $g(x) = He_n(x)$, as applied in Obrist and Schmid, 2003, for Hiemenz flow); (E) classical stability theory based on a local approach with one inhomogeneous direction y.

longer depend on time t, and a separation-of-variables approach can be applied which results in an exponential time behavior of the form $\mathrm{e}^{-\mathrm{i}\omega t}$ for the perturbations, see (B) in figure 1.6. The parameter ω which replaces the time dependence in the perturbation appears as an eigenvalue in the governing system of equations.

$$\omega\ \widetilde{\phi} = \mathcal{L}(\phi_0)\ \widetilde{\phi} \tag{1.2}$$

In this equation the linearized stability operator is denoted by $\mathcal{L}(\phi_0)$, and the eigenfunctions $\widetilde{\phi}$ describe the spatial shape of the modal structures.

If the specific flow configuration allows for further simplifications such as a homogeneous coordinate direction we can apply a separation-of-variables approach again in this direction. This step will eliminate the dependence on this specific coordinate direction at the expense of introducing an additional parameter. In this sense, our stability problem is reduced in size, but our parameter space has increased. For example in our case, we are justified in assuming a homogeneous spanwise z-direction (infinite span assumption) which results in a decomposition of type (C) and introduces a spanwise wavenumber β.

A common approach to linear stability theory (Mack, 1984) is the continued reduction of the stability problem to only one remaining inhomogeneous direction (usually taken as the transverse y-direction). The necessary assumptions for this approach, see (E) in figure 1.6, are often justifiable for generic and simple geometries but remain questionable for even moderately complex flow configurations.

It is noteworthy that an independence of the base flow on a particular coordinate direction is not the only possibility for a separation approach. As long as the base flow is generally separable, e.g., as is the case for Hiemenz flow with $\phi_0(x,y) = x\varphi_0(y)$, the perturbation can be separated as well, sometimes using analytical functions, sometimes using numerical solutions, see (D) in figure 1.6.

Local *vs.* global approach

It is evident from figure 1.6 that the natural progression from a general decomposition to a stability problem follows from (A) to (E). While the first simplifying steps may have been based on valid assumptions, the drastic step down to a local approach, level (E), has been necessary due to limited computer resources and a lack of powerful algorithms for large-scale eigenvalue problems. For this reason, there exists a large body of literature that applies local stability theory based on approach (E). However, with increasing availability of supercomputers as well as recent advances in iterative algorithms we are now in a position to progressively drop unnecessarily simplifying assumptions, to return to more general global approaches and thus to investigate the stability properties of more realistic flow configurations.

Temporal *vs.* spatial framework

In the global stability approach considered in this thesis, see (C) in figure 1.6, we assume real wavenumbers β and complex frequencies $\omega = \omega_r + \mathrm{i}\omega_i$. The real part of ω describes the frequency ω_r of the perturbations while its imaginary part represents the corresponding *temporal* growth rate ω_i. This assumption constitutes a temporal stability problem, where the eigenvalues ω describe the temporal long-term evolution of small-amplitude perturbations. For eigenvalues with negative imaginary parts ($\omega_i < 0$) the corresponding modal structures decay in time whereas eigenvalues with positive imaginary part ($\omega_i > 0$) grow without bounds within the linear framework and render the underlying base flow unstable.

On the other hand, if we assume a real temporal frequency ω but a complex spanwise wavenumber $\beta = \beta_r + \mathrm{i}\beta_i$, we arrive at the spatial stability problem, where β_r describes the spanwise disturbance wavenumber and β_i its corresponding *spatial* growth rate in the spanwise direction. This spatial approach has the advantage of more closely matching the conditions of an experimental setup but the disadvantage of leading to a more complicated numerical problem. While the (more commonly applied) temporal stability problem requires us to solve a linear eigenvalue problem for ω, the spatial stability problem yields a polynomial eigenvalue problem in β which is far more challenging to solve.

Both approaches have been used in the literature, and as recent examples, Robitaillié-Montané (2005) and Heeg (1998) studied the global stability of incompressible and compressible attachment-line flow in the temporal and the spatial framework, respectively, using a local flow model. In the present thesis, we will study a more comprehensive flow model employing the temporal stability framework. This provides the theoretical counterpart to the experimental studies discussed in section §1.1.1, namely, flight tests in a low-disturbance environment and wind-tunnel experiments with small-amplitude perturbations.

1.3 Outline of the thesis

The present thesis consists of two parts. In part I “Global stability of compressible flow about a swept parabolic body” an overview of the topic including the numerical tools employed in this work is presented, whereas part II “Articles” contains articles that appeared, are under review or in preparation. A short description of each article is given at the beginning of part II.

In the next chapter §2, we present our flow model for compressible flow in the leading-edge region of a swept blunt body. This flow model as well as the direct numerical simulation (DNS) code to compute flow fields, described in chapter §3, have been published in “Article 1”. The DNS-based global stability solver, which has been developed in “Article 2”, is outlined in chapter §4. Our results from a global stability analysis of compressible flow about a swept parabolic body are given in chapter §5, and these results are published in “Article 3 to 5”. We conclude the thesis and present an outlook in chapter §6.

Chapter 2

Flow Model: from physics to mathematics

As outlined in the previous chapter, the present thesis is concerned with the stability of compressible flow in the leading-edge region of a swept blunt body. Since we aim at studying a flow configuration that approximates, as closely as possible, the realistic flow situation in size and complexity, a flow model satisfying these requirements has to be defined first. This flow model consists of an approximation of the geometry, a suitable domain of investigation as well as a valid mathematical model, in form of governing equations and appropriate boundary conditions, in order to describe the flow physics inside the domain. Before presenting our flow model in section §2.2, we briefly revisit the existing literature on theoretical and numerical studies on the stability of swept leading-edge flow and discuss remaining questions. These studies have been motivated by a number of early experiments on crossflow instabilities, leading-edge contamination and attachment-line instabilities as summarized in section §1.1.1.

2.1 Previous theoretical and numerical studies

2.1.1 Attachment-line instabilities

First efforts to theoretically assess the stability of flow along the attachment line of a swept blunt body (see figure 2.1a) were made by Poll (1978, 1979). He studied the linear stability of incompressible attachment-line flow based on the Orr–Sommerfeld system using a quasi-parallel flow assumption by setting $u = 0$ for the wall-normal velocity. As a result, Poll demonstrated that the flow becomes linearly unstable to wave-like disturbances propagating along the attachment line for Reynolds numbers $Re_\theta > 270$. However, it was soon realized that non-parallel effects play an important role for the linear stability of this flow, and, as a consequence, the parallel flow assumption has been discarded.

In the following, a simplified model of the attachment-line boundary layer was studied by Hall et al. (1984). This model was based on swept Hiemenz flow (see figure 2.1c) — which represents a similarity solution of the incompressible three-dimensional Navier–Stokes equations for flow in the attachment-line region — and the Görtler–Hämmerlin assumption. This assumption takes the same linear x-dependence (chordwise direction) for the perturbation and the base flow. As a result, their neutral curve shows good agreement with the experimental findings for small-amplitude perturbations ($Re_{\theta,crit} \approx 230$, see section §1.1.1), and they report a critical Reynolds number $Re_{crit} = 583$ ($Re_{\theta,crit} = 235$)[1]. Subsequently, Spalart (1988) and Joslin (1995) — among others — confirmed the above results by investigating the swept Hiemenz flow model

---

[1] For incompressible flows $Re_\theta = 0.404Re$ (see section §1.1.3)

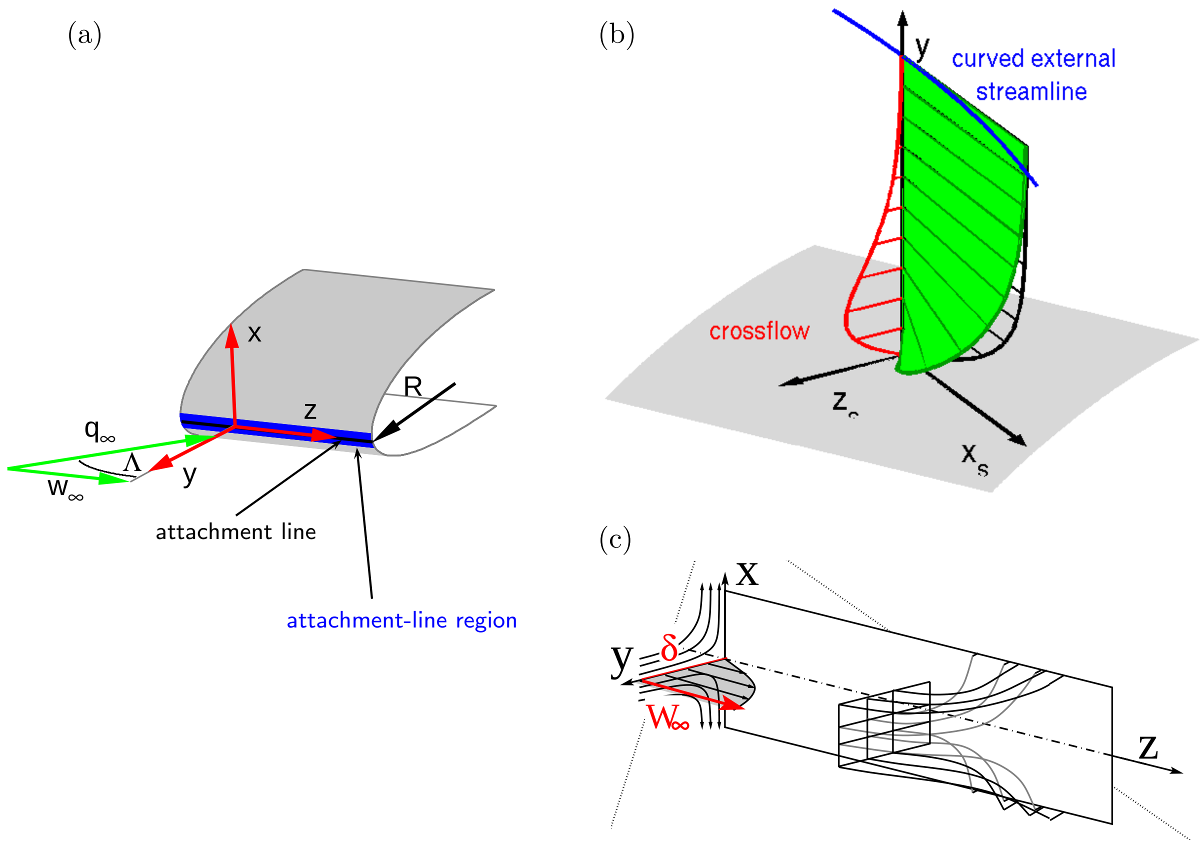

Figure 2.1. In early theoretical and numerical studies, viscous flow near the attachment line of a swept blunt body (a) was investigated using a local flow model for incompressible stagnation-point flow. This flow model is given by swept Hiemenz flow (c), where curvature and compressibility effects have been neglected (taken from Guégan et al., 2006). (b) Schematic of the three-dimensional boundary layer at a position (on the lower surface of the swept blunt body) downstream of the attachment line; x_s and z_s denote the local streamwise and transverse direction, respectively.

using direct numerical simulations (DNS) and thus helped to establish the critical Reynolds number $Re_{crit} = 583$ for attachment-line instabilities in incompressible flow.

In a subsequent study, Lin and Malik (1996) discarded the restrictive Görtler–Hämmerlin assumption and uncovered additional linearly unstable modes. They extended their analysis to compressible flows (Lin and Malik, 1995) and also assessed the stabilizing effect of leading-edge curvature on the stability of incompressible attachment-line flow (Lin and Malik, 1997). The swept Hiemenz flow model has further been studied by global stability theory for incompressible (Theofilis et al., 2003) and compressible flow (Heeg, 1998; Robitaillié-Montané, 2005). The latter investigations are complemented by DNS studies of Le Duc et al. (2006) who report a stabilizing effect of compressibility in the moderate Mach regime.

Subcritical instabilities

Flight tests as well as wind-tunnel experiments revealed that the value of the Reynolds number Re needs to be kept below 245 ($Re_\theta = 0.404Re < 100$) to ensure laminar flow along the attachment line if large-amplitude perturbations are present (see section §1.1.1). This raised the question of possible subcritical instabilities. In a first attempt to close the gap between the critical Reynolds number based on non-parallel linear stability theory ($Re_{crit} = 583$) and the critical value of $Re \approx 245$ from experiments, Hall and Malik (1986) studied large-amplitude disturbances using weakly nonlinear theory and temporal DNS (direct numerical solutions to the initial value problem). As a result, they obtained a subcritical value of $Re \approx 535$. In a further attempt a decade later, Balakumar and Trivedi (1998) computed and followed nonlinear steady states for swept Hiemenz flow and found a minimum critical value of $Re \approx 511$.

2.1.2 Crossflow instabilities

Farther downstream of the attachment line (see figure 2.1b), another type of instability, known as crossflow instabilities, have been experimentally observed as already mentioned in section §1.1.1. An imbalance between centrifugal forces and the streamwise pressure gradient induces curved streamlines throughout the boundary layer, and the resulting crossflow velocity gives rise to stationary or traveling crossflow vortices (Reed and Saric, 1989). In contrast to the viscous attachment-line instability, the crossflow instability is of inviscid type caused by an inflection point in the crossflow component of the three-dimensional base velocity profile (see figure 2.1b). Since the crossflow instability was observed to play a key factor for the design of laminar airfoils (see Saric and Reed, 2003), numerous theoretical and numerical efforts have been undertaken to study the stability of compressible crossflow vortices.

These studies used again local flow models — three-dimensional boundary-layer flow over planar geometries —, and they were mainly based on the parabolized stability equations (e.g. Herbert, 1997) or direct numerical simulations (e.g. Bonfigli and Kloker, 2007). For an overview of the current state-of-the-art the reader is referred to Saric et al. (2003); Bonfigli and Kloker (2007) and references therein.

Connecting attachment-line and crossflow instabilities

Similar to the question about the existence of subcritical instabilities, a possible connection of attachment-line and crossflow instabilities was discussed since the experimental findings of Poll (1979). In particular, the results of Spalart (1989) who obtained solutions off the attachment line that are strongly reminiscent of crossflow vortices have to be mentioned (his incompressible studies were based on direct numerical simulations and the swept Hiemenz flow model).

More recently, an attempt to establish a link between the two mechanisms has been undertaken by Bertolotti (1999). In his investigations, he continued the spatial evolution of higher-order attachment-line modes — which are distinct from the polynomial modes — in the chordwise direction using the parabolized stability equations (PSE). As a result, Bertolotti found that the continued attachment-line modes closely resemble the features and scales of crossflow instabilities.

2.1.3 Remaining questions

Despite these great efforts, a list of questions still remains: (a) can stability theory confirm the critical value of the Reynolds number $Re \approx 245$ ($Re_\theta \approx 100$), (b) what is the exact nature of the connection between attachment-line and crossflow instabilities, (c) what is the influence of acoustic instabilities which are known to exist for flat plate boundary-layer flows (see Mack, 1984), and (d) can we extract the global spectrum and gain a complete picture of the perturbation dynamics of the flow?

The list of remaining questions suggests that local flow models may have reached their limit, and, in order to extend our knowledge of flow stability and laminar-turbulent transition in the leading-edge region of a swept blunt body, it seems timely to base further investigations on a flow configuration that includes a substantially larger range of physical phenomena and that closer represents the realistic flow situation.

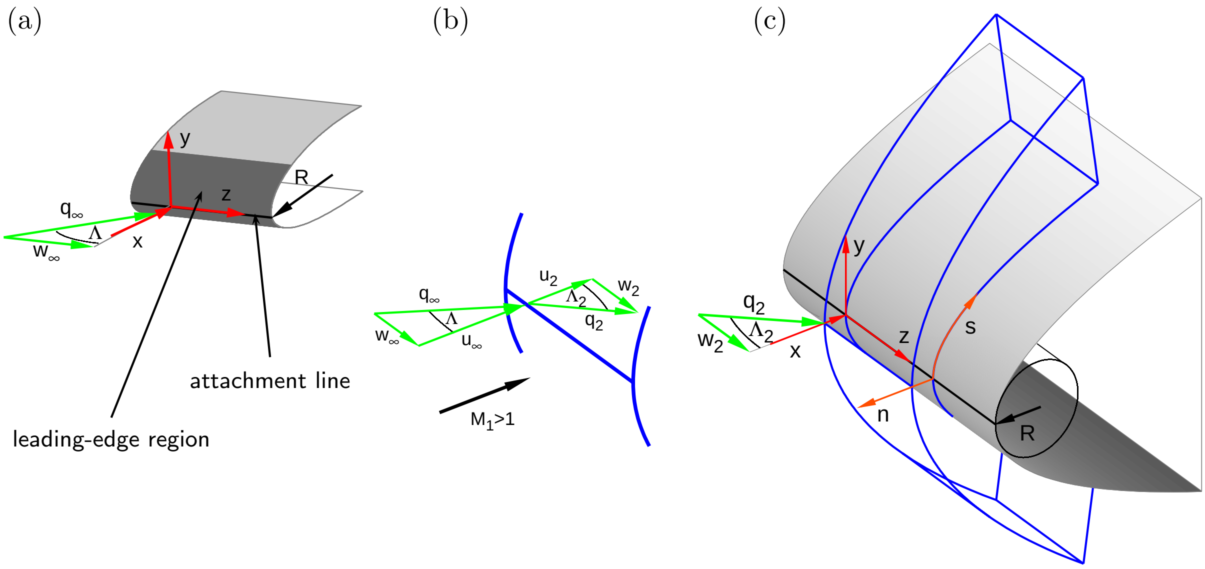

Figure 2.2. From the realistic flow situation to the flow model: compressible flow in the leading-edge region of a swept blunt body (a) is modeled by supersonic flow about a swept parabolic body (c). This flow model exhibits a detached bow shock at the inflow boundary, and a schematic of this bow shock with the relevant flow parameters upstream and downstream of the shock is displayed in (b).

2.2 Our flow model

In our flow model, compressible flow in the leading-edge region of a swept blunt body as marked in dark grey in figure 2.2(a) is modeled by supersonic flow about a swept parabolic body (see figure 2.2c). This parabolic body is assumed to be a rigid wall of infinite span in the spanwise z-direction, and its surface is given by

$$x(y) = \frac{1}{2R} y^2 \qquad \text{with} \qquad -\sqrt{2RL_s} \leq y \leq \sqrt{2RL_s}, \tag{2.1}$$

where R denotes the leading-edge radius of the body and L_s determines the size of the domain in the chordwise s-direction. Open outflow boundaries limit the domain in the latter direction. We further consider flow cases where the oncoming uniform flow is supersonic

$$M_1 = M_\infty \cos\Lambda > 1, \tag{2.2}$$

where M_∞ and M_1 denote the freestream Mach number and its component normal to the shock; as a consequence, the inflow boundary of the computational domain is defined by a detached unsteady bow shock, assumed to be an infinitely-thin moving discontinuity, in the wall-normal n-direction. The presence of such a detached bow shock allows the formulation of physically correct inflow boundary conditions.

The supersonic flow state upstream of the detached bow shock, denoted by the subscript $_\infty$, is obtained as a function of the freestream Mach number M_∞ and the freestream angle Λ, where the freestream pressure, p_∞, and temperature, T_∞, are computed using a given reference state. The Rankine–Hugoniot relations are then employed to calculate the flow quantities downstream of the shock, denoted by the subscript $_2$; figure 2.2(b) shows a schematic of the flow state upstream and downstream of the shock above the stagnation line ($s = 0$). The shock constitutes a sudden decrease in speed for the normal velocity $u_2 < u_\infty$, and, since the sweep velocity $w_2 = w_\infty$ remains unchanged, the flow angle downstream of the bow shock (the sweep angle Λ_2) is larger than the angle Λ of the freestream velocity q_∞. Additionally, the thermodynamic quantities, such as pressure p and temperature T, strongly increase across the shock. Both effects are stronger for larger values of M_1.

2.2.1 Features of our flow model

The generic flow model presented in figure 2.2(c) allows us to study the influence of leading-edge curvature, sweep and angle of attack — even though a zero angle of attack and thus symmetric flow is considered throughout the thesis — as well as compressibility, wall temperature and bow shock-interaction effects on the flow. This model thus comprises a multitude of geometric and physical features. Furthermore, our flow model represents a more realistic configuration that covers *simultaneously* attachment-line and crossflow vortex instabilities. Both types of instabilities are accommodated inside a very thin three-dimensional boundary layer which grows towards the outflow boundaries. Moreover, a curved bow shock leads to curved streamlines downstream of the shock resulting in a rotational inviscid flow field; in the presence of a bow shock, vorticity, acoustic and entropy waves are known to exist as well.

In summary, our flow model exhibits a rich perturbation dynamics on different spatial and temporal scales, and this fact is, as we will see, also reflected in the global spectrum.

2.2.2 Governing parameters

Compressible swept leading-edge flow is described by several physical and geometrical parameters such as sweep velocity, sweep angle and leading-edge radius, and these parameters can be combined to derive a set of non-dimensional numbers. The following six non-dimensional parameters govern our flow model: the leading-edge Reynolds number Re_R, the sweep Reynolds number Re_s, the sweep Mach number Ma_s, the wall temperature ratio θ_w, the Prandtl number Pr and the specific heat ratio γ. In what follows, these numbers are defined and their physical relevance is briefly discussed.

Sweep and curvature effects

As already discussed in section §1.1.3, the influence of sweep and curvature on the flow is governed by two Reynolds numbers[2], the leading-edge Reynolds number Re_R and the sweep Reynolds number Re_s. These non-dimensional numbers describe the outer flow and the flow inside the boundary layer, respectively, and we define them as

$$Re_R = \frac{u_2 R}{\nu_r}, \qquad Re_s = \frac{w_2 \delta}{\nu_r}. \tag{2.3}$$

Herein, the leading-edge radius R is used as the length scale for the outer flow, while δ represents a viscous length scale for the flow inside the boundary layer. This viscous length scale is obtained using the strain rate S_{th} at the wall, at the attachment line,

$$\delta = \left(\frac{\nu_r}{S_{th}}\right)^{1/2}, \tag{2.4}$$

where ν_r denotes the kinematic viscosity evaluated at recovery temperature T_r and stagnation pressure p_s. Since S_{th} is not known *a priori* for our flow model, we resort to the solution of potential flow around a circular cylinder with radius R (see figure 2.2c in black) and derive S_{th} by evaluating the chordwise derivative at the stagnation point.

$$v(x,y) = -2u_2 R^2 \frac{y(x-R)}{(y^2+(x-R)^2)^2}, \tag{2.5}$$

$$S_{th} = \left(\frac{\partial v}{\partial y}\right)_w = \frac{2u_2}{R}. \tag{2.6}$$

---

[2] Note that these two Reynolds numbers fully govern the incompressible case.

It is important to note that the sweep Reynolds number Re_s can be reformulated to display an explicit dependence on the leading-edge Reynolds number Re_R and the sweep angle Λ_2 as well as the leading-edge radius R. We have

$$Re_s = \left(\frac{u_2 R}{2\nu_r}\right)^{1/2} \tan\Lambda_2 = \left(\frac{Re_R}{2}\right)^{1/2} \tan\Lambda_2 = \frac{R}{2\delta}\tan\Lambda_2 \,. \tag{2.7}$$

As we can see, the sweep Reynolds number describes both the influence of sweep and leading-edge curvature. A similar dependence has already been discussed for the Reynolds number Re_θ, which is based on the momentum thickness θ, in section §1.1.3.

Compressibility effects

In the presence of compressibility, acoustic as well as wall temperature effects have to be accounted for, and these effects will be described by the sweep Mach number Ma_s and the wall temperature ratio θ_w. To this end, we define

$$Ma_s = \frac{w_2}{c_2}, \qquad \theta_w = \frac{T_w}{T_r}, \tag{2.8}$$

where c_2 stands for the speed of sound downstream of the shock, and the non-dimensional number θ_w represents the ratio of the temperature T_w at the wall and the recovery temperature T_r evaluated at the stagnation point. The remaining two non-dimensional numbers, the Prandtl number Pr and the specific heat ratio γ, govern the properties of the compressible fluid.

$$Pr = \frac{C_p \mu}{k}, \qquad \gamma = \frac{C_p}{C_v} \tag{2.9}$$

Herein, μ is the dynamic viscosity, k denotes the thermal conductivity, and C_p and C_v stand for the specific heat ratio at constant pressure and constant volume, respectively. The fluid is assumed to be dry air (with a gas constant $R_c = C_p - C_v = 287$ [$\mathrm{Jkg^{-1}K^{-1}}$]) modeled as a perfect gas with constant specific heat ratio $\gamma = 1.4$ and constant Prandtl number $Pr = 0.71$.

Kinematic viscosity ν_r at recovery temperature T_r and stagnation pressure p_s

As was the case for the strain rate S_{th} at the wall, the recovery temperature T_r, which is required to compute ν_r and to define θ_w, is not known in advance. Instead, we resort to results from Reshotko and Beckwith (1958) who theoretically investigated various flow properties of subsonic and supersonic flow about a yawed infinite cylinder. They give the following relation

$$T_r = T_\infty + RF \cdot (T_0 - T_\infty), \tag{2.10}$$

where $RF = 1 - (1-\zeta_w)\sin^2\Lambda$ denotes the stagnation-line recovery factor, and T_0 and T_∞ stand for the total and freestream temperature, respectively; they further provide a table (see table 2.1) with values of the local recovery factor ζ_w for selected freestream conditions (M_∞ and Λ) described by the ratio of T_0 and its component in the wall-normal direction $T_{0,N}$

$$\frac{T_0}{T_{0,N}} = \frac{1 + \frac{\gamma-1}{2} M_\infty^2}{1 + \frac{\gamma-1}{2} M_\infty^2 \cos^2\Lambda} \tag{2.11}$$

and a Prandtl number of $Pr = 0.7$. In our simulations, these values have been linearly interpolated to compute T_r for selected freestream conditions.

The (total) pressure p_s at the stagnation point is determined from

$$\frac{p_s}{p_\infty} = \frac{p_2}{p_\infty}\frac{p_s}{p_2} = \left(\frac{\gamma+1}{2} M_1^2\right)^{\gamma/(\gamma-1)} \left(\frac{\gamma+1}{2\gamma M_1^2 - (\gamma-1)}\right)^{1/(\gamma-1)}, \tag{2.12}$$

Table 2.1. Values of the local recovery factor ζ_w as a function of the temperature ratio $T_0/T_{0,N}$ for yawed stagnation-line flow at $Pr = 0.7$ (from Reshotko and Beckwith, 1958).

$T_0/T_{0,N}$	1.0	1.6	3.0	6.5
ζ_w	0.8485	0.8518	0.8567	0.8627

where $M_1 = M_\infty \cos\Lambda$ and p_∞ is the freestream pressure. This relation (2.12) follows from the Rankine–Hugoniot relation for pressure across a normal shock

$$\frac{p_2}{p_\infty} = 1 + \frac{2\gamma}{\gamma+1}\left(M_1^2 - 1\right) \tag{2.13}$$

and from the subsequent isentropic deceleration of the flow of an inviscid perfect gas into the stagnation point

$$\frac{p_s}{p_2} = \left(1 + \frac{\gamma-1}{2} M_2^2\right)^{\gamma/(\gamma-1)} \tag{2.14}$$

with

$$M_2^2 = \frac{(\gamma-1)M_1^2 + 2}{2\gamma M_1^2 - (\gamma-1)}, \tag{2.15}$$

where M_2 denotes the shock-normal Mach number downstream of the bow shock.

Nonlinear dependence of the governing parameters on the freestream conditions

In section §2.2.2, the governing parameters have been defined using the flow state downstream of the detached bow shock (see figure 2.2b), and this flow state depends, as we will see, nonlinearly on the freestream conditions, notably the freestream Mach number M_∞ and the freestream angle Λ. As an example, the sweep Mach number Ma_s as a function of M_∞ and Λ is obtained by using the definition of the sweep Mach number in (2.3) and the thermodynamic relation for the speed of sound for a perfect gas $c^2 = \gamma RT$.

$$Ma_s = \frac{w_2}{c_2} = \frac{w_\infty}{c_2} = \frac{u_\infty \tan\Lambda}{c_2} = \frac{c_\infty M_1 \tan\Lambda}{c_2} = \left(\frac{T_\infty}{T_2}\right)^{1/2} M_1 \tan\Lambda \tag{2.16}$$

Furthermore, employing the Rankine–Hugoniot relation for the temperature ratio T_2/T_∞, the sweep Mach number can be computed via

$$Ma_s = \frac{\gamma+1}{2} M_1^2 \tan\Lambda \left(\frac{1-\gamma}{2} + \gamma M_1^2\right)^{-1/2} \left(1 + \frac{\gamma-1}{2} M_1^2\right)^{-1/2}, \tag{2.17}$$

where, again, $M_1 = M_\infty \cos\Lambda$ denotes the shock-normal component of M_∞ (see figure 2.2b). For a shock-free configuration, this relation can be written as

$$Ma_s = M_1 \tan\Lambda \left(1 + \frac{\gamma-1}{2} M_1^2\right)^{-1/2}. \tag{2.18}$$

Both equations (2.17) and (2.18) reveal a nonlinear dependence of Ma_s on the freestream conditions, and this dependence is given in figure 2.3. In figure 2.3(a), we show Ma_s as a function of M_1 and Λ, where the solid blue and the dashed black lines represent constant values of Λ and M_∞, respectively. The freestream conditions of the present study are marked by the red cross at $M_\infty = 8.15$ and $\Lambda = 30\,^\circ$ yielding a shock-normal Mach number $M_1 = 7.06$ and a sweep Mach number $Ma_s = 1.25$. Furthermore, figure 2.3(b) demonstrates the evolution of the sweep

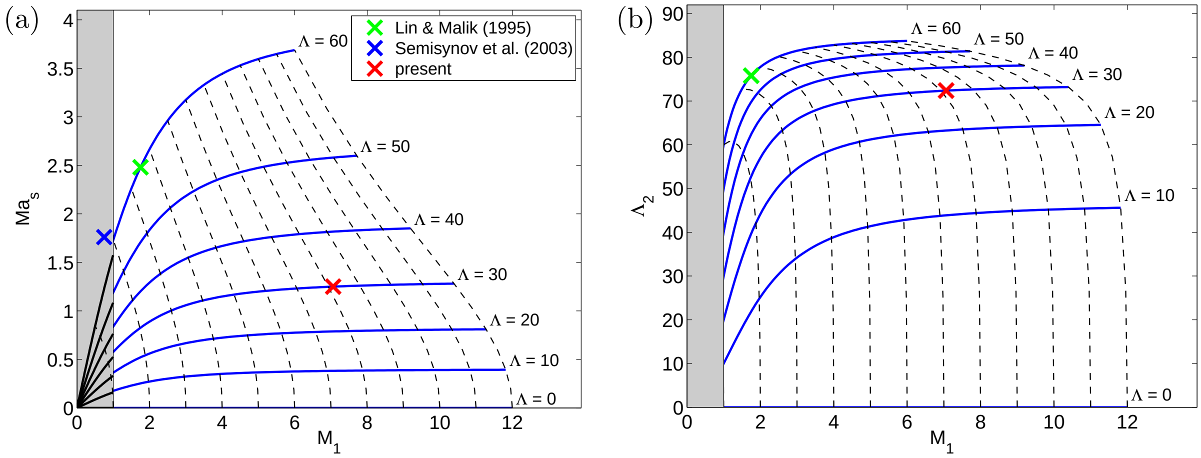

Figure 2.3. (a) Sweep Mach number Ma_s and (b) sweep angle Λ_2 as a function of the shock-normal Mach number $M_1 = M_\infty \cos\Lambda$ and the freestream angle Λ. The region in grey denotes the case where the oncoming flow is subsonic, i.e., $M_1 < 1$ (note that in this case $\Lambda_2 = \Lambda$), and blue lines represent constant values of Λ while dashed black lines depict constant values of M_∞. The red cross marks the freestream conditions of the present study, and the green and blue cross represent the flow conditions which have been used in previous investigations[3].

angle Λ_2 as a function of Λ and M_∞; since the sweep Reynolds number Re_s is a function of Λ_2 (see equation (2.7)), Re_s also depends on the freestream conditions in a nonlinear manner.

Consequently, if one seeks to perform simulations for a selected value of the sweep Mach number Ma_s, a nonlinear system has to be solved to compute M_1 as function of Λ and Ma_s. This task is accomplished employing a (standard) Newton method. Alternatively, equation (2.17) can be reformulated using $\tan\Lambda = u_2/u_\infty \tan\Lambda_2$ and the Rankine–Hugoniot relation for the velocity ratio u_2/u_∞ in order to obtain a dependence of Ma_s on M_1 and Λ_2. This dependence might be useful for a comparison of results with previous studies, when the sweep angle instead of the freestream angle is given.

2.3 Governing equations

In section §2.2, we presented our flow model with its geometry and governing parameters. Now, we have to specify mathematical models to describe the behavior of the flow as well as the properties of the fluid, i.e., dry air, within the considered domain. In this thesis, we will remain in the moderate Mach regime and thus only consider cases where air is known to behave as a continuum. All of the required equations can be found in a standard fluid-mechanical textbook such as the work of Kundu and Cohen (2002), but for completeness' sake we briefly state in what follows the equations used in our study.

2.3.1 The compressible Navier–Stokes equations

The dynamics of compressible viscous flow about a swept parabolic body as shown in figure 2.2(c) is governed by the compressible Navier–Stokes equations which describe the conservation of mass, momentum and energy for Newtonian fluids. These equations have been formulated for the pressure p, the velocities (u, v, w) and the entropy s, and, using Cartesian tensor notation, they read as follows:

---

[3] Lin and Malik (1995) investigated the linear stability of supersonic flow about a swept circular cylinder, and Semisynov et al. (2003) performed experimental and theoretical studies of compressible flow about a 68 ° swept circular cylinder.

$$\frac{\partial p}{\partial t} + u_j \frac{\partial p}{\partial x_j} + \gamma p \frac{\partial u_j}{\partial x_j} = (\gamma - 1)\left(\Phi + \frac{\partial}{\partial x_j}\left(k\frac{\partial T}{\partial x_j}\right)\right), \tag{2.19a}$$

$$\frac{\partial u_i}{\partial t} + u_j \frac{\partial u_i}{\partial x_j} + \frac{1}{\varrho}\frac{\partial p}{\partial x_i} = \frac{1}{\varrho}\frac{\partial}{\partial x_j}\left(\mu\left(\frac{\partial u_i}{\partial x_j} + \frac{\partial u_j}{\partial x_i}\right) - \frac{2}{3}\mu\frac{\partial u_k}{\partial x_k}\delta_{ij}\right), \tag{2.19b}$$

$$\frac{\partial s}{\partial t} + u_j \frac{\partial s}{\partial x_j} = \frac{R_c}{p}\left(\Phi + \frac{\partial}{\partial x_j}\left(k\frac{\partial T}{\partial x_j}\right)\right) \tag{2.19c}$$

with

$$\Phi \equiv \frac{1}{2}\mu\left(\frac{\partial u_i}{\partial x_j} + \frac{\partial u_j}{\partial x_i}\right)^2 - \frac{2}{3}\mu\left(\frac{\partial u_k}{\partial x_k}\right)^2 .$$

Herein, the variables ϱ and T denote the density and the temperature, and, as before, R_c, μ and k stand for the gas constant, the dynamic viscosity and the thermal conductivity, respectively; δ_{ij} represents the Kronecker delta. In a more compact form, this system of nonlinear partial differential equations can formally be written as

$$\frac{\partial \phi}{\partial t} = \mathcal{F}(\phi) \tag{2.20}$$

with $\phi = (p, u, v, w, s)^T$ and the nonlinear operator $\mathcal{F}(\phi)$ representing the spatial terms of the compressible Navier–Stokes equations. For the curvi-linear formulation of the above system of equations (2.19a–c), which will be used in our numerical implementation, the reader is referred to Mack and Schmid (2009). A set of consistent boundary and initial conditions will be discussed in chapter §3 when their implementation is described.

Thermodynamic relations

We further consider the motion of dry air modeled as a calorically perfect gas, and, employing Gibbs fundamental relation $dh = Tds + dp/\varrho$ with $dh = C_p dT$ as well as the equation of state for a perfect gas $p = \varrho R_c T$, the thermodynamic density ϱ and temperature T are found via the following equations of state

$$\varrho = p^{1/\gamma} \exp\left(-\frac{s}{C_p}\right), \tag{2.21}$$

$$T = \frac{1}{R_c} p^{\gamma - 1/\gamma} \exp\left(\frac{s}{C_p}\right). \tag{2.22}$$

Material laws

At this point, we are left with an open system of seven equations where two properties of the fluid, i.e., the dynamic viscosity μ and the thermal conductivity k, remain unknown. These properties will depend on the temperature T, and this dependence is modeled by Sutherland's and Fourier's law, respectively. We have

$$\mu = \mu_0 \left(\frac{T}{T_0}\right)^{\frac{3}{2}} \frac{T_0 + S}{T + S}, \tag{2.23}$$

$$k = \frac{C_p}{Pr}\mu . \tag{2.24}$$

In the former equation, $S = 110.4$ [K] denotes the Sutherland temperature (for air at ambient conditions), T_0 is the reference temperature (chosen as the total temperature), and μ_0 represents the reference viscosity for the latter temperature.

#	equation/relation
(1–5)	compressible Navier–Stokes equations
(6)	$\varrho = \varrho(p,s) = pR_cT = p^{1/\gamma} \exp\left(-\frac{s}{C_p}\right)$
(7)	$T = T(p,s) = \frac{1}{R_c} p^{\gamma-1/\gamma} \exp\left(\frac{s}{C_p}\right)$
(8)	$\mu = \mu(T) = \mu_0 \left(\frac{T}{T_0}\right)^{\frac{3}{2}} \frac{T_0 + S}{T + S}$
(9)	$k = k(T) = \frac{C_p}{Pr} \mu(T)$

Table 2.2. Governing equations and relations for the nine unknowns.

2.3.2 The linearized Navier–Stokes equations

The evolution of small disturbances as studied in a linear stability analysis is governed by the equations for the perturbations. These equations are derived by linearizing the compressible Navier–Stokes equations, the thermodynamic relations and the material laws; for the sake of clarity, these equations and relations are summarized in table 2.2. To this end, we decompose a flow field $\phi = (p,u,v,w,s)^T$ into a (steady) base state[4] ϕ_0 and a fluctuation state ϕ'.

$$\phi(x,y,z,t) = \phi_0(x,y,z) + \epsilon\phi'(x,y,z,t) \qquad \text{with} \qquad \epsilon \ll 1 \tag{2.25}$$

By inserting (2.25) into the nonlinear Navier–Stokes equations and by keeping only terms of $\mathcal{O}(\epsilon)$ one arrives at the equations for the perturbations. As an example, the Euler part of these equations, i.e., the left-hand side in (2.19a–c), reads as

$$\frac{\partial p'}{\partial t} + u_{0,j}\frac{\partial p'}{\partial x_j} + u_j'\frac{\partial p_0}{\partial x_j} + \gamma p_0 \frac{\partial u_j'}{\partial x_j} + \gamma p' \frac{\partial u_{0,j}}{\partial x_j} = 0, \tag{2.26a}$$

$$\frac{\partial u_i'}{\partial t} + u_{0,j}\frac{\partial u_i'}{\partial x_j} + u_j'\frac{\partial u_{0,i}}{\partial x_j} + \frac{1}{\varrho_0}\frac{\partial p'}{\partial x_i} - \frac{1}{\varrho_0^2}\frac{\partial p_0}{\partial x_i}\varrho' = 0, \tag{2.26b}$$

$$\frac{\partial s'}{\partial t} + u_{0,j}\frac{\partial s'}{\partial x_j} + u_j'\frac{\partial s_0}{\partial x_j} = 0. \tag{2.26c}$$

The linearized right-hand side of the Navier–Stokes equations and the linearized form of the material laws (2.23) and (2.24) can be found in a similarly straight-forward manner. Furthermore, using Gibbs fundamental relations, the perturbation quantities for the density and the temperature are obtained as

$$\varrho' = \frac{\varrho_0}{\kappa p_0} p' - \frac{\varrho_0}{C_p} s', \tag{2.27}$$

$$T' = \frac{1}{\varrho_0 C_p} p' + \frac{T_0}{C_p} s'. \tag{2.28}$$

In addition, we are required to specify physically consistent boundary conditions for the perturbation quantities at the boundary points in our flow model (see figure 2.2c). At the wall we employ the no-slip conditions which set all velocity components to zero, i.e, $u' = v' = w' = 0$, and, since this wall is assumed adiabatic, the heat-flux normal to it is zero as well.

---

[4] The base flow might also be time dependent, but here we concentrate on steady states.

$$\frac{\partial T'}{\partial n} = \frac{1}{\varrho_0}\frac{\partial p'}{\partial n} - \frac{1}{\varrho_0^2}\frac{\partial \varrho_0}{\partial n}p' + T_0\frac{\partial s'}{\partial n} + \frac{\partial T_0}{\partial n}s' = 0 \tag{2.29}$$

This equation (2.29) follows from the wall-normal derivative of (2.28); furthermore, the pressure p' has to satisfy the compatibility condition which is ensured using the momentum equation in the wall-normal direction as described in Robitaillié-Montané (2005). Away from the wall all perturbation quantities are assumed to decay to zero in the freestream. The outflow boundaries as well as the periodic direction will be incorporated in the spatial discretization schemes, where one-sided stencils are employed for the outflow boundaries (as suggested by Heeg, 1998). An initial condition is not required since no time marching will be performed.

Finally, the linearized Navier–Stokes equations for the perturbations, the relations for the remaining disturbance quantities and the boundary conditions can be combined to obtain the more compact form

$$\frac{\partial \phi'}{\partial t} = \mathcal{L}(\phi_0)\phi', \tag{2.30}$$

where $\mathcal{L}(\phi_0)$ denotes the linear stability operator. We will later come back to this equation.

Chapter 3

Direct Numerical Simulations: computing flow fields

Now, that we have defined our flow model to study flow in the leading-edge region of a swept blunt body, we introduce our direct numerical simulation (DNS) code to compute flow fields. Over the past decades direct numerical simulation (DNS) has established itself as a widely used tool in computational fluid dynamics to address and study complex flow problems. It represents an approach to compute flow fields by approximating the exact solutions of the continuous Navier–Stokes equations at discrete points in space and discrete instances in time. The spatial discretization results in a computational grid, and direct numerical simulations aim at capturing all relevant physical features of the flow by spatially resolving all dynamic scales on this grid. Consequently, direct numerical simulations limit modeling efforts to a minimum and thus represent our method of choice for producing high-quality flow fields which will later be used to extract stability information. In what follows, we start with an overview of implementation details of our direct numerical simulations in section §3.1, show computed (steady) flow fields in section §3.2 and present results from a long-term integration of the initial value problem in section §3.3.

3.1 Overview of the numerical implementation

3.1.1 Grid generation

In our direct numerical simulations (DNS), flow fields are computed by solving the nonlinear compressible Navier–Stokes equations (2.19a–c) in a curvi-linear formulation on a three-dimensional, time-dependent grid shown in figure 3.1(a). The time dependence of the grid stems from the fact that the detached bow shock, modeled as a discontinuity surface, defines the moving grid line at the inflow boundary (see figure 3.1b in blue).

This non-uniformly distributed, body-fitted grid is generated via a three-step process as illustrated in figure 3.2. This process consists of (a) the formation of a unit cube with uniformly-distributed grid points in the normal ξ-, the chordwise η- and the spanwise ζ-direction[1], (b) the redistribution of these grid points in ξ and η in order to sufficiently resolve physically relevant regions in our flow model, i.e., the region near the stagnation line ($\xi = 1$, $\eta = 0.5$) as well as close to the wall ($\xi = 1$), and (c) the parabolic mapping of the redistributed unit cube. In the latter step, the unit cube is mapped onto the physical domain, in which the detached bow shock and the surface of the parabolic body define the limiting grid lines in the n-direction, using a conformal mapping. Finally, the metric coefficients ξ_x, ξ_y, ξ_z, η_x, etc., which need to be specified

---

[1] Note that the domain is inhomogeneous in the ξ- and η-direction, but homogenous in the spanwise ζ-direction which is a consequence of the infinite span assumption in z.

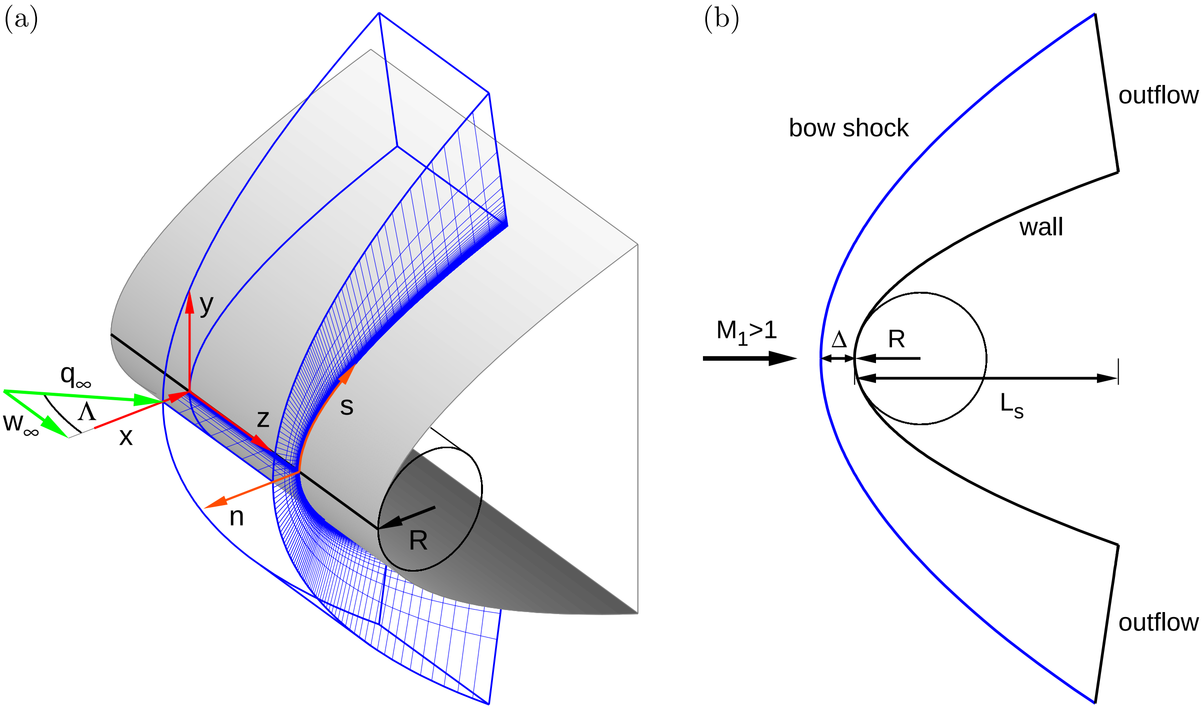

Figure 3.1. (a) Sketch of our three-dimensional flow model showing the parabolic body (in grey), the employed coordinate systems and the body-fitted computational grid with its grid-point distribution (in blue). (b) Schematic of the physical domain in the s-η-plane, its boundary conditions and the relevant geometric parameters; the detached bow shock is depicted in blue.

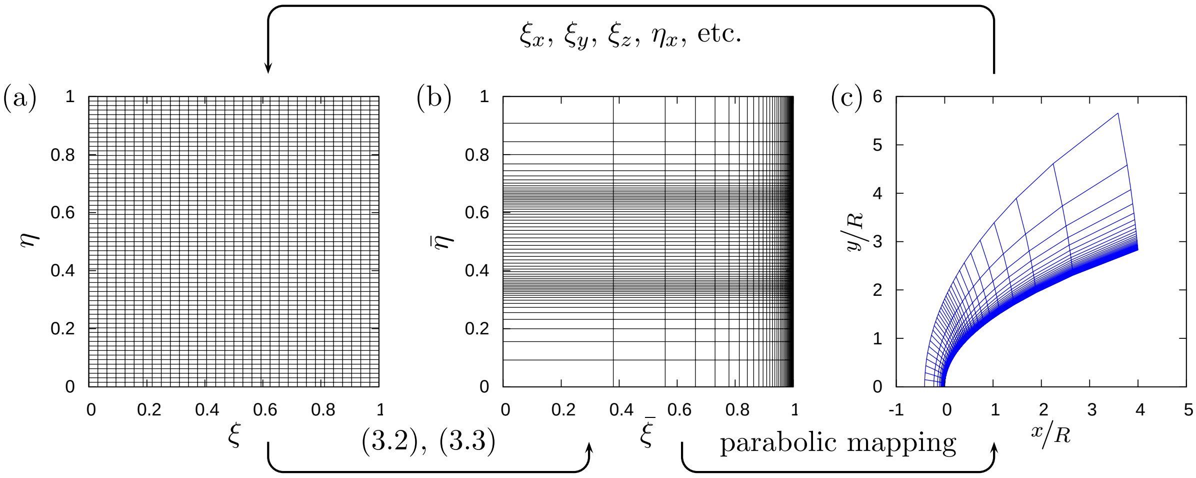

Figure 3.2. Steps of the grid generation process: (a) uniformly-distributed unit cube in the computational domain (ξ, η, ζ, t), (b) unit cube with redistributed grid points and (c) upper half of the body-fitted grid in the physical domain (x, y, z, t); for sake of clarity only every fourth and eight grid point are shown in the ξ- and η-direction, respectively, and $L_s = 0.4$ [m] and $R = 0.1$ [m] have been used in the parabolic mapping.

in the curvi-linear formulation of the Navier–Stokes equations, are obtained by differentiating the body-fitted grid (x, y, z) with respect to (ξ, η, ζ) and inverting the resulting Jacobian matrix. This is accomplished numerically using the same higher-order central schemes as for the spatial derivatives of the dependent variables.

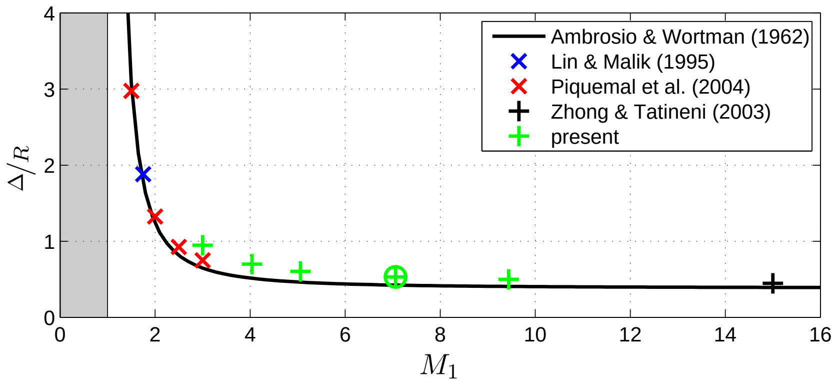

Figure 3.3. Evolution of the normalized shock detachment distance Δ/R as a function of M_1: empirical correlation (3.1) as proposed by Ambrosio and Wortman (1962), and numerically obtained values for cylindrical (x) and parabolic bodies (+)[2]; subsonic region in grey. The circled plus marks the value of M_1 for the present studies.

3.1.2 Domain size

The parabolic mapping requires us to specify the leading-edge radius R of the parabolic body, the (initial) shock detachment distance Δ (at $s = 0$) of the bow shock, and the size of the domain in the chordwise direction, L_s, (see figure 3.1b). In addition, the extension of the domain in the spanwise direction, L_z, has to be chosen. The first parameter, the leading-edge radius R, describes the geometry of the parabolic body, and this parameter is chosen as constant; i.e., $R = 0.1$ [m] in the present thesis. Experimentalists would set this parameter by choosing a certain leading-edge geometry for their experimental model.

The second parameter, the shock detachment distance Δ, defines the position of the detached bow shock. Since this bow shock is modeled as a moving discontinuity surface whose physically correct position and shape is not known in advance and furthermore changes in time, an initial guess for the position and shape of the corresponding grid line is required. We already assumed this grid line to be parabolic in the grid generation process in section §3.1.1; to further specify its initial position, we resort to the following empirical correlation (Ambrosio and Wortman, 1962)

$$\frac{\Delta}{R} = 0.386 \exp\left(\frac{4.67}{M_1^2}\right), \tag{3.1}$$

where M_1 denotes the shock-normal Mach number at $s = 0$ (see figure 3.1b), to compute Δ. This expression results from a correlation of experimental data for supersonic and hypersonic flow around circular cylinders with radius R (see Billig, 1967), and a comparison of values for Δ/R calculated using (3.1) with numerically obtained values (evaluated for steady state solutions) for cylindrical and parabolic bodies is given in figure 3.3. It can be seen that, for both body shapes, (3.1) provides a good estimate as an initial guess for Δ; however, this estimate deteriorates for parabolic bodies as M_1 is decreased. We can also see that the extent of the domain in the normal n-direction (see figure 3.1) largely depends on the shock-normal Mach number; for smaller values of M_1 the domain is enlarged and thus an increasing number of grid points will be required in the n-direction.

We are left with specifying the proper limit of the domain at the outflow boundaries by choosing the third parameter L_s. As discussed in section §2.2.1, our flow model comprises a multitude of dynamical structures; in particular, three-dimensional boundary-layer instabilities which appear in form of vortical structures downstream of the stagnation line are expected

---

[2] Lin and Malik (1995) investigated the linear stability of supersonic flow about a swept circular cylinder, Piquemal et al. (2004) computed supersonic viscous flow about a circular cylinder using a Brinkman-penalization method, and Zhong and Tatineni (2003) performed receptivity studies on hypersonic flow about a parabolic body.

to dominate the flow situation for a large parameter range. To accommodate these vortical structures the physical domain has to extend sufficiently far in the chordwise s-direction, and a value of $L_s = 0.4$ has been found to satisfy this requirement. The last parameter which is given by the size of the domain in the periodic z-direction, L_z, will be considered when it is needed.

3.1.3 Spatial resolution

The quality and accuracy of flow simulations and flow analyses not only depend on the proper size of the domain but also on the resolution in space. This resolution has to be sufficient to capture all relevant physical features of the flow, and, in our case, three types of computations, each with its specific requirement, can be distinguished: (i) computations of steady state solutions, (ii) stability studies of coherent structures and (iii) simulations of transition and turbulence. The latter case, which requires us to resolve all spatial scales down to the Kolmogorov length, is beyond the scope of the present work.

The computation of steady state solutions as well as the investigation of boundary-layer instabilities, which are the focus of the present work, requires us to cluster grid points toward the wall to sufficiently resolve the boundary layer. Furthermore, the resolution of vortical structures inside the boundary layer necessitates a grid-point clustering in the leading-edge region of the parabolic body, and for guidance we can rely on the results of Sesterhenn (2004). The chosen grid-point distribution is indicated in figure 3.1(a). The former grid stretching (Anderson et al., 1988) clusters grid points towards the parabolic body. It amounts to computing

$$\bar{\xi} = \frac{\kappa \xi}{1 - \kappa + \xi(2\kappa - 1)}, \tag{3.2}$$

where $\xi \in [0, 1]$ and $\bar{\xi} \in [0, 1]$ denote the uniformly-spaced and stretched grid points, respectively, and κ is the stretching parameter. As a result, this function maps the interval $[1/2, 1]$ to $[\kappa, 1]$ and thus clusters half the grid points in the latter interval. The values of n_1 and κ for the present study are given in table 3.1.

Table 3.1. Grid stretching in n

n_1	κ
128	0.95
256	0.92

To further cluster grid points in the leading-edge region of the parabolic body, a semi-analytical technique based on several error functions is employed in the η-direction. In this technique the redistribution of the grid points is described by a second-order ordinary differential equation

$$\frac{d^2\bar{\eta}}{d\eta^2} - \frac{f_{gsr}(\eta)}{\Delta\eta}\frac{d\bar{\eta}}{d\eta} = 0, \tag{3.3}$$

where $\Delta\eta$ denotes the grid spacing of the equi-spaced grid with $\eta \in [0, 1]$, and $f_{gsr}(\eta) = (\Delta\bar{\eta}_{i+1} - \Delta\bar{\eta}_i)/\Delta\bar{\eta}_i$ represents the relative grid stretching ratio at the location $\bar{\eta}_{i+1}$ of the stretched grid. This grid stretching ratio function $f_{gsr}(\eta)$ is constructed using a linear combination of m error functions, each with its own control parameters $(a_j, \sigma_j, b_j, e_j)$.

$$f_{gsr}(\eta) = \frac{1}{2}\sum_{j=1}^{m} a_j \left(\operatorname{erf}\left(\sigma_j(\eta - b_j)\right) + (-1)^{e_j}\right) \tag{3.4}$$

In order to obtain the grid points $\bar{\eta}$ of the stretched grid equation (3.3) has to be integrated twice; the first integration can be performed analytically, whereas the second integration was done numerically using Simpson's rule. This grid stretching technique was chosen due to its flexibility in locally refining the grid in the leading-edge region, and, in this work, four error functions are employed to redistribute n_2 grid points in the chordwise direction. Furthermore, pairs of error functions have been chosen to obtain a symmetric grid distribution with respect to the stagnation line, and their control parameters are given in table 3.2.

Table 3.2. Grid stretching in s; control parameters of the four error functions.

n_2	$a_{1,2}$	$a_{3,4}$	$\sigma_{1,2}$	$\sigma_{3,4}$	$b_{1,2}$	$b_{3,4}$	$e_{1,3}$	$e_{2,4}$
255	0.085	-0.025	7	15	0.21	0.45	2	1
511	0.085	-0.022	5	10	0.14	0.40	2	1

3.1.4 Details of the numerical scheme

To finally solve the governing equations on the body-fitted grid displayed in figure 3.1(a), numerical schemes for the discretization in space and time together with the previously described boundary conditions have to be implemented. As sketched in figure 3.1(b), the physical domain is limited by a detached unsteady bow shock in the normal direction, and this bow shock serves as a distinct inflow boundary condition which is incorporated via a shock-fitting technique (Moretti, 1987). In this technique the local shock-normal velocity is determined by a characteristic compatibility equation downstream of the shock, and the flow variables across the shock are governed by the Rankine–Hugoniot relations. Along the surface of the body no-slip boundary conditions in conjunction with an adiabatic wall[3] are employed. At the chordwise edges of the computational domain characteristic non-reflecting boundary conditions are imposed, and periodic spatial differentiation schemes are applied in the homogeneous z-direction (infinite span assumption).

For the discretization in space we resort to higher-order compact finite-difference schemes with symmetric stencils (Lele, 1992; Adams and Shariff, 1996). Due to the spectral-like resolution of these schemes as well as their narrow finite-difference stencils — which is necessary to obtain stable boundary closures for high-order schemes — , compact schemes have become popular for direct numerical simulations (DNS), and today they are widely used in computational fluid dynamics (CFD) and computational aero-acoustics (CAA). However, compact schemes with symmetric stencils are known to be sensitive to boundary condition formulation and aliasing errors, and consequently they are susceptible to numerical instabilities. Inherently dissipative numerical schemes can be used to cope with this problem, and among these techniques we resort to CULD, a fifth-order compact upwind low-dissipation scheme as designed by Adams and Shariff (1996). To take further advantage of the CULD scheme, the governing equations have been recast in a characteristic-type formulation (Sesterhenn, 2001), where the Euler part, i.e., the left-hand side in (2.19a–c), is decomposed into plane acoustic, shear and entropy waves. As a consequence, the propagation of these waves can be computed depending on their propagation direction using an upwind scheme such as CULD. The dissipative and diffusive terms, i.e., the right-hand side in (2.19a–c), are discretized using a sixth-order central compact scheme in conjunction with a fourth- and third-order scheme for boundary closure (Lele, 1992).

---

[3] Note that this implies a wall temperature ratio of $\theta_w = 1$.

The semi-discretized system of equations

$$\frac{d\boldsymbol{\phi}}{dt} = \mathbf{F}(\boldsymbol{\phi}), \tag{3.5}$$

where $\mathbf{F}$ represents the discretized right-hand side of the nonlinear Navier–Stokes equations, is integrated in time via an explicit fourth-order low-storage Runge–Kutta scheme (Kennedy et al., 2000). To ensure the numerical stability of the time integration, a stability condition proposed by Müller (1990) is employed to control the time step. For further details of the numerical scheme as well as the direct numerical simulations (DNS) in general the reader is referred to Mack and Schmid (2009).

3.2 Base flow

A linear stability analysis amounts to computing and classifying the various types of instability mechanisms, their modal structure in space and their temporal behavior characterized by the disturbance growth and frequency. In a first step towards such an analysis we need to compute a steady base flow. In what follows, we first motivate our choice of the governing parameters and then present the computed steady state solutions.

3.2.1 Choice of the governing parameters

The present investigations are based on the direct numerical studies of Sesterhenn (2004) who considered flow situations where the oncoming flow is hypersonic, i.e., the shock-normal Mach number is $M_1 > 3$. As freestream conditions he chose a Mach number of $M_\infty = 8.15$ and an angle of $\Lambda = 30\,^\circ$ yielding a sweep Mach number of $Ma_s = 1.25$; the resulting values for the shock-normal Mach number upstream, M_1, and downstream, M_2, of the bow shock and the sweep angle Λ_2 are given in table 3.3. We will use the same freestream conditions to compare the present results with the findings of Sesterhenn (2004).

Table 3.3 also shows the computed values of the freestream pressure p_∞, the freestream temperature T_∞ and the freestream Reynolds number Re_∞, where a total temperature $T_0 = 728$ [K] and a total pressure $p_0 = 1.55 \cdot 10^6$ [Pa] have been used as a reference state. These freestream conditions result in a value of $S_{th} = 3704$ [1/s] for the strain rate at the wall (see equation (2.6)), and this value will be used later to normalize the frequency and the associated growth rate of the computed instabilities. The freestream Reynolds number is defined as $Re_\infty = 2q_\infty R\rho_\infty/\mu_\infty$, where a leading-edge radius $R = 0.1$ [m] is used as the reference length scale; the value displayed in table 3.3 has been computed for a sweep Reynolds number of $Re_s = 800$. For the definition of the governing parameters the reader is referred to section §2.2.2.

Table 3.3. Overview of the flow quantities and parameters for our choice of the governing parameters: $Re_s = 800$, $Re_R = 129136$, $Ma_s = 1.25$ and $\theta_w = 1$.

M_∞	Λ	p_∞ [in Pa]	T_∞ [in K]	M_1	M_2	Λ_2	Re_∞
8.15	$30\,^\circ$	140.38	50.93	7.06	0.397	$72.4\,^\circ$	$3.53 \cdot 10^6$

This choice for the governing parameters leads to a supersonic flow in the spanwise z-direction, and, based on the existing literature for compressible stagnation-point and boundary-layer flow, appreciable compressibility effects are expected. Furthermore, the compressibility effects in the normal and the spanwise direction crucially depend on the position in the domain, and, as we will see in the next section, subsonic as well as supersonic flow regimes are present. Moreover, according to the findings of Sesterhenn (2004) this flow configuration will be unstable to boundary-layer instabilities.

3.2.2 Computation of steady states

Steady state solutions $\phi_0(x, y, z) = (p_0, u_0, v_0, w_0, s_0)^T$ are reached by integrating the discretized governing equations in time using direct numerical simulations. This procedure is possible since the flow problem is stable with respect to two-dimensional perturbations thus allowing a simple time-integration toward a steady state solution. As a consequence, more sophisticated techniques such as (Jacobian-free) Newton–Krylov techniques (Knoll and Keyes, 2004) or selective frequency damping (Åkervik et al., 2006) can be avoided. Nevertheless, even in our case these techniques may substantially reduce the computational time to reach a steady state solution.

Furthermore, the assumption of infinite span permits us to eliminate the z-dependence, but not the w-component, from $\phi_0(x, y, z)$ and to reduce the computations to a problem with only two independent variables x and y. From this solution the full three-dimensional base flow can be recovered.

Initial condition

As an initial condition in (3.5) we extend the values p_2, u_2, v_2, w_2, s_2 of the pressure, the velocities and the entropy along the grid line downstream of the bow shock, in the normal direction toward the wall. To this end, the pressure is chosen as constant, and a potential mapping is employed to calculate the remaining flow quantities such that they satisfy the boundary conditions at the wall. This choice was tested for a number of freestream conditions (see green symbols in figure 3.3) and was found to give robust direct numerical simulations.

It is worth mentioning that initial conditions which better approximate the solution can be found. However, these conditions require in general a rather large effort concerning the implementation, but do not show a significant computational benefit for our flow model.

Base flow

The converged three-dimensional base flow for $Re_s = 800$, $Re_R = 129136$, $Ma_s = 1.25$ and $\theta_w = 1$ is visualized in figure 3.4. In figure 3.4(a) and (b) we display the temperature T and pressure field p, and for the present choice of flow parameters we obtain a maximum temperature $T = 703$ [K] and a maximum pressure $p = 9076$ [Pa] at the stagnation point. The values of these quantities decrease toward the outflow boundaries. The (previously discussed) subsonic and supersonic regions of the flow in a plane normal to the parabolic body are indicated in figure 3.4(a), where the distribution of the Mach number based on the u- and v-velocity is shown; the iso-contour line in red represents the sonic line. It can be seen that the flow is subsonic near the attachment line, and thus acoustic waves may lead to a strong interaction between the boundary layer and the detached bow shock. This is in contrast to the flow situation further downstream of the attachment line where the flow exhibits an increasingly supersonic character.

In figure 3.4(b), we further visualize the three-dimensional velocity field in terms of streamlines. The typical curvature of these streamlines in the inviscid outer flow region, near the attachment line and inside the boundary layer reveals a highly three-dimensional boundary layer flow, in particular, downstream of the stagnation line. In addition, the streamlines describe a local and nearly two-dimensional flow field in the vicinity of the attachment line, and, as this flow field evolves in the chordwise direction, the thickness of the boundary layer δ_{99} grows by about a factor of 6 from 2.38δ (at $s_w = 0$) to 14.5δ (at $s_w = 2604\delta$); the variable s_w denotes the surface arclength along the parabolic body[4]. This boundary-layer growth is illustrated in figure 3.4(c), where we plot the spanwise w-velocity at selected positions in the s-direction (see legend). As already mentioned before, as a consequence of the infinite span assumption, no boundary-layer growth exists in the spanwise direction.

---

[4] $s_w(x) = \sqrt{x}\sqrt{x + R/2} + R/2 \ln((\sqrt{x} + \sqrt{x + R/2})/\sqrt{R/2})$

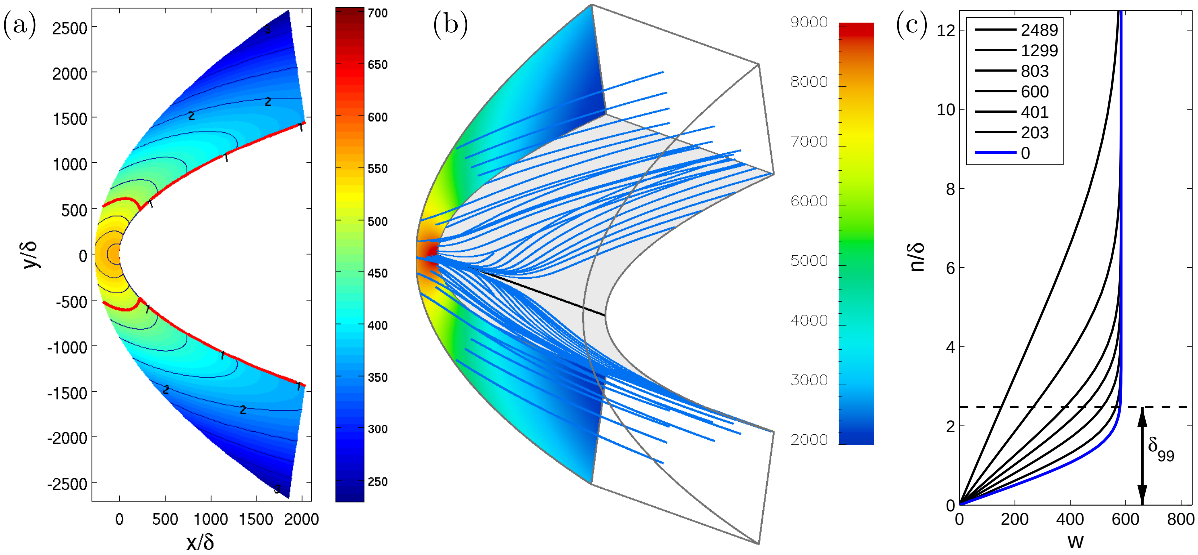

Figure 3.4. Computed steady base flow for $Re_s = 800$, $Re_R = 129136$, $Ma_s = 1.25$ and $\theta_w = 1$: (a) temperature field T [in K] and iso-contour lines of the Mach number in the s-n-plane (sonic line in red); (b) streamlines (in blue) and pressure field p [in Pa]. The resolution is 128×511 points in the normal n- and the chordwise s-direction, respectively. (c) Spanwise velocity w [in m/s] at selected positions [in δ] (see legend) in the positive s-direction; $\delta_{99} \approx 2.38\delta$ indicates the thickness of the boundary layer along the attachment line; $\delta \approx 1.968 \cdot 10^{-4}$ [m] for the present choice of parameters.

In the previous computations, a value $\kappa = 0.95$ was used to cluster the $n_1 = 128$ grid points in the wall-normal direction. In order to assess the quality of the computational grid and to gain some information about the boundary-layer scales, a number of quantities for sweep Reynolds numbers of 400, 600 and 800 are displayed in table 3.4. This table shows that the number of grid points inside the boundary layer increases, since δ_{99} increases, as the Reynolds number is decreased, and that a value of $n_1 = 128$ appears sufficient to resolve the boundary layer. Note that the viscous length scale satisfies $\delta \sim \sqrt{\nu_r} \sim 1/Re_s$; for the definition of δ the reader is referred to equation (2.4). Due to the smoothness of the steady base flow in the chordwise s-direction, the base flow is well resolved in s.

Table 3.4. Boundary-layer thickness δ_{99} and number of grid points inside the boundary layer along the stagnation line for selected values of Re_s and n_1.

	$Re_s = 400$		$Re_s = 600$		$Re_s = 800$	
	($\delta = 3.935 \cdot 10^{-4}$ m)		($\delta = 2.624 \cdot 10^{-4}$ m)		($\delta = 1.968 \cdot 10^{-4}$ m)	
n_1	128	256	128	256	128	256
# of points in δ_{99}	33	44	24	31	19	24
δ_{99} [in 10^{-4} m]	9.404	9.402	6.264	6.256	4.698	4.690
δ_{99}/δ	2.390	2.389	2.388	2.385	2.386	2.383

Comparison of theoretical and numerically obtained stagnation quantities

For the definition of the governing parameters in section §2.2.2, the value of the kinematic viscosity ν_r, and thus the sweep Reynolds number Re_s, has been based on theoretical results from Reshotko and Beckwith (1958) for the value of the recovery temperature T_r (see equation

Table 3.5. Comparison of theoretical and numerically obtained values for the stagnation quantities.

	T_r [in K]	p_s [in Pa]	ν_r [in m^2/s]	Re_s
theoretical	702.71	9075.35	$1.434 \cdot 10^{-4}$	800
simulation	703.37	9075.68	$1.436 \cdot 10^{-4}$	800

(2.10)) and on the theoretical value of the stagnation pressure p_s (see equation (2.12)). Table 3.5 displays a comparison of the theoretical and the numerically obtained values for the recovery temperature T_r and the stagnation pressure p_s, with good agreement. As a consequence, the value of the sweep Reynolds number Re_s remains unchanged.

3.3 Long-time integration of the initial value problem

After discussing the computation of steady state solutions in the previous section we proceed with stability investigations of the base flow. To this end, we perturb the steady base flow $\boldsymbol{\phi}_0(x,y,z)$ with an arbitrary, three-dimensional perturbation field of small amplitude $\epsilon\boldsymbol{\phi}(x,y,z,t)'$, such that nonlinear effects can be neglected,

$$\frac{d\boldsymbol{\phi}}{dt} = \mathbf{F}(\underbrace{\boldsymbol{\phi}_0 + \epsilon\boldsymbol{\phi}'}_{\boldsymbol{\phi}}), \tag{3.6}$$

and perform direct numerical simulations (DNS) to follow the evolution of the small-amplitude perturbation in time. As time progresses the solution of the initial value problem (3.6) converges toward the least stable global mode before it saturates due to nonlinearities (since the nonlinear Navier–Stokes equations have been implemented).

As an initial perturbation field we take

$$\epsilon\boldsymbol{\phi}' = \epsilon(p_2, u_2, v_2, w_2, s_2)^T \boldsymbol{f} \tag{3.7}$$

with $\epsilon = 10^{-8}$. The vector $(p_2, u_2, v_2, w_2, s_2)^T$ represents the flow quantities downstream of the detached bow shock (see section §2.2), and $\boldsymbol{f}$ denotes a field of random numbers (white noise). This approach closely follows previous investigations on the linear stability of stagnation-point flow where, for instance, incompressible swept Hiemenz flow (Spalart, 1988; Theofilis, 1998) and compressible stagnation-point flow over a swept flat plate (Le Duc et al., 2006) as well as compressible flow about a swept parabolic body (Sesterhenn, 2004) were studied.

Results

In our three-dimensional direct numerical studies, the extension of the domain in the spanwise periodic z-direction, given by the parameter L_z, defines the fundamental length of wave-like disturbances traveling in z. As fundamental length, we chose a value of $L_z = 2\pi/\bar{\beta} = 28\delta$, and for this choice[5] of L_z, boundary-layer instabilities in form of co-rotating vortices inside the boundary layer, a typical feature of the crossflow instability, are expected to destabilize the flow (see Sesterhenn, 2004). Furthermore, a resolution of $128 \times 511 \times 8$ points in the normal n-, the chordwise s- and the spanwise z-direction are used ($n_3 = 8$ grid points in z have been found to be sufficient to resolve the modal structures).

---

[5] $L_z = 28\delta$ corresponds to a value of $\beta = \bar{\beta}\,\delta = 0.224$ for the non-dimensional wavenumber.

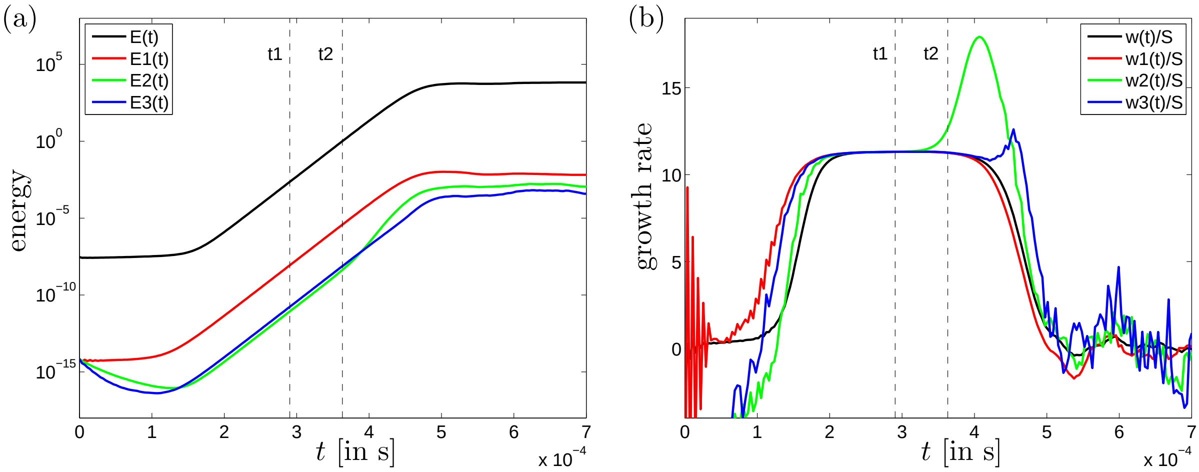

Figure 3.5. (a) Total $E(t)$ and modal energy $E_m(t)$ and (b) total $w(t)$ and modal growth rate $w_m(t)$ of the first three modal structures as a function of time t. The growth rate is normalized using the strain rate at the wall: $S_{th} = 2u_2/R = 3704$ [1/m] for the present freestream conditions. The dashed lines represent the positions in time at which the flow field is visualized in figure 3.6.

As a result, the temporal evolution of the kinetic energy and the corresponding growth rate of the disturbed (steady) base flow are presented in figure 3.5. In figure 3.5(a), we show the evolution of the total $E(t)$ and the modal energy $E_m(t)$ for the fundamental and two higher-order modal structures as time progresses. The modal energy has been found using a Fourier transformation in the homogeneous z-direction. It can be seen that both the total and the modal energy grow exponentially over a distinct time period before they saturate in a nonlinear manner. The corresponding values of the total, $w(t)$, and the modal energy growth rate, $w_m(t)$, of the these structures — computed via

$$w(t) = \frac{1}{2}\frac{\log E(t+\Delta t) - \log E(t)}{\Delta t}, \tag{3.8}$$

$$w_m(t) = \frac{1}{2}\frac{\log E_m(t+\Delta t) - \log E_m(t)}{\Delta t}, \tag{3.9}$$

where Δt denotes the temporal difference between two consecutive flow fields — is presented in figure 3.5(b). In this figure, the plateau with $w/S_{th} \approx 11.3$ represents the exponentially growing regime in figure 3.5(a), and the growth of the fundamental modal structure confirms a linear instability (red line). The first higher-order mode exhibits the same modal growth before it becomes unstable to secondary instabilities (green line). Only three spanwise harmonic structures have been plotted in figure 3.5(b) as a consequence of the spatial resolution, $n_3 = 8$, in this direction. The same modal growth of all three structures can be interpreted as a phase locking of harmonics whose superposition produces steeper gradients in the spanwise direction.

The spatial distribution of the exponentially growing modal structures at $t = 2.91 \cdot 10^{-4}$ [s] and $t = 3.63 \cdot 10^{-4}$ [s] (see dashed lines in figure 3.5) is plotted in figure 3.6. The application of the Q-criterion reveals co-rotating vortical structures, visualized by iso-surfaces, which display typical features of crossflow instabilities (figure 3.6a). Cross-cuts of these vortices are given in figure 3.6(c,d), and the results indicate that the vortical structures first appear close to the edge of the boundary layer and that these structures become increasingly pronounced inside the boundary layer as they evolve in the chordwise s-direction; farther downstream they disappear again. It is also found that the dominant part of the vortices lies farther downstream as time progresses and eventually breaks down. To indicate the associated acoustic field, we also show the divergence of the velocity field in figure 3.6(b).

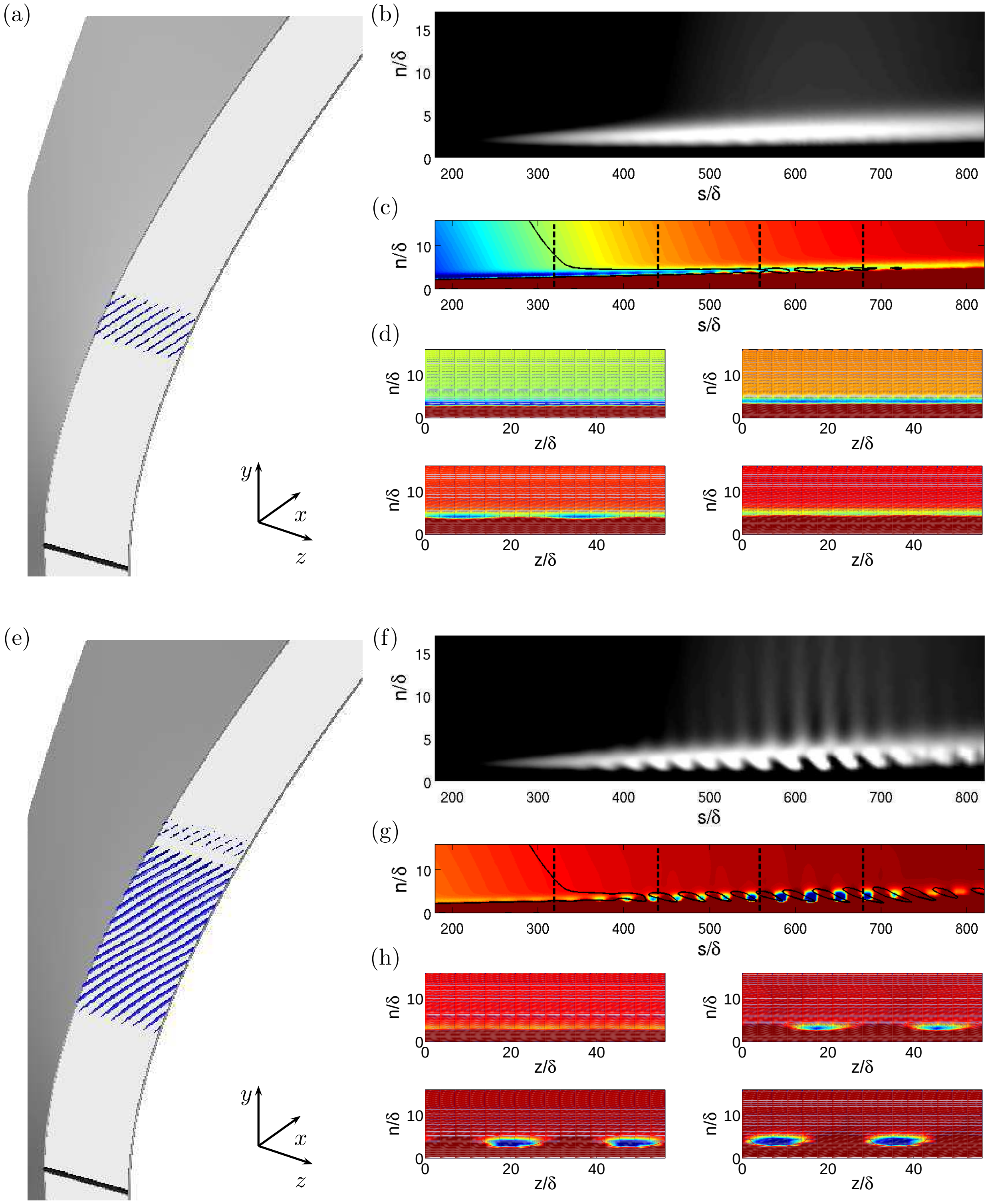

Figure 3.6. Results from a long-term integration of the initial value problem displayed at $t_1 = 2.91 \cdot 10^{-4}$ [s] (top) and $t_2 = 3.63 \cdot 10^{-4}$ [s] (bottom): (a,e) vortical structures visualized by iso-surfaces of the Q-criterion (in blue); the surface of the upper half of the parabolic body is displayed in light grey (attachment line in black). (b,f) Divergence of the velocity field in the s-n-plane. (c,g) Distribution of the vortical structures using a cross-cut in the s-n-plane; the black lines denote one representative iso-line of the Q-criterion. (d,h) Cross-cuts of the vortical structures in the n-z-plane at selected positions in the chordwise s-direction; see dashed lines in (c,g).

Chapter 4

Global Stability Solver: decomposing flow fields

The direct numerical simulations in the previous chapter demonstrated that our flow is unstable to three-dimensional perturbations. We will now apply hydrodynamic stability theory and use the concept of eigenvalues to study the asymptotic behavior of these instabilities. In a temporal framework, this behavior is described by the linearized Navier–Stokes equations, and a corresponding eigenvalue problem $\omega\widetilde{\phi} = \mathcal{L}(\phi_0)\widetilde{\phi}$ has to be solved (see section §1.2). The characteristic stability information is then contained in the eigenfunctions $\widetilde{\phi}$, which present the spatial shape of the instabilities, and the corresponding eigenvalues ω, which describe the associated temporal dynamics of the instabilities. Adopting a linear algebra notation with the matrix $\mathbf{A} \equiv \mathbf{L}(\boldsymbol{\phi}_0)$, the vector $\mathbf{x} \equiv \widetilde{\boldsymbol{\phi}}$ and the eigenvalue $\lambda \equiv \omega$ the discrete form of this eigenvalue problem reads

$$\lambda\mathbf{x} = \mathbf{A}\mathbf{x}, \qquad \lambda \in \mathbb{C}, \quad \mathbf{x} \in \mathbb{C}^n, \quad \mathbf{A} \in \mathbb{C}^{n\times n}, \tag{4.1}$$

where $\mathbb{C}$ denotes the set of scalar complex numbers, $\mathbb{C}^n$ the set of n-dimensional complex-valued vectors and $\mathbb{C}^{n\times n}$ the set of complex-valued matrices of size $n \times n$ with n as the size of the eigenvalue problem.

The standard algorithm to solve (4.1) is based on the QR method, a quasi-direct technique which dates back to the 1960s. This method reduces a matrix $\mathbf{A}$ to Schur form and thus computes all of its eigenvalues by performing $\mathcal{O}(n^3)$ operations. However, in most fluid-dynamical applications only the least stable eigenvalues are required to answer questions of interest, and more efficient iterative methods, performing $\mathcal{O}(n^2)$ operations, are favored. If, in addition, the structure of the matrix $\mathbf{A}$ can be further exploited, an even more efficient implementation of a hydrodynamic stability solver is feasible. Moreover, in these techniques eigen-information can be extracted directly from computed flow fields, for instance, without forming and storing the large-scale linear stability matrix $\mathbf{L}(\boldsymbol{\phi}_0)$. The Arnoldi method and its variants are among such iterative techniques; they will be introduced in section §4.2 and §4.3.

4.1 The QR method

The standard technique to solve the eigenvalue problem (4.1) is given by the implicitly shifted QR method (see Trefethen and Bau, 1997). This method constitutes the second phase in a two-step decomposition process, where, in a first step, $\mathbf{A}$ is brought to upper Hessenberg form using a unitary matrix $\mathbf{V}$

$$\mathbf{AV} = \mathbf{VH}, \qquad \mathbf{V} \in \mathbb{C}^{n\times n}, \quad \mathbf{H} \in \mathbb{C}^{n\times n} \tag{4.2}$$

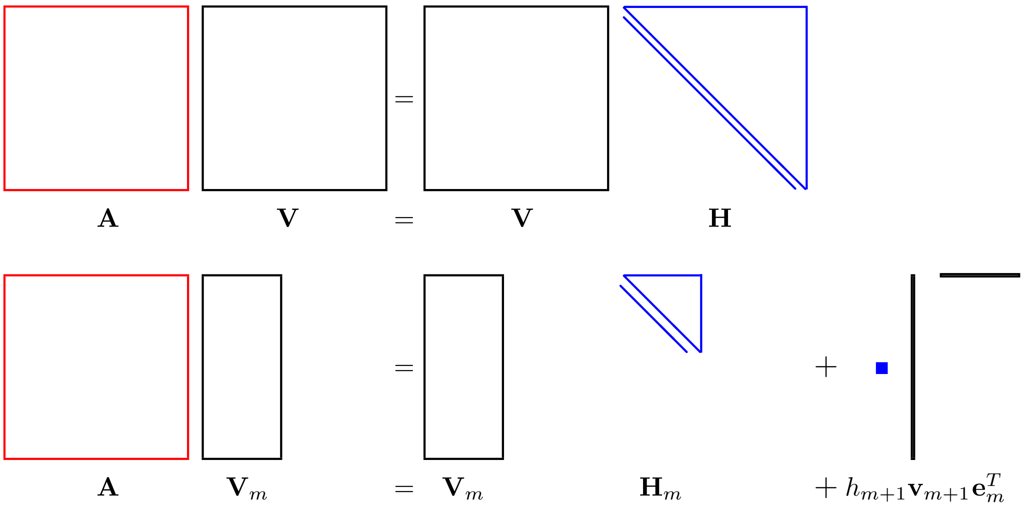

Figure 4.1. Sketch of the Hessenberg reduction of a matrix $\mathbf{A}$: (top) full reduction as performed in the first step in the QR method, and (bottom) partial reduction as obtained by using the Arnoldi method.

with $\mathbf{H}$ denoting a Hessenberg matrix, i.e., a matrix with zeros below the first subdiagonal. This direct step is commonly achieved either by Householder reduction or by the numerically less stable modified Gram–Schmidt (MGS) algorithm. The latter technique, however, has the added benefit that it can be stopped at any point of the reduction process thus resulting in a partial reduction to Hessenberg form. We will later come back to this advantage.

In a second step, QR iterations are performed to reduce the subdiagonal elements of $\mathbf{H}$ to zero until the system is eventually converged to Schur form

$$\mathbf{AQ} = \mathbf{QU}, \qquad \mathbf{Q} \in \mathbb{C}^{n\times n}, \quad \mathbf{U} \in \mathbb{C}^{n\times n}. \tag{4.3}$$

As a result, the matrix $\mathbf{A}$ is decomposed into a unitary matrix $\mathbf{Q}$ and an upper triangular matrix $\mathbf{U}$ whose diagonal contains the eigenvalues of $\mathbf{A}$; the associated eigenvectors can be found in a straight-forward manner.

The QR method requires a total work of $\mathcal{O}(n^3)$ flops, and for matrices $\mathbf{A}$ of moderate size, e.g., of dimension $n \sim \mathcal{O}(10^5)$, the reduction to Schur form and the quasi-direct solution of the eigenvalue problem (4.1) are still feasible. However, as the size of our problem increases, (4.1) results in a large-scale eigenvalue problem, and its direct solution becomes prohibitively expensive; in this case, iterative techniques such as the Arnoldi method represent the algorithms of choice.

4.2 The Arnoldi method

Instead of performing a complete reduction of the matrix $\mathbf{A}$ to Hessenberg form (see equation (4.2)), we take advantage of the Gram–Schmidt procedure and stop the process after m iterations with $m \ll n$. This results in a *partial* reduction to Hessenberg form

$$\mathbf{AV}_m = \mathbf{V}_m\mathbf{H}_m + \mathbf{f}_m\mathbf{e}_m^T, \qquad \mathbf{V}_m \in \mathbb{C}^{n\times m}, \quad \mathbf{H}_m \in \mathbb{C}^{m\times m}, \quad \mathbf{f}_m \in \mathbb{C}^{n\times 1}, \tag{4.4}$$

where $\mathbf{V}_m = [\mathbf{v}_1, \mathbf{v}_2, \ldots, \mathbf{v}_m]$ represents an m-dimensional orthonormal basis, $\mathbf{H}_m$ denotes an upper Hessenberg matrix, $\mathbf{f}_m = h_{m+1}\mathbf{v}_{m+1}$ is the residual vector orthogonal to the basis $\mathbf{V}_m$, and $\mathbf{e}_m$ stands for a unit-vector in the m-th component. For small values of h_{m+1}, the eigenvalues

$\{\theta_j\}$ of $\mathbf{H}_m$, the so-called Ritz values, are approximations to the eigenvalues $\{\lambda_j\}$ of $\mathbf{A}$, and the associated eigenvectors $\widetilde{\mathbf{x}}_j$ of $\mathbf{A}$, the so-called Ritz vectors, are obtained as

$$\widetilde{\mathbf{x}}_j = \mathbf{V}_m \mathbf{y}_j, \qquad \mathbf{y}_j \in \mathbb{C}^{m\times 1}, \tag{4.5}$$

where $\mathbf{y}_j$ denotes the eigenvector of $\mathbf{H}_m$ associated with the eigenvalue θ_j. In general, some of the Ritz pairs $(\widetilde{\mathbf{x}}_j,\theta_j)$ closely approximate associated eigenpairs $(\mathbf{x}_j,\lambda_j)$ of $\mathbf{A}$, and the accuracy of each approximation is measured by

$$\|\mathbf{A}\widetilde{\mathbf{x}}_j - \theta_j\widetilde{\mathbf{x}}_j\| = |\beta_m \mathbf{e}_m^T \mathbf{y}_j| \tag{4.6}$$

with $\beta_m = \|\mathbf{f}_m\|$.

The method based on the Gram–Schmidt decomposition in (4.4) is known as the Arnoldi method (see Sorensen, 2002). This method constructs an orthonormal basis $\mathbf{V}_m$ of the Krylov subspace sequence

$$\mathcal{K}_m(\mathbf{A},\mathbf{v}_1) = \operatorname{span}\{\mathbf{v}_1, \mathbf{A}\mathbf{v}_1, \mathbf{A}^2\mathbf{v}_1, \ldots, \mathbf{A}^{m-1}\mathbf{v}_1\} \tag{4.7}$$

which consists of repeated applications of a matrix $\mathbf{A}$ to an initial vector $\mathbf{v}_1$, and this basis $\mathbf{V}_m$ is used to perform a partial reduction to Hessenberg form. In other words, the application of the Arnoldi method results in a projection of the full stability problem given by the matrix $\mathbf{A}$ onto a lower m-dimensional vector space

$$\mathbf{V}_m^* \mathbf{A} \mathbf{V}_m = \mathbf{H}_m, \tag{4.8}$$

where the basis vectors in $\mathbf{V}_m$ decide which eigenpairs $(\mathbf{x}_j,\lambda_j)$ of $\mathbf{A}$ are approximated; the superscript * in (4.8) denotes the Hermitian conjugate.

After performing QR iterations of the small Hessenberg matrix $\mathbf{H}_m$ and thus driving the subdiagonal elements of $\mathbf{H}_m$ to zero, the method results in an *approximation* to a partial Schur decomposition of $\mathbf{A}$. We have

$$\mathbf{A}\mathbf{Q}_m = \mathbf{Q}_m \mathbf{U}_m, \qquad \mathbf{Q}_m \in \mathbb{C}^{n\times m}, \quad \mathbf{U}_m \in \mathbb{C}^{m\times m}. \tag{4.9}$$

This decomposition always exists, and the diagonal elements of $\mathbf{U}_m$ represent a specific subset of k eigenvalues of the full decomposition (4.3) of the matrix $\mathbf{A}$. Thus, the Arnoldi method produces an approximation of a specific subset of k eigenvalues of $\mathbf{A}$.

4.2.1 Implicit restarting

The quality of the approximation usually improves as the dimension m of the Krylov subspace sequence $\mathcal{K}_m$ increases. In practice, however, the dimension of this subspace is limited by memory restrictions, and its ortho-normalization is progressively affected by numerical errors as m increases[1]. The latter problem can be accounted for by explicitly re-orthogonalizing the basis vectors and a common way is using the DGKS method (Daniel et al., 1976).

To limit the dimension m of the Krylov subspace, the Arnoldi factorization (4.4) needs to be periodically restarted with a new starting vector $\mathbf{v}^+$. Explicit and implicit restarting techniques exist, and from these techniques we choose the *Implicitly Restarted Arnoldi Method* (IRAM) as proposed by Sorensen (1992). This implicit restarting strategy computes the new starting vector $\mathbf{v}^+$ by a polynomial approximation of Krylov vectors that favors k desired Ritz pairs $(\widetilde{\mathbf{x}}_j,\theta_j)$ while damping $p = m - k$ undesired ones. As a result, desired eigen-information is continually compressed into a k-dimensional subspace.

---

[1] Note that for $m = n$ the Arnoldi method performs a full Hessenberg reduction of $\mathbf{A}$ just as the Householder reduction in the QR method.

Favoring a certain set of Ritz pairs furthermore implies that implicit restarting can be used as a simple means of convergence control. The (un-restarted) Arnoldi method converges — just like the power iteration as the simplest iterative method to approximate one eigenpair $(\mathbf{x}_1,\lambda_1)$ of $\mathbf{A}$ (see Trefethen and Bau, 1997) — to eigenvalues of largest modulus. In most cases, however, these eigenvalues are not the physically relevant ones, and implicit restarting allows us to direct the convergence of the Arnoldi method toward, for instance, eigenvalues with largest real or imaginary part (see, e.g., Lehoucq et al., 1998).

4.2.2 Matrix-free implementation

Apart from avoiding a complete Schur decomposition of $\mathbf{A}$, the Arnoldi method, as well as Krylov subspace methods in general, has a further advantage. The form of the Krylov subspace sequence (4.7) indicates that the linear stability matrix $\mathbf{A}$ does not need to be formed explicitly; rather, only matrix-vector products are necessary to perform the Arnoldi decomposition. These matrix-vector products are readily obtained from numerical simulations via

$$\begin{aligned}\mathbf{A}\mathbf{v}_i &= \frac{\mathbf{F}(\boldsymbol{\phi}_0+\epsilon\mathbf{v}_i)-\mathbf{F}(\boldsymbol{\phi}_0)+\mathcal{O}((\epsilon\mathbf{v}_i)^2)}{\epsilon}\\ &\approx \frac{\mathbf{F}(\boldsymbol{\phi}_0+\epsilon\mathbf{v}_i)-\mathbf{F}(\boldsymbol{\phi}_0)}{\epsilon} \quad \text{with} \quad i=1,2,\dots,m-1, \qquad (4.10)\end{aligned}$$

where ϵ is a user-specified parameter, $\boldsymbol{\phi}_0$ stands for the (discrete) base flow, $\mathbf{v}_i$ denotes the i-th Krylov vector (as the disturbance field), and $\mathbf{F}$ represents the discretized right-hand side of the nonlinear Navier–Stokes equations (see equation (3.5)). This first-order finite-difference approximation of the linear stability (Jacobian) matrix $\mathbf{A}$ allows a matrix-free framework where right-hand side evaluations from direct numerical simulations (DNS) provide the input for the iterative global stability solver, i.e., the matrix-vector products $\mathbf{A}\mathbf{v}_i$ for a given input vector $\mathbf{v}_i$ (see figure 4.2). Such a matrix-free approach further reduces memory requirements considerably and removes the problem of explicitly forming and storing the Jacobian matrix $\mathbf{A}$.

Figure 4.2. DNS-based matrix-free implementation as a block box to compute $\mathbf{A}\mathbf{v}_i$.

The choice of ϵ is, however, not obvious (see Knoll and Keyes, 2004): if ϵ is too large, the derivative will be poorly approximated and if ϵ is too small, the result will be contaminated by roundoff errors. A widely used choice is given by

$$\epsilon = \frac{\|\boldsymbol{\phi}_0\|}{\|\mathbf{v}_i\|}\epsilon_0, \qquad (4.11)$$

where ϵ_0 is a small parameter, and $\|\cdot\|$ denotes the 2-norm. For this parameter, a value of $\epsilon_0 = 10^{-8}$ has been found to be optimal for the extraction of global modes for a compressible mixing layer in Mack and Schmid (2010), and the independence of the results for compressible flow about a swept body with respect to ϵ has also been corroborated over a range of many decades of the value of ϵ_0.

4.3 The Cayley-transformed Arnoldi method

As discussed in section §4.2.1, implicitly restarting the Arnoldi method already allows us to direct the convergence toward a distinct region of the eigenvalue spectrum such as the least-stable part. However, any thorough investigation of complex fluid flow behavior requires us

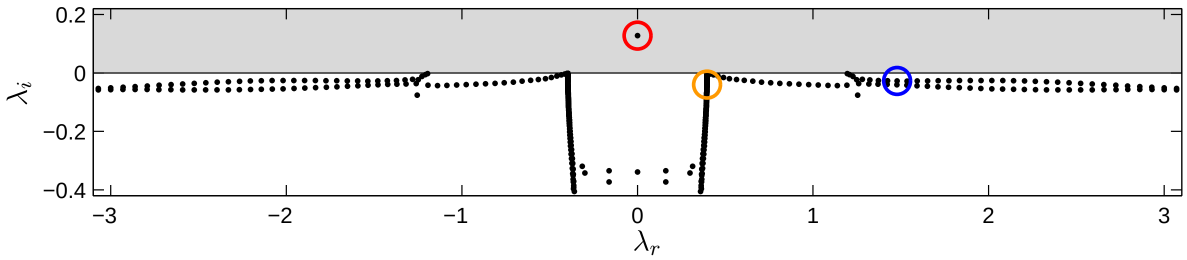

Figure 4.3. Typical spectrum of a compressible mixing layer at a Mach number of 0.5; the eigenvalues ($\lambda \equiv \omega$) depicted in circles belong to the unstable shear mode (in red), to a damped shear-layer mode (in orange) and a fast-moving weakly-damped acoustic mode (in blue). The unstable half-plane is shown in grey. Note that only the physically most relevant part of the spectrum is displayed.

to focus on specific parts of the global spectrum, and these parts might not contain the least-stable eigenvalues. To illustrate this problem we consider the (full) spectrum of a compressible mixing layer, shown in figure 4.3, which was obtained using the local stability approach (see section §1.2). This spectrum consists of an unstable (discrete) shear mode (red circle), two (continuous) shear-layer branches at a frequency $\lambda_r \approx \pm 0.4$ as well as two acoustic branches with weakly-damped but fast-moving acoustic modes. It thus possesses all the relevant physical features of our full problem. For spectra of such type, the implicitly restarted Arnoldi method (IRAM) converges toward the unstable shear mode as well as modes which are weakly damped, i.e., modes with $\lambda_i \approx 0$. This implies that stronger-damped modes such as the acoustic mode circled in blue or the shear-layer mode circled in orange cannot be computed (except for a rather large dimension m of the Krylov subspace). To extract selected modes from the acoustic and the shear-layer branch and to direct the convergence of the Arnoldi method toward these modes a transformation of the complex eigenvalue plane can be used.

Such a transformation also has the advantage of accelerating convergence. This benefit arises from the fact that high resolution simulations of complex fluid flow physics (with, e.g., the coexistence of shear and acoustic modes as illustrated in our example spectrum, see figure 4.3) may lead to an unpredictable and erratic convergence behavior of the Arnoldi method. In short, both convergence control and convergence acceleration are needed for an effective and powerful DNS-based global stability solver.

4.3.1 Cayley transformation

To control and accelerate the convergence behavior of the Arnoldi method the *Cayley transformation* (Garratt et al., 1993) is applied. This transformation consists of a two-parameter conformal mapping of the complex plane and, for standard eigenvalue problems $\lambda\mathbf{x} = \mathbf{A}\mathbf{x}$, it is defined as

$$\mathbf{T}_C(\sigma,\mu) = (\mathbf{A} - \sigma\mathbf{I})^{-1}(\mathbf{A} - \mu\mathbf{I}), \qquad \mathbf{T}_C \in \mathbb{C}^{n\times n}, \quad \sigma,\mu \in \mathbb{C}, \tag{4.12}$$

where σ and μ are the mapping or Cayley parameters, and $\mathbf{I}$ denotes the identity matrix[2]. The eigenvalues λ of $\mathbf{A}$ are then recovered from the eigenvalues ξ of the transformed problem via

$$\lambda = \frac{\sigma\xi - \mu}{\xi - 1}, \qquad \xi \in \mathbb{C}, \tag{4.13}$$

while the eigenvectors $\mathbf{x}$ are not affected by the transformation. This is a consequence of the invariance properties of linear transformations such as the Cayley transformation; the Arnoldi method preserves these properties when computing Ritz pairs $(\widetilde{\mathbf{x}}_j, \xi_j)$ of $\mathbf{T}_C$.

---

[2] Note that for generalized eigenvalue problems $\lambda\mathbf{B}\mathbf{x} = \mathbf{A}\mathbf{x}$ the identity matrix $\mathbf{I}$ has to be replaced by the mass matrix $\mathbf{B}$.

The first Cayley parameter in (4.12), the complex parameter σ, acts as a shift parameter, and for $\mathrm{Imag}\{\lambda\} < \mathrm{Imag}\{\sigma\} < \mathrm{Imag}\{\mu\}$ eigenvalues close to it are mapped far into the right-half plane while eigenvalues far from it are mapped close to one. The second complex parameter μ introduces an additional stretching-and-rotation effect on the transformed spectrum. Its major role, however, consists in controlling the condition number of the linear transformation, and, for this reason, the Cayley transformation generally yields a better-conditioned linear system than the more commonly applied shift-invert transformation (see Lehoucq and Salinger, 2001). This is an important advantage for an iterative solution — recall that a matrix-free implementation prohibits a direct solution since only matrix-vector products are available (see figure 4.2). An iterative solution, however, restricts the choice of Cayley parameters, and the resulting linear system yields solutions only if the shift parameter σ is chosen sufficiently far from an eigenvalue, thus avoiding an ill-conditioned matrix[3] (see, e.g, Burroughs et al., 2004).

Figure 4.4 demonstrates the Cayley transformation for our example spectrum presented in figure 4.3. At the top of figure 4.4(a), four parameter settings from σ_1 to σ_4 (with $\mu_r = \sigma_r$ and $\mu_i/\sigma_i = 5$) are marked in red. For these choices of parameters the Cayley transformation maps the neutral line $\lambda_i = 0$ of the original spectrum onto a circle with diameter μ_i/σ_i, and, by moving the shift parameter σ from σ_1 to σ_4, this circle is rotated in the complex plane. As a consequence, selected modes can be rotated into the green region which depicts the area accessible to the Arnoldi method (implicit restarting which favors eigenvalues with largest real part is employed). Thus, by using the implicitly restarted Arnoldi method (IRAM) in conjunction with a spectral transformation such as the Cayley transformation a large set of unstable and stable modes traveling with different frequencies λ_r can be computed. The general mapping between the complex λ- and the complex ξ-plane is further visualized by the dashed Cartesian grid in figure 4.4(a) and its mapped counterparts in figure 4.4(b–e).

The possibility of computing eigenvalues from selected regions of the global spectrum can be explained by looking at the Krylov subspace sequence for the Cayley-transformed problem

$$\mathcal{K}_m(\mathbf{T}_C, \mathbf{v}_1) = \mathrm{span}\{\mathbf{v}_1, \mathbf{T}_C\mathbf{v}_1, \mathbf{T}_C^2\mathbf{v}_1, \ldots, \mathbf{T}_C^{m-1}\mathbf{v}_1\}. \tag{4.14}$$

By ortho-normalizing this subspace, the Arnoldi method constructs an ortho-normal basis $\mathbf{V}_m$ which is used to project a matrix $\mathbf{A}$ onto a lower m-dimensional subspace $\mathbf{V}_m^*\mathbf{A}\mathbf{V}_m = \mathbf{H}_m$. It is the set of basis vectors in $\mathbf{V}_m$ that decides which eigenpairs $(\mathbf{x}_j,\lambda_j)$ of $\mathbf{A}$ are approximated, and the Cayley transformation as well as implicit restarting allows us to control the Arnoldi method while constructing $\mathbf{V}_m$.

Inexact solutions of the Cayley transformation

The Cayley transformation (4.12) requires the solution of the following large-scale non-Hermitian linear system

$$(\mathbf{A} - \sigma\mathbf{I})\mathbf{v}_{j+1} = (\mathbf{A} - \mu\mathbf{I})\mathbf{v}_j \tag{4.15}$$

for each outer step of the Arnoldi method to construct the $(j+1)$-th Krylov vector in (4.14). To accomplish this task, we resort to the BiCGStab algorithm (van der Vorst, 1992), a stabilized variant of the Bi-Conjugate Gradient Iteration, since it results in low memory requirements owing to its three-term recurrence relation.

However, the solution of the linear system (4.15) by iterative means can only be obtained approximately; as a consequence, the Cayley transformation (4.12) is necessarily inexact, and sufficiently accurate and robust solutions of (4.15) have to be attempted in order to obtain a suitable Krylov subspace sequence (4.14). For a discussion on inexact transformations the reader is referred to Meerbergen and Roose (1997).

---

[3] Considerations like this can be ignored when a direct inversion is attempted.

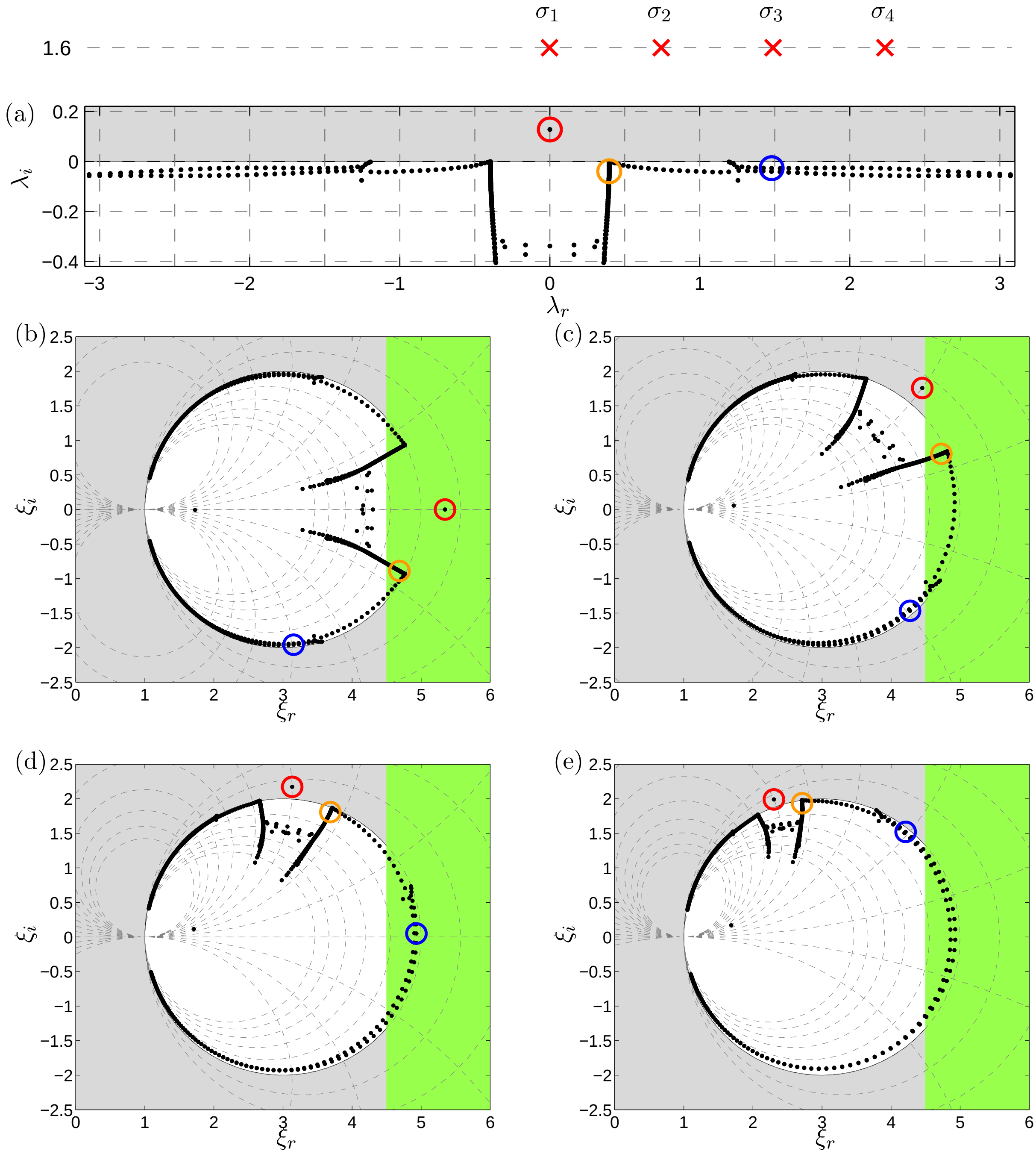

Figure 4.4. Demonstration of the Cayley transformation: as marked by red crosses on the top of the untransformed spectrum (a) four shifts (σ_1–σ_4) have been chosen, and the associated Cayley-transformed spectra are shown in (b–e). The rotation of these spectra is the result of the devision of two complex numbers in the Cayley transformation, and the wanted eigenvalues are the right-most ones; accessible region of IRAM in green. A dashed Cartesian grid and the unstable half-plane (in grey) as well as their mapped counterparts are also displayed.

4.3.2 ILU-based preconditioning

An efficient iterative solution of the linear system (4.15) requires a reliable and robust preconditioning technique. This has also been stated by Benzi (2002) who considers preconditioning as the “most critical ingredient in the development of efficient solvers for challenging problems in scientific computation”. For this reason, there exists a large body of literature on preconditioning strategies, and for an overview the reader is referred to Benzi (2002). Furthermore, state-of-the-art preconditioning techniques require in general a preconditioning matrix in explicit form, as reported by Knoll and Keyes (2004). These authors also discuss matrix-free preconditioning strategies for linear systems and conclude that "the only iterative method that can be implemented in a fashion that is literally matrix-free is a Krylov method".

With this in mind, we maintain a matrix-free implementation via direct numerical simulations (see section §4.2.2) but assume the preconditioning matrix $\mathbf{P}$ in explicit form. Applying this (shifted) preconditioning matrix $\mathbf{P}_\sigma = \mathbf{P} - \sigma\mathbf{I}$ from the right, the preconditioned version of the linear system (4.15) reads

$$(\mathbf{A} - \sigma\mathbf{I})\mathbf{P}_\sigma^{-1}\mathbf{P}_\sigma\mathbf{v}_{j+1} = (\mathbf{A} - \mu\mathbf{I})\mathbf{v}_j. \tag{4.16}$$

As we can see, preconditioning comes at the expense of solving an additional linear system in order to invert $\mathbf{P}_\sigma$, and this system has to be solved each time a matrix-vector product is required in the BiCGStab algorithm. Note that the Arnoldi iteration and thus the Krylov subspace sequence (4.14) are not affected by $\mathbf{P}_\sigma$.

Ideal preconditioning would result in eigenvalues of $\mathbf{A}_\sigma\mathbf{P}_\sigma^{-1} = (\mathbf{A} - \sigma\mathbf{I})(\mathbf{P} - \sigma\mathbf{I})^{-1}$ at one. In practice, however, one has to be content with a clustering of the eigenvalues of $\mathbf{A}_\sigma\mathbf{P}_\sigma^{-1}$ about one. These eigenvalues depend on four factors: (i) the discretization used to form $\mathbf{A}$, (ii) the choice of $\mathbf{P}$ (discretization, formulation, etc.), (iii) the technique employed to efficiently invert $\mathbf{P}_\sigma$ and (iv) the choice of the shift parameter σ.

Concerning the discretization used to obtain the (linear stability) matrix $\mathbf{A}$, the action of $\mathbf{A}$ on a given flow field $\mathbf{v}_i$ is approximated using a matrix-free implementation (4.10) where evaluations from direct numerical simulations (DNS) provide the input. Our DNS is based on fifth- and sixth-order compact schemes (see section §3.1.4) and this implies the same discretization in $\mathbf{A}$. For the preconditioning matrix $\mathbf{P}$ we choose an explicit second-order finite-difference approximation of the linear stability matrix $\mathbf{L}(\boldsymbol{\phi}_0)$. This matrix is formed explicitly using the linearized Navier–Stokes equations (see section §2.3.2) and stored using the compact sparse row (CSR) format as supported by the open-source package SPARSKIT (Saad, 1994).

Furthermore, owing to the sparsity of $\mathbf{P}$ we can take advantage of efficient incomplete decomposition techniques. The degree of "incompleteness" is given by the chosen sparsity structure of the decomposition. For general matrices, the LU-decomposition results in upper/lower triangular matrices that are dense. Incomplete decompositions, on the other hand, yield matrices that have a characteristic sparsity pattern and can be inverted efficiently by standard algorithms. In our case we choose an incomplete LU-decomposition, i.e., the dual truncation technique ILUT(p,τ) in which dropping values during the factorization is based on two user-specified parameters: the fill level p and the drop tolerance τ (Saad, 2003). As a dropping rule for a given fill level, maximally p super-diagonal and p sub-diagonal elements are kept in each row of the incomplete decomposition of $\mathbf{P}$.

Choice of the fill level p and the drop tolerance τ

The size of the fill level p, at least for values within a range that still optimizes memory requirements, does not substantially influence the convergence behavior, and Osei-Kuffuor and Saad (2007) report that "the rule of thumb is to take a large [p] value, and use [τ] to control the amount of fill-in." Using this suggestion, ILUT-based preconditioning has been tested for two flow cases, a compressible mixing layer and compressible flow about a swept parabolic body, and it was found to be capable of dramatically improving the convergence rate for BiCGStab. For the former (simple) flow case, we have identified a fill level $p = 10$ as satisfying this requirement, and we found a drop tolerance $\tau = 0.01 - 0.005$ to be an optimal choice for ILUT(10,τ) in terms of cost-efficiency of our DNS-based global stability solver. The results for the second, more complicated flow case indicate, however, that this time a larger value of the fill level, e.g.,

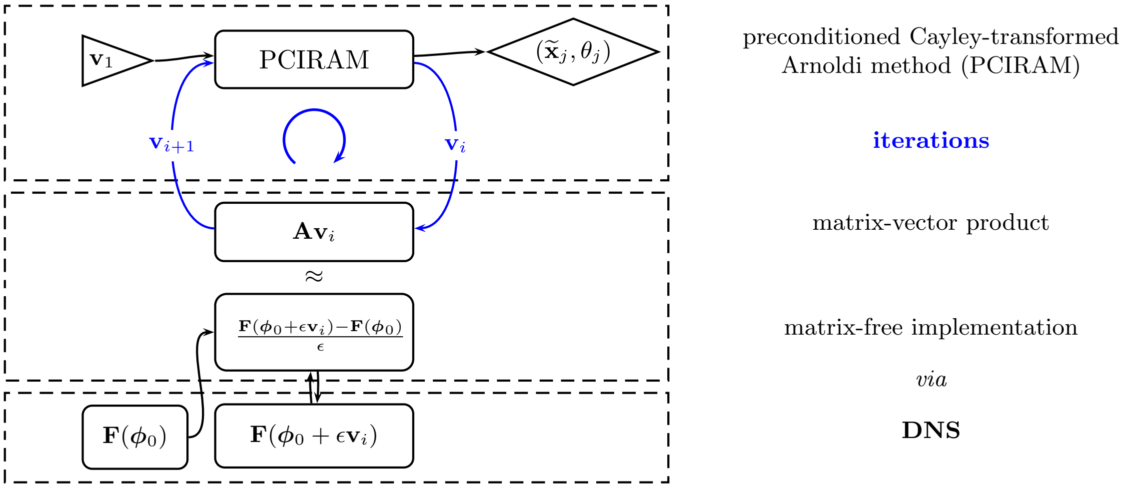

Figure 4.5. Sketch of a (compact) form of our proposed DNS-based global stability solver (abbreviated as PCIRAM) as presented in Mack and Schmid (2010). The dashed boxes represent different components of the algorithm which could be replaced in a modular manner, e.g., instead of direct numerical simulations (DNS), Large-Eddy simulations (LES) could be used to provide the required input for the matrix-free implementation.

$p = 40$, is required to obtain a robust preconditioner[4]; again, a drop tolerance $\tau = 0.01 - 0.005$ seems to be an appropriate choice. For details the reader is referred to the results in Mack and Schmid (2010).

4.3.3 Proposed DNS-based global stability solver

A sketch that illustrates the basic parts of our proposed DNS-based global stability solver is given in figure 4.5 — a more detailed sketch can be found in Mack and Schmid (2010). The program is written based on the Fortran 90/95 standard and features real as well as complex arithmetic. It is furthermore written in a modular manner where each block in figure 4.5 could be replaced by an alternative technique. The upper block represents the preconditioned Cayley-transformed implicitly restarted Arnoldi method (PCIRAM), the block in the middle illustrates the matrix-free implementation where direct numerical simulations (lower block) provide the required input. Starting with an initial guess $\mathbf{v}_1$, approximations to the eigenpairs in form of Ritz pairs $(\widetilde{\mathbf{x}}_j, \theta_j)$ are computed. Their convergence is checked using the Ritz estimate

$$|\beta_m \mathbf{e}_m^T \mathbf{y}_j| \leq \max(\epsilon_M \|\mathbf{H}_m\| \ , \ tol_A \cdot |\theta_j|),$$

where $\beta_m = \|\mathbf{f}_m\|$, ϵ_M stands for machine epsilon and tol_A denotes a user-specified tolerance parameter. The convergence of the ILU-preconditioned BiCGStab is checked via

$$\|\mathbf{r}_i\| \leq tol_B \cdot \|\mathbf{b}\|,$$

where $\mathbf{r}_i$ denotes the current residual error, tol_B is a user-specified tolerance parameter and $\mathbf{b}$ denotes the right-hand side of the linear system. In summary, our DNS-based global stability solver requires the user to specify a list of parameters which are related to the implicitly restarted Arnoldi method (m, k, tol_A), the matrix-free implementation (ϵ_0), the Cayley transformation (σ, μ), the iterative linear solver (tol_B) and the ILUT-preconditioner (p,τ). Additionally, the starting vectors $\mathbf{v}_1$ and $\mathbf{v}_{j+1,0}$ for the Arnoldi method and the iterative linear solver need to be chosen.

---

[4] It it also worth mentioning that among the common incomplete decomposition techniques such as ILU(k), ILU(τ) and ILUT(p,τ) (Saad, 2003), the latter technique has been found to perform by far superior.

The solver shown in figure 4.5 was designed and its various components were assessed in Mack and Schmid (2010) using a simple test case, a compressible mixing layer. This way, valuable insight and experience in using the solver parameters to influence convergence properties and solution quality could be gained. A parameter choice that has been found to perform "optimal" consists of $tol_A = 10^{-4}$ and $tol_B = 10^{-5}$ (see Lehoucq and Salinger, 2001, for a discussion on this issue). As we will see, the most sensitive "parameter" in our DNS-based global stability solver is the spatial resolution of the computed flow fields and thus the quality of the direct numerical simulations.

4.4 Note on alternative methods

In the existing literature, a large variety of iterative global stability solvers have been used to study fluid-dynamical problems, and from a conceptual point of view virtually all of these techniques can be described by the modular concept shown in figure 4.5. In what follows, we briefly discuss some of these alternative methods.

Matrix-based techniques I

Krylov subspace methods for hydrodynamic stability analysis of the incompressible Navier–Stokes equations were first introduced by Edwards et al. (1994). They employed the implicitly restarted Arnoldi method (IRAM), and their investigation of moderately complex flow situations allowed a matrix-based implementation and did not require any type of spectral transformation. In the following years, IRAM in conjunction with a shift-invert transformation became a popular tool to address larger and more complex flow problems. A state-of-the-art review of this tool, as well as Krylov subspace techniques in general, applied to a wide range of fluid flows of aerodynamical interest is given by Theofilis (2003) with special emphasis on the global linear stability of non-parallel and three-dimensional flow configurations. In general, the investigations involved a dense linear stability matrix $\mathbf{A}$ — as a result of a spectral discretization of the governing equations — , and the matrix $\mathbf{A}$ is inverted using direct methods. The shift-invert technique has also been compiled into the open-source package ARPACK (Lehoucq et al., 1998) which today is widely used for a range of stability problems. The direct inversion of a dense matrix, however, still restricts the method to moderately-sized problems.

This restriction can be overcome if the linear stability matrix $\mathbf{A}$ is designed to be sparse — i.e., by employing finite-difference or finite-element methods for the spatial discretization — ; this sparsity can then be exploited by powerful direct sparse solvers (Davis and Duff, 1997; Amestoy et al., 2007) as, e.g., recently demonstrated by Marquet et al. (2008).

Matrix-based techniques II

The situation completely changes, however, if iterative solutions of the linear system are attempted. First, the Cayley transformation rather than the more commonly applied shift-invert transformation has to be employed, since the Cayley transformation in general yields a better-conditioned linear system than the shift-invert transformation (see Lehoucq and Salinger, 2001). Furthermore, Lehoucq and Meerbergen (1998) report "the superior numerical performance of a Cayley transformation over that of a shift-invert transformation within an Arnoldi method when using an iterative linear solver". Second, and even more important, preconditioning the linear system solver becomes a crucial component of the Cayley-transformed Arnoldi method. This issue was stressed by Zhang (2000) who performed a comparative study of the ILU-preconditioned Krylov subspace solvers BiCGStab, GMRES and TFQMR applied to a variety of problems from academic and industrial computational fluid dynamics (CFD). This author concludes that "the quality of the preconditioner is more critical than the choice of the Krylov subspace accelerator in designing a preconditioned iterative solver for large scale CFD applications".

For the sake of completeness, a further class of Krylov subspace methods known as subspace iteration techniques is worth mentioning. As an example, Heeg and Geurts (1998) successfully applied the Jacobi–Davidson method (Sleijpen et al., 1996) in conjunction with ILU-preconditioned BiCGStab in their studies on spatial instabilities on the incompressible attachment-line flow.

Matrix-free techniques

Despite the popularity of matrix-based techniques only matrix-free methods introduce a maximum amount of flexibility in extracting linear stability information: direct numerical simulations (DNS) can provide Jacobian information via (4.10), as can Large-Eddy simulations (LES), Detached-Eddy simulations (DES), vortex-particle methods and even commercial codes. In conclusion, if the linear stability matrix is available in explicit form, and if this matrix exhibits a large degree of sparsity, the shift-invert Arnoldi method with a direct inversion of the linear system displays the method of choice (owing to the recent progress of powerful direct solvers and their parallel variants). However, if we cannot rely on such a (sparse) matrix, and if we wish to keep a large degree of flexibility, matrix-free solvers are the preferred algorithms.

Chapter 5

Global Stability Analysis: extracting physical mechanisms

In the previous chapter §4 we developed a DNS-based global stability solver to extract stability information directly from numerical simulations. A direct numerical simulation (DNS) code has been implemented in chapter §3, and this code is used to compute flow fields for compressible flow about a swept parabolic body, our flow model for compressible flow about a swept blunt body which has been presented in chapter §2.

In what follows, the DNS-based global stability solver is applied to study the temporal stability of small-amplitude perturbations in order to extract the underlying physical mechanisms present in our flow model. As the Krylov subspace is augmented by subsequent calls to the direct simulation code, the Cayley-transformed Arnoldi method provides an approximate spectrum that increases in complexity but also in accuracy. This spectrum will reflect the rich and complex perturbation dynamics of our flow situation.

5.1 The global spectrum

The iteratively computed global spectrum is shown in figure 5.1. This global spectrum reflects the richness of physical processes present in the flow configuration under investigation. It consists of (mostly unstable) discrete boundary-layer modes (region I, in red) that express the flow characteristics inside the boundary layer, of acoustic modes that describe the presence of (stable and unstable) sound waves (region I, II and III, in blue) and of (stable) wave packet modes (region IV, in green) that represent the dynamics of general perturbations in the freestream. The latter type of modes is complemented by the partial spectrum (region IV, in grey) obtained by directly solving for the eigenvalues of the Jacobian matrix — i.e., the discretized linear stability operator in equation (2.30) — for an embedded and significantly smaller sub-domain located near the attachment line. Furthermore, modes that account for the interaction of the detached bow shock with the parabolic body exist as well (see region V, in black).

For the current parameter choice — i.e., a sweep Reynolds number of $Re_s = 800$, a leading-edge Reynolds number of $Re_R = 129136$, a sweep Mach number of $Ma_s = 1.25$, an adiabatic wall ($\theta_w = 1$) and a disturbance wavenumber $\beta = 0.314 = 2\pi/L_z$ (with L_z as the fundamental length scale of the perturbations, nondimensionalized by the viscous length scale δ, in the spanwise z-direction) —, the discrete boundary-layer branch (in red) features the most unstable global modes.

The global spectrum (see figure 5.1) also shows that the physical processes described by different types of global modes exhibit a distinct but characteristic frequency ω_r. The boundary-layer modes (in red), for instance, prevail inside the boundary layer, and the modes displayed in figure 5.1 travel with a phase speed of approximately 12% to 37% of the (mean) spanwise

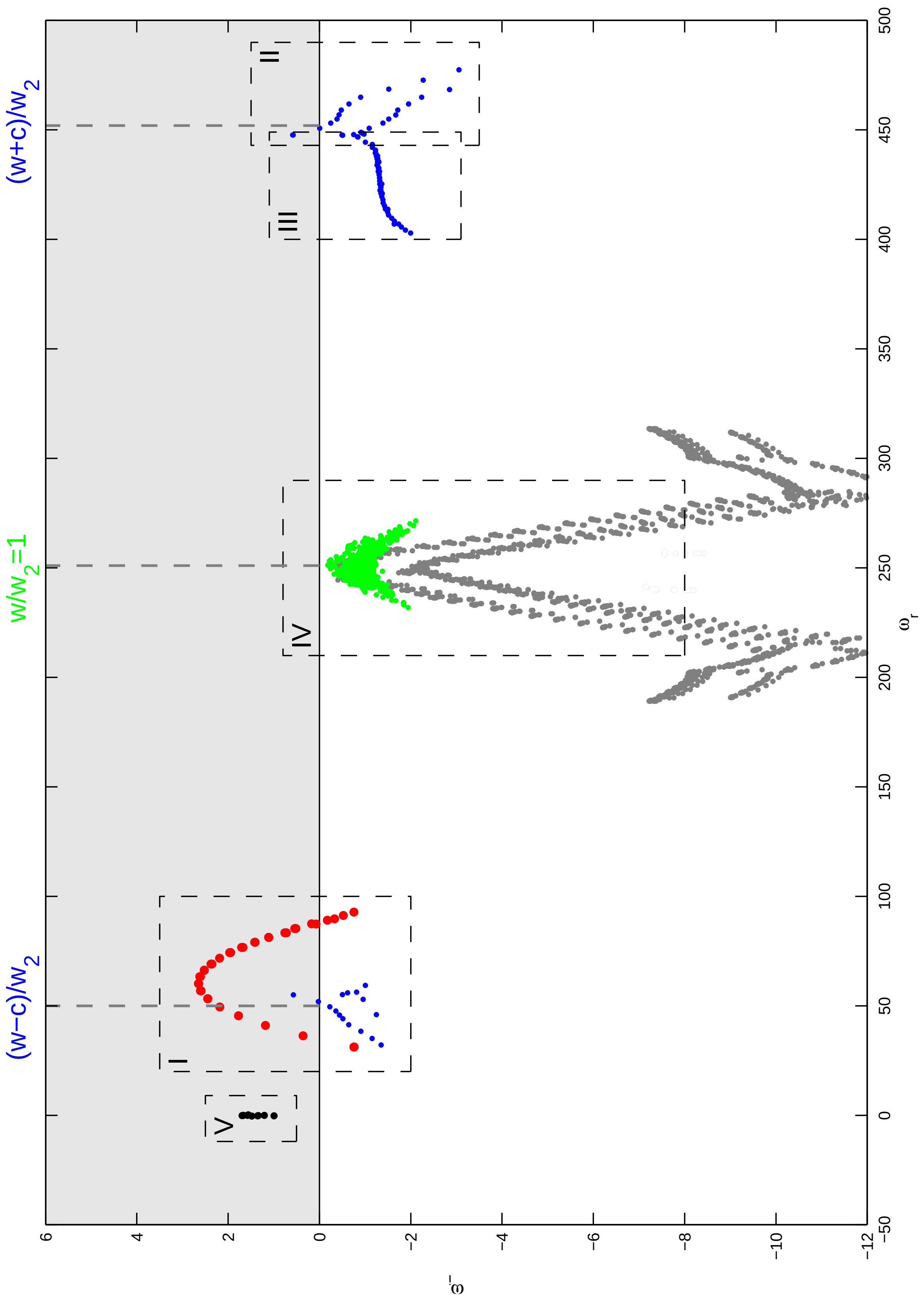

Figure 5.1. Global spectrum showing the frequency ω_r and the corresponding growth rate ω_i of the iteratively computed modal structures ($Re_s = 800$, $Re_R = 129136$, $Ma_s = 1.25$, $\theta_w = 1$ and $\beta = 0.314$); the eigenvalues ω have been nondimensionalized using the strain rate $S_{th} = 2u_2/R = 3704$ [1/m]. Each region shows the least-stable eigenvalues belonging to boundary-layer modes (region I), acoustic modes (region I, II and III), wave packet modes (region IV) and shock-interaction modes (region V); unstable-half plane in grey.

Table 5.1. Overview of base flow and perturbation quantities for $Re_s = 800$ and $\beta = 0.314$ ($S_{th} = 3704$ [1/s], $\delta = 1.968 \cdot 10^{-4}$ [m]). The (normalized) frequency ω_r associated with the spanwise velocity w is found as $\omega_r = f_r/S_{th} = w\beta/(S_{th}\delta)$.

		$w_2 - c_2$	$12\%\, w_2$	$37\%\, w_2$	w_2	$w_2 + c_2$
base flow:	speed w [m/s]	116.6	70.0	215.7	583.1	1049.6
	w/w_2	0.2	-	-	1	1.8
	f_r/S_{th}	50.24	30.1	92.9	251.20	452.16
spectrum:	ω_r	54.95	31.1	92.8	251.26	447.68
type of mode:		acoustic	boundary-layer		wave packet	acoustic

velocity ($w_{mean} \approx w_2$) in the z-direction; the frequency ω_r corresponding to the (mean) spanwise velocity is obtained via

$$\omega_{r,mean} \approx \frac{w_2\beta}{S_{th}\delta} \tag{5.1}$$

with $w_2 = 583.1$ [m/s], $\delta = 1.968 \cdot 10^{-4}$ [m] and $S_{th} = 3704$ [1/s] (see table 5.1 for further details). The acoustic modes (in blue), on the other hand, move downstream and upstream in z with a phase speed of approximately $w_2 \pm c_2$, respectively, where c_2 stands for the speed of sound in the freestream. This speed of $w_2 \pm c_2$ corresponds to frequencies $\omega_r = f_r/S_{th}$ of 452.16 and 50.24 (see table 5.1). Last but not least, the wave packet modes (in green) move with approximately the (mean) velocity w_2, which corresponds to $\omega_r = f_r/S_{th} = 251.20$ (see table 5.1), since they mainly capture the dynamics of perturbations in the freestream.

In the following sections, we will present more details about each identified type of instability, marked as region I to V in the global spectrum (see figure 5.1).

5.2 Boundary-layer modes – region I

Concentrating on boundary-layer modes (see red dots in region I in figure 5.1), the employed global stability solver identified, for our flow parameters, an eigenvalue branch of typical parabolic shape. This branch consists of stable and unstable discrete modes whose frequency ω_r ranges from 31.1 to 92.8 (see figure 5.2b); the maximum growth rate $\omega_i = 2.64$ is achieved for $\omega_r = 60.1$. Owing to the inherent symmetry properties of the flow the eigenvalues appear double at closer inspection, and the associated modes exhibit characteristic symmetry properties with respect to the attachment line.

The same figure 5.2(a) further displays four global modes, denoted by B1–B4, from the boundary-layer branch in figure 5.2(b). The modes are visualized by iso-surfaces of the (normalized) velocity $u(x, y, z) = \text{Real}\{\widetilde{u}(x, y)\,(\cos\beta z + \mathrm{i}\sin\beta z)\}$, and they belong to a slow-moving mode (B1), a slightly faster-moving mode (B2), the most unstable mode (B3) and a representative fast-moving mode (B4); the associated eigenvalues are depicted by circles in figure 5.1(b). The amplitude distribution of the mode B1 displays typical features of both attachment-line instabilities and crossflow vortices and thus clearly demonstrates a link between the attachment-line and the crossflow dynamics. It convincingly shows that the global modes of the boundary-layer branch depicted in figure 5.2(b) have typical attachment-line properties while still connecting to the familiar crossflow pattern farther downstream from the attachment line.

The faster-moving global modes (modes with a higher phase velocity ω_r) show a substantially stronger component of the crossflow instability, and its maximum amplitude is located farther downstream from the attachment line. This property is more evident in figure 5.3(a) where we present body-fitted cross-cuts of the four global modes displayed in figure 5.2(b) at a distance

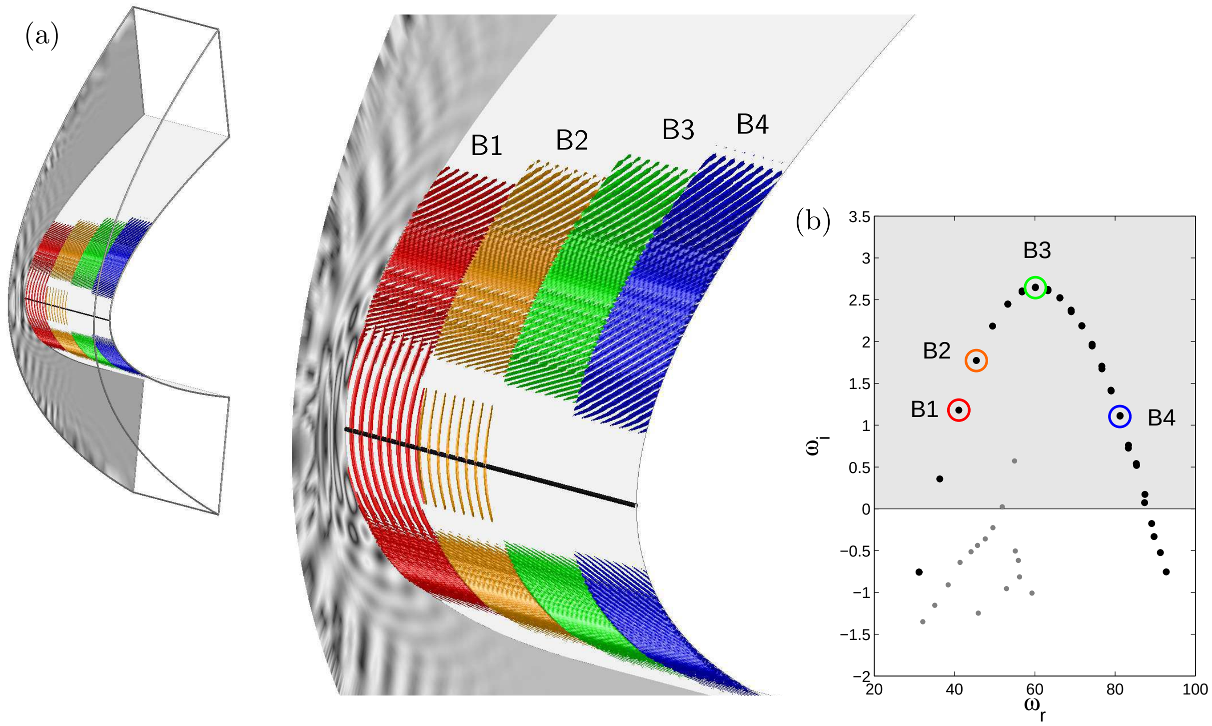

Figure 5.2. (a) Four representative global modes (B1–B4) from the boundary-layer branch. The relevant region I of the global spectrum (see figure 5.1) is shown in (b), where the eigenvalues corresponding to the four global modes are depicted by circles. The modes are further visualized by iso-surfaces of the normal velocity $u(x, y, z) = \text{Real}\{\tilde{u}(x, y) (\cos \beta z + \mathrm{i} \sin \beta z)\}$, and eight wavelengths, stretched by a factor of two, in the spanwise z-direction are used to display each mode (attachment line in black). Contours of the weak pressure field (in the s-n-plane) associated with the mode B1 are shown in the background.

of half the boundary-layer thickness from the wall. These cross-cuts again demonstrate the two-dimensional character of the global modes near the attachment line and the typical curved shape of crossflow instabilities further downstream. With the spanwise wavenumber $\beta = 2\pi/L_z$ held constant for the modes, the clearly visible difference in the spatial orientation of the crossflow vortices is a consequence of a corresponding difference in the equivalent "local chordwise wavenumber". This same "local chordwise wavenumber" parameterizes the parabolic eigenvalue branch of the associated global boundary-layer modes in figure 5.2(b). An equivalent parabolic shape would be obtained in *local* stability analyses as the least-stable eigenvalue is traced as a function of the chordwise wavenumber.

Comparison with existing results

The spatial shape of the global modes presented in figure 5.3(a), i.e., a two-dimensional character near the attachment line and the curved shape of crossflow vortices farther downstream have been studied locally in the past. The former feature is reminiscent of results from stability computations by Joslin (1995) who observed a similar spatial evolution of three-dimensional disturbances in an incompressible attachment-line boundary layer (see figure 5.4a); curved co-rotating vortical structures nearly aligned with the external streamlines are typical for crossflow instabilities as, for instance, shown by Bonfigli and Kloker (2007) (see figure 5.4b). Further evidence linking the local behavior of the global modes near the attachment line to a typical local attachment-line mode is given in figure 5.3(b) where the characteristic linear dependence in the chordwise s-direction of the velocity component $v(x, y, z)$ is visible over a significant range in s before it saturates to connect to the crossflow behavior further downstream. Figure 5.3(c) shows the symmetric shape of the corresponding normal velocity component $u(x, y, z)$.

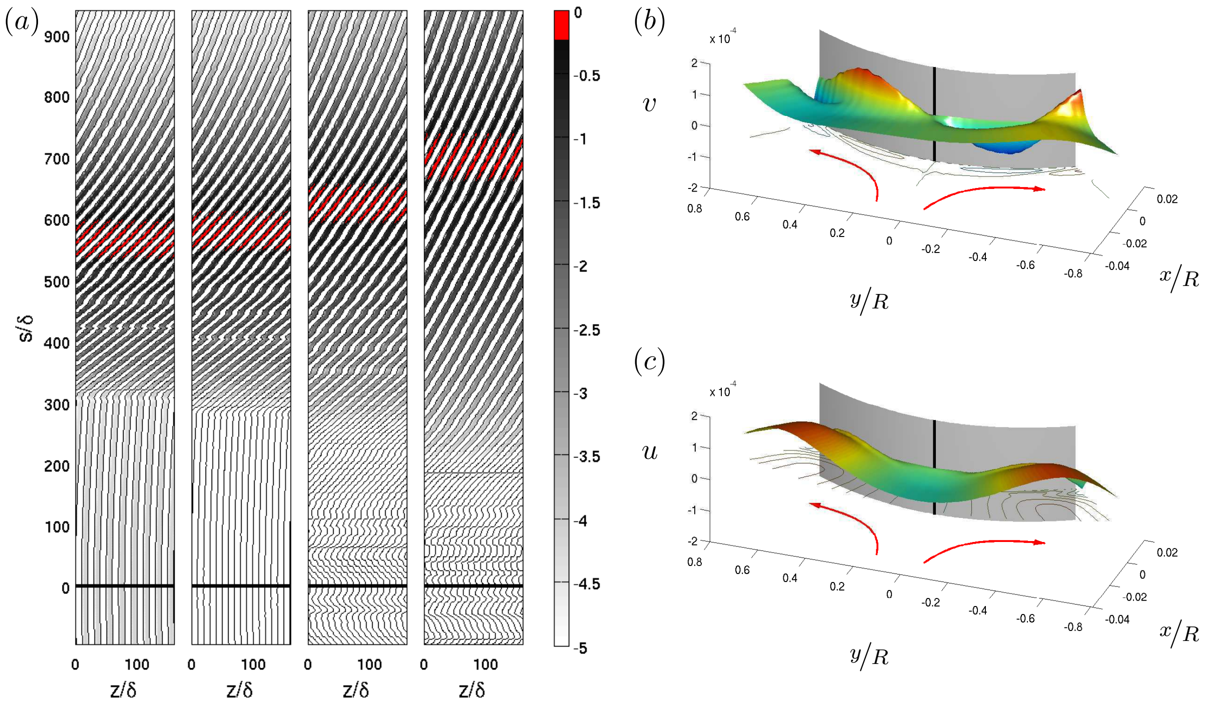

Figure 5.3. (a) Top view of the spatial distribution of the four global modes (B1–B4) shown in figure 5.2 in the s-n-plane using cross-cuts at approximately half the boundary-layer thickness δ_{99}. A log-scale is used to visualize the positive values of u (largest amplitude in red), and eight wavelengths in the spanwise z-direction are used to visualize each mode (attachment line in black). (b,c) Spatial shape of the mode B1 (see figure 5.2a) near the attachment line.

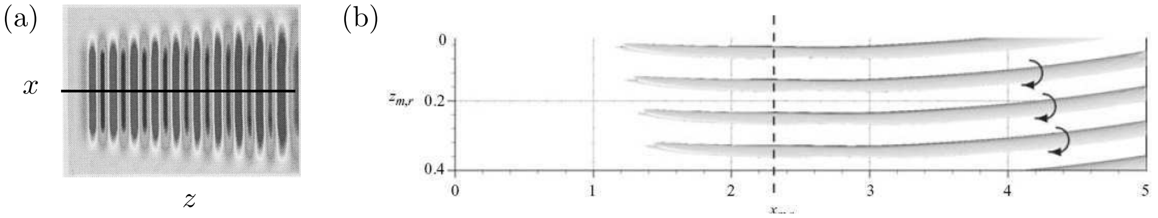

Figure 5.4. (a) Top view of the spatial distribution of a traveling mode (normal velocity) as presented by Joslin (1995); attachment line in black, relabeled coordinate system. He performed direct numerical simulations (DNS) to study the linear stability of an incompressible attachment-line boundary layer (swept Hiemenz flow model) for the (sweep) Reynolds number $Re = 570$ and the perturbation frequency $\omega = 0.1249$. (b) Large-amplitude traveling vortices visualized using λ_2-isosurfaces (taken from DNS of Bonfigli and Kloker, 2007); arrows indicate the rotation direction of the crossflow vortices. In both figures, the flow direction is from the left to the right.

5.3 Acoustic modes – region I, II and III

5.3.1 Acoustic instabilities (type A)

Due to the presence of compressibility, the global spectrum also features distinct sets of slow- and fast-moving acoustic global modes (see blue dots in region I and II in figure 5.1, respectively) which describe the presence of sound waves. These modes travel with approximately $w_2 \pm c_2$ in the spanwise z-direction (see table 5.1) as already discussed in section §5.1. In figure 5.5(a), we display region II of the global spectrum (see figure 5.1) which contains the fast-moving set of acoustic modes. It is found that these modes can be divided into symmetric S-modes — the spatial distribution of all disturbance quantities except for the chordwise velocity v is symmetric with respect to the attachment line — and antisymmetric A-modes. Furthermore, each S-mode

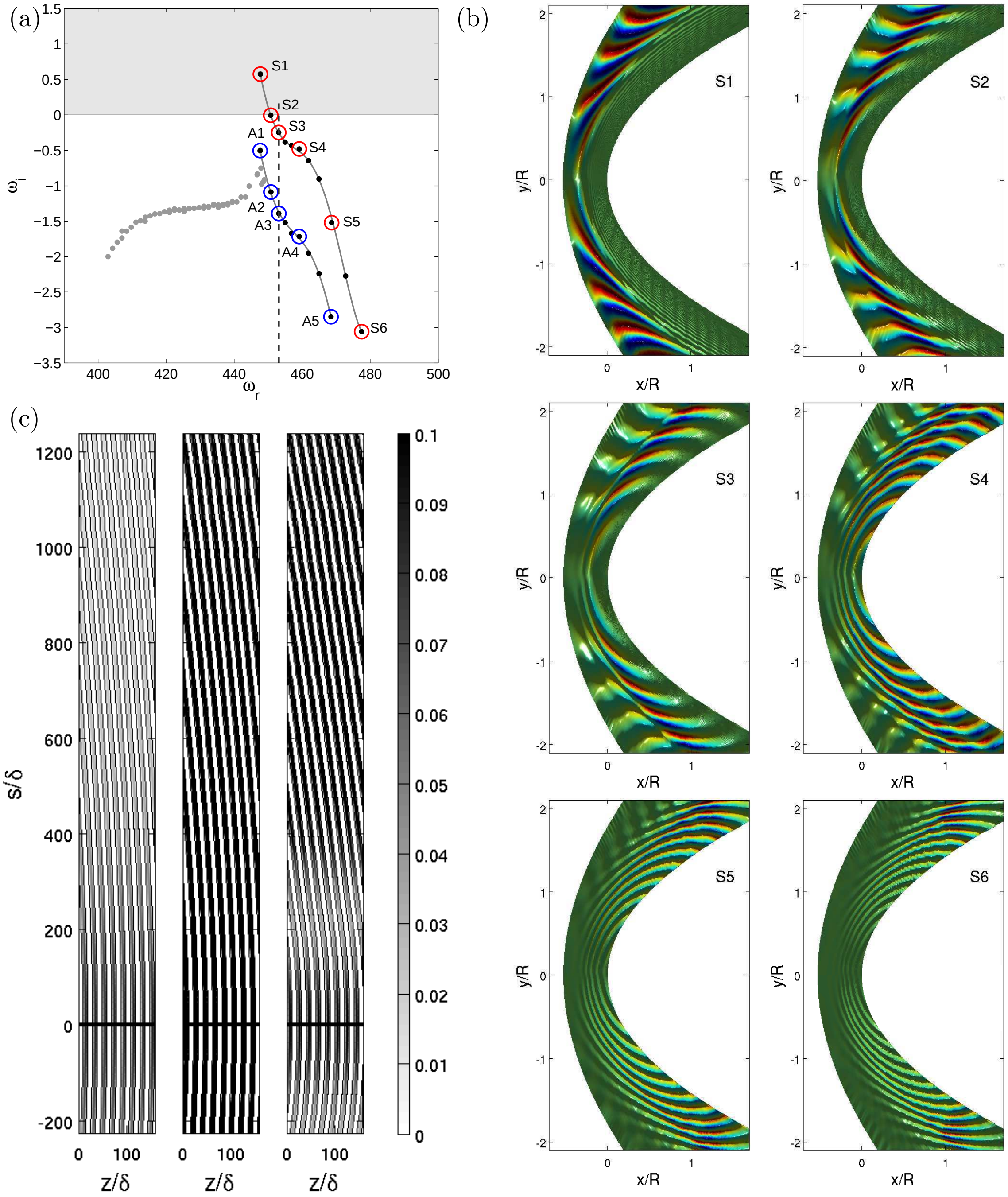

Figure 5.5. (a) Computed region of the global spectrum containing the fast-moving set of acoustic modes (see region II and III in figure 5.1). (b) Spatial structure of a sample of associated global acoustic modes belonging to the eigenvalues S1–S6 from the S-branch depicted by red circles in (a). The modes are visualized by the chordwise velocity v in the x-y-plane (the green hue corresponds to vanishing amplitudes, large amplitudes in red). (c) Body-fitted cut of the acoustic modes S3, S4 and S5 in a plane parallel to the wall at a location close to the boundary layer ($\approx 4\delta_{99}$); attachment line in black.

is found to pair with an A-mode at the same frequency ω_r, e.g., $\omega_{r,S2} = \omega_{r,A2}$ (see dashed line in figure 5.5a). Moreover, either type of modes describes a distinct branch in the eigenvalue spectrum, indicated by the grey line in figure 5.5(a), where the modes on the A-branch are always more stable than the modes on the S-branch.

The spatial structure of a representative sample of acoustic modes from the S-branch is presented in figure 5.5(b); the corresponding eigenvalues of these modes are circled in red in

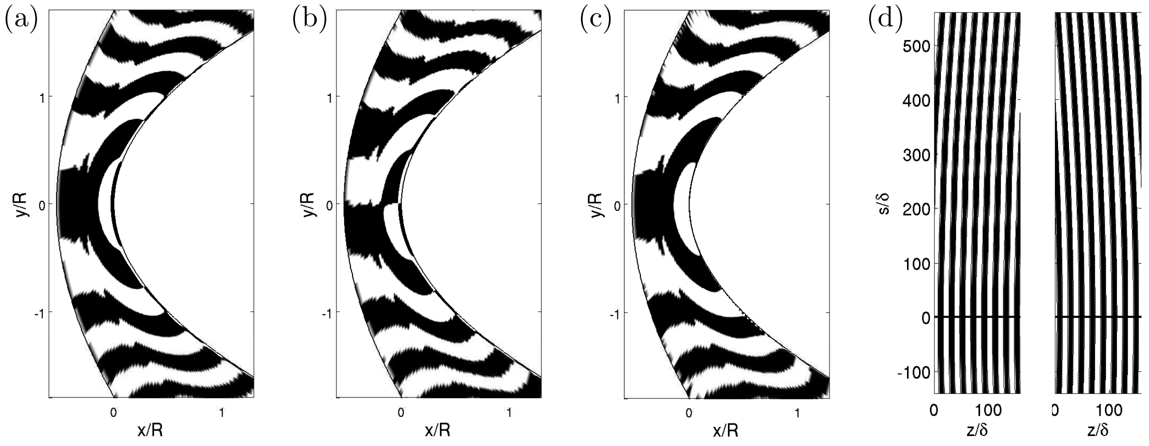

Figure 5.6. Sign of the pressure distribution sign(p) of selected global acoustic modes in the x-y-plane: (a) S-mode (S3) and (b) A-mode (A3) from the fast-moving set of acoustic modes (see figure 5.5a); (c) mode corresponding to S3, from the slow-moving set of acoustic modes denoted by S3^{-} (see blue dots in region I in figure 5.1). (d) Body-fitted cut of the acoustic modes S3^{-} and S3 in a wall-parallel plane at $\approx 4\delta_{99}$.

figure 5.5(a) and denoted by S1–S6. All modes are visualized by the amplitude distribution of the chordwise velocity v in the x-y-plane. The unstable (S1) and the marginally stable mode (S2) reveal a dominant spatial structure downstream of the detached bow shock, and this structure decays toward the surface of the body; the bow shock acts as a flexible “wall” which prevents sound waves from traveling upstream of the shock. More stable modes (S3–S6) are more pronounced in the half of the physical domain which is adjacent to the body, and they exhibit smaller spatial structures as they are increasingly tilted and damped; the smaller the spatial structures, the larger is the (local) chordwise “wavenumber” α and thus the propagation angle of the oblique traveling acoustic waves. This feature is clearly visible in figure 5.5(c), where we present a body-fitted cut of the modes S3, S4 and S5 at a plane parallel to the parabolic body.

The unstable mode S1 exhibits a small value of α and thus displays an approximately two-dimensional wave traveling in the spanwise z-direction. This mode further shows no strong interaction with the shock; rather, the bow shock reacts to the structure of the mode by adjusting its spatial shape. However, for larger values of α, the oblique traveling acoustic waves strongly interact with the bow shock resulting in a small energy loss (S2, S3). Finally, for even larger α structures close to the parabolic body prevail (S4, S5 and S6). To aid the reader in comparing the different coordinates of figure 5.5(b) and (c) we provide a table showing the equivalence of the Cartesian x-coordinate and the body-fitted arclength $s_w(x)$ for selected values of x (see table 5.2).

In figure 5.6, we present a comparison of three acoustic global modes belonging to the S- and A-branch of the fast-moving set of acoustic modes (see region II in figure 5.1) as well as an acoustic mode from the corresponding slow-moving symmetric branch (marked by blue dots in region I in figure 5.1). As an example we concentrate on the mode S3 and its associated mode A3 (see dashed line in figure 5.5a). From the slow-moving set of acoustic modes we choose the

Table 5.2. Values of the body-fitted arclength coordinate $s_w(x)$ as a function of the Cartesian x-coordinate for $0 \leq x \leq L_x$: $s_w(x) = \sqrt{x}\sqrt{x+R/2} + R/2\ln((\sqrt{x}+\sqrt{x+R/2})/\sqrt{R/2})$ along the wall. For the present investigation we have $R = 0.1$ [m], $L_x = 0.4$ [m] and $\delta = 1.9677 \cdot 10^{-4}$ [m].

x/R	0	0.5	1	1.5	2	2.5	3	3.5	4
s_w/δ	0	583	914	1215	1503	1784	2061	2334	2604

image mode (denoted by S3$^-$) to S3, i.e., the mode with the identical decay rate ω_i as S3 but with a frequency ω_r corresponding to a spanwise velocity of $w \approx w_2 - c_2$. Regarding the spatial shape of these three modes it is found that the sign of the pressure distribution sign(p) is nearly identical (see figure 5.6). Besides the above-mentioned chordwise symmetric/anti-symmetric structure of these modes the two fast-moving modes exhibit a characteristic wall layer that decreases as we proceed downstream from the attachment line (figure 5.6a,b); this feature is absent for the slow-moving mode S3$^-$ (figure 5.6c). Furthermore, the body-fitted cuts of S3$^-$ and S3 in figure 5.6(d) show the upstream ($\approx w_2 - c_2$) and downstream ($\approx w_2 + c_2$) moving character of the acoustic modes.

5.3.2 Acoustic instabilities (type B)

In addition to the acoustic modes presented in section §5.3.1, another type of global acoustic modes exists. The dominant part of these modes lies in the freestream, and they display a characteristic structure in a local region between the detached bow shock and the attachment line (see figure 5.7). Starting with the global mode in figure 5.7(a), which represents the first mode $A1$ of the A-branch shown in the previous section §5.3.1, we again observe a symmetric spatial distribution for the chordwise velocity component v in the freestream (visualized by the sign of v). As we proceed along the eigenvalue branch marked in black in figure 5.7(g), an

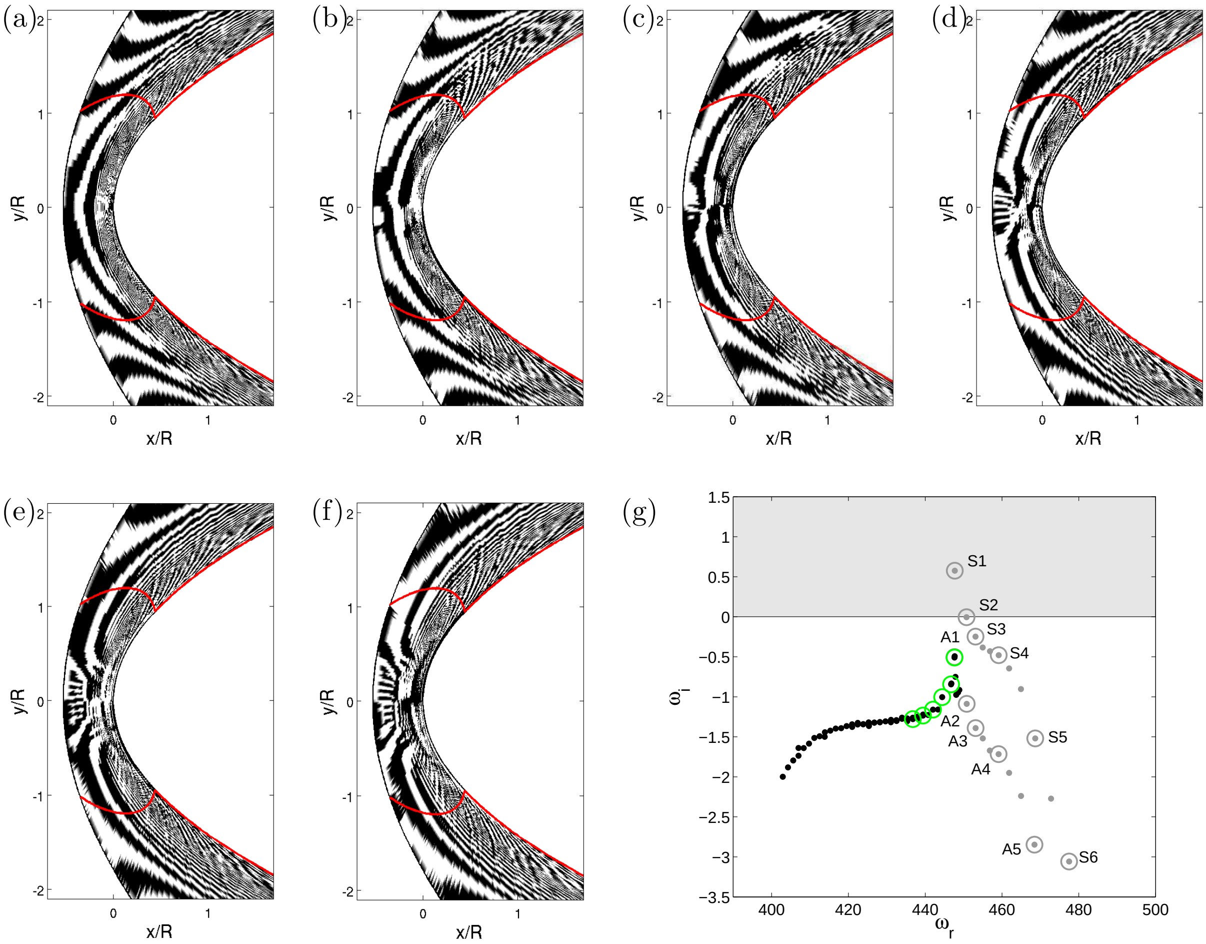

Figure 5.7. (a)–(f) Sample of a further type of global acoustic modes visualized by the sign of the chordwise velocity, sign(v), in the x-y-plane; sonic line, i.e., $Ma = (u^2 + v^2)^{1/2}/c = 1$, in red. (g) The black dots display the corresponding eigenvalues in the global spectrum (see region III in figure 5.1); the eigenvalues circled in green belong to the global modes (a)–(f).

interesting behavior emerges. It appears that a localized region between the bow shock and the attachment line decouples itself — in terms of distinct spatial scales — from the regions downstream from the attachment line. This decoupling is already visible, even though barely, in figure 5.7(a) directly behind the bow shock at $x = 0$. Progressing further along the eigenvalue branch this feature becomes more pronounced as the localized region further extends in a semi-circular fashion from its point of origin towards the body, and as the structure within shows increasingly finer scales (see figure 5.7b–f). It appears that the symmetry properties of the structures inside and outside the localized region are uninfluenced by each other. The range of scales, on the other hand, indicates a link between the two regions: generally speaking, the smaller the scales inside the localized region, the coarser the structures on the outside (see figure 5.7d–f).

This type of modes is believed to account for the interaction of a moving flexible shock and a rigid curved surface, and these modes are reminiscent of localized standing waves. The increasingly finer spatial scales of the higher-order modes are linked to higher damping rates. The localized spatial shape of the modes is also influenced by the different reflective behavior (impedance) of acoustic waves by the curved solid surface (perfect reflection) and the curved flexible shock (imperfect reflection).

5.4 Wave packet modes – region IV

Returning to the global spectrum in figure 5.1 a distinct set of eigenvalues centered around the mean spanwise velocity is clearly visible. This region IV is again plotted in figure 5.8(a), and it shows a dense clustering of damped eigenvalues confined to a triangular-shaped region. The exact location of individual eigenvalues within this region is highly sensitive to numerical

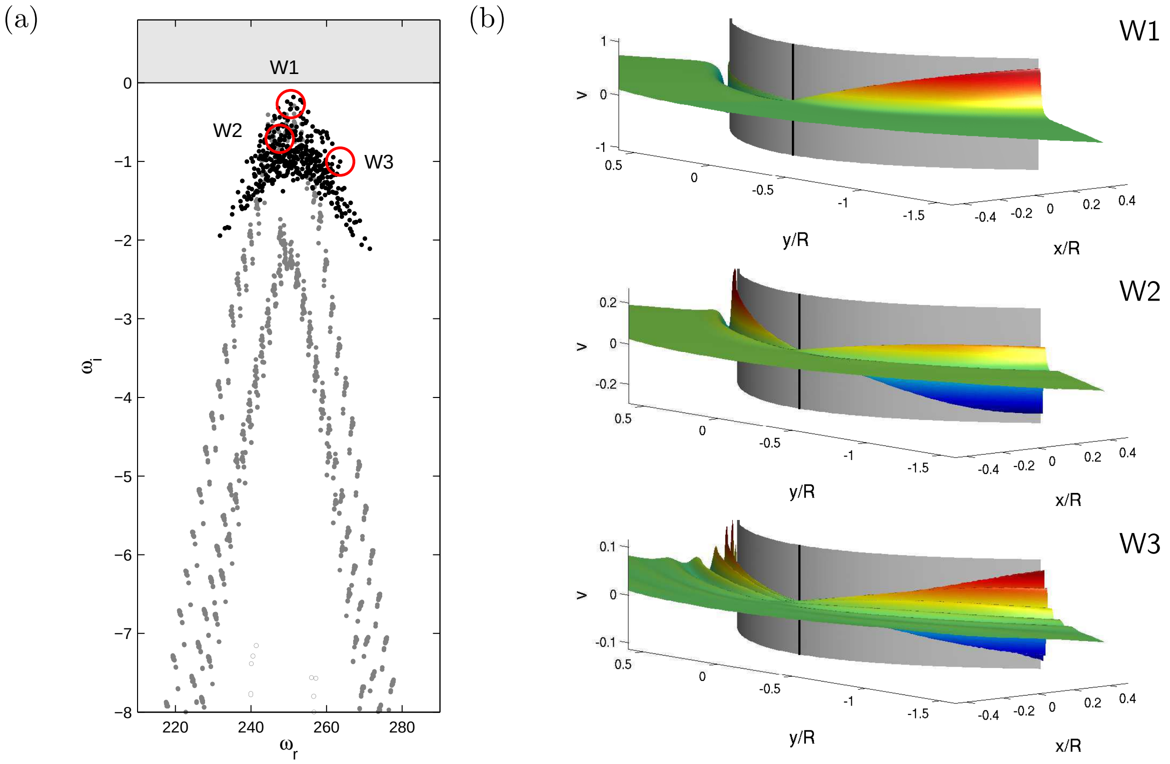

Figure 5.8. (a) Computed region of the global spectrum containing the eigenvalues belonging to wave packet modes (see region IV in figure 5.1). (b) Three representative wave packet modes ($W1$, $W2$ and $W3$) are visualized by the (normalized) chordwise velocity v; attachment line in black.

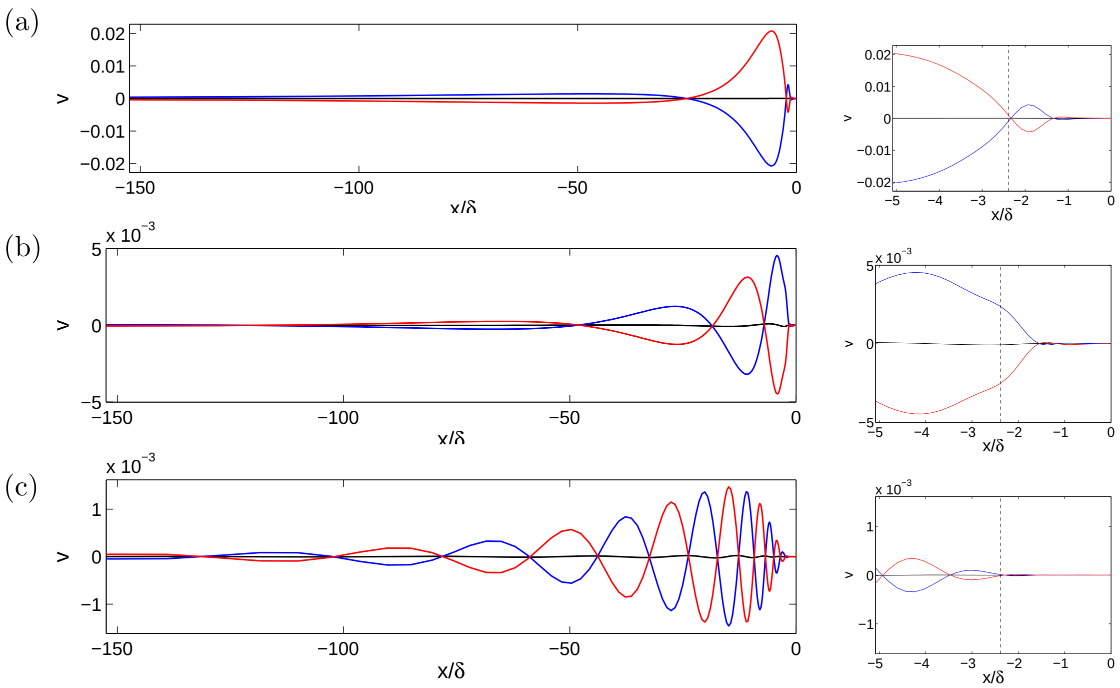

Figure 5.9. Amplitude distribution of the three wave packet modes shown in figure 5.8: (a) W1, (b) W2 and (c) W3. The modes are visualized using cross-cut profiles at the attachment line (in black) and at selected positions near the attachment line.

details. For this reason, it can be assumed, and will be later argued, that this part of the spectrum consists of an area which is progressively filled by the discrete eigenvalues as the numerical parameters (resolution, starting vector, Cayley parameters, convergence tolerances, etc.) but not the physical parameters are varied.

The location and distribution of the eigenvalues in region IV suggest a link to the continuous spectrum, familiar from boundary layers (Grosch and Salwen, 1978; Balakumar and Malik, 1992) and other semi-infinite and bi-infinite viscous shear flows. In the boundary-layer case, the continuous spectrum can be determined by a constant coefficient Orr–Sommerfeld equation for the freestream. Its solutions are given by bounded exponential and trigonometric functions; the location of the spectrum is defined by a line parameterized by a wall-normal wavenumber.

In contrast, our governing equations evaluated in the freestream still retain a dependence on the wall-normal coordinate via the non-uniform base velocity. As a consequence, the solutions in the freestream are no longer wave trains (as, for instance, in the boundary layer) but rather localized wave packets. As an example, three representative modes (W1, W2 and W3) from region IV are displayed in figure 5.8(b) which show the spatial distribution of v in the normal direction in form of a wave packet; this property is even more visible in figure 5.9 where we present cross-cut profiles of W1, W2 and W3 in the normal direction near the attachment line. These cross-cuts also demonstrate that the wave packet modes extend into the boundary layer (see figure 5.9, on the right) and thus establish a connection between boundary-layer and exterior perturbation dynamics. They are thus certain to play a critical role in the receptivity of boundary-layer instabilities to the external disturbance environment (see, e.g., Zaki and Durbin, 2005).

A consequence of the wave packet shape is its parameterization by *two* variables, a wall-normal local wavenumber and the location of the wave packet peak (Trefethen, 2005; Obrist and Schmid, 2009). For this reason, the associated continuous spectrum is area-filling as the continuous spectrum for the boundary layer was line-filling due to only *one* variable, the wall-normal local wavenumber.

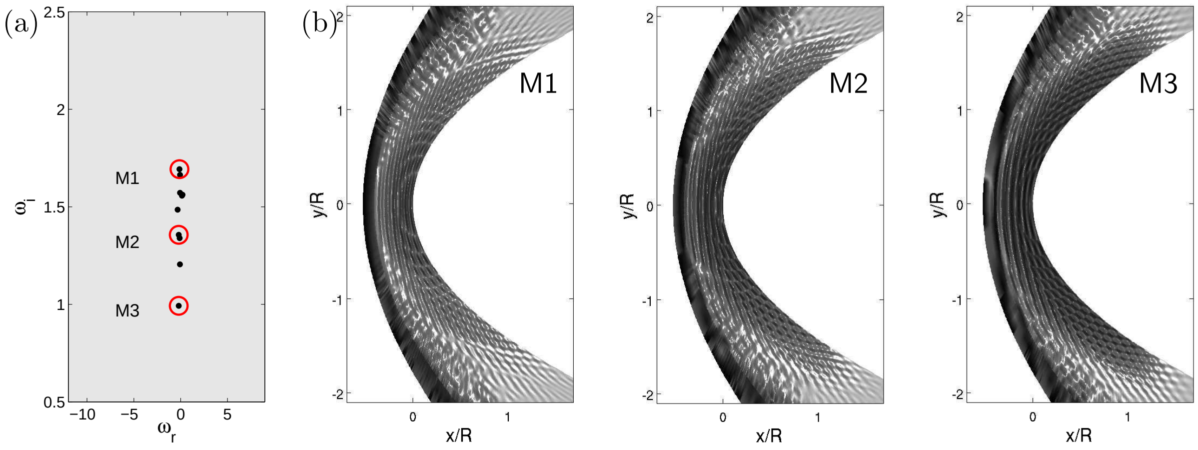

Figure 5.10. (a) Computed region of the global spectrum containing the shock-related modes (see region V in figure 5.1). (b) Spatial structure of a sample of associated global modes belonging to the eigenvalues M1, M2 and M3 in (a). The modes are visualized by the (normalized) pressure in the x-y-plane.

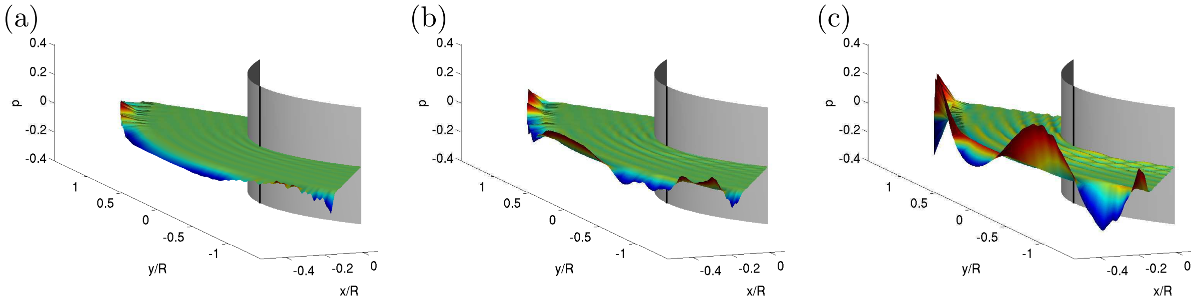

Figure 5.11. Three-dimensional visualization of the three shock-related global modes M1, M2 and M3 displayed in figure 5.10.

5.5 Shock-related modes – region V

The DNS-based global stability solver uncovered a fourth type of global modes. These modes appear to be always unstable and to feature near zero frequency ($\omega_r \approx 0$). The relevant region V in the global spectrum (see figure 5.1) is shown in figure 5.10(a). The spatial structure of three representative modes (M1, M2 and M3), visualized by the pressure, is displayed in figure 5.10(b). These modes are found (i) to be symmetric with respect to the attachment line, (ii) to exhibit their largest amplitude — which is rather erratic in the downstream direction — at the grid line defining the inflow boundary, and (iii) to feature small and oscillating structures near the attachment line; the latter structures are more pronounced for less amplified modes. The listed features are more evident in figure 5.11. Furthermore, the particular spatial distribution of the global modes indicates a strong interaction between the detached moving bow shock and the surface of the body; hence, the notion shock-related global modes. Moreover, the observation that these modes disappear if the shock-fitting technique is replaced by a non-reflecting boundary condition at the inflow boundary confirms this conjecture.

However, even though these global modes exhibit a characteristic and mostly smooth spatial shape, the corresponding eigenvalues, in particular the growth rate ω_i, are not converged. Instead, the growth rate varies randomly between $0 \lesssim \omega_i \lesssim 5$ when changing the parameters of the DNS-based global stability solver[1] (m, k and ϵ_0; not tol_A), the grid resolution (n_1, n_2)

---

[1] The untransformed Arnoldi method was used to delineate the effects of the parameters m, k, tol_A and ϵ_0 from those of the Cayley transformation.

as well as the physical parameters (β, Re_s and Ma_s). Thus, further investigations are required. Moreover, the presence of these modes leads to serious convergence problems for the Arnoldi method, in particular, if no transformation is applied.

5.6 Parameter studies

Compressible flow around a swept parabolic body is governed by a large number of parameters (see section §2.2.2) describing various flow quantities, fluid properties and geometric characteristics of the flow configuration. For a particular choice of parameters, i.e., $Re_s = 800$, $Re_R = 129136$, $Ma_s = 1.25$, $\theta_w = 1$ and $\beta = 0.314$, the global spectrum (see figure 5.1) revealed that the only temporal instabilities arise from boundary-layer and/or acoustic modes. To gain further insight into the global stability properties of both types of instabilities, we present a parametric study of their stability behavior by varying the spanwise disturbance wavenumber $\beta = 2\pi/L_z$ and the leading-edge Reynolds number Re_R. In particular, we focus on the stability of the global modes in region I and II in figure 5.1.

The first parametric study allows us to investigate the linear stability of a computed base flow with respect to spanwise-propagating perturbations with a fundamental length scale L_z. The second parametric study assesses the influence of the leading-edge Reynolds number Re_R, via the leading-edge radius R, on the stability of the flow. This influence is particularly important for the global stability of the boundary-layer modes since curvature effects have a strong impact on the stability of boundary-layer modes as discussed in section §1.1.2 and §1.1.3. Such a study requires, for each value of Re_R, the computation of a steady base flow, even though the freestream conditions remain fixed. While for these two parameter studies the freestream conditions remain unchanged, investigating the influence of additional parameters (sweep angle, sweep Mach number, wall temperature ratio, etc.) requires a substantial effort owing to the added complication of a nonlinear dependence of the these parameters on the freestream conditions (see section §2.2.2 for details).

Influence of the spanwise disturbance wavenumber β

The computed temporal spectra of the (most unstable) boundary-layer modes for selected spanwise wavenumbers $0.071 \leq \beta \leq 0.349$ are shown in figure 5.12(a). For a given value of β, the frequency ω_r and its corresponding growth rate ω_i reveal an unstable discrete branch as discussed in section §5.2. Each branch displays a maximum value of the growth rate ω_i, and this value appears to grow steadily up to a wavenumber $\beta = 0.213$ before decaying again (see crossflow branch in figure 5.13a); the same figure 5.13(a) indicates that the boundary-layer modes are unstable for $0.061 \leq \beta \leq 0.363$. Such a dependence of ω_i on the spanwise disturbance wavenumber β is typical for boundary-layer instabilities and, for instance, has been reported by Lin and Malik (1996) for attachment-line instabilities.

By adjusting the parameters in the Cayley transformation of our DNS-based global stability solver, we are also able to focus on the computation of fast-moving acoustic modes (see region II in figure 5.1). In figure 5.12(b), we present the influence of β on the stability of these modes. We observe clusters of discrete acoustic eigenvalues where the least-stable mode belongs to the S-branch (see section §5.3.1 for details). This mode is, similar to the most unstable boundary-layer mode, unstable for a specific range of spanwise wavenumbers $0.118 \leq \beta \leq 0.585$ (see acoustic branch in figure 5.13a). It is furthermore evident from the same figure 5.13(a) that the overall prevailing instability can come from either branch depending on the spanwise scale of the perturbation.

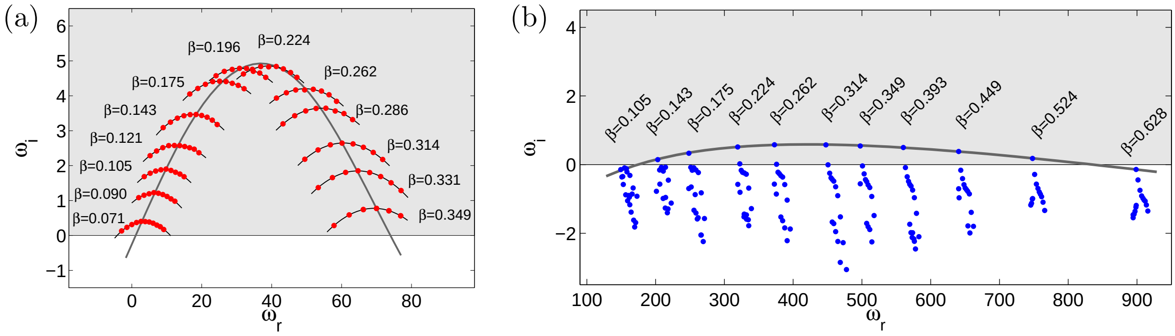

Figure 5.12. Influence of the spanwise disturbance wavenumber β on the temporal stability of boundary-layer (a) and acoustic modes (b); ω_r denotes the disturbance frequency and ω_i the corresponding growth rate. The solid lines in dark grey describe the evolution of the maximum temporal growth rate $\omega_{i,max}$, and the evolution of $\omega_{i,max}$ as a function of β for either type of instability is shown in figure 5.13(a); unstable half-plane in grey.

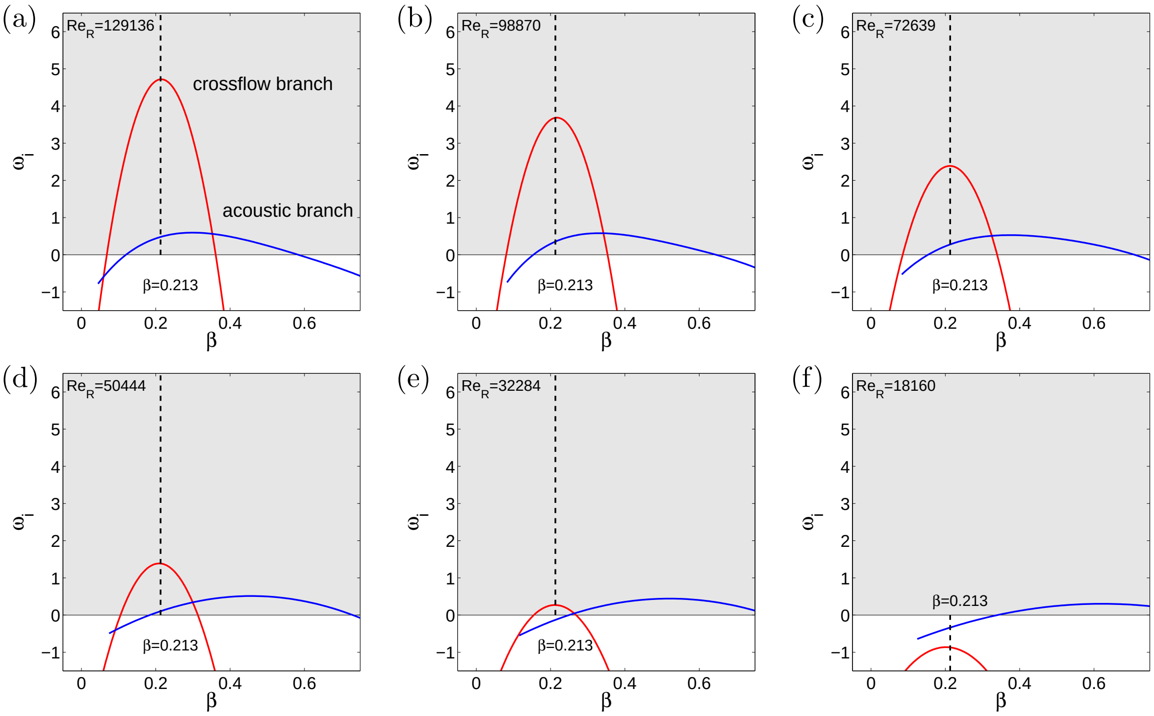

Figure 5.13. Influence of β on the maximum growth rate $\omega_{i,max}$ for boundary-layer (in red) and acoustic instabilities (in blue) for selected values of the leading-edge Reynolds number Re_R; unstable half-plane in grey.

Influence of the leading-edge Reynolds number Re_R

The influence of the leading-edge Reynolds number Re_R on the global stability of the flow is demonstrated in figure 5.13. As expected, a stabilizing effect due to a convex curvature parameterized by the leading-edge radius R has been found as Re_R is decreased from 129136 (see figure 5.13a) to 18160 (see figure 5.13f)[2]. This observation is in accordance with wind-tunnel

---

[2] As mentioned in section §2.2.2, variations in the leading-edge Reynolds number Re_R cause a proportional change in the leading-edge radius R (as well as in the sweep Reynolds number Re_s) — see equation (2.7) — and, as a consequence, Re_s decreases from 800 to 300 (with a step size of 100) as Re_R is decreased from 129136 to 18160 (see table 5.3).

$$Re_R = \frac{1}{2}\left(\frac{R}{\delta}\right)^2 = 2\left(\frac{Re_s}{\tan\Lambda_2}\right)^2$$

Table 5.3. Overview showing the values for the sweep Reynolds number Re_s, the leading-edge Reynolds number Re_R, the non-dimensionalized leading-edge radius R/δ and the viscous length δ for selected parameter choices. The parameters $\bar{R}^*$ and $Re_{D,\infty}$ represent alternative definitions for the Reynolds number.

Re_s	Re_R	R/δ	δ in 10^{-4} [m]	$\bar{R}^*$	$Re_{D,\infty} \times 10^5$
800	129136	508	1.968	840	35.3
700	98870	445	2.249	735	27.0
600	72639	381	2.624	630	19.6
500	50444	318	3.148	525	13.8
400	32284	254	3.935	420	8.8
300	18160	191	5.247	315	5.0
200	8071	127	7.871	210	2.2

experiments on a swept wing as reported in Bippes (1999) and with theoretical studies on the effect of leading-edge curvature using local models of the attachment-line boundary layer (Lin and Malik, 1997).

Furthermore, the results in figure 5.13 show that the boundary-layer modes (denoted by crossflow branch) exhibit significantly larger growth rates ω_i than the acoustic modes for large values of Re_R. These growth rates decay linearly with Re_R, and the maximum growth rate $\omega_{i,max}$ is always found at a critical spanwise wavenumber of $\beta = 0.213$ (see dashed lines in figure 5.13). The acoustic modes, on the other hand, show rather weak growth rates, do not scale linearly with Re_R and do not show a Reynolds number independent critical value of β.

To aid the reader in comparing the present findings with results from the literature we given an overview showing the values for the present definition of the sweep Reynolds number Re_s and the leading-edge Reynolds number Re_R as well as the corresponding values from alternative definitions of the Reynolds number in table 5.3. In this table, $\bar{R}^*$ denotes the sweep Reynolds number

$$\bar{R}^* = \left(\frac{u_2 R}{2\nu^*}\right)^{1/2} \tan\Lambda_2, \tag{5.2}$$

where the kinematic viscosity ν^* is evaluated at a reference temperature T^* as proposed by Poll (1984) (reference temperature concept for compressible flows). This reference temperature is obtained by

$$T^* = T_e + 0.1(T_w - T_e) + 0.6(T_r - T_e) \tag{5.3}$$

with the T_e, T_w and T_r as the temperature at the boundary-layer edge, the temperature at the wall and the recovery temperature, respectively. The freestream Reynolds number $Re_{D,\infty}$ is defined as

$$Re_{D,\infty} = \frac{q_\infty D}{\nu_\infty}, \tag{5.4}$$

where D denotes the length scale (the diameter of a circular cylinder) and ν_∞ stands for the kinematic viscosity in the freestream.

The neutral curve

The neutral curve for supersonic flow about a swept parabolic body is presented in figure 5.14. In this figure, we display contours of constant growth rate ω_i for the boundary-layer modes (red lines) and the acoustic modes (blue lines). The presence of unstable global modes of boundary-layer as well as acoustic type yields a composite neutral stability curve delineating parameter regimes across which either boundary-layer or acoustic modes change from stable to unstable — this feature was already discussed in figure 5.13 which shows cross-cut profiles of the neutral curve

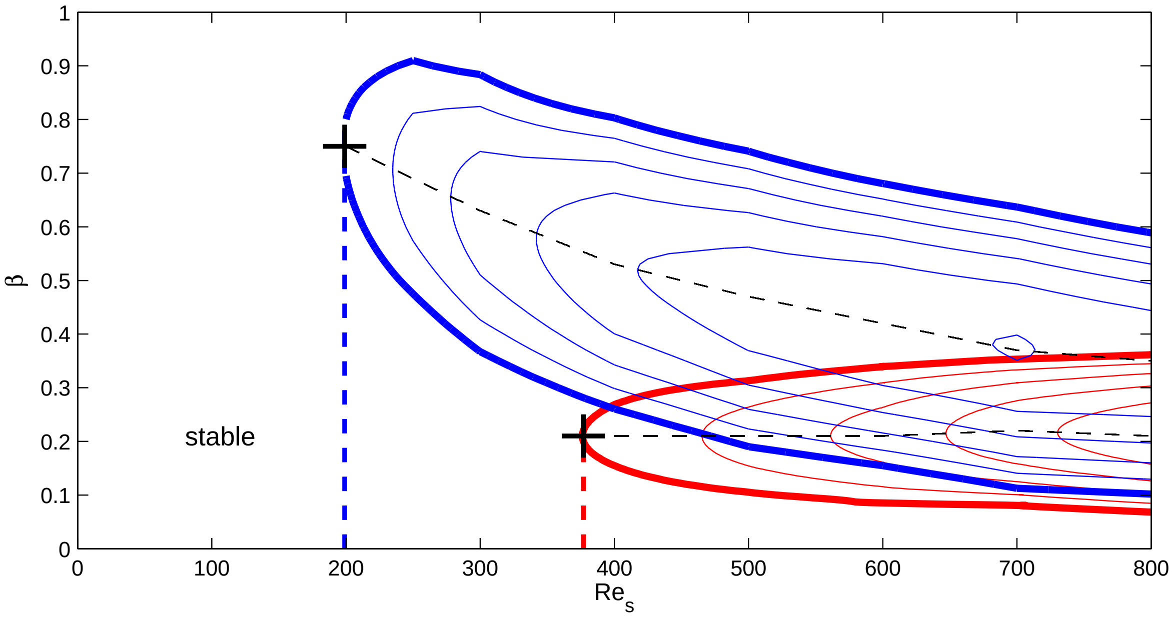

Figure 5.14. Neutral curve for supersonic flow about a swept parabolic body for a sweep Mach number $Ma_s = 1.25$ and an adiabatic wall (boundary-layer modes in red, acoustic modes in blue); the thick contour lines represent zero growth ($\omega_i = 0$); contour spacing for the boundary-layer modes $\Delta\omega_i = 1$, contour spacing for the acoustic modes $\Delta\omega_i = 0.1$. The dashed lines indicate the evolution of the maximum value of the growth rate.

for selected values of Re_s. Boundary-layer instabilities prevail for small spanwise wavenumbers β and cease to exist below a critical Reynolds number of $Re_{s,crit} \approx 377$ (for $\beta = 0.213$). For rather large values of the spanwise disturbance wavenumber β acoustic instabilities dominate the linear stability of the flow even for sweep Reynolds numbers $Re_{s,crit} < 377$. However, for $Re_s < 195$ acoustic instabilities cease to exist as well.

Chapter 6

Conclusions and outlook

The present thesis attempts, for the first time, a global stability analysis of compressible flow about a swept parabolic body. What has initially been motivated by the goal to extent our current knowledge of swept leading-edge flow in general and our still incomplete understanding of boundary-layer transition on blunt bodies in particular, not only led to new insight into boundary-layer instabilities but also revealed a number of new types of instabilities. A profound understanding of all involved instability mechanisms is crucial for an efficient design and a proper performance of, for instance, high-performance aircraft. A necessary prerequisite to perform such a comprehensive study of swept leading-edge flow was the extension of available numerical techniques and the development of an advanced and powerful simulation-based global stability solver.

Considerable progress in computational resources and the invention of high-performance iterative techniques for the efficient solution of large-scale eigenvalue problems allowed us to develop such a technique in this thesis in form of a DNS-based global stability solver. This solver represents a robust and powerful numerical tool to extract stability information directly from numerical simulations. It features a matrix-free implementation, a spectral transformation to access selected parts of the global spectrum as well as preconditioning techniques in order to robustify the solver and to enhance its performance. Even though the complexity of a DNS-based global stability analysis goes far beyond the complexity of direct numerical simulations (DNS), the limitations and shortcomings of local or simplified flow models and the promise of obtaining new results call for the combination of these two techniques; in other words, such a tool can produce quantitative flow characteristics whose contribution to our understanding of fluid behavior far surpasses existing ones.

In our studies, flow in the leading-edge region of a yawed blunt body is modeled by compressible flow about a swept parabolic body. This flow model treats the flow in the vicinity of the stagnation line and the region further downstream as one entity. This is in contrast to previous theoretical and numerical studies where both regions have been studied separately — a necessary approach to apply standard techniques — using distinct simplifying local flow models. Results from these local investigations still constitute most of our current understanding of swept leading-edge flow despite a number of unanswered but practically relevant questions. In this sense, this thesis attempts to address some of these questions using a flow model that closer approximates a realistic flow situation. To compute the flow fields direct numerical simulations of the nonlinear governing equations are performed using shock-fitting, moving curvilinear grids and higher-order compact schemes.

The global stability solver has then been applied to explore different regions of the global spectrum and to compute the associated instabilities. This spectrum provides a complete picture of the temporal perturbation dynamics of the flow, and a wide and rich variety of modes has been uncovered: boundary-layer modes, different types of acoustic modes, wave packet modes and shock-acoustic interaction modes. Each type of these modes has been cataloged and analyzed as to their symmetry, spatial location and physical significance. For instance, the spatial structure of the boundary-layer modes demonstrated, for the first time in a definitive manner, a connection between instabilities in the vicinity of the stagnation line and the crossflow vortices further downstream. This finding was a direct consequence of using a more comprehensive model for swept leading-edge flow and studying its stability by applying a global stability approach.

A parameter study varying the spanwise wavenumber and the sweep Reynolds number reproduced a preferred spanwise length-scale and a critical Reynolds number for a boundary-layer or acoustic instability. For certain parameter choices, the acoustic modes have been found to dominate the boundary-layer modes. Finally, the critical sweep Reynolds number for boundary-layer instabilities was found to lie in the subcritical regime and to approach the measured critical value for large-amplitude perturbations. This finding strongly suggests that the for decades unexplained gap between theory and experiments can now be closed by investigations based on a proper global stability analysis.

Outlook

The results presented in this thesis amply demonstrate that a global stability approach combined with a proper flow model is the method of choice for analyzing the stability behavior of complex flows in complex geometries. In particular, the novel findings in this thesis should provide enough motivation for further studies on flow about a swept parabolic body. As an example, two specific issues would be worth investigating: the temporal evolution of a superposition of boundary-layer modes to assess non-modal effects and localized convective behavior, and the influence of an angle of attack on the stability behavior of the flow. It is known from experimental and numerical studies that the properties of the flow are altered appreciably if a non-zero angle of attack α is considered and that beyond a certain value of α, the flow exhibits a separation bubble in a region downstream from the stagnation line. This separation bubble is a consequence of changes in the chordwise pressure gradient, and it is known from boundary-layer flows that it significantly affects the inherent stability properties of the flow. Such a study is also very important from an engineering point of view since virtually any flow situation encountered for aerodynamically loaded bodies, such as wings or blades, features a non-symmetric flow configuration.

The specific example of compressible flow about a swept parabolic body, as presented in this thesis, clearly demonstrates the feasibility and potential of a DNS-based global stability concept. From an even more general point of view, simulation-based flow analysis is expected to evolve into a powerful and important tool to investigate fluid behavior. Receptivity, sensitivity and input-output behavior are among these analyses where a simulation-based approach would open the range of applications. In this case, flow fields from simulations will provide the input data for the analysis, and consequently we may be able to analyze complex flows that we can simulate with a sufficient degree of accuracy and fidelity. This same general concept of simulation-based analysis can easily be extended to process flow fields from other simulation techniques, such as large-eddy simulations (LES) or detached-eddy simulations (DES). It is thus necessary to advance simulation techniques as well as efficient algorithms for large-scale linear systems. As a final statement, it is hoped that simulation-based flow analysis, as demonstrated in this thesis, will mature into a valuable tool and will have a significant impact on complex flow applications of academic and industrial interest alike.

> *“Echt krass was man mit Mathematik alles rauskriegt”*
> anonymous

Acknowledgments

The present doctoral thesis is based on a research project carried out by the author during his affiliation with the Laboratoire d’Hydrodynamique (LadHyX), École Polytechnique. I would like to deeply thank the directors of that institution, Patrick Huerre and Jean-Marc Chomaz, for their warm hospitality and support. Large parts of the research have also been conducted during stays at the University of Washington (UW), Seattle, the Technische Universität München (TUM) and the Universität der Bundeswehr München (UniBwM), and all institutions as well as their directors are thanked for welcoming and supporting me. Financial support from the Deutsche Forschungsgemeinschaft (DFG) and the German National Academic Foundation (Studienstiftung des Deutschen Volkes) is gratefully acknowledged.

A number of people have vitally contributed to this project, and, first of all, I want to express my deep gratitude to Prof. Peter Schmid. Peter, it want to say “Thank you very much!” for the continuous support and the patient way you were guiding me throughout my doctoral thesis. It has always been strongly motivating and stimulating to see your thoroughgoing attitude and enthusiasm about teaching and scientific research, and it was an honor and pleasure for me to discuss scientific and everyday matters alike.

I am also very thankful to Prof. Rainer Friedrich for the personal and professional support I received at the “Fluid Dynamics Group” (TUM). I would furthermore like to express my appreciations to Prof. Jörn Sesterhenn for his support while I was staying at the “Institute of Numerical Mathematics” (UniBwM) and for providing information and suggestions regarding the numerical simulations as well as the vast body of literature on the stability of swept leading-edge flow. In addition, I want to express my gratitude to Prof. Jean-Paul Bonnet, Prof. Patrick Huerre, Dr. Dominik Obrist and Prof. Nigel Peake for being part of my jury.

My research activities at several universities not only allowed me to experience different cultures and various academic institutions but also to get to know a large number of people. At this point I have to mention my dear friend and officemate Jan Schulze (le bird). Thanks a lot for the enriching discussions and the generous support no matter if it was about research or teaching. It was great to hang out with you. I further want to thank the former colleagues from the TUM: Christoph, Inga, Aaron and Somnath, as well as my fellows from the UniBwM: Gisela, Olivier and Alex, for their kind support and for sharing knowledge. To this day, I still very much appreciate the time I could spent at the “Department of Applied Mathematics” (UW) in Seattle, and I want say “Thanks guys!” for your kindness and hospitality during my stays. Special greetings go to my bodies Jon, Damon, Rafa and master Will.

“Cher labo”, it was a great pleasure for me to be part of the LadHyX team. It is a wonderful place to study the fundamentals of fluid mechanics, to meet open-minded people and to discuss the particularities of the French way of life (“Le trafic du RER B est fortement perturbé”). In a more or less erratic selection I want to thank Emmanuel, Pascal, Sabine, Antoine, Paul, Charles, Paul, Carlo, François, Lutz, Daniel, Alexandre, Tonio, Sandrine et Thérèse. I also want to say “See you” to the Postdocs and former doctoral students: Julien, Eletta, Jimmy, Ashley, Fulvio and Alan, Axel, Claire, Rémi, Mat, Fred, Gregory. “Good luck” to all the prospective doctoral students: Maria-Luisa, Elena, Alex, Yu, Cristóbal, Shehryar, Gianluca, Xavier, Yongyun, Pierre, Rémi, John, Joran, Juhno, Madiha, Christelle, Benoît and Miguel.

Short-term stays and the need for housing in Paris appeared to be as challenging as solving global stability problems, and I want to express my sincere thanks to all of those who gave me shelter while I was a SDF: Joe, Beatrix and Hagay, Karin, Rémi, Mat, Ben, Cristóbal, Olivier, Xavier and Alex.

It is needless to stress the importance of family and friends, and special greetings go to some close friends from my engineering studies: Manne, Michi, Dani and Paparol. I also want to thank my lady Guni and my siblings Maria and Wolfgang. Last but not least, I'm deeply indebted to my parents who permanently supported me during my engineering as well as my doctoral studies.

Palaiseau, November 2009
Christoph Mack

Bibliography

Åkervik, E., Brandt, L., Henningson, D. S., Hœpfner, J., Marxen, O., and Schlatter, P. (2006). Steady solutions of the Navier–Stokes equations by selective frequency damping. *Phys. Fluids*, 18(068102).

Adams, N. A. and Shariff, K. (1996). A high-resolution hybrid compact–ENO scheme for shock–turbulence interaction problems. *J. Comput. Phys.*, 127:27–51.

Ambrosio, A. and Wortman, A. (1962). Stagnation point shock detachment distance for flow around spheres and cylinders. *ARS J.*, 32:281.

Amestoy, P. R., Duff, I. S., and Koster, J. (2007). *MUltifrontal Massively Parallel Solver (MUMPS).* http://mumps.enseeiht.fr/.

Anderson, D., Tannehill, J., and Pletcher, R. (1988). *Computational Fluid Mechanics and Heat Transfer.* Hemisphere Publishing Corporation.

Bagheri, S., Schlatter, P., Schmid, P., and Henningson, D. (2009). Global stability of a jet in crossflow. *J. Fluid Mech.*, 624:33–44.

Balakumar, P. and Malik, M. R. (1992). Discrete modes and continuous spectra in supersonic boundary layers. *J. Fluid Mech.*, 239:631–656.

Balakumar, P. and Trivedi, P. A. (1998). Finite amplitude stability of attachment line boundary layers. *Phys. Fluids*, 10(9).

Benzi, M. (2002). Preconditioning Techniques for Large Linear Systems: A Survey. *J. Comput. Phys.*, 182:418–477.

Bertolotti, F. P. (1999). On the connection between cross-flow vortices and attachment-line instabilities. In *IUTAM Symp. on Laminar-Turbulent Transition*, pages 625–630, Sedona, USA.

Billig, F. S. (1967). Shock-wave shapes around spherical- and cylindrical-nosed bodies. *J. Spacecraft Rockets*, 4(6):822–823.

Bippes, H. (1999). Basic experiments on transition in three-dimensional boundary layers dominated by crossflow instability. *Prog. Aero. Sci.*, 35:363–412.

Bonfigli, G. and Kloker, M. (2007). Secondary instability of crossflow vortices: validation of the stability theory by direct numerical simulation. *J. Fluid Mech.*, 583:229–272.

Burroughs, E. A., Romero, L. A., Lehoucq, R. B., and Salinger, A. G. (2004). Linear stability of flow in a differentially heated cavity via large-scale eigenvalue calculations. *Int. Journal of Num. Meth. for Heat & Fluid Flow*, 14:803–822.

Creel, T. T., Beckwith, I. E., and Chen, F. J. (1987). Transition on swept leading-edges at Mach 3.5. *J. Aircraft*, 24(10):710–717.

Cumpsty, N. A. and Head, M. R. (1969). The calculation of the three-dimensional turbulent boundary layer. Part III Comparison of attachment-line calculations with experiment. *Aero. Q.*, 20:99–113.

Daniel, J., Gragg, W. B., Kaufmann, L., and Steward, G. W. (1976). Reorthogonalization and stable algorithms for updating the Gram–Schmidt QR factorization. *Math. Comput.*, 30:772–795.

Davis, T. A. and Duff, I. S. (1997). An unsymmetric-pattern multifrontal method for sparse LU factorization. *SIAM J. Matrix Anal. Applics.*, 18:140–158.

Edwards, W. S., Tuckerman, L. S., Friesner, R. A., and Sorensen, D. C. (1994). Krylov methods for the incompressible Navier–Stokes equations. *J. Comput. Phys.*, 110:82–102.

Gaillard, L., Benard, E., and Alziary de Roquefort, T. (1999). Smooth leading edge transition in hypersonic flow. *Experiments in Fluids*, 26:169–176.

Garratt, T. J., Moore, G., and Spence, A. (1993). A generalised Cayley transform for the numerical detection of Hopf bifurcations in large systems. In *Contributions in numerical mathematics*, volume 2 of *World Sci. Ser. Appl. Anal.*, pages 177–195. World Sci. Publishing.

Gaster, M. (1965). A simple device for preventing turbulent contamination on swept leading edges. *J. Roy. Aero. Soc.*, 69:788.

Gray, W. E. (1952). The effect of wing sweep on laminar flow. Technical Report RAE TM Aero 255, British Royal Aircraft Establishment.

Grosch, C. E. and Salwen, H. (1978). The continuous spectrum of the Orr–Sommerfeld equation. Part I. The spectrum and the eigenfunctions. *J. Fluid Mech.*, 87:33–54.

Guégan, A., Schmid, P. J., and Huerre, P. (2006). Optimal energy growth and optimal control in swept Hiemenz flow. *J. Fluid Mech.*, 566:11–45.

Hall, P. and Malik, M. (1986). On the instability of a three-dimensional attachment-line boundary layer: weakly nonlinear theory and a numerical approach. *J. Fluid Mech.*, 163:257–282.

Hall, P., Malik, M., and Poll, D. I. A. (1984). On the stability of an infinite swept attachment-line boundary layer. *Proc. R. Soc. Lond.*, A 395:229–245.

Heeg, R. (1998). *Stability and transition of attachment-line flow.* PhD thesis, Universiteit Twente, Enschede.

Heeg, R. S. and Geurts, B. J. (1998). Spatial instabilities of the incompressible attachment-line flow using sparse matrix Jacobi–Davidson techniques. *Applied Scientific Research*, 59:315–329.

Herbert, T. (1997). Parabolized stability equations. *Annu. Rev. Fluid Mech.*, 29:245–283.

Joslin, R. D. (1995). Direct simulation of evolution and control of three-dimensional instabilities in attachment-line boundary layers. *J. Fluid Mech.*, 291:369–392.

Joslin, R. D. (1996). Simulation of nonlinear instabilities in an attachment-line boundary layer. *Fluid Dyn. Res.*, 18:81–97.

Kennedy, C. A., Carpenter, M. H., and Lewis, R. M. (2000). Low–storage, explicit Runge–Kutta schemes for the compressible Navier–Stokes equations. *Appl. Numer. Math.*, 35:177–219.

Knoll, D. A. and Keyes, D. E. (2004). Jacobian-free Newton–Krylov methods: a survey of approaches and applications. *J. Comput. Phys.*, 193(2):357–397.

Kundu, P. K. and Cohen, I. M. (2002). *Fluid Mechanics, Second Edition.* Academic Press.

Le Duc, A., Sesterhenn, J., and Friedrich, R. (2006). Instabilities in compressible attachment-line boundary layers. *Phys. Fluids*, 18(044102).

Lehoucq, R. B. and Meerbergen, K. (1998). Using generalized Cayley transformations within an inexact rational Krylov sequence method. *SIAM J. Matrix Anal. Appl.*, 20(1):131–148 (electronic).

Lehoucq, R. B. and Salinger, A. G. (2001). Large-scale eigenvalue calculations for stability analysis of steady flows on massively parallel computers. *Int. J. Numer. Meth. Fluids*, 36:309–327.

Lehoucq, R. B., Sorensen, D. C., and Yang, C. (1998). *ARPACK Users' Guide.* Software, Environments, and Tools. Society for Industrial and Applied Mathematics (SIAM), Philadelphia, PA. Solution of Large-Scale Eigenvalue Problems with Implicitly Restarted Arnoldi Methods.

Lele, S. K. (1992). Compact finite difference schemes with spectral-like resolution. *J. Comput. Phys.*, 103:16–42.

Lin, R. S. and Malik, M. R. (1995). Stability and transition in compressible attachment-line boundary-layer flow. Technical Report 952041, SAE.

Lin, R. S. and Malik, M. R. (1996). On the stability of attachment-line boundary layers. Part 1. The incompressible swept Hiemenz flow. *J. Fluid Mech.*, 311:239–255.

Lin, R. S. and Malik, M. R. (1997). On the stability of attachment-line boundary layers. Part 2. The effect of leading edge curvature. *J. Fluid Mech.*, 333:125–137.

Mack, C. J. and Schmid, P. J. (2009). Direct numerical simulations of hypersonic flow about a swept parabolic body. *Comput. Fluids.* submitted.

Mack, C. J. and Schmid, P. J. (2010). A preconditioned Krylov technique for global hydrodynamic stability analysis of large-scale compressible flows. *J. Comput. Phys.*, 229(3):541–560.

Mack, L. M. (1984). Boundary layer linear stability theory. In *Special Course on Stability and Transition of Laminar Flow*, number AGARD–R–709. AGARD.

Marquet, O., Sipp, D., and Jacquin, L. (2008). Sensitivity analysis and passive control of cylinder flow. *J. Fluid Mech.*, 615:221–252.

Meerbergen, K. and Roose, D. (1997). The restarted Arnoldi method applied to iterative linear system solvers for the computation of rightmost eigenvalues. *SIAM J. Matrix Anal. Appl.*, 18(1):1–20.

Moretti, G. (1987). Computations of flows with shocks. *Annu. Rev. Fluid Mech.*, 19.

Morkovin, M. V., Reshotko, E., and Herbert, T. (1994). Transition in open flow systems – a reassessment. *Bull. Am. Phys. Soc.*, 39.

Müller, B. (1990). Linear stability condition for explicit Runge–Kutta methods to solve the compressible Navier–Stokes equations. *Math. Methods i. Appl. Sci.*, 12:139–151.

Obrist, D. and Schmid, P. J. (2003). On the linear stability of swept attachment-line boundary layer flow. Part 1. Spectrum and asymptotic behaviour. *J. Fluid Mech.*, 493:1–29.

Obrist, D. and Schmid, P. J. (2009). Algebraically decaying modes and wave packet pseudomodes in swept Hiemenz flow. *J. Fluid Mech.* in press.

Oertel, Jr., H. and Stank, R. (1999). Dynamics of localized disturbances in transonic wing boundary layers. *AIAA*, pages Paper 94–0001.

Osei-Kuffuor, D. and Saad, Y. (2007). A comparison of preconditioners for complex-valued matrices. Technical report, University of Minnesota Supercomputing Institute Research Report UMSI 2007/139.

Pfenninger, W. (1965). Some results form the X-21 programm. Part I - Flow phenomena at the leading edge of swept wings. Technical Report 97, AGARDograph.

Pfenninger, W. (1977). Laminar flow control – Laminarization. special course on concepts for drag reduction. Technical Report 654, AGARD.

Pfenninger, W. and Bacon, J. W. (1969). Amplified laminar boundary layer oscillations and transition at the front attachment line of a 45 ° swept flat-nosed wing with and without boundary layer suction. In *Viscous Drag Reduction*. C. S. Wells.

Piquemal, A. S., Chiavassa, G., and Donat, R. (2004). A Brinkman-penalization method for compressible viscous flows. *Comput. Fluids*. submitted.

Poll, D. I. A. (1978). Some aspects of the flow near a swept attachment line with particular reference to boundary layer transition. Technical Report CoA 7805, Cranfield Institute of Technology.

Poll, D. I. A. (1979). Transition in the infinite swept attachment-line boundary layer. *Aero. Q.*, 30:607–628.

Poll, D. I. A. (1983). The development of intermittent turbulence on a swept attachment line including the effects of compressibility. *Aero. Q.*, XXXIV:1–23.

Poll, D. I. A. (1984). Transition description and prediction in three-dimensional flows. In *Special Course on Stability and Transition of laminar Flow*, pages 5/1–5/23. AGARD.

Poll, D. I. A. (1985). Some observations of the transition process on the windward face of a long yawed cylinder. *J. Fluid Mech.*, 150:329–356.

Reed, H. L. and Saric, W. S. (1989). Stability of three-dimensional boundary layers. *Annu. Rev. Fluid Mech.*, 21:235–284.

Reed, H. L., Saric, W. S., and Arnal, D. (1996). Linear stability theory applied to boundary layers. *Annu. Rev. Fluid Mech.*, 28:389–428.

Reshotko, E. (1994). Boundary layer instability, transition, and control. *Dryden Lecture in Research*, pages AIAA Paper 94–0001.

Reshotko, E. and Beckwith, I. E. (1958). Compressible laminar boundary layer over a yawed infinite cylinder with heat transfer and arbitrary Prandtl number. Technical Report 1379, National Advisory Committee for Aeronautics.

Robitaillié-Montané, C. (2005). *Une approche non locale pour l'étude des instabilités linéaires. Application à l'écoulement de couche limite compressible le long d'une ligne de partage.* PhD thesis, École Nationale Supérieure, Lyon.

Saad, Y. (1994). SPARSKIT: a basic tool kit for sparse matrix computations - Version 2.

Saad, Y., editor (2003). *Iterative Methods for Sparse Linear Systems, Second Edition.* Society for Industrial and Applied Mathematics.

Saric, W. S. and Reed, H. L. (2003). Crossflow Instabilities – Theory & Technology. In *AIAA Paper*, number 2003–0771.

Saric, W. S., Reed, H. L., and White, E. B. (2003). Stability and transition of three-dimensional boundary layers. *Annu. Rev. Fluid Mech.*, 35:413–440.

Semisynov, A. I., Fedorov, A. V., Novikov, V. E., Semionov, N. V., and Kosinov, A. D. (2003). Stability and transition on a swept cylinder in a supersonic flow. *Journal of Applied Mechanics and Technical Physics*, 44:212–220.

Sesterhenn, J. (2001). A characteristic-type formulation of the Navier–Stokes equations for high-order upwind schemes. *Comput. Fluids*, 30:37–67.

Sesterhenn, J. (2004). *Strömungsinstabilitäten im Staulinienbereich schiebender Tragflügel.* Habilitationsschrift, TU München.

Sleijpen, G. L. G., Booten, A. G. L., Fokkema, D. R., and van der Vorst, H. A. (1996). Jacobi–Davidson type methods for generalized eigenproblems and polynomial eigenproblems. *BIT*, 36:595–633.

Sorensen, D. C. (1992). Implicit application of polynomial filters in a k-step Arnoldi method. *SIAM J. Matrix Anal. Appl.*, 13(1):357–385.

Sorensen, D. C. (2002). Numerical methods for large eigenvalue problems. *Acta Numer.*, 11:519–584.

Spalart, P. R. (1988). Direct numerical study of leading-edge contamination. In *AGARD-CP-438*, pages 5/1–5/13.

Spalart, P. R. (1989). Direct numerical study of crossflow instability. In *IUTAM Laminar-Turbulent Symposium III*, pages 621–630.

Theofilis, V. (1998). On linear and nonlinear instability of the incompressible swept attachment-line boundary layer. *J. Fluid Mech.*, 355:193–227.

Theofilis, V. (2003). Advances in global linear instability analysis of nonparallel and three-dimensional flows. *Prog. Aero. Sci.*, 39:249–315.

Theofilis, V., Fedorov, A., Obrist, D., and Dallmann, D. (2003). The extended Görtler–Hämmerlin model for linear instability of three-dimensional incompressible swept attachment-line boundary layer flow. *J. Fluid Mech.*, 487:271–313.

Trefethen, L. N. (2005). Wave packet pseudomodes of variable coefficient differential operator. *Proc. Roy. Soc. A*, 461(2062):3099–3122.

Trefethen, L. N. and Bau, D. (1997). *Numerical Linear Algebra.* Society for Industrial and Applied Mathematics (SIAM), Philadelphia, PA.

van der Vorst, H. A. (1992). Bi-CGSTAB: A fast and smoothly converging variant of Bi-CG for the solution of non-symmetric linear systems. *SIAM J. Sci. Statist. Comput.*, 13:631–644.

Zaki, T. A. and Durbin, P. A. (2005). Mode interaction and the bypass route to transition. *J. Fluid Mech.*, 531:85–111.

Zhang, J. (2000). Preconditioned Krylov subspace methods for solving nonsymmetric matrices from CFD applications. *Comput. Methods Appl. Mech. Engrg.*, 189:825–840.

Zhong, X. and Tatineni, M. (2003). High-order non-uniform grid schemes for numerical simulation of hypersonic boundary-layer stability and transition. *J. Comput. Phys.*, 190:419–458.

Part II

Articles

Summary of Articles

Article 1: Direct numerical simulations of hypersonic flow about a swept parabolic body

C. J. Mack and P. J. Schmid

A three-dimensional model for compressible flow in the leading-edge region of a swept blunt body is presented. Direct numerical simulations (DNS) are then performed to compute the flow fields by resolving all spatial scales. The implemented DNS-code solves the compressible Navier–Stokes equations and features a body-fitted moving grid, a shock-fitting technique as well as high-order compact schemes. Results from flow simulations and stability analyses are presented.

Article 2: A preconditioned Krylov technique for global hydrodynamic stability analysis of large-scale compressible flows

C. J. Mack and P. J. Schmid

A robust and effective DNS-based global stability solver is developed to investigate the linear temporal stability of large-scale compressible flows. This solver combines iterative Krylov-subspace methods and direct numerical simulations (DNS) — using a matrix-free implementation — and additionally features a spectral transformation of the complex eigenvalue plane as well as preconditioning techniques. Such a transformation adds the required flexibility to our global stability algorithm and thus allows access to specific parts of the full global spectrum. The performance of the algorithm is demonstrated on two flow cases, a compressible mixing layer and compressible flow about a swept parabolic body.

Article 3: Global stability of swept flow around a parabolic body: connecting attachment-line and crossflow modes

C. J. Mack, P. J. Schmid and J. L. Sesterhenn

The global linear stability of compressible flow about a swept parabolic body of infinite span — the flow model presented in "Article 1" — is investigated using the DNS-based iterative eigenvalue method developed in "Article 2". The computed global spectrum shows an unstable eigenvalue branch consisting of boundary-layer modes whose amplitude distributions exhibit typical characteristics of both attachment-line and crossflow instabilities. The presented results furthermore establish a link between these two instability mechanisms which, so far, have only been studied separately and locally.

Article 4: Global stability of swept flow around a parabolic body: features of the global spectrum

C. J. Mack and P. J. Schmid

The computed global spectrum provides a comprehensive picture of the temporal perturbation dynamics of the flow and, as a result, a wide and rich variety of modes has been uncovered: stable and unstable boundary-layer modes, different types of stable and unstable acoustic modes and stable wave packet modes have been found. A parameter study varying the spanwise perturbation wavenumber and the sweep Reynolds number reproduced a preferred spanwise length-scale and a critical Reynolds number for a boundary-layer or acoustic instability. Convex leading-edge curvature has been found to have a strongly stabilizing effect on boundary-layer modes but only a weakly stabilizing effect on acoustic modes. Furthermore, for certain parameter choices, the acoustic modes have been found to dominate the boundary-layer modes.

Article 5: Global stability of swept flow around a parabolic body: the neutral curve

C. J. Mack and P. J. Schmid

The onset of transition in the leading-edge region of a swept blunt body such as a swept aircraft wing crucially depends on the stability characteristics of the flow. For this reason, the parameter study in “Article 4” has been extended. The resulting neutral curve displays two overlapping regions of exponential growth and two critical Reynolds numbers, one for boundary-layer instabilities and one for acoustic instabilities. Furthermore, global modes combining features from both boundary-layer and acoustic instabilities are presented and discussed. In conclusion, the employed global stability approach is expected to shed more light on the rich perturbation dynamics of swept leading-edge flow, particularly, in the subcritical regime.

Article 1

Direct numerical simulations of hypersonic flow about a swept parabolic body

By C. J. Mack[1,2] and P. J. Schmid[1]

[1]Laboratoire d'Hydrodynamique (LadHyX), CNRS-École Polytechnique,
F-91128 Palaiseau, France

[2]Department of Numerical Mathematics, Universität der Bundeswehr (UniBw),
D-85577 Munich, Germany

Published in *Comput. Fluids* (2009), submitted

Direct numerical simulations (DNS) of hypersonic flow about a swept parabolic body have been performed to compute flow in the leading-edge region of a swept blunt body. The implemented direct numerical simulation code solves the compressible Navier–Stokes equations and features a body-fitted moving grid, a shock-fitting technique as well as high-order compact schemes to spatially resolve all dynamic scales. Flow simulations have been conducted, and it has been shown that results from direct numerical simulations can provide the required input for various types of flow analyses such as studies of flow stability and receptivity. The accuracy of these types of analysis, however, critically depends on the quality of the simulations, and special care has to be taken to capture the relevant physical features. In our case, three-dimensional direct numerical simulations have been performed to compute the unsteady flow about a swept parabolic body, and the obtained results provided the motivation and guidance for a DNS-based linear stability analysis. This investigation is only one of many examples where (direct) numerical simulations combined with quantitative flow analysis techniques provide a more comprehensive insight into the governing physical processes of a complex flow.

1 Introduction

Over the past decades direct numerical simulations (DNS) have established themselves as a widely used tool in computational fluid dynamics to address and study complex flow problems. They aim at capturing all relevant physical features of the flow by spatially resolving all dynamic scales and thus limiting modeling efforts to a minimum. Owing to progress both in terms of hardware, notably with the availability of supercomputers, and software, such as fast and efficient algorithms, the solution of large-scale flow problems has become feasible. Consequently, the applications of state-of-the-art direct numerical simulations are truly impressive in scope and complexity, ranging from flows in complex three-dimensional geometries to flows which are governed by multiple spatio-temporal scales, from reactive to acoustically-dominated flows, from particle-laden flows to flows with complex material properties. The numerical techniques to treat such a variety of flow problems are equally impressive. Moving grids and adaptive mesh refinement, higher-order compact schemes, shock-capturing and shock-fitting techniques and efficient time-advancement methods are nowadays commonplace in computational fluid dynamics. Fast elliptic and iterative solvers, and their parallel implementations, even taking into account specific hardware architectures, are part of a sophisticated, comprehensive, but readily accessible toolbox to consider the even most challenging flow applications. It should not come as a surprise then that high-quality data produced by direct numerical simulations is available for a large number of flow cases of academic and industrial interest. However, it has to be acknowledged that data of such amount and detail contains far more useful information than can be obtained by inspection alone. In this sense, a successful direct numerical simulation of a complex flow problem should less be a result by itself but rather provide the starting point for a quantitative analysis.

The goal of any scientific study of a fluid-dynamical process is not in the reproduction of its physical features by direct numerical simulations but in the extraction of the governing underlying mechanisms from the data the DNS produces. In other words, we are interested in the intrinsic flow behavior captured by the dynamics of coherent structures. Traditionally, flow behavior has been described by its response to initial conditions and external excitation, leading to stability and receptivity analysis, respectively. In recent years, the manipulation of fluid flow by passive or active means has joined these more traditional approaches and introduced concepts of sensitivity, optimization, control and model reduction to yield a more encompassing definition of flow behavior. In this article, we will concentrate on the stability behavior of hypersonic flow about a swept parabolic body and demonstrate the concept of DNS-based stability analysis. In its simplest form DNS-based stability analysis consists of the long-term evolution of a small-amplitude initial perturbation which in general converges toward the least-stable eigenfunction. Mathematically, this procedure corresponds to a power iteration based on the linear (Jacobian) stability matrix. If more information about the modal structure of the flow is required or desirable, an iterative Krylov technique such as the Arnoldi method (Edwards et al., 1994; Mack and Schmid, 2010) has to be applied. In this technique, repeated application of the linear stability matrix to selected flow fields produces a low-dimensional representation of the full stability matrix whose eigenvalues can then be evaluated by direct means. Again, this is an example of combining DNS with a quantitative flow analysis technique. In our case, the direct numerical simulation provides the product of the Jacobian matrix and specific flow fields via a matrix-free implementation (Mack and Schmid, 2010). Our specific flow configuration is governed by a rich perturbation dynamics consisting of multiple instabilities at a variety of temporal and spatial scales (Mack, 1984; Bippes, 1999) and thus requires both a flexible and robust (global) stability solver and high-quality flow fields from simulations that capture all relevant physical features.

Hydrodynamic stability theory plays a central role especially in transition research of open and wall-bounded shear flows. Our understanding of hydrodynamic instabilities and transition

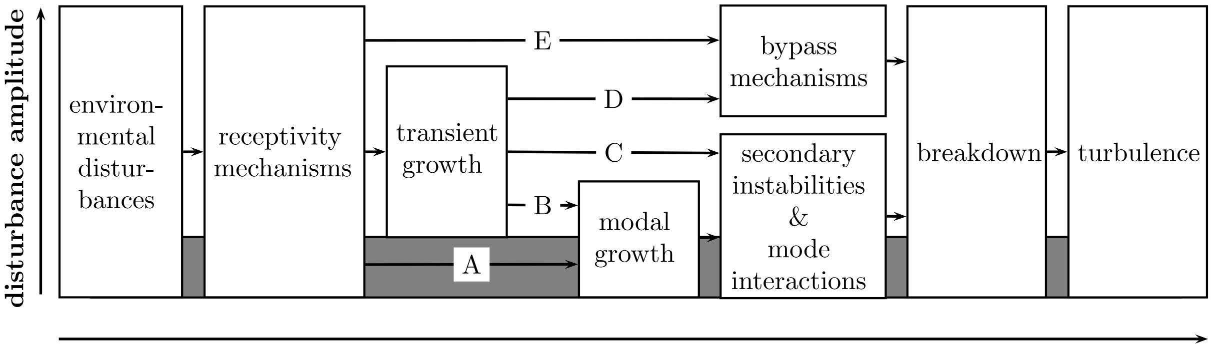

Figure 1. Roadmap to transition as suggested by Morkovin et al. (1994) (see Reshotko, 1994).

scenarios is mainly based on a remarkable body of literature for local flow models and simplifying assumptions, such as swept Hiemenz flow for flow near the attachment line of a swept blunt body or three-dimensional boundary-layers for flow over swept wings. Nevertheless, for even moderately complex flow configurations these (local) models are often not sufficient to fully describe or capture the global flow behavior. The rationale for using local models — the constraints imposed by a lack of computer resources and algorithms to treat high-dimensional and multi-physics flows — is no longer a valid argument, as high-performance computers and fast algorithms are readily available. It is thus timely to extend our knowledge of transition scenarios for simple generic geometries (e.g., boundary layers, channel flows, open shear flows) to configurations that include a substantially larger range of physical phenomena and that represent a closer approximation to realistic flow situations. As guidance for such an investigation we rely on the roadmap suggested by Morkovin et al. (1994) (see figure 1) which has been deduced from an abundance of experiments and numerical simulations (see Reshotko, 1994, and references therein). It consists of a conceptual link between environmental disturbances and the onset of breakdown to turbulent fluid motion via five distinct paths. Even though, for hypersonic flow about a swept blunt body multiple instability scenarios or a combination thereof are conceivable, we will concentrate on the low disturbance environment case given by path A (see figure 1 in grey). This path is characterized by (i) receptivity of the laminar flow to external perturbations, (ii) linear modal growth of boundary-layer-type instabilities, followed by (iii) nonlinear breakdown into turbulence.

In our analysis, we can rely on a vast body of literature on the receptivity (see, e.g., Zhong and Tatineni, 2003; Haddad et al., 2005, for an overview) as well as on the stability of swept attachment-line and boundary-layer flows (see, e.g., Joslin, 1996; Saric et al., 2003; Le Duc et al., 2006, in references therein). In particular, stability investigations using results from direct numerical simulations consist of the work by Spalart (1988) who was the first to perform direct numerical simulations (DNS) of the incompressible attachment-line boundary-layer flow (swept Hiemenz flow model) in order to confirm the findings of theoretical studies for the temporal framework, i.e., the existence of attachment-line instabilities. This was followed by a study of crossflow instabilities (Spalart, 1990) using a rather large computational domain in the chordwise direction to accommodate the developing crossflow vortices. The spatial framework was addressed by Joslin (1995) who obtained, similar to Spalart (1988), the results found by linear stability theory based on a similarity solution. In a subsequent DNS study, Joslin (1996) confirmed the existence of higher-order polynomial modes. The linear as well as nonlinear regime for perturbations in incompressible attachment-line boundary layers has been treated by Theofilis (1998). Theofilis et al. (2003) used direct numerical simulations to confirm theoretical results for higher-order modes, i.e., an extention of the common Görtler–Hämmerlin model (Hall et al., 1984). Compressibility effects on the attachment-line boundary-layer flow have been addressed recently by Le Duc et al. (2006) for the temporal setting. The majority of the direct numerical simulations mentioned above was motivated by a desire to verify local modal stability results, and for this reason local models have also been adopted for the numerical simulations. Attempts to incorporate compressibility, wall temperature effects as well as curvature into stability calculations of swept blunt bodies were undertaken by, e.g., Kazakov (1990) and Lin and Malik (1995, 1997), but despite significant efforts a uniform generic model is still missing. In summary, it can be stated that investigations of the stability behavior of flow about swept blunt bodies have mainly used two local models: the flow near the attachment line and the crossflow-dominated three-dimensional boundary-layer flow further downstream from the attachment line (see Saric et al., 2003; Bonfigli and Kloker, 2007, and references therein).

The availability of the necessary tools for a global approach to flow around swept blunt bodies as well as the shortcomings of the two local models in providing global information about the flow behavior (Mack et al., 2008) motivates and suggests a DNS-based global stability analysis

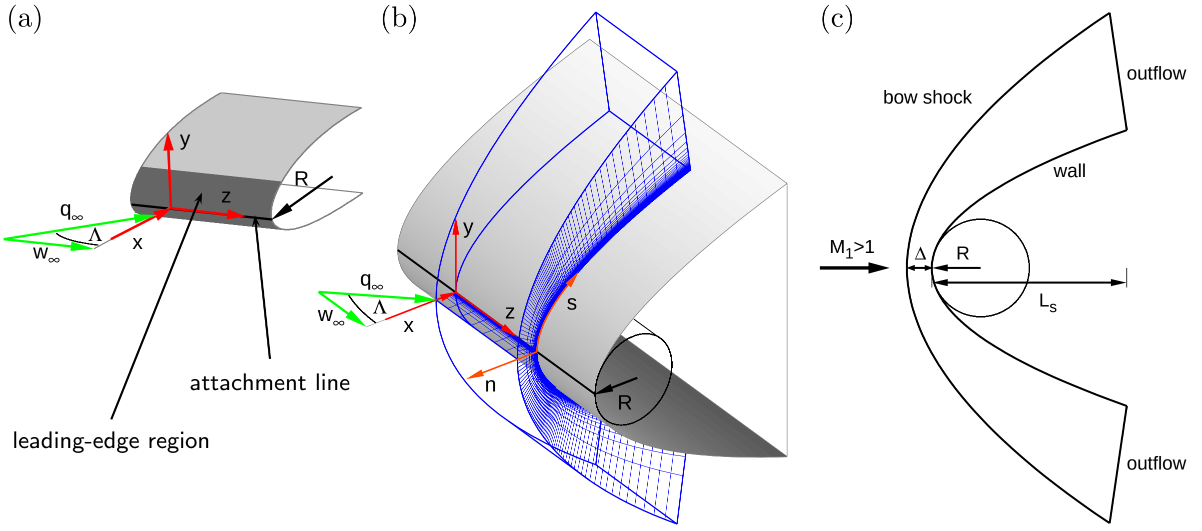

Figure 2. (a) Sketch of a swept blunt body showing the attachment line (in black), the leading-edge region (in dark grey), the oncoming velocity q_∞ and the freestream angle Λ (yielding a sweep velocity w_∞) as well as the local Cartesian coordinate system. (b) Sketch of the three-dimensional flow model showing the parabolic body (in grey), the employed coordinate systems and the body-fitted computational grid with its grid-point distribution (in blue). (c) Schematic of the physical domain, its boundary conditions and the relevant geometric parameters.

as already outlined above. For a successful analysis of this type three requirements have to be satisfied: (i) the flow fields from direct numerical simulations have to be of sufficiently high quality to capture all relevant physical scales and phenomena, (ii) the algorithms processing these flow fields to extract stability information have to be flexible, efficient and robust (Mack and Schmid, 2010), and (iii) a flow model (geometric configuration, governing equations, material properties, etc.) has to be chosen that approximates, as closely as possible, the realistic flow situation in size and complexity. Our flow model for hypersonic flow about a swept blunt body, together with the governing parameters and equations, is presented in section §2. This is followed by a description of the implementation of our direct numerical simulation (section §3), and we show results of flow simulations as well as stability computations in section §4.

2 Flow model - hypersonic flow about a swept parabolic body

For the present investigations we consider hypersonic flow about a swept parabolic body of infinite span (see figure 2b) to model flow in the leading-edge region of a swept blunt body (see figure 2a). Such flows form a local stagnation flow near the attachment line, and the presence of sweep considerably alters the flow as it leads to a three-dimensional highly-curved boundary-layer flow further downstream. In this model, the oncoming flow impinges onto the body with a velocity q_∞ and a sweep angle Λ yielding a sweep velocity w_∞. The local Cartesian coordinate system (in red) is given by the x-, y- and spanwise z-direction pointing along the attachment line. The local parabolic coordinate system (in orange) consists of the chordwise s-direction and the normal n-direction pointing along grid lines in the downstream direction and along grid lines normal to the wall, respectively (see figure 2b).

The surface of the parabolic body is given by

$$x(y) = \frac{1}{2R}y^2 \qquad \text{with} \qquad -\sqrt{2RL_s} \leq y \leq \sqrt{2RL_s}, \tag{2.1}$$

where R denotes the leading-edge radius of the body and L_s sets the size of the domain in the chordwise s-direction (see figure 2c). The domain is defined by a rigid wall and open outflow boundaries. We further consider flow cases where the oncoming flow is supersonic

$$M_1 = M_\infty \cos \Lambda > 1, \tag{2.2}$$

where M_∞ and M_1 denote the freestream Mach number and its component normal to the shock; thus, the computational domain is limited by a detached unsteady bow shock in the wall-normal n-direction (see figure 2c), and this shock is assumed to be an infinitely thin moving discontinuity. The hypersonic flow state upstream of the detached bow shock, denoted by the subscript $_\infty$, is obtained as a function of the freestream Mach number M_∞ and the freestream angle Λ using the total temperature $T_0 = 728$ [K] and the total pressure $p_0 = 1.55 \cdot 10^6$ [Pa] as a reference state. The Rankine–Hugoniot relations are then employed to calculate the flow quantities downstream of the bow shock, denoted by the subscript $_2$, which will be used in the following section to define the governing parameters.

This three-dimensional flow model comprises a multitude of geometric and physical features and, thus, allows us to study the influence of leading-edge curvature, sweep angle and angle of attack as well as compressibility, wall temperature and bow shock-interaction effects on the flow. Furthermore, swept leading-edge flow is known to be susceptible to several instability mechanisms (see, e.g., Bippes, 1999, for an overview) which will lead to transitional features as well as turbulence. Consequently, the physical domain has to extend sufficiently far in the chordwise direction (downstream of the attachment line) and the computational grid has to be locally refined to cover these features. Finally, we do not take advantage of the symmetry properties of the flow even though we consider a zero angle of attack in the present investigations.

2.1. *Governing parameters*

The flow model depicted in figure 2(b) is governed by a number of non-dimensional parameters. We define a sweep Reynolds number Re_s, a leading-edge parameter R_δ, a sweep Mach number Ma_s, and a wall temperature ratio θ_w as

$$Re_s = \frac{w_2 \delta}{\nu_r}, \qquad R_\delta = \frac{R}{\delta}, \qquad Ma_s = \frac{w_2}{c_2}, \qquad \theta_w = \frac{T_w}{T_r}, \tag{2.3}$$

where w_2 and c_2 are the sweep velocity and the speed of sound downstream of the bow shock (at $y = 0$), respectively, δ represents a viscous length scale, and ν_r denotes the kinematic viscosity evaluated at recovery temperature T_r and stagnation pressure p_s. In the present work we consider an adiabatic wall, and thus the ratio of the temperature T_w at the wall and T_r is $\theta_w = 1$. The viscous length scale in (2.3) is obtained using the strain rate S at the wall, at the attachment line, which follows from the chordwise derivative of the potential solution of flow around a circular cylinder with radius R evaluated at the stagnation point.

$$\delta = \left(\frac{\nu_r}{S}\right)^{1/2} \qquad \text{with} \qquad S = \left(\frac{\partial v}{\partial y}\right)_w = \frac{2u_2}{R} \tag{2.4}$$

Herein, u_2 denotes the wall-normal velocity downstream of the shock.

In order to compute the kinematic viscosity ν_r at T_r and p_s we resort to Reshotko and Beckwith (1958) who theoretically investigated supersonic flow about a yawed infinite cylinder. They give the following relation

$$T_r = T_\infty + RF \cdot (T_0 - T_\infty), \tag{2.5}$$

where $RF = 1 - (1 - \xi_w)\sin^2 \Lambda$ denotes the stagnation-line recovery factor, and T_0 and T_∞ stand for the total and freestream temperature, respectively; they further provide a table with values of ξ_w for selected freestream conditions (M_∞ and Λ) and a Prandtl number of $Pr = 0.7$. In our simulations, these values have been linearly interpolated to compute T_r for selected freestream conditions. The total pressure p_s at the stagnation point is determined from

$$\frac{p_s}{p_\infty} = \left(\frac{\gamma+1}{2}M_1^2\right)^{\gamma/(\gamma-1)} \left(\frac{\gamma+1}{2\gamma M_1^2-(\gamma-1)}\right)^{1/(\gamma-1)}, \tag{2.6}$$

where $M_1 = M_\infty \cos\Lambda$, p_∞ is the freestream pressure and γ denotes the specific heat ratio. This relation (2.6) follows from the Rankine–Hugoniot relation for pressure across a normal shock and from the subsequent isentropic deceleration of the flow of an inviscid perfect gas into the stagnation point.

2.2. *Governing equations*

2.2.1 *Cartesian formulation*

The dynamics of hypersonic viscous flow about a swept parabolic body as shown in figure 2(b) is governed by the unsteady three-dimensional compressible Navier-Stokes equations which have been formulated for the pressure p, the velocities (u, v, w) and the entropy s. Using Cartesian tensor notation, these equations read as follows:

$$\frac{\partial p}{\partial t} + u_j\frac{\partial p}{\partial x_j} + \gamma p\frac{\partial u_j}{\partial x_j} = (\gamma-1)\left(\Phi + \frac{\partial}{\partial x_j}\left(k\frac{\partial T}{\partial x_j}\right)\right), \tag{2.7a}$$

$$\frac{\partial u_i}{\partial t} + u_j\frac{\partial u_i}{\partial x_j} + \frac{1}{\varrho}\frac{\partial p}{\partial x_i} = \frac{1}{\varrho}\frac{\partial}{\partial x_j}\left(\mu\left(\frac{\partial u_i}{\partial x_j}+\frac{\partial u_j}{\partial x_i}\right) - \frac{2}{3}\mu\frac{\partial u_k}{\partial x_k}\delta_{ij}\right), \tag{2.7b}$$

$$\frac{\partial s}{\partial t} + u_j\frac{\partial s}{\partial x_j} = \frac{R_c}{p}\left(\Phi + \frac{\partial}{\partial x_j}\left(k\frac{\partial T}{\partial x_j}\right)\right) \tag{2.7c}$$

with

$$\Phi \equiv \frac{1}{2}\mu\left(\frac{\partial u_i}{\partial x_j}+\frac{\partial u_j}{\partial x_i}\right)^2 - \frac{2}{3}\mu\left(\frac{\partial u_k}{\partial x_k}\right)^2.$$

Herein, the variables ϱ, T, μ and k denote, respectively, the density, the temperature, the dynamic viscosity and the thermal conductivity, and $R_c = 287$ [$\mathrm{Jkg^{-1}K^{-1}}$] represents the gas constant for dry air and δ_{ij} the Kronecker delta.

We further consider the motion of a compressible fluid modeled as a calorically perfect gas, and employing Gibbs fundamental relation as well as the equation of state for a perfect gas $p = \varrho R_c T$ the temperature T and the density ϱ are obtained via the following equations of state

$$T = \frac{1}{R_c}p^{\gamma-1/\gamma}\exp\left(\frac{s}{C_p}\right), \tag{2.8}$$

$$\varrho = p^{1/\gamma}\exp\left(-\frac{s}{C_p}\right) \tag{2.9}$$

with C_p as the specific heat ratio at constant pressure.

The system of equations is closed by applying Sutherland's and Fourier's law to model the dynamic viscosity μ and the thermal conductivity k, respectively,

$$\mu = \mu_0\left(\frac{T}{T_0}\right)^{\frac{3}{2}}\frac{T_0+S}{T+S}, \tag{2.10}$$

$$k = \frac{C_p}{Pr}\mu, \tag{2.11}$$

where $S = 110.4$ [K] denotes the Sutherland temperature, T_0 is the reference temperature (chosen as the total temperature), and μ_0 represents the reference viscosity for the latter temperature; a constant specific heat ratio $\gamma = 1.4$ and a constant Prandtl number of $Pr = 0.71$ are assumed.

2.2.2 *Curvi-linear formulation*

In order to solve the compressible Navier–Stokes equations (2.7a–c) on a time-dependent, curvi-linear and non-uniformly distributed grid, new (spatial) coordinates are defined

$$\xi^l = \xi^l(x_j, t) \quad \text{with} \quad j, l = 1, 2, 3 \tag{2.12}$$

to rewrite these equations; the first derivative then reads

$$\frac{\partial}{\partial x_j} = \frac{\partial \xi^l}{\partial x_j}\frac{\partial}{\partial \xi^l} = \xi^l_{,j}\frac{\partial}{\partial \xi^l}, \tag{2.13}$$

where the subscript $_{,j}$ denotes partial derivatives with respect to the physical coordinates (x, y, z, t) in the curvi-linear domain. Using these expressions and introducing contravariant velocity components $u^l = \xi^l_{,t} + \xi^l_{,j}u_j$, where $\xi^l_{,t}$ stems from the time dependency of the grid, the governing equations (2.7a–c) have been reformulated for curvi-linear grids in index notation. These equations read as follows in the computational domain (ξ, η, ζ, t):

$$\frac{\partial p}{\partial t} + u^l\frac{\partial p}{\partial \xi^l} + \gamma p \xi^l_{,j}\frac{\partial u_j}{\partial \xi^l} = (\gamma - 1)\left(\Phi + \xi^k_{,j}\frac{\partial}{\partial \xi^k}\left(k\xi^l_{,j}\frac{\partial T}{\partial \xi^l}\right)\right), \tag{2.14a}$$

$$\frac{\partial u_i}{\partial t} + u^l\frac{\partial u_i}{\partial \xi^l} + \frac{1}{\varrho}\xi^l_{,i}\frac{\partial p}{\partial \xi^l} = \frac{1}{\varrho}\xi^l_{,j}\frac{\partial}{\partial \xi^l}\left(\mu\left(\xi^l_{,j}\frac{\partial u_i}{\partial \xi^l} + \xi^l_{,i}\frac{\partial u_j}{\partial \xi^l}\right) - \frac{2}{3}\mu\xi^l_{,k}\frac{\partial u_k}{\partial \xi^l}\delta_{ij}\right), \tag{2.14b}$$

$$\frac{\partial s}{\partial t} + u^l\frac{\partial s}{\partial \xi^l} = \frac{R_c}{p}\left(\Phi + \xi^k_{,j}\frac{\partial}{\partial \xi^k}\left(k\xi^l_{,j}\frac{\partial T}{\partial \xi^l}\right)\right), \tag{2.14c}$$

where Φ is obtained in a straight-forward manner. This system of nonlinear equations can formally be written as

$$\frac{\partial \phi}{\partial t} = \mathcal{F}(\phi) \tag{2.15}$$

with $\phi = (p, u, v, w, s)^T$, and $\mathcal{F}$ represents the right-hand side of the nonlinear compressible Navier–Stokes equations.

3 Direct numerical simulations

As already mentioned in the introduction, over the past decades direct numerical simulations (DNS) based on higher-order discretization schemes have established themselves as a widely used tool to investigate complex flow problems. For these simulations, the solution of the governing equations is directly obtained by solving a system of nonlinear partial differential equations in space and time. In what follows, we describe details of the implementation of the present direct numerical simulation to solve (2.15) for hypersonic flow about a swept parabolic body of infinite span as displayed in figure 2(b).

3.1. *Grid generation*

The flow is computed using a three-dimensional, non-uniformly distributed, body-fitted grid (see figure 2b) which is generated via a three-step process as displayed in figure 3. This process consists of (a) the computation of a uniformly-distributed unit cube which is non-periodic in the (wall-normal) ξ- as well as the (chordwise) η-direction and periodic, due to the assumption of

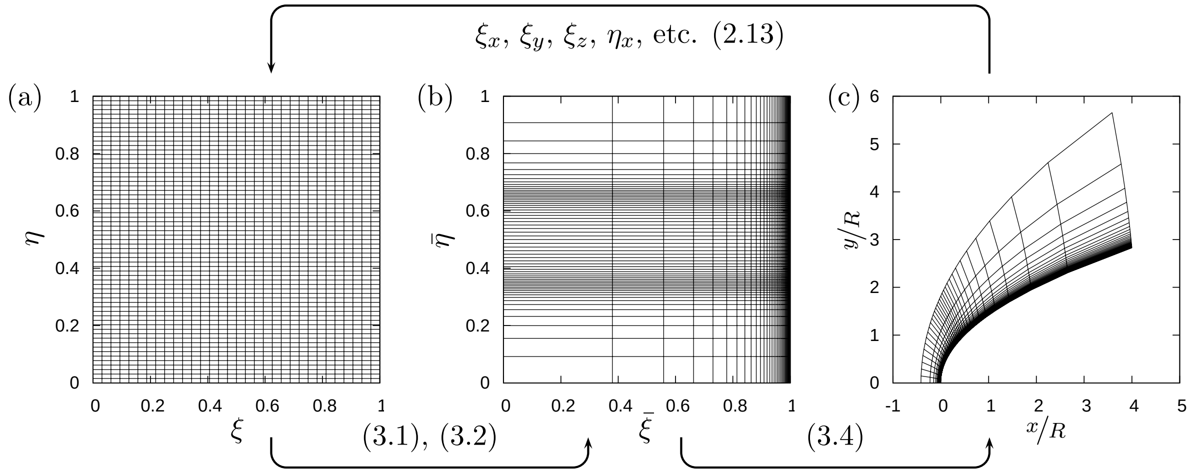

Figure 3. Various steps of the grid generation process: (a) uniformly-distributed unit cube in the computational domain (ξ, η, ζ, t), (b) stretched unit cube $(\bar{\xi}, \bar{\eta}, \bar{\zeta}, t)$ and (c) upper half of the body-fitted grid in the physical domain (x, y, z, t), where the size of the domain in the chordwise direction has been chosen as $L_s = 0.4$ [m]; every fourth and eight grid point are shown in the ξ- and η-direction, respectively, and a leading-edge radius of $R = 0.1$ [m] has been used.

infinite span, in the (spanwise) ζ-direction, (b) an appropriate grid stretching in the ξ- and η-direction in order to sufficiently resolve physically relevant regions and (c) the parabolic mapping of the stretched unit cube. Consequently, the combined transformation maps the computational domain (ξ, η, ζ, t) into the physical domain (x, y, z, t) between a detached bow shock and the parabolic body (see figure 2c for a schematic of the physical domain). Finally, the metric coefficients ξ_x, ξ_y, ξ_z, η_x, etc. in (2.14a–c) are obtained by differentiating the body-fitted grid (x, y, z) with respect to (ξ, η, ζ) and inverting the resulting Jacobian matrix. This is accomplished numerically using the same higher-order central schemes as for the spatial derivatives of the dependent variables (see section §3.3).

3.1.1 *Grid stretching*

A grid stretching is applied in the wall-normal ξ- as well as in the chordwise η-direction to cluster the grid points in the physically relevant regions, i.e., the viscous three-dimensional boundary layer and the leading-edge region, respectively. The former grid stretching (Anderson et al., 1988) clusters the grid points towards the parabolic body in order to sufficiently resolve the boundary layer. It amounts to computing

$$\bar{\xi} = \frac{\kappa \xi}{1 - \kappa + \xi(2\kappa - 1)}, \tag{3.1}$$

where $\xi \in [0, 1]$ and $\bar{\xi} \in [0, 1]$ denote the uniformly-spaced and stretched grid points, respectively, and κ is the stretching parameter. As a result, this function maps the interval $[1/2, 1]$ to $[\kappa, 1]$ and thus clusters half of the grid points in the latter interval. In the present study, a value $\kappa = 0.95$ is used to cluster the $n_1 = 128$ grid points in the wall-normal direction and thus resolve the viscous boundary layer with at least 20 grid points.

To further cluster the grid points in the leading-edge region of the parabolic body, a semi-analytical technique based on several error functions is employed in the η-direction. Within this technique the redistribution of the grid points is described by a second-order ordinary differential equation

$$\frac{d^2\bar{\eta}}{d\eta^2} - \frac{f_{gsr}(\eta)}{\Delta\eta}\frac{d\bar{\eta}}{d\eta} = 0, \tag{3.2}$$

where $\Delta\eta$ denotes the grid spacing of the equi-spaced grid with $\eta \in [0,1]$, and $f_{gsr}(\eta) = (\Delta\bar{\eta}_{i+1} - \Delta\bar{\eta}_i)/\Delta\bar{\eta}_i$ represents the relative grid stretching ratio at the location $\bar{\eta}_{i+1}$ of the stretched grid. This grid stretching ratio function $f_{gsr}(\eta)$ is constructed using a linear combination of m error functions, each having its own control parameters $(a_j, \sigma_j, b_j, e_j)$.

$$f_{gsr}(\eta) = \frac{1}{2}\sum_{j=1}^{m} a_j \left(\operatorname{erf}\left(\sigma_j(\eta - b_j)\right) + (-1)^{e_j}\right) \tag{3.3}$$

In order to obtain the grid points $\bar{\eta}$ of the stretched grid equation (3.2) has to be integrated twice; the first integration can be performed analytically, whereas the second integration was done numerically using the Simpson's rule (see Schaupp et al., 2008, and references therein for further details). This grid stretching technique was chosen owing to its flexibility in locally refining the grid in the leading-edge region, and, in this work, four error functions are employed to redistribute $n_2 = 511$ grid points in the chordwise direction. Furthermore, pairs of error functions have been chosen to obtain a symmetric grid distribution with respect to the attachment line, and their control parameters are given in table 1.

Table 1. Control parameters of the four error functions for $n_2 = 511$.

$a_{1,2}$	$a_{3,4}$	$\sigma_{1,2}$	$\sigma_{3,4}$	$b_{1,2}$	$b_{3,4}$	$e_{1,3}$	$e_{2,4}$
0.085	-0.022	5	10	0.14	0.4	2	1

3.1.2 *Parabolic mapping*

In a final step, the stretched unit cube is mapped into the physical domain (x, y, z, t) between a detached bow shock and the parabolic body using a conformal mapping. This results in an analytic, orthogonal grid, where the grid lines at $\xi_{min} = \bar{\xi}_{min} = 0$ and $\xi_{max} = \bar{\xi}_{max} = 1$ define the detached bow shock and the surface of the parabolic body, respectively (see figure 3). Since the bow shock represents a moving discontinuity whose position and shape is not known in advance and furthermore changes in time, an initial guess for the corresponding grid line is required. To this end, we assume this (initial) grid line to be parabolic with a shock detachment distance Δ_0 (at $s = 0$). The parabolic mapping is then given by the following relations to obtain a three-dimensional, body-fitted grid about a parabolic body.

$$x(\bar{\xi}, \bar{\eta}, 0) = \frac{\Delta_0}{3} - \frac{\Delta_0}{3}\left(\bar{\xi} - 2\right)^2 + 4L_s\left(\bar{\eta} - \frac{1}{2}\right)^2, \tag{3.4a}$$

$$y(\bar{\xi}, \bar{\eta}, 0) = -2\sqrt{2RL_s}\left(\bar{\xi} - 2\right)\left(\bar{\eta} - \frac{1}{2}\right), \tag{3.4b}$$

$$z(\zeta) = \zeta L_z \tag{3.4c}$$

Herein, L_s and L_z define the size of the physical domain in the chordwise (see Eq. 2.1) and the spanwise direction, respectively, and Δ_0 is found by applying the following empirical correlation (Ambrosio and Wortman, 1962)

$$\frac{\Delta_0}{R} = 0.386\ \exp\left(\frac{4.67}{M_1^2}\right), \tag{3.5}$$

where M_1 denotes the shock-normal Mach number at $s = 0$ (see figure 2c). This expression results from a correlation of experimental data for supersonic and hypersonic flow around circular cylinders with radius R (see Billig, 1967). A comparison of values for Δ_0/R calculated using

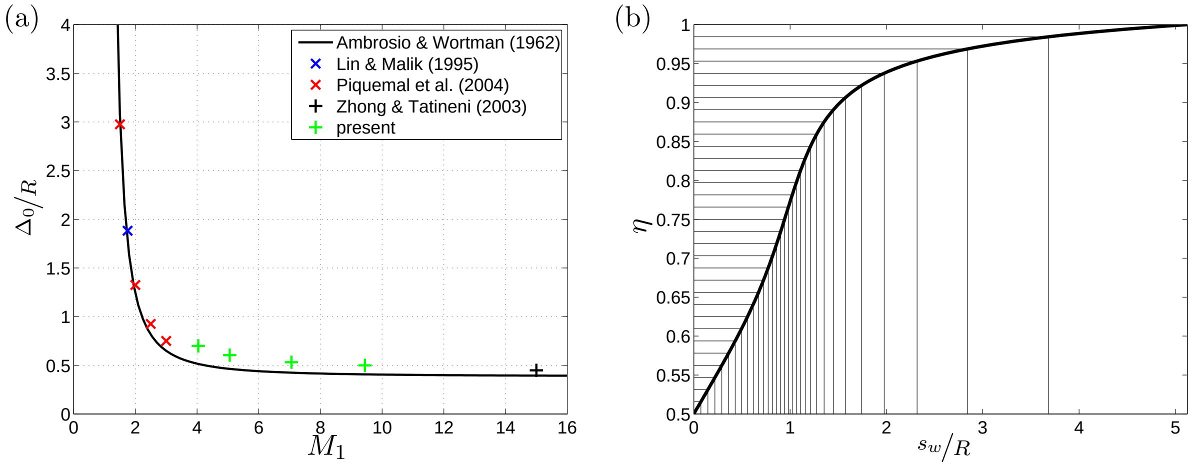

Figure 4. (a) Normalized shock detachment distance Δ_0/R as a function of M_1: empirical correlation (3.5) as proposed by Ambrosio and Wortman (1962); numerically obtained values for cylindrical (x) and parabolic bodies (+). (b) Effect of grid stretching and parabolic mapping on the grid distribution s_w of the physical grid along the surface of the upper half of the parabolic body ($L_s = 0.4$ [m], $R = 0.1$ [m]; every eight grid point is shown). The control parameters of the grid stretching are given in table 1, and η denotes the equi-spaced grid as displayed in figure 3(a).

(3.5) with numerically obtained values (evaluated for steady state solutions) for cylindrical and parabolic bodies is given in figure 4(a). It is found that, for both body shapes, (3.5) provides a good estimate as an initial guess for Δ_0; however, this estimate deteriorates for parabolic bodies for decreasing values of M_1.

It has to be mentioned that the parabolic mapping has an additional stretching effect on the grid-point distribution in the chordwise direction. Consequently, the control parameters in (3.3) are rather difficult to tune and the quality of the grid needs to be discussed for the final grid, e.g., by looking at the grid-point distribution along the surface arclength $s_w(x) = \sqrt{x}\sqrt{x+R/2} + R/2\ln((\sqrt{x} + \sqrt{x+R/2})/\sqrt{R/2})$ along the parabolic body. The grid-point distribution of the present computations is displayed in figure 4(b), where s_w is shown as a function of the equi-spaced grid η in the chordwise direction. The employed grid stretching leads to a clustering of the grid points in the leading-edge region (e.g., $0 \leq s_w/R \lesssim 1.4$), and these grid points are substantially stretched towards the outflow boundaries.

3.2. *Boundary and initial conditions*

In the wall-normal direction, the computational domain is limited by a detached unsteady bow shock assumed as an infinitely thin moving discontinuity as sketched in figure 2(c). Consequently, this bow shock serves as a distinct inflow boundary condition which is incorporated via a shock-fitting technique. In this technique the local shock-normal velocity is determined by a characteristic compatibility equation downstream of the shock, and the flow variables across the shock are governed by the Rankine–Hugoniot relations. This technique allows the use of a coarse mesh downstream of the shock; it further exhibits the advantage that the jump conditions can be satisfied exactly without introducing errors into the computational domain. For a description of the shock-fitting technique (Moretti, 1987) the reader is referred to, e.g., Fabre et al. (2001). Along the surface of the body no-slip boundary conditions in conjunction with an adiabatic wall are employed. At the chordwise edges of the computational domain characteristic non-reflecting boundary conditions are imposed, and periodic spatial differentiation schemes are applied in the homogeneous z-direction (see infinite span assumption). For details on handling the boundary conditions the reader is referred to Sesterhenn (2001) and the references therein.

As an initial condition in (2.15) we extend the values of the pressure, the velocities and the entropy downstream of the bow shock p_2, u_2, v_2, w_2 and s_2, respectively, in the wall-normal direction. To this end, the pressure is chosen as constant, and a potential mapping is employed to calculate the remaining flow quantities such that they satisfy the boundary conditions at the wall. This choice was found to give robust direct numerical simulations. It is worth mentioning that initial conditions which better approximate the solution can be found. However, these conditions require in general a rather large effort for the implementation and do not show a significant computational benefit for our flow model.

3.3. *Discretization in space and time*

The governing equations, i.e., the compressible Navier–Stokes equations (2.14a–c), are then solved on the body-fitted grid displayed in figure 3(c). For the spatial discretization we resort to higher-order compact finite-difference schemes (Lele, 1992; Adams and Shariff, 1996). Due to the spectral-like resolution of these schemes as well as their narrow finite-difference stencils — which is necessary to obtain stable boundary closures for high-order schemes — , compact schemes have become popular for direct numerical simulations (DNS), and today they are widely used in computational fluid dynamics (CFD) as well as computational aero-acoustics (CAA).

A commonly used family of such compact schemes can be written as

$$\beta_- f'_{i-2} + \alpha_- f'_{i-1} + f'_i + \alpha_+ f'_{i+1} + \beta_+ f'_{i+2} = \frac{1}{h} \sum_{\nu=-\nu_l}^{\nu_r} a_\nu f_{i+\nu}, \tag{3.6}$$

where $\beta_\pm$, $\alpha_\pm$ and a_ν denote the coefficients, h is the uniform grid spacing, and f_i and f'_i represent a discretized function and its first derivative at the grid point i, respectively. By choosing these coefficients, schemes of various order of spatial accuracy and spectral resolution can be designed. In order to compute the first derivative vector $\mathbf{f}'$ in (3.6), a sparse linear system has to be solved.

$$\mathbf{A}\mathbf{f}' = \mathbf{B}\mathbf{f} \tag{3.7}$$

Herein, $\mathbf{A}$ and $\mathbf{B}$ represent the banded coefficient matrices and $\mathbf{f}$ denotes the input vector. For tri-diagonal matrices $\mathbf{A}$, such linear systems can be efficiently inverted using the Thomas algorithm; for cyclic tri-diagonal or penta-diagonal $\mathbf{A}$ a modified version has to be used.

However, compact schemes with symmetric stencils are known be sensitive to boundary condition formulation and aliasing errors, and consequently they are susceptible to numerical instabilities. To cope with this problem explicit filters, artifical damping terms or inherently dissipative numerical schemes can be used (see, e.g., Kloker, 1998, for an overview). In the present studies, we resort to the latter technique and employ the compact upwind scheme CULD as designed by Adams and Shariff (1996). This fifth-order scheme features an upwind biased stencil which adds a certain amount of numerical dissipation to the spatial discretization and thus damps poorly resolved waves (see figure 5b). It also includes (stable) boundary closures, and its coefficients can be found in Adams and Shariff (1996). To take advantage of the CULD scheme, the governing equations have been recast in a characteristic-type formulation (Sesterhenn, 2001), where the Euler part, i.e., the left-hand side in (2.14a–c), is decomposed into plane acoustic, shear and entropy waves. As a consequence, the propagation of these waves can be computed depending on their propagation direction using an upwind scheme such as CULD.

Furthermore, the dissipative and diffusive terms, i.e., the right-hand side in (2.14a–c), are discretized using a sixth-order central compact scheme with $\alpha_\pm = 1/3$ and $\beta_\pm = 0$ (Lele, 1992); the purely dispersive character of this scheme for inner grid points is demonstrated in figure 5(b). Boundary closure in the non-periodic ξ- and η-direction is achieved using a third-order one-sided ($\alpha_+ = 3$, $\alpha_- = 0$, $\beta_\pm = 0$) and a fourth-order central scheme ($\alpha_\pm = 1/4$, $\beta_\pm = 0$) at the boundary grid points and the points next to them, respectively (Carpenter et al., 1993,

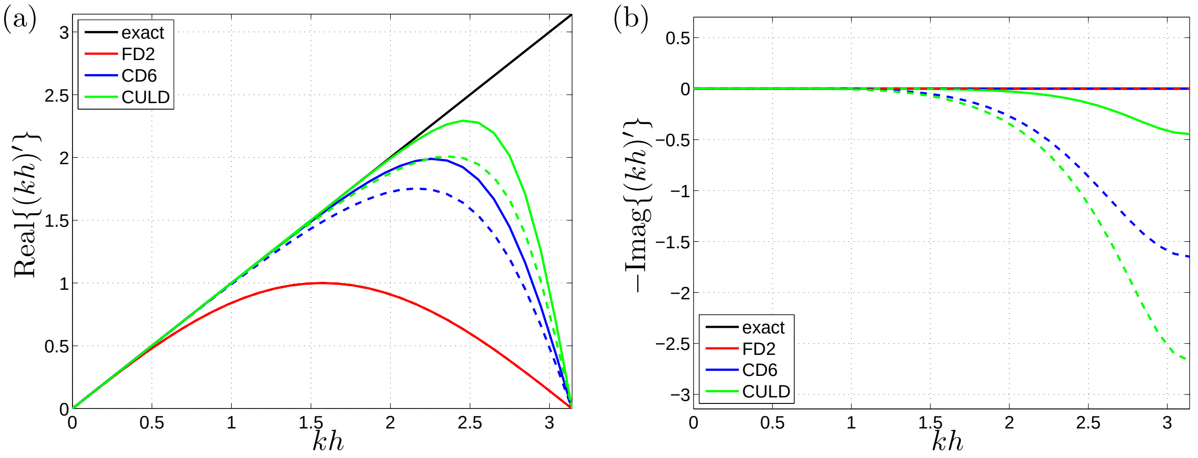

Figure 5. Dispersion (a) and dissipation (b) of the employed central and upwind compact scheme for a non-periodic domain; $CD6$ and $CULD$ denote the sixth-order compact and the compact upwind scheme, respectively, and $FD2$ stands for a (standard) second-order finite difference scheme. We show the modified wavenumber $(kh)'$ vs. the wavenumber kh for the first derivatives as obtained by a matrix analysis of an harmonic function, where the solid and the dashed lines display the transfer behavior of the schemes at an inner and the $(n_1 - 2)$-th grid point, respectively.

have shown that a stable boundary closure for a sixth-order central compact scheme can only be found for a third-order boundary scheme; this leads to a stable scheme which is globally of fourth order). For performance reasons as well as for the ease of implementation, this scheme is applied twice to compute the second derivatives. Boundary closure, however, modifies the dispersion and dissipation properties of compact schemes (see figure 5 dashed lines), and the central scheme becomes dissipative even for grid points other than the boundary points; this is a consequence of their global character. For considerations regarding boundary treatment and grid non-uniformity for higher-order finite-difference schemes see, e.g., Adams and Shariff (1996); Chung and Tucker (2003).

The semi-discretized system of equations

$$\frac{d\boldsymbol{\phi}}{dt} = \mathbf{F}(\boldsymbol{\phi}) \tag{3.8}$$

is integrated in time via an explicit fourth-order low-storage Runge–Kutta scheme (Kennedy et al., 2000); $\mathbf{F}$ represents the discretized right-hand side of the nonlinear Navier–Stokes equations. In all simulations we use a stability parameter of $\mathrm{C}_s = 0.9$, based on the definition proposed by Müller (1990), to control the time step $dt = \min(dt_\xi, dt_\eta, dt_\zeta)$. For instance, the time step dt_ξ in the ξ-direction is obtained via the expression

$$dt_\xi = \mathrm{C}_s \frac{2.5}{(kh)'_{max}} \left(\frac{\Delta\xi^2}{|u^1 + c\sqrt{g_\xi}|\Delta\xi + 4g_\xi \nu / Pr} \right)_{min}, \tag{3.9}$$

where the factor 2.5 stems from the stability region of the employed fourth-order Runge–Kutta method, and $(kh)'_{max}$ is the maximum value of the real part of the modified wavenumber of CULD (see figure 5a); $\Delta\xi$, u^1, c and ν denote the grid spacing of the equi-spaced grid, the contravariant velocity in ξ (see section 2), the speed of sound and the kinematic viscosity, respectively, and $g_\xi = \xi_x^2 + \xi_y^2 + \xi_z^2$. The time step dt_η and dt_ζ are found in a similar manner. The time-step criterion (3.9) incorporates convection and diffusion, and for convectively-dominated flows it represents the well-known CFL condition. Furthermore, it is found that the applied compact spatial schemes in conjunction with a Runge–Kutta method lead to a stable and robust direct numerical simulation (see Sesterhenn, 2001, for an analysis of the numerical stability).

4 Results

The above-described direct numerical simulation is employed to compute hypersonic flow about a swept parabolic body (see figure 2b) and to study its behavior. As already mentioned in the introduction, this flow configuration is characterized by a rich perturbation dynamics featuring a wealth of hydrodynamic instabilities. These instabilities are described by the dynamics of coherent structures at a variety of spatial and temporal scales, and we are interested in their spatial distribution as well as their temporal behavior. To resolve all spatial scales, a resolution of $128 \times 511 \times 8$ grid points in the normal n-, the chordwise s- and the spanwise z-direction, respectively, has been used in what follows.

4.1. *Flow simulations*

In a first attempt, direct numerical simulations are conducted to follow the spatio-temporal evolution of the flow. To this end, we choose the governing parameters as $Re_s = 800$, $R_\delta = 508$ and $Ma_s = 1.25$ ($Re_\infty = 2q_\infty R\rho_\infty/\mu_\infty = 3.53 \cdot 10^6$ with $R = 0.1$ [m], $M_\infty = 8.15$, $\Lambda = 30\,^\circ$), consider an adiabatic wall ($\theta_w = 1$) and further use a domain size $L_z = 2\pi/\beta = 28\delta$, where the parameter L_z defines the fundamental length of the wave-like disturbance traveling in the periodic z-direction; a value of $L_z = 28\delta$ corresponds to a non-dimensional wavenumber $\beta^\star = \beta\,\delta = 0.224$. For this parameter choice the flow configuration, in particular the existing three-dimensional boundary layer, is known to be highly unstable to crossflow instabilities (see Mack et al., 2008), characterized by co-rotating vortices, and we expect to identify this type of instability in form of coherent structures inside the boundary layer by inspection only.

As a result, the flow field at time $t = 1.10 \cdot 10^{-3}$ [s] is presented in figure 6. In figure 6(a), we visualize the spatial distribution of coherent structures by iso-surfaces of the Q-criterion; the identified structures are a consequence of the well-known crossflow instability (Bippes, 1999). They align with an angle of approximately $61\,^\circ$ (with respect to the attachment line) in the chordwise direction, become unstable to secondary instabilities and eventually break down as they evolve downstream (see figure 6a,c); this transition scenario is sketched in figure 1. Cross-cuts of the coherent structures at two selected positions in the chordwise s-direction (see figure 6c dashed lines) are shown in figure 6(d). Furthermore, as a consequence of the instability and breakdown, acoustic waves are generated and are radiated into the far-field (see figure 6a,b).

To briefly summarize, these results clearly demonstrate the fluid-dynamical complexity of the flow configuration under investigation and reveal at the same time its interesting and challenging flow physics. The displayed coherent structures undergo a multi-stage transition process, and several features of this process can already be observed. However, the involved structures can only be discussed from a phenomenological point of view, and a sound understanding of the transition process as well as its governing mechanisms requires a more comprehensive analysis of the flow. Among the common concepts of receptivity, stability and sensitivity we resort, in what follows, to a linear stability analysis to study the inherent perturbation dynamics of the flow within a temporal framework.

4.2. *Linear stability analysis*

A linear stability analysis amounts to computing and classifying the various types of instability mechanisms, their modal structure in space as well as their temporal behavior characterized by the disturbance growth and frequency. In a first step towards such an analysis a steady base flow has to be computed. The temporal stability of this base flow to three-dimensional perturbations can then be investigated by the long-term solution of an initial value problem or by solving a large-scale eigenvalue problem for the underlying stability matrix (global stability analysis). In this article, we will first resort to the former method for reasons of simplicity; a full global stability analysis calls for more sophisticated techniques, such as Krylov subspace methods, and will be attempted later.

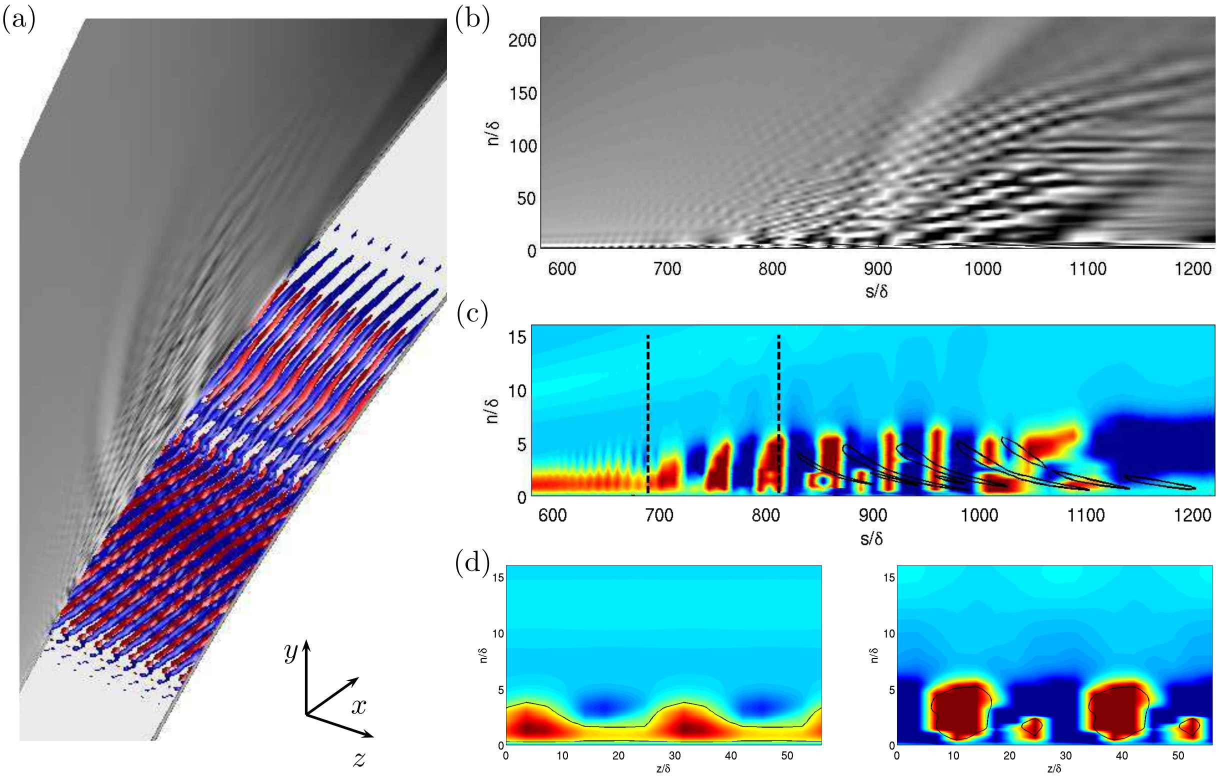

Figure 6. Results from flow simulations: (a) visualization of vortical structures by iso-surfaces of the Q-criterion (positive and negative values are displayed in red and blue, respectively, and eight wavelengths in z are used to visualize the structures); upper half of the parabolic body in light grey. Furthermore, the divergence of the velocity field (-600 in black, -1800 in white) in the s-n-plane is shown in the back as well as in (b). (c) Distribution of the vortical structures, stretched by a factor of ten in n, using a cross-cut in the s-n-plane; the black lines denote one representative iso-line of the Q-criterion. (d) Cross-cuts in the n-z-plane at selected positions in the chordwise s-direction; see dashed lines in (c).

4.2.1 *Steady state solution*

The governing equations are integrated in time until a steady base flow $\phi_0 = (p_0, u_0, v_0, w_0, s_0)^T$ is reached. The assumption of infinite span permits us to eliminate the z-dependence, but not the w-component, from $\phi_0(x, y, z)$ and to reduce the computations to a problem with only two independent variables x and y. From this solution the full three-dimensional base flow can be recovered. This procedure is possible since the two-dimensional problem is stable with respect to two-dimensional perturbations thus allowing a simple time-integration toward a steady state solution. As a consequence, more sophisticated techniques such as (Jacobian-free) Newton–Krylov techniques (Knoll and Keyes, 2004) or selective frequency damping (Åkervik et al., 2006) can be avoided. Nevertheless, even in our case these techniques may substantially reduce the computational time to reach a steady state solution.

The converged three-dimensional base flow for $Re_s = 800$, $R_\delta = 508$, $Ma_s = 1.25$ and $\theta_w = 1$ is visualized in figure 7. In figure 7(a) and (b) we display the temperature T and pressure field p, and for the present choice of flow parameters we obtain a recovery temperature $T_r = 703$ [K] and a (total) pressure $p_s = 9076$ [Pa] at the stagnation point. The values of these quantities decrease toward the outflow boundaries. The subsonic and supersonic region of the flow in a plane normal to the parabolic body are indicated in figure 7(a), where the distribution of the Mach number based on the u- and v-velocity is shown; the iso-contour line in red represents the sonic line. It can be seen that the flow is subsonic near the attachment line, and thus acoustic

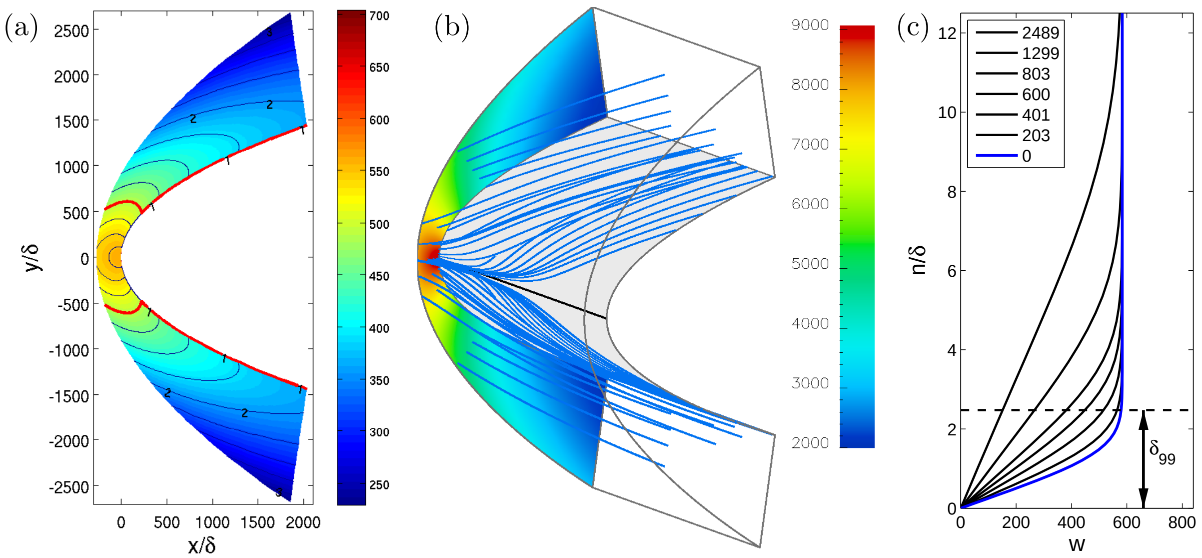

Figure 7. Computed steady base flow for $Re_s = 800$, $R_\delta = 508$, $Ma_s = 1.25$ and $\theta_w = 1$: (a) temperature field T [in K] and iso-contour lines of the Mach number in the s-n-plane (sonic line in red); (b) streamlines (in blue) and pressure field p [in Pa]. The resolution is 128×511 points in the normal n- and the chordwise s-direction, respectively. (c) Spanwise velocity w [in m/s] at selected positions [in δ] (see legend) in the positive s-direction; $\delta_{99} \approx 2.38\delta$ indicates the thickness of the boundary layer along the attachment line; $\delta \approx 1.97 \cdot 10^{-4}$ [m] for the present choice of parameters.

waves may lead to a strong interaction between the boundary layer and the detached bow shock. In figure 7(b), we further visualize the three-dimensional velocity field in terms of streamlines. The typical curvature of these streamlines in the inviscid outer flow region as well as near the attachment line and inside the boundary layer reveals a highly three-dimensional boundary layer flow, in particular, downstream of the attachment line. In addition, the streamlines describe a local and nearly two-dimensional flow field in the vicinity of the attachment line, and, as this flow field evolves in the chordwise direction, the thickness of the boundary layer δ_{99} grows about a factor of approximately 6 from 2.38δ (at $s_w = 0$) to 14.5δ (at $s_w = 2604\delta$). This boundary-layer growth is illustrated in figure 7(c), where we plot the spanwise w-velocity at selected positions in the s-direction (see legend). It has to be mentioned that, as a consequence of the infinite span assumption, no boundary-layer growth exists in the spanwise direction.

The computation of steady state solutions $\phi_0(x, y, z)$ via time-stepping techniques raises the question about the point in time at which the time advancement is stopped. A steady-state solution which is sufficiently resolved in space and sufficiently converged in time must be attempted prior to a stability analysis. Therefore, we consider a base flow as converged when the residual error $\|r\|$, i.e., norm of the difference between two subsequent flow fields normalized with the number of unknowns, does not change significantly. As a result, the evolution of this residual error $\|r\|$ as a function of the number of time steps as well as the sweep Reynolds number Re_s is displayed in figure 8(a), where a value $\mathrm{C}_s = 0.9$ has been used in (3.9) to ensure the stability of our time integration. In criterion (3.9), the time step dt is limited by a combination of convective $dt \sim 1/|u+c|$ and diffusive effects $dt \sim 1/\nu$; in the present simulations, dt is dominated by viscous effects. As the sweep Reynolds number $Re_s = w_2\delta/\nu_r = w_2/(\nu_r S)^{1/2}$ (see section §2.1) is decreased from 800 to 200, the kinematic viscosity $\nu_r \sim 1/Re_s^2$ increases. As a consequence, the time step decreases from $dt = 3.63 \cdot 10^{-8}$ [s] to $dt = 1.90 \cdot 10^{-8}$ [s], and, thus, more evaluations of the right-hand side are required to reach the steady state (see figure 8a). In all cases, the minimum value of $\|r\|$ is reached after time $t \approx 1.4 \cdot 10^{-2}$ [s]. It deserves mentioning that the employed fourth-order Runge–Kutta method was found to be more efficient in terms of

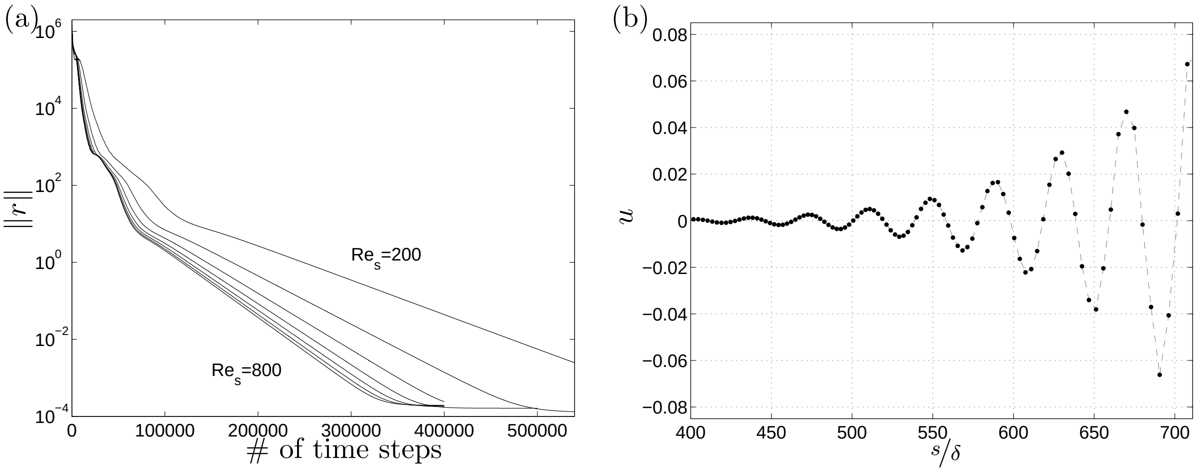

Figure 8. (a) Evolution of the residual error $\|r\|$ as a function of the number of time steps for selected sweep Reynolds numbers $Re_s = 200, 300, \ldots, 800$; the time advancement was accomplished by a fourth-order Runge–Kutta method, and $\mathrm{C}_s = 0.9$ has been used. (b) Spatial distribution of the velocity component $u(s, n, z)$ of the most unstable modal structure along a grid line in the s-direction at half the boundary-layer thickness.

computational time than a third-order low-storage Runge–Kutta method (Williamson, 1980).

Before proceeding with stability investigations of the converged base flow, the required resolution of the computational grid is discussed. As already mentioned above, the accuracy of flow simulations and flow analyses depends on the resolution in space which has to be sufficient to capture all relevant physical features. In our case, three types of flow computations, each with its specific requirement, can be distinguished: (i) computations of steady state solutions, (ii) stability studies and (iii) simulations of transition as well as turbulence. The steady base flow features a thin boundary layer in the wall-normal direction, and $n_1 = 128$ grid points have been found to ensure a grid-independent solution for the used grid stretching (see section §3.1.1). Furthermore, as the sweep Reynolds number Re_s is decreased from 800 to 200 the thickness of the boundary layer $\delta_{99} \approx 2.38\delta$ along the attachment line grows by a factor of 4 from $\delta = R/508$ to $\delta = R/127$ (see table 2 for the linear dependence of $\delta = R/R_\delta$ and Re_s). As a consequence, the number of grid points inside the boundary layer grows from 20 to 52. In addition, the base flow is smooth in the chordwise s-direction and $n_2 = 127$ grid points have been found to be sufficient to compute the flow field.

This is in contrast to subsequent stability analyses, where, e.g., small structures are known to exist inside the boundary layer as demonstrated in figure 6. The size of these structures, in particular in the chordwise direction, mainly depends on the spanwise wave length $L_z = 2\pi/\beta$, and the shorter the wave-like perturbations in z, the higher the required resolution in space. For instance, at least 9 grid points were used to properly resolve the most unstable structures for $Re_s = 800$ and $L_z = 28\delta$ in the region $-711 \leq s/\delta \leq 711$ (see figure 8b for a body-fitted cut in the chordwise s-direction at half the boundary-layer thickness, and see figure 4b for the grid-point distribution for $0 \leq s_w/R \lesssim 1.4$). Spatially over resolving the problem should be avoided since the subsequent flow analyses will become increasingly expensive.

Finally, transitional and turbulent simulations demand an even higher resolution such that the dynamics at all spatial scales down to the Kolmogorov length are captured. For these

Table 2. Linear dependence of the leading-edge parameter R_δ and the sweep Reynolds number Re_s.

R_δ	127	191	254	318	381	445	508
Re_s	200	300	400	500	600	700	800

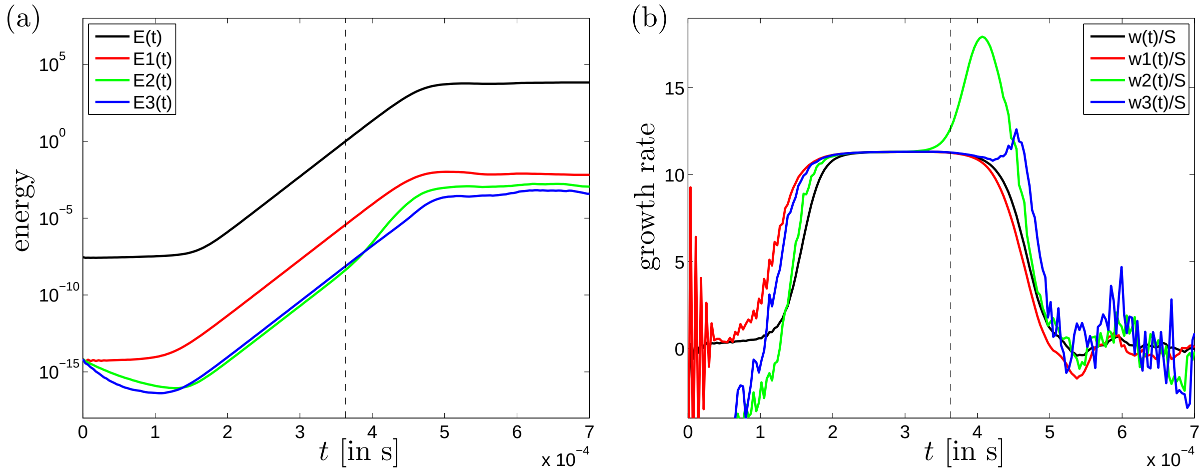

Figure 9. (a) Total $E(t)$ and modal energy $E_m(t)$ and (b) total $w(t)$ and modal growth rate $w_m(t)$ of the first three modal structures as a function of time t; $S = 2u_2/R$ denotes the inverse time scale, i.e., the strain rate at the wall as defined in (2.4). The dashed line represents the position in time at which the flow is visualized in figure 10.

type of simulations, a very high resolution would be mandatory for our Reynolds number of $Re_\infty = 2q_\infty R\rho_\infty/\mu_\infty = 3.53 \cdot 10^6$; however, such turbulent flow simulations are not the scope of the present article.

4.2.2 *Long-time integration of the initial value problem*

After discussing the computation of steady state solutions in the previous section we proceed with stability investigations of the base flow displayed in figure 7. To this end, the steady base flow $\phi_0(x, y, z)$ is perturbed with an arbitrary, three-dimensional perturbation field of small amplitude $\epsilon\phi(x, y, z, t)'$ (such that nonlinear effects can be neglected).

$$\frac{\partial\phi}{\partial t} = \mathcal{F}(\underbrace{\phi_0 + \epsilon\phi'}_{\phi}) \tag{4.1}$$

The solution of this initial value problem (4.1) converges toward the least stable global mode as time progresses before it saturates due to nonlinearities. As perturbation field we take $\epsilon\phi' = \epsilon(p_2, u_2, v_2, w_2, s_2)^T f$, where $\epsilon = 10^{-8}$, the vector $(p_2, u_2, v_2, w_2, s_2)^T$ represents the flow quantities downstream of the detached bow shock (see section §2), and f denotes a field of random numbers. The solution of (4.1) is obtained from direct numerical simulations (DNS).

As a result, the temporal evolution of the kinetic energy as well as the corresponding growth rate of the disturbed (steady) base flow is presented in figure 9. In figure 9(a), we show the evolution of the total $E(t)$ and the modal energy $E_m(t)$ for the fundamental and two higher-order modal structures as time progresses. The modal energy has been found using a Fourier transformation in the homogeneous z-direction. It can be seen that both the total and the modal energy grow exponentially over a distinct time period before they saturate nonlinearly. The corresponding values of the total, $w(t)$, and the modal energy growth rate, $w_m(t)$, of the modal structures — computed via

$$w(t) = \frac{1}{2}\frac{\log E(t+\Delta t) - \log E(t)}{\Delta t}, \tag{4.2}$$

$$w_m(t) = \frac{1}{2}\frac{\log E_m(t+\Delta t) - \log E_m(t)}{\Delta t}, \tag{4.3}$$

where Δt denotes the temporal difference between two flow fields — is presented in figure 9(b). In this figure, the plateau with $w/S \approx 11.3$ represents the exponentially growing regime in

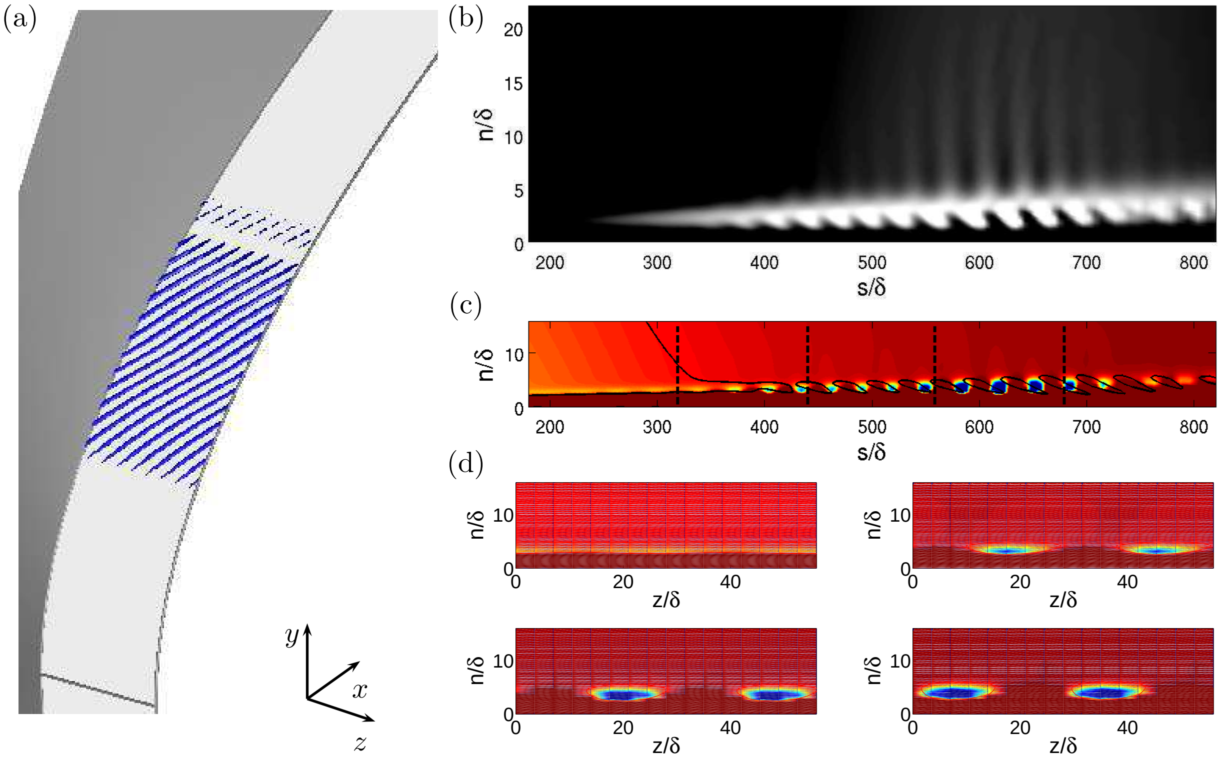

Figure 10. Results from a long-term integration of the initial value problem: (a) visualization of vortical structures by iso-surfaces of the Q-criterion (in blue); the surface of the upper half of the parabolic body is displayed in light grey (attachment line in black). The divergence of the velocity field (-1300 in black, -1800 in white, stretched by a factor of ten in n) in the s-n-plane is shown in (b). (c) Distribution of the vortical structures using a cross-cut in the s-n-plane; the black lines denote one representative iso-line of the Q-criterion. (d) Cross-cuts in the n-z-plane at selected positions in the chordwise s-direction; see dashed lines in (c).

figure 9(a), and the growth of the fundamental modal structure confirms a linear instability (red line). The first higher-order mode exhibits the same modal growth before it becomes unstable to secondary instabilities (green line). Only three spanwise harmonic structures have been plotted in figure 9(b) as a consequence of the spatial resolution, $n_3 = 8$, in this direction. The same modal growth of all three structures can be interpreted as a phase locking of harmonics producing steeper gradients in the spanwise direction. This phenomenon is also evident in figure 6(d), where a spanwise cross-cut at two positions in the chordwise s-direction shows the formation of approximately rectangular structures, starting from a sinusoidal shape, as the flow evolves downstream.

The spatial distribution of the exponentially growing modal structures at $t = 3.63 \cdot 10^{-4}$ [s] (see dashed lines in figure 9) is plotted in figure 10. The application of the Q-criterion reveals co-rotating vortical structures, visualized by iso-surfaces, which display typical features of crossflow instabilities. Cross-cuts of these vortices are given in figure 10(c,d), and the results indicate that the vortical structures first appear close to the edge of the boundary layer and that these structures become more and more pronounced inside the boundary layer as they evolve in the chordwise s-direction; further downstream they disappear again. It is also found that the dominant part of the vortices lies further downstream as time progresses and eventually breaks down. To indicate the acoustic field, we additionally show the divergence of the velocity field in figure 10(a,b).

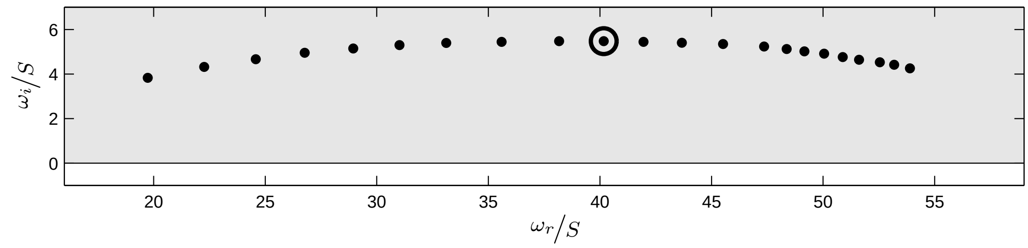

Figure 11. Results from a global stability analysis showing the most unstable eigenvalues of the temporal global spectrum for a disturbance wavenumber $\beta = 2\pi/28\delta$ ($\beta^\star = \beta\delta = 0.224$); ω_r describes the frequency and ω_i the corresponding growth rate of the global modes; unstable half-plane in grey. The shown eigenvalues belonging to boundary-layer modes of the crossflow type (see Mack et al., 2008).

4.2.3 *Global stability analysis*

The above long-term integration of the initial value problem (4.1) uncovered a linear instability mechanism, where the most unstable coherent structures are characterized by co-rotating vortices. To obtain more information about these vortices and to gain further insight into the inherent modal structures of the flow we perform a global stability analysis. To this end, we superimpose a disturbance field $\phi'(x, y, z, t)$ on the steady base flow $\phi_0(x, y, z)$ and assume the perturbations of the following traveling wave form.

$$\phi'(x, y, z, t) = \widetilde{\phi}(x, y)\mathrm{e}^{\mathrm{i}(\beta z - \omega t)} \tag{4.4}$$

Herein, $\widetilde{\phi}(x, y)$ denotes the complex amplitude and β the real spanwise wavenumber of the perturbation, and the temporal long-term evolution of the perturbation is given by ω whose real part ω_r describes the frequency and whose imaginary part ω_i represents the growth. This (global) stability approach results in a large-scale eigenvalue problem, and, for its solution, iterative techniques have to be employed. These techniques allow us to compute a given number of approximations to some eigenpairs of the stability (Jacobian) matrix, and, as already mentioned in the introduction, they use the flow fields produced by direct numerical simulations (DNS) as their input. Such a DNS-based global stability analysis has been attempted in Mack et al. (2008) for the present flow configuration, and a detailed description of the DNS-based global stability solver can be found in Mack and Schmid (2010).

The results in figure 11 represent an iteratively computed subset of the full global spectrum for $\beta = 2\pi/28\delta$ ($\beta^\star = 0.224$), and the depicted eigenvalues belong to unstable global boundary-layer modes of the crossflow type (see Mack et al., 2008). These (discrete) eigenvalues lie on a distinct branch, and, in the present global stability analysis, eigenvalues with ω_r/S ranging from 19.7 to 53.9 have been computed. Furthermore, the growth rate of the most unstable global mode of this branch is $\omega_{i,max}/S = 40.2$ (see circle in figure 11). The spatial distribution of the associated global mode is given in figure 12(a), where we display the distribution of the u-velocity using iso-surfaces. Cross-cuts in the s-n- and the n-z-plane of this mode can be seen in figure 12(b) and (c), respectively, and the pressure field is visualized in figure 12(a). It should be mentioned that, in their parametric study, Mack et al. (2008) obtained a maximum modal growth rate $\omega_{i,max}$ for $\beta^\star = 0.213$ and the same choice of the governing parameters.

In general, the rather large growth rates of the boundary-layer modes can be explained by the inflectional nature of the crossflow instability, since instabilities based on inflectional profiles can be inviscidly unstable. These modes describe the dominant instability mechanism for the present flow configuration (and choice of parameters), and this instability could also be observed by computing the long-term evolution of the perturbed steady state. However, only the most unstable vortical structure could be obtained. Furthermore, the rich perturbation dynamics of hypersonic flow about a swept parabolic body gives rise to further types of instabilities such as,

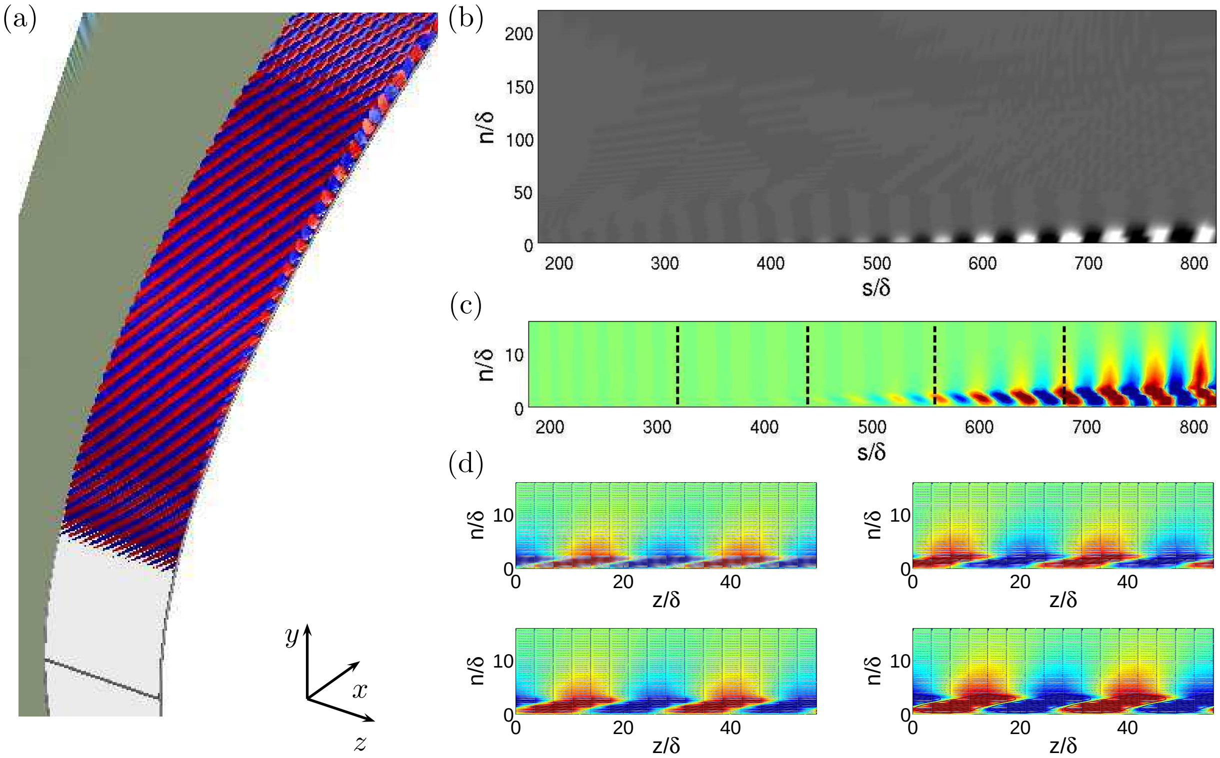

Figure 12. Results from a global stability analysis: (a) visualization of the most unstable global mode, depicted by a circle in figure 11, using the u-velocity (positive and negative values of iso-surfaces are displayed in red and blue, respectively, and eight wavelengths in z are used to visualize the mode). (b) Spatial shape of the pressure p in the s-n-plane. (c) Distribution of the global modes using a cross-cut in the s-n-plane; the structures were stretched by a factor of five in the normal n-direction. (d) Cross-cuts in the n-z-plane at selected positions in the chordwise s-direction; see dashed lines in (c).

e.g., acoustic global modes (see Mack and Schmid, 2010). Only a global stability analysis is able to provide a complete picture of the perturbation dynamics of the flow.

5 Discussion and Conclusions

Over the past decades, direct numerical simulations (DNS) have a reached a level of maturity which allows the computation of a wide range of complex flows characterized by multi-physics phenomena. At the same time, powerful algorithms for the iterative solution of large-scale eigenvalue problems have shown remarkable progress. The need and promise of stability information for complex flow configurations, such as hypersonic flow about a swept blunt body, as well as the limitations and shortcomings of local or simplified flow models calls for the combination of these two techniques to obtain quantitative flow measures that far surpass the existing ones.

In this article, a flow model for three-dimensional hypersonic flow about a swept blunt body has been presented and direct numerical simulations of the nonlinear governing equations using shock-fitting, moving curvilinear grids and higher-order compact schemes have been conducted. Based on experimental evidence, crossflow-dominated structures are expected and have been observed in our flow simulations. Subsequently, the most dominant of these structures has been confirmed by a long-time integration of small-amplitude perturbations superimposed on a steady state solution. Finally, a proper global stability analysis combining direct numerical simulations and iterative eigenvalue techniques produced multiple crossflow-dominated structures together with the temporal global spectrum. This specific example clearly demonstrates the feasibility of a DNS-based global stability concept.

In summary, DNS-based flow analysis, such as the one presented above, is expected to evolve into a powerful and important tool to investigate fluid behavior. In this manner, such tools are hoped to have a significant impact on flow applications of academic and industrial interest alike. Since direct numerical simulations will have to furnish high-quality data for DNS-based analysis tools, continued efforts for the advancement of DNS techniques are imperative. At the same time, the development of efficient iterative algorithms and their combination into a robust DNS-based flow analysis tool is equally important.

Acknowledgements

Financial support from the Deutsche Forschungsgemeinschaft (DFG), the Studienstiftung des Deutschen Volkes, the Alexander-von-Humboldt Foundation and the ANR program "Chaires d'excellence" is gratefully acknowledged.

References

Åkervik, E., Brandt, L., Henningson, D. S., Hœpfner, J., Marxen, O., and Schlatter, P. (2006). Steady solutions of the Navier–Stokes equations by selective frequency damping. *Phys. Fluids*, 18(068102).

Adams, N. A. and Shariff, K. (1996). A high-resolution hybrid compact–ENO scheme for shock-turbulence interaction problems. *J. Comput. Phys.*, 127:27–51.

Ambrosio, A. and Wortman, A. (1962). Stagnation point shock detachment distance for flow around spheres and cylinders. *ARS J.*, 32:281.

Anderson, D., Tannehill, J., and Pletcher, R. (1988). *Computational Fluid Mechanics and Heat Transfer.* Hemisphere Publishing Corporation.

Billig, F. S. (1967). Shock-wave shapes around spherical- and cylindrical-nosed bodies. *J. Spacecraft Rockets*, 4(6):822–823.

Bippes, H. (1999). Basic experiments on transition in three-dimensional boundary layers dominated by crossflow instability. *Prog. Aero. Sci.*, 35:363–412.

Bonfigli, G. and Kloker, M. (2007). Secondary instability of crossflow vortices: validation of the stability theory by direct numerical simulation. *J. Fluid Mech.*, 583:229–272.

Carpenter, M. H., Gottlieb, D., and Abarbanel, S. (1993). The stability of numerical boundary treatments for compact high order finite-difference schemes. *J. Comput. Phys.*, 108:272–295.

Chung, Y. M. and Tucker, P. G. (2003). Accuracy of higher-order finite difference schemes on nonuniform grids. *AIAA*, 41:No. 8.

Edwards, W. S., Tuckerman, L. S., Friesner, R. A., and Sorensen, D. C. (1994). Krylov methods for the incompressible Navier–Stokes equations. *J. Comput. Phys.*, 110:82–102.

Fabre, D., Jacquin, L., and Sesterhenn, J. (2001). Linear interaction of a cylindrical entropy spot with a shock. *Phys. Fluids*, 13(8):2403–2422.

Haddad, O. M., Erturk, E., and Corke, T. C. (2005). Acoustic receptivity of the boundary layer over parabolic bodies at angles of attack. *J. Fluid Mech.*, 536:377–400.

Hall, P., Malik, M., and Poll, D. I. A. (1984). On the stability of an infinite swept attachment-line boundary layer. *Proc. R. Soc. Lond.*, A 395:229–245.

Joslin, R. D. (1995). Direct simulation of evolution and control of three-dimensional instabilities in attachment-line boundary layers. *J. Fluid Mech.*, 291:369–392.

Joslin, R. D. (1996). Simulation of three-dimensional symmetric and asymmetric instabilities in attachment-line boundary layers. *AIAA J.*, 34:2432–2434.

Kazakov, A. V. (1990). Effect of surface temperature on the stability of swept attachment line boundary layer. *Fluid Dyn.*, 25(6):875–878.

Kennedy, C. A., Carpenter, M. H., and Lewis, R. M. (2000). Low–storage, explicit Runge–Kutta schemes for the compressible Navier–Stokes equations. *Appl. Numer. Math.*, 35:177–219.

Kloker, M. (1998). A robust high-resolution split-type compact FD scheme for spatial direct numerical simulation of boundary-layer transition. *Applied Scientific Research*, 59:353–377.

Knoll, D. A. and Keyes, D. E. (2004). Jacobian-free Newton–Krylov methods: a survey of approaches and applications. *J. Comput. Phys.*, 193(2):357–397.

Le Duc, A., Sesterhenn, J., and Friedrich, R. (2006). Instabilities in compressible attachment-line boundary layers. *Phys. Fluids*, 18:044102.

Lele, S. K. (1992). Compact finite difference schemes with spectral-like resolution. *J. Comput. Phys.*, 103:16–42.

Lin, R. S. and Malik, M. R. (1995). Stability and transition in compressible attachment-line boundary-layer flow. Technical Report 952041, SAE.

Lin, R. S. and Malik, M. R. (1997). On the stability of attachment-line boundary layers. Part 2. The effect of leading edge curvature. *J. Fluid Mech.*, 333:125–137.

Mack, C. J. and Schmid, P. J. (2010). A preconditioned Krylov technique for global hydrodynamic stability analysis of large-scale compressible flows. *J. Comput. Phys.*, 229(3):541–560.

Mack, C. J., Schmid, P. J., and Sesterhenn, J. L. (2008). Global stability of swept flow around a parabolic body: connecting attachment-line and crossflow modes. *J. Fluid Mech.*, 611:205–214.

Mack, L. M. (1984). Boundary layer linear stability theory. In *Special Course on Stability and Transition of Laminar Flow*, number AGARD–R–709. AGARD.

Moretti, G. (1987). Computations of flows with shocks. *Annu. Rev. Fluid Mech.*, 19.

Morkovin, M. V., Reshotko, E., and Herbert, T. (1994). Transition in open flow systems – a reassessment. *Bull. Am. Phys. Soc.*, 39.

Müller, B. (1990). Linear stability condition for explicit Runge–Kutta methods to solve the compressible Navier–Stokes equations. *Math. Methods i. Appl. Sci.*, 12:139–151.

Piquemal, A. S., Chiavassa, G., and Donat, R. (2004). A Brinkman-penalization method for compressible viscous flows. *Comput. Fluids.* submitted.

Reshotko, E. (1994). Boundary layer instability, transition, and control. *Dryden Lecture in Research*, pages AIAA Paper 94–0001.

Reshotko, E. and Beckwith, I. E. (1958). Compressible laminar boundary layer over a yawed infinite cylinder with heat transfer and arbitrary Prandtl number. Technical Report 1379, National Advisory Committee for Aeronautics.

Saric, W. S., Reed, H. L., and White, E. B. (2003). Stability and transition of three-dimensional boundary layers. *Annu. Rev. Fluid Mech.*, 35:413–440.

Schaupp, C., Sesterhenn, J., and Friedrich, R. (2008). On a method for direct numerical simulation of shear layer/compression wave interaction for aeroacoustic investigations. *Comput. Fluids*, 37:463–474.

Sesterhenn, J. (2001). A characteristic-type formulation of the Navier–Stokes equations for high-order upwind schemes. *Comput. Fluids*, 30:37–67.

Spalart, P. R. (1988). Direct numerical study of leading-edge contamination. In *AGARD-CP-438*, pages 5/1–5/13.

Spalart, P. R. (1990). Direct numerical study of crossflow instability. In *Laminar-Turbulent Transition (IUTAM)*, pages 621–630.

Theofilis, V. (1998). On linear and nonlinear instability of the incompressible swept attachment-line boundary layer. *J. Fluid Mech.*, 355:193–227.

Theofilis, V., Fedorov, A., Obrist, D., and Dallmann, D. (2003). The extended Görtler–Hämmerlin model for linear instability of three-dimensional incompressible swept attachment-line boundary layer flow. *J. Fluid Mech.*, 487:271–313.

Williamson, J. H. (1980). Low-storage Runge–Kutta schemes. *J. Comput. Phys.*, 35:48–56.

Zhong, X. and Tatineni, M. (2003). High-order non-uniform grid schemes for numerical simulation of hypersonic boundary-layer stability and transition. *J. Comput. Phys.*, 190:419–458.

Article 2

A preconditioned Krylov technique for global hydrodynamic stability analysis of large-scale compressible flows

By C. J. Mack[1,2] and P. J. Schmid[1]

[1]Laboratoire d'Hydrodynamique (LadHyX), CNRS-École Polytechnique,
F-91128 Palaiseau, France

[2]Department of Numerical Mathematics, Universität der Bundeswehr (UniBw),
D-85577 Munich, Germany

Published in *J. Comput. Phys.* (2010), **229**, pp. 541–560

The combination of iterative Krylov-based eigenvalue algorithms and direct numerical simulations (DNS) has proven itself an effective and robust tool in solving complex global stability problems of compressible flows. A Cayley transformation is required to add flexibility to our stability solver and to allow access to specific parts of the full global spectrum which would be out of reach without such a transformation. In order to robustify the overall global stability solver an efficient ILU-based preconditioner has been implemented. With this Cayley-transformed DNS-based Krylov method two flow cases were successfully investigated: (i) a compressible mixing layer, a rather simple but well-known problem, which served as a test case and (ii) a supersonic flow about a swept parabolic body, a challenging large-scale flow configuration.

1 Introduction

Linear hydrodynamic stability analysis plays a central role in identifying the dynamic behavior of infinitesimal perturbations superimposed on a steady base flow. It is a crucial component for understanding the underlying mechanisms in a large variety of fluid-dynamical applications. A sound understanding of the prevailing instability mechanisms for general shear layers is, in turn, required to optimize and manipulate the inherent flow properties.

A classical tool to study the temporal instability of such flows is given by *local* stability theory, which in general relies on the existence of two homogeneous and one inhomogeneous spatial coordinate direction. This approach dates back nearly a hundred years and leads to an eigenvalue problems of moderate size which can be solved by standard direct techniques. The assumption of two homogeneous directions, however, restricts local stability theory to flows with simple geometries and simple flow physics. More complex and technologically relevant flow situations with several inhomogeneous directions and/or complicated flow physics such as supersonic flow about blunt bodies, are beyond its reach. Instead, this type of flow situations requires a *global* rather than a local approach.

Over the past decades direct numerical simulations (DNS) based on high-order spatial discretization schemes have established themselves as a widely used tool to study complex flow problems. They aim at capturing all relevant physical features of the flow by spatially resolving all dynamic scales; thus, no modeling efforts are required. The range of applications of state-of-the-art direct numerical simulations is truly impressive in scope and complexity, and it is the aim of global hydrodynamic stability analysis — and the objective of this article — to harness these strengths and capabilities.

Even though the global stability problem can be mathematically formulated, the lack of multiple homogeneous directions yields a linear stability matrix whose sheer size makes a direct solution prohibitively expensive (Theofilis, 2003). Limited computational resources call for iterative eigenvalue methods (see, e.g., Edwards et al., 1994, for applications of iterative techniques in fluid mechanics) that extract stability information from the linearized flow in an approximate manner. Among these iterative solution techniques Krylov subspace methods (Sorensen, 2002) are particular popular for fluid-dynamical applications. Even though an explicit formulation and storage of the stability matrix is a feasible alternative when combined with parallelization efforts (Kitsios et al., 2009), we will focus on a Jacobian- or matrix-free environment where the necessary information for the global stability problem is directly extracted from direct numerical simulations.

Compressible global stability problems have only recently been tackled (see, e.g., Crouch et al., 2007, 2009, for a study of the onset of transonic shock buffeting). Large-scale complex flow problems featuring multiple (temporal/spatial) scales and multi-physics (shear and compressibility effects, acoustic waves, etc.) exhibit a complicated spectrum which requires special means to extract the relevant flow behavior. In addition, an erratic convergence history of standard iterative techniques is observed which calls for additional physics-based measures, such as spectral transformations and preconditioning, to improve their convergence towards specific global modes. Spectral transformations deform the complex eigenvalue plane in order to make specific parts of the global spectrum accessible to iterative eigenvalue methods (an approach of this type has been proposed by Morzynski et al., 1999). However, these transformations come at the expense of solving a large-scale linear system which, in accordance with the above procedures, has to be accomplished using a preconditioned iterative method based on a matrix-free approach.

Krylov subspace methods for hydrodynamic stability analysis of the *incompressible* Navier–Stokes equations were first introduced by Edwards et al. (1994). Their investigation of moderately complex flow situations allowed a simpler Jacobian-based implementation and did not require any type of spectral transformation. In the following years similar techniques have been compiled into the open-source package ARPACK (Lehoucq et al., 1998). A comparative study of transformed Krylov subspace techniques applied to problems from computational fluid dynamics can be found in, e.g., Morzynski et al. (1999), Tuckerman et al. (2000) and Zhang (2000), and further large-scale stability calculations have been performed by Lehoucq and Salinger (2001) and Burroughs et al. (2004). The above studies, however, take advantage of the explicit presence of the linear stability matrix. More recently, Arbenz et al. (2005) compared eigensolvers for large-scale three-dimensional modal analysis using AMG-preconditioned iterative techniques; all matrices are semi-positive definite and are, again, available explicitly. A state-of-the-art review of Krylov subspace techniques applied to a wide range of fluid flows of aerodynamical interest is given by Theofilis (2003) with special emphasis on the global linear stability of non-parallel and three-dimensional flow configurations. Based on his encompassing study we conclude that further progress in the field of global stability analysis has to involve a purely iterative and matrix-free approach which provides the starting point of this article.

Preconditioning techniques (see, e.g., Knoll and Keyes (2004); Nejat and Ollivier-Gooch (2008) for a recent overview) help improve the convergence of the linear system solver. In a survey article, Benzi (2002) provides a detailed overview of recent preconditioning strategies for large linear systems mainly focusing on incomplete factorization techniques (ILU) and sparse approximate inverses (SPAI). A general discussion on algebraic multigrid (AMG) as a preconditioner can be found in Trottenberg et al. (2000), and a specific application to AMG-accelerated BiCGStab is given in Füllenbach and Stüben (2002). While these references concentrate on preconditioning strategies for linear systems arising in Newton–Krylov methods, the literature on transformation and preconditioning techniques for large-scale eigenvalue problems is relatively sparse.

In this article we combine preconditioned Krylov-based techniques and direct numerical simulations (DNS) to obtain a robust DNS-based Jacobian-free global stability solver for compressible flows. In this manner, our contribution represents, on one hand, a generalization of the work of Edwards et al. (1994) towards compressible flows and, on the other hand, provides an extension of current tools for the global stability analysis of non-parallel and three-dimensional flows, as alluded to by Theofilis (2003). It builds on previous global stability studies of compressible flow such as the work of Theofilis and Colonius (2004) who investigate the behavior of cavity flows for a wide range of Mach numbers, the study of Robinet (2007) who treats the interaction of a shock with a laminar boundary layer within a global stability framework and the investigations of Crouch et al. (2007, 2009) who treat the onset of transonic shock buffeting as a global stability problem. Even though these studies are based on compressible governing equations they do not follow the approach taken in this article where an iterative stability solver is coupled to a direct numerical simulation code, thus performing a DNS-based (matrix-free) global stability analysis.

In a historical and methodological context the linear stability of compressible flows can be studied by the following approaches: (a) the direct solution of a one-dimensional local stability problem, (b) the long-time integration of a direct numerical simulation (DNS) starting with small-amplitude perturbations, (c) the direct or iterative solution of the global linear stability matrix, and (d) the preconditioned iterative solution of a global linear stability problem. In this article we develop the methodology for the latter approach (d) based on direct numerical simulations. In section §2 we present our test case, a compressible mixing layer, formulate the governing equations, briefly describe the linear stability theory for approaches (a), (c) and (d) and display our reference spectrum. This is followed by the description of the DNS-based global stability solver for approach (c) (section §3) and our Cayley-transformed version (section §4). We conclude with results in section §5.

2 Compressible mixing layer: reference spectrum and DNS

It will be useful and instructive to demonstrate the global stability analysis of complex flows with the help of a somewhat simplified flow configuration that possesses all the relevant physical and numerical features of the full problem while still allowing a comparison with reference solutions or analytical results. This way, we can design and assess the important components of the DNS-based global stability solver and gain valuable insight and experience in using the governing parameters to influence convergence properties and solution quality.

In view of the desired fields of application we consider a fully compressible flow that is dominated by advective, diffusive and wave-propagation phenomena. These features will be reflected in the associated global spectrum in form of shear modes, acoustic modes and combinations thereof which displays the typical features of many high-speed flows arising in aeronautical applications. The chosen reference flow configuration, however, should be sufficiently simple to still allow a solution by direct means; this point will particularly aid in the quality assessment of each approximate step taken in the overall global stability algorithm.

A flow configuration that satisfies most, if not all, of the above described prerequisites is the compressible mixing layer. A hyperbolic-tangent base velocity profile is assumed, and the flow field is subsequently linearized about this analytic base state resulting in the linearized compressible Navier–Stokes equations governing the perturbation field. The stability of this flow has been studied extensively, and the two landmark papers on this subject have been published by Michalke (1964) and Blumen (1970).

2.1. *Governing equations*

The dynamics of the mixing layer is governed by the compressible Navier–Stokes equations which have been formulated, using Cartesian tensor notation, for the pressure p, the velocities (u, v, w) and the entropy s. We define a viscous length scale δ (shear layer thickness), a Reynolds number Re, a Mach number Ma and a Prandtl number Pr as

$$\delta = \frac{2u_\infty}{\omega_\delta}, \qquad Re = \frac{u_\infty \delta}{\nu}, \qquad Ma = \frac{u_\infty}{c_\infty}, \qquad Pr = \frac{C_p \mu}{k}, \tag{2.1}$$

where $\omega_\delta = (du/dy)_{y=0}$ and the subscript $_\infty$ stands for the freestream quantities. The remaining variables ν, μ, c_∞, C_p and k denote, respectively, the kinematic and dynamic viscosity, the speed of sound, the specific heat at constant pressure and the thermal conductivity. Using these expressions, the compressible Navier–Stokes equations can be rewritten in the following non-dimensionalized form:

$$\frac{\partial p}{\partial t} + u_j \frac{\partial p}{\partial x_j} = -\gamma^2 p \frac{\partial u_j}{\partial x_j} + (\gamma - 1)\left(\frac{\gamma Ma^2}{Re}\Phi + \frac{\gamma}{(\gamma-1)RePr}\frac{\partial}{\partial x_j}\left(k\frac{\partial T}{\partial x_j}\right)\right), \tag{2.2a}$$

$$\frac{\partial u_i}{\partial t} + u_j \frac{\partial u_i}{\partial x_j} = -\frac{1}{\gamma Ma^2 \varrho}\frac{\partial p}{\partial x_i} + \frac{1}{Re\varrho}\frac{\partial}{\partial x_j}\left(\mu\left(\frac{\partial u_i}{\partial x_j} + \frac{\partial u_j}{\partial x_i}\right) - \frac{2}{3}\mu\frac{\partial u_k}{\partial x_k}\delta_{ij}\right), \tag{2.2b}$$

$$\frac{\partial s}{\partial t} + u_j \frac{\partial s}{\partial x_j} = \frac{\gamma Ma^2}{Re}\Phi + \frac{\gamma}{(\gamma-1)RePr}\frac{\partial}{\partial x_j}\left(k\frac{\partial T}{\partial x_j}\right) \tag{2.2c}$$

with

$$\Phi \equiv \frac{1}{2}\mu\left(\frac{\partial u_i}{\partial x_j} + \frac{\partial u_j}{\partial x_i}\right)^2 - \frac{2}{3}\mu\left(\frac{\partial u_k}{\partial x_k}\right)^2 .$$

Herein, a freestream entropy $s_\infty = R_c$ was assumed, where R_c denotes the gas constant. The variables γ, ϱ and T represent the specific heat ratio, the density and the temperature, respectively.

The non-dimensionalized base flow in the streamwise x-direction is given by

$$u_0(x, y, z) = \tanh(y) \qquad -\infty < y < +\infty , \tag{2.3}$$

where the subscript $_0$ stands for base flow quantities; y and z represent the normal and the spanwise coordinate direction, respectively (see figure 1). The base pressure $p_0(x, y, z) = 1$ and the base entropy $s_0(x, y, z) = 1$ are assumed to be constant.

The compressible Navier–Stokes equations, the equation of state, Fourier's law for the thermal conductivity and Sutherland's law, where ambient conditions are used as a reference state, for the viscosity fully describe the flow. For all simulations shown in this article, we consider the motion of a compressible fluid modeled as a perfect gas with constant specific heat ratio $\gamma = 1.4$ and constant Prandtl number Pr $= 0.71$.

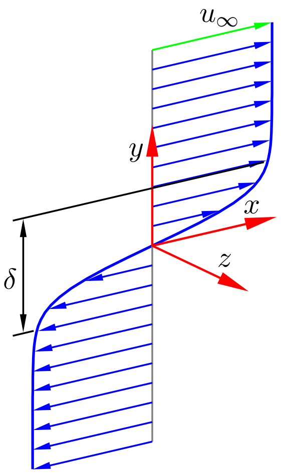

Figure 1. Sketch of a mixing layer showing the base velocity profile (in blue), some of the relevant flow parameters and the Cartesian coordinate system (in red).

2.2. *Linear stability analysis*

In a next step towards a linear stability analysis we assume a three-dimensional small-amplitude perturbation field $\epsilon\phi' = \epsilon(p', u', v', w', s')^T$ superimposed on a steady base flow ϕ_0.

$$\phi(x, y, z, t) = \phi_0(x, y, z) + \epsilon\phi'(x, y, z, t) \tag{2.4}$$

From this the linearized Navier–Stokes equations for the perturbations

$$\frac{\partial \phi'}{\partial t} = \mathcal{J}(\phi_0)\phi' \tag{2.5}$$

are obtained, where $\mathcal{J}(\phi_0)$ denotes the linear stability operator. The compressible mixing layer (see figure 1) is then assumed to be homogeneous in the x- and the z-direction, and periodic boundary conditions are applied in these directions. In the remaining inhomogeneous y-direction, all disturbance quantities are assumed to decay exponentially in the freestream.

2.2.1 *Local stability approach*

Referring back to approach (a), mentioned at the end of the introduction, and taking advantage of the separability of the governing equations in the two homogeneous coordinate directions, the disturbance field $\phi'(x, y, z, t)$ can be taken of the following traveling-wave form

$$\phi'(x, y, z, t) = \widetilde{\phi}(y)\mathrm{e}^{\mathrm{i}(\alpha x + \beta z - \omega t)}, \tag{2.6}$$

where $\widetilde{\phi}(y)$ denotes the complex amplitude, and α and β are the real wavenumbers of the perturbation in the streamwise and the spanwise direction, respectively. The temporal long-term evolution of this type of disturbance is characterized by ω whose real part describes the frequency ω_r and whose imaginary part the corresponding growth rate ω_i. Upon substitution of the above expression (2.6) into the perturbation equations (2.5) we obtain a *one-dimensional* eigenvalue problem $\omega\,\widetilde{\phi} = \mathcal{J}(\phi_0)\,\widetilde{\phi}$ for ω and $\widetilde{\phi}$. Once the dependence on the inhomogeneous y-direction is eliminated by a sixth-order compact finite difference scheme (Lele, 1992) using n_y grid points, we arrive at an eigenvalue problem for the linear stability matrix, i.e., the $5n_y \times 5n_y$ Jacobian matrix, which can be solved numerically by direct means for each wavenumber pair (α,β) and for each value of the remaining parameters.

2.2.2 *Global stability approach*

Many flow problems are characterized by a complex geometry or complex flow physics which no longer permits an assumption of the form (2.6), e.g., owing to several inhomogeneous coordinate directions. Supersonic flow about a swept parabolic body, which will be considered later in this article (see section §5), represents an example of this type. In this case, a *global* rather than a *local* stability approach has to be considered which forms the basis for approach (c) and (d) as mentioned at the end of the introduction.

For the global approach the disturbance field $\phi'(x, y, z, t)$ is assumed to satisfy

$$\phi'(x, y, z, t) = \widetilde{\phi}(x, y)\mathrm{e}^{\mathrm{i}(\beta z - \omega t)}, \tag{2.7}$$

where, as before, $\widetilde{\phi}(x, y)$ denotes the complex amplitude and β the real spanwise wavenumber of the perturbation. This formulation is referred to as *BiGlobal* in Theofilis (2003). The long-term temporal stability of the perturbation is given by the global eigenvalue ω. Under these assumptions and an appropriate discretization of the x- and y-dependence, the *two-dimensional* (global) stability problem can formally be written as

$$\omega\ \widetilde{\boldsymbol{\phi}}(\boldsymbol{x}, \boldsymbol{y}) = \mathbf{J}(\boldsymbol{\phi}_0)\ \widetilde{\boldsymbol{\phi}}(\boldsymbol{x}, \boldsymbol{y}), \tag{2.8}$$

where $\mathbf{J}(\boldsymbol{\phi}_0)$ represents the $n \times n$ linear stability matrix (the Jacobian), i.e., the discretized Navier–Stokes equations linearized about the base state $\boldsymbol{\phi}_0$, with $n = 5n_x n_y$ as the dimension of this (complex-valued) eigenvalue problem; n_x and n_y denote the number of grid points in the x- and y-direction, respectively.

For linear stability matrices of moderate size, e.g., a dimension $n \sim \mathcal{O}(10^5)$, this eigenvalue problem can still be solved directly (see, e.g., Theofilis (2003) for a discussion on the solution of global eigenvalue problems). For more complex flow configurations which require a large domain as well as a high spatial resolution, however, the direct solution of the (global) eigenvalue problem (2.8) is prohibitively expensive. Instead, iterative solution techniques have to be employed to extract pertinent stability information.

2.3. *Long-time integration of the initial value problem*

An alternative approach to address the stability of complex flows is given by the long-time solution of a linearized initial value problem

$$\frac{\partial \phi}{\partial t} = \mathcal{F}(\underbrace{\phi_0 + \epsilon\phi'}_{\phi}), \tag{2.9}$$

where $\mathcal{F}$ represents the right-hand side of the nonlinear Navier–Stokes equations. The solution of (2.9) could be obtained from direct numerical simulations (see, e.g., Theofilis, 2003; Le Duc et al., 2006, for applications in fluid dynamics). This technique corresponds to approach (b) as mentioned at the end of the introduction. Starting with an arbitrary initial condition of small amplitude $\epsilon\phi'$ (such that nonlinear effects can be neglected) superimposed on a steady base flow ϕ_0, the solution of the initial value problem converges towards the least-stable global mode as time progresses. The corresponding global eigenvalue can be computed from this global mode in a straightforward manner.

2.4. *Reference spectrum*

A typical spectrum of the compressible mixing layer is displayed in figure 2(a), and the values of the four eigenvalues depicted in circles are shown in table 3. This multi-branch spectrum was obtained using the local stability approach (see section §2.2.1), and it reveals characteristic

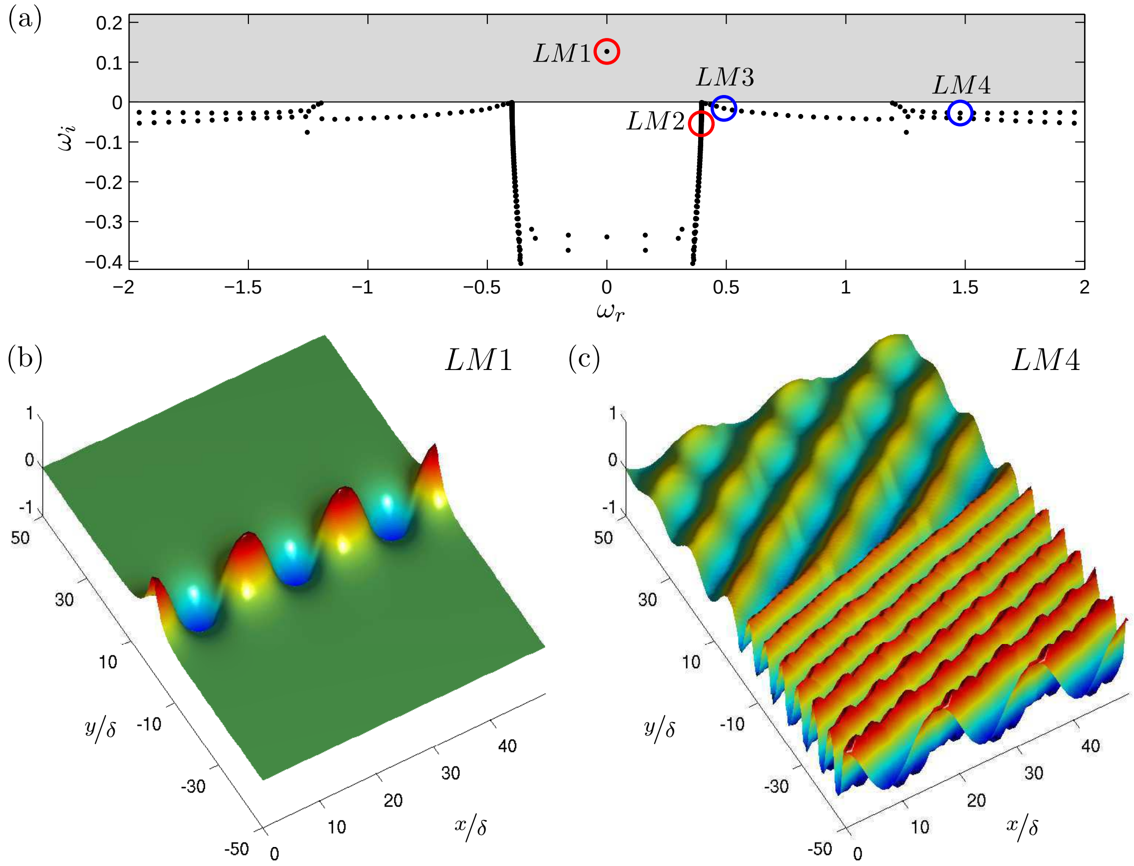

Figure 2. (a) Directly computed reference spectrum of a compressible mixing layer for $Re = 1000$, $Ma = 0.5$, $\alpha = 0.397$ and $\beta = 0$ (see table 4, ConfigIV); $n_y = 201$ grid points were used to resolve the inhomogeneous y-direction; unstable half-plane in grey. The spatial structure of two (local) modes is visualized by the (normalized) disturbance pressure using three periods in the periodic x-direction: (b) unstable (discrete) shear mode ($LM1$), (c) faster-moving acoustic mode ($LM4$) from the acoustic branch.

features such as (i) acoustic modes with very small damping but rather high phase velocities (which reflects the fact that sound waves propagate quickly and without significant attenuation in their amplitude), (ii) shear-layer modes displaying small phase velocities (which reflects the fact that shear instabilities propagate with the local base velocity which is rather small inside the shear layer), and (iii) a continuous spectrum of modes that describes the perturbation dynamics in the freestream and ensures the completeness of the eigenfunction basis (Schmid and Henningson, 2001). Instabilities (with $\omega_i > 0$) are observed only on the shear-layer branch. The spatial structure of two representative eigenfunctions, one from the shear-layer branch ($LM1$) and one from the acoustic branch ($LM4$) are shown in figure 2(b,c).

Table 3. Values of the four eigenvalues $\omega = \omega_r + \mathrm{i}\omega_i$ marked by circles in figure 2(a); they belong to the unstable shear mode ($LM1$), a representative weakly-damped mode from the continuous shear-layer branch ($LM2$) and a slow-moving ($LM3$) as well as a faster-moving mode ($LM4$) from the acoustic branch.

Mode	$LM1$	$LM2$	$LM3$	$LM4$
ω_r	0	0.395973	0.459261	1.478955
ω_i	0.127146	-0.040255	-0.010807	-0.027631

This spectrum which displays many features of more complex spectra for compressible flows will serve as a reference spectrum on which we will develop, test and validate iterative solution techniques for the global hydrodynamic stability problem.

2.5. *Direct numerical simulations and validation of the code*

The direct numerical simulations (DNS) are performed on a non-uniformly distributed grid using n_x and n_y grid points in the x- and y-direction with a clustering of the n_y grid points near $y = 0$ to better resolve the shear layer. The governing equations are solved using a characteristic-type formulation (Sesterhenn, 2001) and discretized employing fifth- and sixth-order compact difference schemes for the inviscid and viscous terms, respectively (Adams and Shariff, 1996; Lele, 1992). For the initial value problem the temporal discretization is accomplished by a fourth-order Runge–Kutta scheme (see Mack and Schmid, 2009, for details).

In what follows, all numerical investigations will focus on four selected flow configurations (Config I–IV) that represent a range of physical and numerical features. The governing parameters for these examples are given in table 4.

To validate the code direct solutions of the one-dimensional eigenvalue problem (section §2.2.1) as well as solutions of the two-dimensional initial value problem (2.9) via direct numerical simulations are performed. In table 5 these results are compared with Blumen's findings for selected parameter combinations (Config I–III), and the results for the parameter choice of our reference case (Config IV) are shown too. In this manner, the Jacobian (used as a preconditioner) and the DNS-code are validated. In addition, results from the solution of the two-dimensional (global) eigenvalue problem (2.8) obtained from a DNS-based iterative stability solver (without transformation) are included as well. The used Krylov subspace method that generated the latter results is described in section §3, its spectrally (Cayley-) transformed version is developed in section §4 and evaluated using the given reference spectrum (see figure 2).

Table 4. Governing parameters of the four selected flow configurations (Config I–IV) which are defined by the shear-layer thickness δ, the Reynolds number Re, the Mach number Ma as well as the disturbance wavenumbers α and β.

Config #	δ	Re	Ma	α	β
I	0.1	$\to \infty$	0.1	0.433	0
II	0.1	$\to \infty$	0.5	0.397	0
III	0.1	$\to \infty$	0.9	0.208	0
IV	0.1	1000	0.5	0.397	0

Table 5. Growth rate ω_i of the unstable shear mode as obtained by using the approaches (a)–(c) described at the end of the introduction; a resolution of $n_x = 32$ and $n_y = 201$ grid points is used; Blumen's results are also included. For Config IV the unstable shear mode could not be computed via approach (b).

Config #	Blumen (1970)	*approach* (a) matrix-based	*approach* (b) DNS-based	*approach* (c) DNS-based
I	0.187	0.187521	0.1875	0.187521
II	0.141	0.141161	0.1412	0.141167
III	0.055	0.054731	0.0547	0.054723
IV	-	0.127146	-	0.127155

3 Iterative stability analysis

The global linear stability analysis of complex fluid flows leads to a non-Hermitian eigenvalue problem (2.8) whose solution requires iterative algorithms such as Krylov subspace methods. In many fluid-dynamical applications only a few eigenvalues are needed to answer questions of interest, a requirement that also favors iterative techniques. In what follows, we adopt a linear algebra notation with the matrix $\mathbf{A} \equiv \mathbf{J}(\boldsymbol{\phi}_0)$, the vector $\mathbf{x} \equiv \widetilde{\boldsymbol{\phi}}$ and the eigenvalue $\lambda \equiv \omega$, yielding a standard eigenvalue problem given as $\lambda\mathbf{x} = \mathbf{A}\mathbf{x}$.

3.1. *Krylov subspace methods*

A common class of iterative eigenvalue algorithms is based on the premise that the full stability problem can be projected onto a lower m-dimensional vector space given by an m-dimensional Krylov subspace sequence

$$\mathcal{K}_m(\mathbf{A}, \mathbf{v}_1) = \text{span}\{\mathbf{v}_1, \mathbf{A}\mathbf{v}_1, \mathbf{A}^2\mathbf{v}_1, \ldots, \mathbf{A}^{m-1}\mathbf{v}_1\}. \tag{3.1}$$

This sequence consists of repeated applications of a matrix $\mathbf{A}$ to an initial vector $\mathbf{v}_1$. The spectrum of the subsequent projected system then approximates the spectrum of the full stability problem given by $\mathbf{A}$.

Among the general class of Krylov subspace methods, we choose the *Implicitly Restarted Arnoldi Method* (IRAM) proposed by Sorensen (1992). This method is briefly described as follows (for a more complete discussion the reader is referred to the cited author): The Arnoldi method constructs an orthonormal basis $\mathbf{V}_m = [\mathbf{v}_1, \mathbf{v}_2, \ldots, \mathbf{v}_m]$ of the Krylov subspace $\mathcal{K}_m$ which is then used to decompose a matrix $\mathbf{A}$ in the following way:

$$\mathbf{A}\mathbf{V}_m = \mathbf{V}_m\mathbf{H}_m + \mathbf{f}_m\mathbf{e}_m^T. \tag{3.2}$$

$\mathbf{H}_m$ denotes an m-dimensional upper Hessenberg matrix (with $m \ll n$), $\mathbf{f}_m$ is the residual vector orthogonal to the basis $\mathbf{V}_m$, and $\mathbf{e}_m$ represents a unit-vector in the m-th component. Multiplying both sides of (3.2) from the left by $\mathbf{V}_m^*$ and using the fact that $\mathbf{V}_m$ is unitary, we obtain

$$\mathbf{V}_m^*\mathbf{A}\mathbf{V}_m = \mathbf{H}_m, \tag{3.3}$$

where the superscript * denotes the Hermitian conjugate. The eigenvalues $\{\theta_j\}$ of the Hessenberg matrix $\mathbf{H}_m$, the so-called Ritz values, are approximations of the eigenvalues $\{\lambda_j\}$ of the matrix $\mathbf{A}$, and the associated eigenvectors $\widetilde{\mathbf{x}}_j$ of $\mathbf{A}$, the so-called Ritz vectors, can be calculated using the orthonormal basis $\mathbf{V}_m$ as

$$\widetilde{\mathbf{x}}_j = \mathbf{V}_m\mathbf{y}_j, \tag{3.4}$$

where $\mathbf{y}_j$ denotes the eigenvector of $\mathbf{H}_m$ associated with the eigenvalue θ_j. In general, some of the Ritz pairs $(\widetilde{\mathbf{x}}_j,\theta_j)$ closely approximate the eigenpairs $(\mathbf{x}_j,\lambda_j)$ of $\mathbf{A}$, and the quality of this approximation usually improves as the dimension m of the Krylov subspace sequence $\mathcal{K}_m$ increases. In practice, however, the dimension of this subspace is limited by memory restrictions, and its ortho-normalization is progressively affected by numerical errors as m increases. For this reason, the Arnoldi factorization (3.2) needs to be periodically restarted with a new starting vector $\mathbf{v}^+$.

Sorensen's implicit restarting strategy (Sorensen, 1992) computes this new starting vector $\mathbf{v}^+$ by a polynomial approximation of Krylov vectors that damps $p = m - k$ undesired Ritz pairs, where k denotes the number of desired Ritz pairs. Lehoucq and Scott (1996) and Morgan (1996) studied the issue of restarting and compared implicit restarting with other schemes; furthermore, Morgan (1996) and Sorensen (2002) concluded that using implicit restarting and applying exact shifts in connection with the Arnoldi method is optimal. For details, including a discussion on the convergence behavior, we refer the reader to the above-mentioned literature.

For the sake of completeness, a further class of Krylov subspace methods known as subspace iteration techniques (see, e.g., Sorensen, 2002) is worth mentioning. As an example, Heeg and Geurts (1998) successfully applied these techniques in their studies on spatial instabilities of the incompressible attachment-line flow.

3.2. *Jacobian-free framework*

The form of the Krylov subspace sequence (3.1) indicates that the Jacobian matrix $\mathbf{A} \equiv \mathbf{J}(\boldsymbol{\phi}_0)$ does not need to be formed explicitly; rather, only matrix-vector products are necessary to perform the Arnoldi decomposition. These matrix-vector products are readily obtained from direct numerical simulations (DNS) via

$$\mathbf{A}\mathbf{v}_i \approx \frac{\mathbf{F}(\boldsymbol{\phi}_0 + \epsilon \mathbf{v}_i) - \mathbf{F}(\boldsymbol{\phi}_0)}{\epsilon} = \left.\frac{\partial \mathbf{F}(\boldsymbol{\phi})}{\partial \boldsymbol{\phi}}\right|_{\boldsymbol{\phi}=\boldsymbol{\phi}_0} \mathbf{v}_i + \mathcal{O}(\epsilon) \qquad \text{with} \qquad i = 1, 2, \ldots, m-1, \tag{3.5}$$

where ϵ is a user-specified parameter, $\boldsymbol{\phi}_0$ and $\mathbf{v}_i \equiv \boldsymbol{\phi}'$ denote, as before, the base flow and a disturbance field, respectively, and $\mathbf{F}$ represents the discretized right-hand side of the nonlinear Navier–Stokes equations. This first-order finite difference approximation of the Jacobian matrix $\mathbf{J}(\boldsymbol{\phi}_0)$ allows a Jacobian-free framework where right-hand side evaluations from direct numerical simulations provide the input for the iterative stability solver. Consequently, an explicit linearization of the governing equations (2.2) is no longer required. A matrix-free approach reduces memory requirements considerably and removes the problem of explicitly forming and storing the high-order Jacobian matrix. This advantage significantly simplifies the overall global stability method.

The choice of ϵ is, however, not obvious: if ϵ is too large, the derivative will be poorly approximated and if ϵ is too small, the result will be contaminated by roundoff errors. A widely used choice represents

$$\epsilon = \frac{\|\boldsymbol{\phi}_0\|_2}{\|\mathbf{v}_i\|_2}\epsilon_0, \tag{3.6}$$

where ϵ_0 is a small parameter which is typically chosen somewhat larger than the square root of machine epsilon. For a discussion on common choices for ϵ as well as higher-order approximations for equation (3.5) the reader is referred to Knoll and Keyes (2004) and the references therein.

It should be mentioned though, that this matrix-free formulation further introduces a considerable amount of flexibility in forming the linear stability matrix. The call to the right-hand side $\mathbf{F}$ in equation (3.5), which in our case consists of a direct numerical simulation code for the compressible Navier–Stokes equations, can easily be substituted by other numerical discretizations of the corresponding governing equations. In particular, the entire hierarchy of common models for high-Reynolds number flows in complex geometries (such as, e.g., Large-Eddy simulations (LES), Detached-Eddy simulations (DES), vortex-particle methods and even commercial codes) can be treated within the same framework. Stability results using this Jacobian-free framework can thus be obtained for any flow whose main features can be captured to a sufficient degree of accuracy by appropriate numerical simulations.

4 Convergence acceleration and control

The need for convergence acceleration arises from the fact that high resolution simulations of complex fluid flow physics (with, e.g., the coexistence of shear and acoustic modes as illustrated in our reference spectrum, see figure 2a) lead to an unpredictable and erratic convergence behavior of the simple Arnoldi method (without transformation). In addition, any thorough investigation of complex fluid flow behavior requires us to focus on specific parts of the global spectrum. For example, to investigate the acoustic near- and far-field as to its structure and directivity it is necessary to extract global modes from the acoustic branch. To direct the convergence of the Arnoldi method towards these modes a transformation of the complex eigenvalue plane can be used. In short, both convergence acceleration and convergence control are desired for an effective DNS-based global stability solver. It must be stressed, however, that any technique employed to accelerate or control the convergence of the global stability solver has to be of an iterative and matrix-free nature to preserve the applicability of the method to a wide range of complex fluid-dynamical problems.

4.1. *Inexact Cayley transformation*

To accelerate and control the convergence behavior of the global stability algorithm the *Cayley transformation* (Garratt et al., 1993) is applied. This transformation consists of a two-parameter conformal mapping of the complex plane and, for generalized eigenvalue problems of the form $\lambda \mathbf{B}\mathbf{x} = \mathbf{A}\mathbf{x}$, is defined as

$$\mathbf{T}_C(\sigma, \mu) \equiv (\mathbf{A} - \sigma \mathbf{B})^{-1}(\mathbf{A} - \mu \mathbf{B}), \tag{4.1}$$

where σ and μ are the mapping parameters. For standard eigenvalue problems, as it is the case for our problem, we have $\mathbf{B} = \mathbf{I}$ where $\mathbf{I}$ denotes the identity matrix. This transformation represents a more general mapping than the more commonly applied shift-invert technique (see, e.g., Ericsson and Ruhe, 1980; Theofilis, 2003).

The complex parameter σ acts as a shift parameter, and eigenvalues close to it are mapped far into the right-half plane for $\mathrm{Imag}\{\lambda\} < \mathrm{Imag}\{\sigma\} < \mathrm{Imag}\{\mu\}$ while eigenvalues far from it are mapped close to one (see figure 3). The second complex parameter μ introduces an additional stretching-and-rotation effect on the transformed spectrum. Its major role, however, consists in controlling the condition number of the linear transformation. For this reason, the Cayley transformation in general yields a better-conditioned linear system than the shift-invert transformation (see Lehoucq and Salinger, 2001), an important advantage for its iterative solution. In addition, Lehoucq and Meerbergen (1998) report "the superior numerical performance of a Cayley transformation over that of a shift-invert transformation within an Arnoldi method when using an iterative linear solver".

The eigenvalues λ of $(\mathbf{A}, \mathbf{B})$ are then recovered from the eigenvalues ξ of the transformed problem via

$$\lambda = \frac{\sigma \xi - \mu}{\xi - 1}, \tag{4.2}$$

while the eigenvectors $\mathbf{x}$ are not affected by the transformation.

Figure 3 demonstrates the Cayley transformation for our reference spectrum (see figure 2a). Two parameter settings for σ and μ are displayed: the first parameter combination focuses on the unstable shear mode $LM1$ (see table 3) whereas the second parameter combination aims at extracting a specific mode $LM4$ from the acoustic branch. The first configuration illustrates the possibility of convergence acceleration of the Arnoldi method, while the second configuration demonstrates the Cayley transformation as a convergence control tool. The general mapping between the complex λ- and the complex ξ-plane is further visualized by the dashed Cartesian grid in figure 3(a) and its mapped counterparts in figure 3(b,c). For an overview of available acceleration techniques we refer the reader to Bai (1992).

The Cayley transformation (4.1) requires the solution of the following generally non-Hermitian linear system

$$(\mathbf{A} - \sigma \mathbf{I})\mathbf{v}_{j+1} = (\mathbf{A} - \mu \mathbf{I})\mathbf{v}_j \tag{4.3}$$

for each outer step of the Arnoldi method to construct the $(j+1)$-th Krylov vector in (3.1). This is accomplished by using a Krylov-based iterative linear solver. From the commonly applied techniques of Generalized Minimum Residual (GMRES) method (Saad and Schultz, 1986),

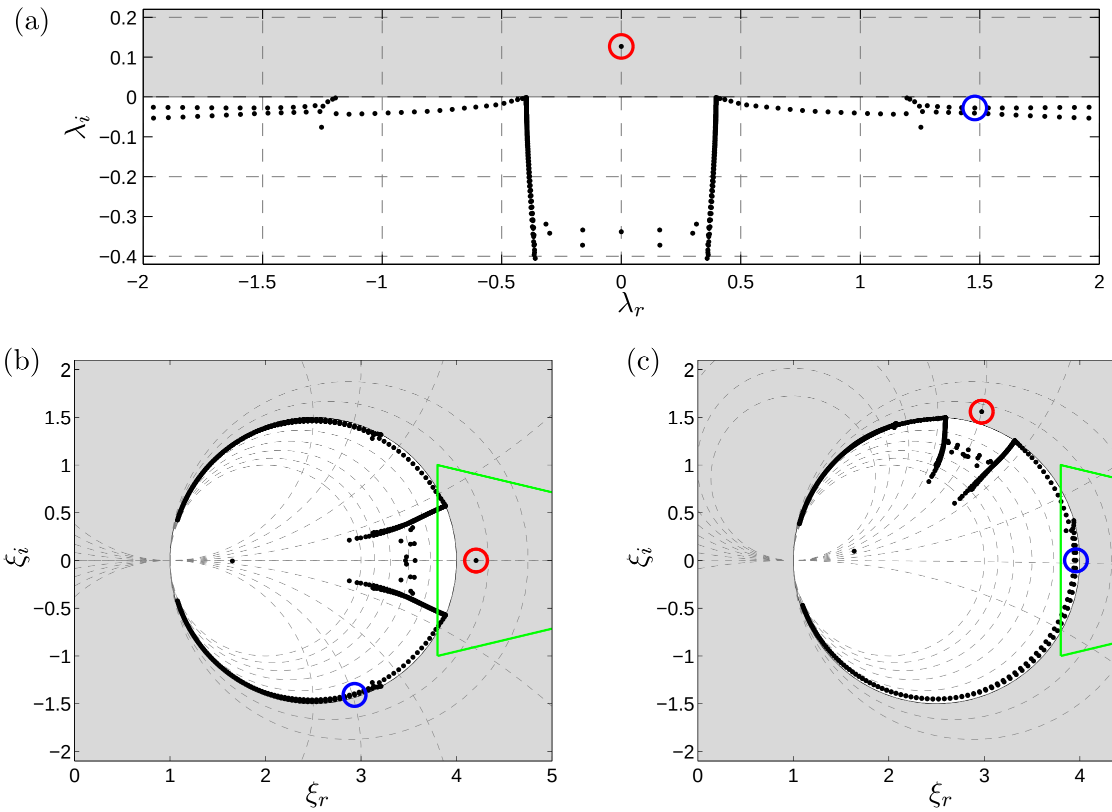

Figure 3. (a) Relabeled reference spectrum ($\lambda \equiv \omega$) as presented in figure 2(a); the two eigenvalues marked by circles belong to ω_{LM1} (in red) and ω_{LM4} (in blue); (b) and (c) display Cayley-transformed spectra for the mapping parameters $\sigma = \text{Real}\{\omega_{LM1}\} + 2\text{i}$ and $\mu = \text{Real}\{\omega_{LM1}\} + 8\text{i}$ and $\sigma = \text{Real}\{\omega_{LM4}\} + 2\text{i}$ and $\mu = \text{Real}\{\omega_{LM4}\} + 8\text{i}$, respectively. A dashed Cartesian grid as well as the unstable half-plane (in grey) and their mapped counterparts are also shown. The green line indicates the region of convergence of the Cayley-transformed Arnoldi method.

stabilized Bi-Conjugate Gradient Iteration (BiCGStab) (van der Vorst, 1992) and transpose-free quasi minimum residual (TFQMR) method (Freund, 1993), we choose the BiCGStab algorithm since its three-term recurrence relation results in low memory requirements. The solution of the linear system (4.3) by an iterative method can only be approximate; as a consequence, the Cayley transformation (4.1) is necessarily inexact (see, e.g., Meerbergen and Roose, 1997, for a discussion on inexact transformations).

The necessity of an iterative solution technique for solving (4.3), however, restricts the choice of Cayley parameters, and the resulting linear system yields solutions only if the shift parameter σ is chosen sufficiently far from an eigenvalue, thus avoiding an ill-conditioned matrix. Considerations like this can be ignored when a direct inversion is attempted. For a discussion of the choice of the Cayley parameters the reader is referred to, e.g., Burroughs et al. (2004) and the references therein.

4.2. *Preconditioning*

An efficient iterative solution of (4.3) requires a reliable and robust preconditioning technique. This has also been stated by Benzi (2002) who considers preconditioning as the “most critical ingredient in the development of efficient solvers for challenging problems in scientific computation”. For this reason, there exists a large body of literature on preconditioning strategies, and the reader is referred to, e.g., Benzi (2002), Osei-Kuffuor and Saad (2007) and Nejat and Ollivier-Gooch (2008) for an overview.

State-of-the-art preconditioning techniques require in general a preconditioning matrix in explicit form, as reported by Knoll and Keyes (2004). These authors also discuss Jacobian-free preconditioning strategies for linear systems and conclude that "the only iterative method that can be implemented in a fashion that is literally matrix-free is a Krylov method".

In our global stability algorithm we maintain a Jacobian-free implementation via direct numerical simulations but assume the preconditioning matrix in explicit form. Applying this (shifted) preconditioning matrix $\mathbf{P}_\sigma = \mathbf{P} - \sigma\mathbf{I}$ from the right, the modified expression of the finite difference approximation (3.5) reads

$$\mathbf{A}\,\underbrace{\mathbf{P}_\sigma^{-1}\mathbf{p}}_{\widehat{\mathbf{p}}} \approx \frac{\mathbf{F}(\boldsymbol{\phi}_0 + \epsilon\mathbf{P}_\sigma^{-1}\mathbf{p}) - \mathbf{F}(\boldsymbol{\phi}_0)}{\epsilon}, \tag{4.4}$$

where $\mathbf{p}$ denotes an iteration vector in the BiCGStab algorithm (see van der Vorst (1992) for details). This expression has to be evaluated each time a matrix-vector product is required in the inner iteration, the solution of equation (4.3), of the Krylov-based linear solver. The outer Arnoldi iteration is not affected by $\mathbf{P}_\sigma$.

Preconditioning the inner iterations raises two important questions related to the choice of $\mathbf{P}$ and the manner of solving the required linear system $\mathbf{P}_\sigma\widehat{\mathbf{p}} = \mathbf{p}$. For $\mathbf{P}$ we choose a second-order finite difference approximation of the Jacobian matrix. Owing to the sparsity of $\mathbf{P}$ we can take advantage of efficient incomplete decomposition techniques. The degree of "incompleteness" is given by the chosen sparsity structure of the decomposition. For general matrices, the LU-decomposition results in upper/lower triangular matrices that are dense. Incomplete decompositions, on the other hand, yield matrices that have a characteristic sparsity pattern and can be inverted efficiently by standard algorithms. In our case we choose an incomplete LU-decomposition, i.e., the dual truncation technique ILUT(p,τ) in which dropping during the factorization is based on two user-specified parameters: the fill level p and the drop tolerance τ (Saad, 2003). This strategy was successfully applied by Osei-Kuffuor and Saad (2007) to precondition complex-valued matrices, and as a dropping rule for a given fill level maximally p super-diagonal and p sub-diagonal elements are kept in each row of LU.

Denoting our low-order approximation of the Jacobian matrix by $\mathbf{P}_{low}$ we can recast equation (4.4) as follows

$$\mathbf{A}_{high}\mathbf{P}_{low,\sigma}^{-1}\mathbf{p} \approx \frac{\mathbf{F}_{high}(\boldsymbol{\phi}_0 + \epsilon\mathbf{P}_{low,\sigma}^{-1}\mathbf{p}) - \mathbf{F}_{high}(\boldsymbol{\phi}_0)}{\epsilon}, \tag{4.5}$$

which illustrates the combination of high-order Jacobian evaluation with low-order preconditioning, denoted by the subscripts $_{high}$ and $_{low}$, respectively. For the sake of simplicity, these subscripts are omitted for $\mathbf{A}$ and $\mathbf{P}$ in the following.

Ideal preconditioning would result in eigenvalues of $\mathbf{A}_\sigma\mathbf{P}_\sigma^{-1} = (\mathbf{A} - \sigma\mathbf{I})(\mathbf{P} - \sigma\mathbf{I})^{-1}$ at one. In practice, however, one has to be content with a clustering of the eigenvalues of $\mathbf{A}_\sigma\mathbf{P}_\sigma^{-1}$ about one. The quality of a preconditioner can thus be measured by the distance of these eigenvalues from one but also by their distance from the origin which is necessary to avoid ill-conditioning. These eigenvalues depend on four factors: (i) the discretization in $\mathbf{A} \equiv \mathbf{J}(\boldsymbol{\phi}_0)$, (ii) the choice of $\mathbf{P}$ (discretization, formulation, etc.), (iii) the technique employed to efficiently invert $\mathbf{P}_\sigma$ and (iv) the choice of the shift parameter σ.

4.3. *Proposed global stability algorithm (PCIRAM)*

In summary, our proposed DNS-based global stability solver consists of the five steps (S1–S5) shown below (a sketch that illustrates the algorithm can be found in figure 4). This solver requires the user to specify several parameters which are related to the implicitly restarted Arnoldi method (m, k, tol_A), the Jacobian-free implementation (ϵ_0), the Cayley transformation (σ, μ), the iterative linear solver (tol_B) and the ILUT-preconditioner (p,τ). Additionally, the starting vectors $\mathbf{v}_1$ and $\mathbf{v}_{j+1,0}$ for the Arnoldi method and the iterative linear solver are required.

S1. Compute the base flow $\boldsymbol{\phi}_0$ (if not available in analytic form)

S2. Compute and save $\mathbf{F}_{high}(\boldsymbol{\phi}_0)$ (required for the Jacobian-free framework)

$\Longrightarrow$ Call right-hand side in DNS to compute $\mathbf{F}_{high}(\boldsymbol{\phi}_0)$

S3. Setup the preconditioning matrix $\mathbf{P}$ by a low-order approximation of the high-order Jacobian matrix $\mathbf{A}$, and compute the incomplete LU-decomposition of $\mathbf{P}_\sigma = \mathbf{P} - \sigma\mathbf{I}$.

S4. Perform outer Arnoldi iterations to solve the (global) eigenvalue problem

$$\lambda\,\mathbf{x} = \mathbf{A}\,\mathbf{x}$$

- (A) Choose initial condition $\mathbf{v}_1$
- (B) Iterate *until convergence*: for $j = 1, 2, \ldots$
  - B.1 Apply Cayley transformation and compute $\mathbf{v}_{j+1}$

    $$(\mathbf{A} - \sigma\mathbf{I})\,\mathbf{v}_{j+1} = \underbrace{(\mathbf{A} - \mu\mathbf{I})\,\mathbf{v}_j}_{\mathbf{b}}$$

    - (a) Obtain the matrix-vector product in $\mathbf{b}$ using

      $$\mathbf{A}\mathbf{v}_j \approx \frac{\mathbf{F}_{high}(\boldsymbol{\phi}_0 + \epsilon\mathbf{v}_j) - \mathbf{F}_{high}(\boldsymbol{\phi}_0)}{\epsilon}$$

      $\Longrightarrow$ Call right-hand side in DNS to compute $\mathbf{F}_{high}(\boldsymbol{\phi}_0 + \epsilon\mathbf{v}_j)$

    - (b) Perform inner iterations of ILU-preconditioned BiCGStab to solve

      $$(\mathbf{A} - \sigma\mathbf{I})\mathbf{P}_\sigma^{-1}\mathbf{P}_\sigma\mathbf{v}_{j+1} = \mathbf{b}$$

      - (b.1) Choose initial condition $\mathbf{v}_{j+1,0}$
      - (b.2) Iterate *until convergence*: for $i = 1, 2, \ldots$
        - a) Incomplete solution of $\mathbf{P}_\sigma\widehat{\mathbf{p}} = \mathbf{p}$
        - b) Obtain the matrix-vector product via

          $$\mathbf{A}\widehat{\mathbf{p}} \approx \frac{\mathbf{F}_{high}(\boldsymbol{\phi}_0 + \epsilon\widehat{\mathbf{p}}) - \mathbf{F}_{high}(\boldsymbol{\phi}_0)}{\epsilon}$$

          $\Longrightarrow$ Call right-hand side in DNS to compute $\mathbf{F}_{high}(\boldsymbol{\phi}_0 + \epsilon\widehat{\mathbf{p}})$

        - c) Check for convergence of $\mathbf{v}_{j+1,i}$ via

          $$\|\mathbf{r}_i\|/\|\mathbf{b}\| \leq tol_B,$$

          where $\mathbf{r}_i$ denotes the current residual error and tol_B is a user-specified tolerance parameter.
  - B.2 Check for convergence of the desired Ritz pairs $(\widetilde{\mathbf{x}}_j,\theta_j)$ using the Ritz estimate

    $$|\beta_m\mathbf{e}_m^T\mathbf{y}_j| \leq \max(\epsilon_M\|\mathbf{H}_m\|\ ,\ tol_A \cdot |\theta_j|),$$

    where $\beta_m = \|\mathbf{f}_m\|$, ϵ_M stands for machine epsilon and tol_A denotes a user-specified tolerance parameter.

S5. Finally, recover eigenvalues λ of $\mathbf{A}$ via

$$\lambda = \frac{\sigma\theta - \mu}{\theta - 1},$$

while the eigenvectors $\mathbf{x}$ follow from $\widetilde{\mathbf{x}}$.

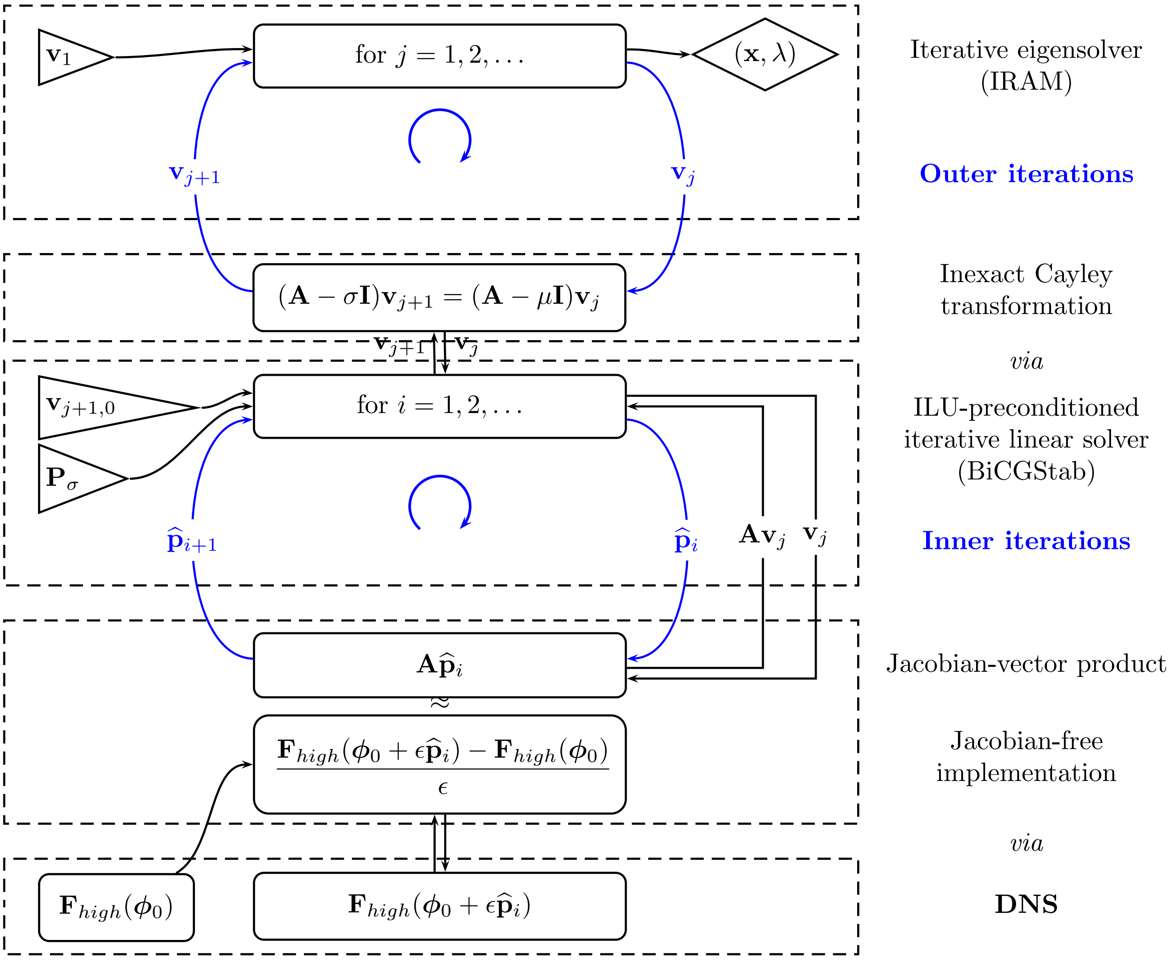

Figure 4. Sketch of our proposed DNS-based global stability algorithm (abbreviated as PCIRAM). The left column shows the required input such as the starting vectors $\mathbf{v}_1$ and $\mathbf{v}_{j+1,0}$, and, as a result, approximations to the eigenpairs $(\mathbf{x}, \lambda)$ are obtained; $\mathbf{A}$ denotes the high-order Jacobian matrix. The dashed boxes represent different components of the algorithm which could be replaced in a modular manner, e.g., instead of direct numerical simulations (DNS), Large-Eddy simulations (LES) could be used to provide the required input for the Jacobian-free implementation.

5 Results

After having established and analyzed the components of an iterative global stability solver based on direct numerical simulations (DNS), we now demonstrate its effectiveness in extracting information of the perturbation dynamics on two examples. The first example continues our test case of the compressible mixing layer introduced in section §2. The second example concerns supersonic flow about a swept parabolic body where the global treatment of the associated stability problem will yield new physical results and provide a significant numerical challenge to our global stability algorithm.

All numerical simulations shown in this article have been performed on an SGI Altix 4700 with a clock rate of 1.6 GHz. For all cases considered in the next sections, the initial condition $\mathbf{v}_1$ for the implicitly restarted Arnoldi method (IRAM) has been taken as a field of randomly distributed values, localized in space in order to satisfy the appropriate boundary conditions.

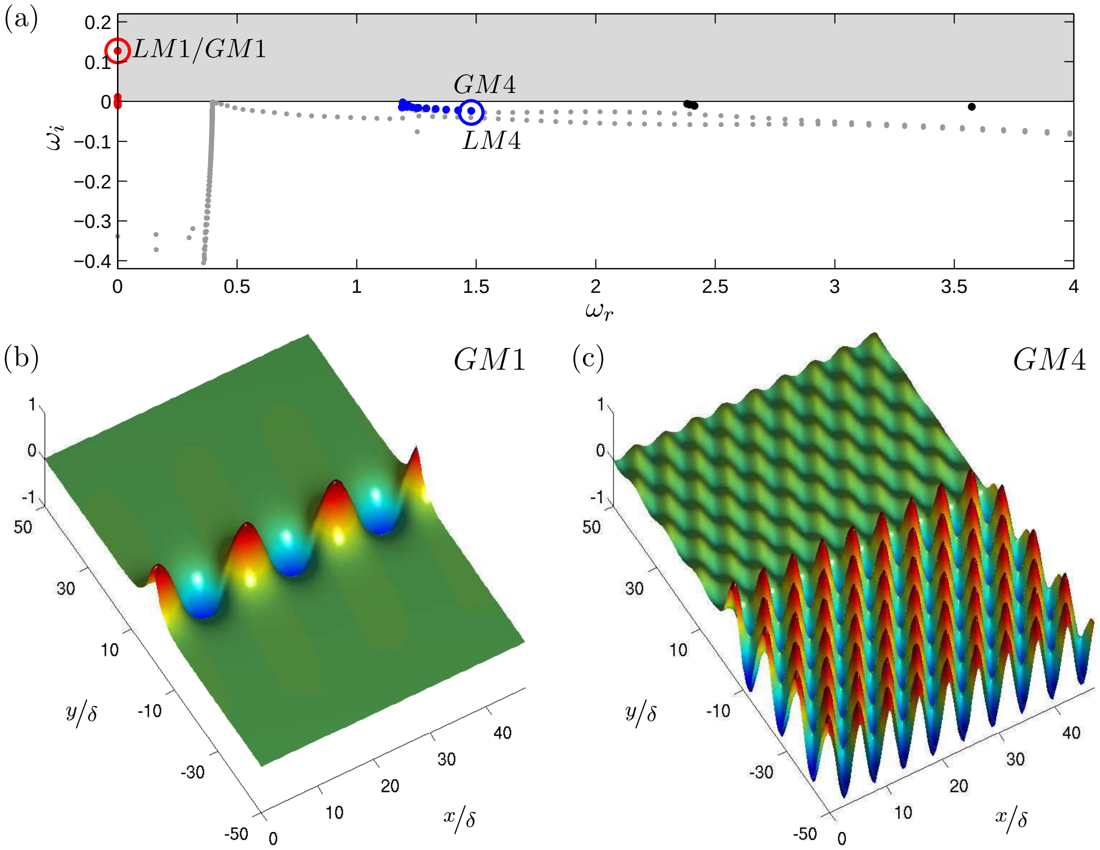

Figure 5. (a) Two spectra (in red and blue) which have been computed via our DNS-based global stability solver PCIRAM using the Cayley transformations displayed in figure 3(b) and (c), respectively. The eigenvalues belonging to ω_{LM1} and ω_{LM4} (see table 3) are indicated by circles; the directly obtained spectrum (in dark grey) as well as the unstable half-plane (in light grey) are also shown. The associated global modes $GM1$ (b) and $GM4$ (c) are visualized by the real part of the (normalized) pressure. Parameters given in table 4 (Config. IV) have been chosen, and 32×201 grid points have been used to resolve the x- and the inhomogeneous y-direction, respectively.

5.1. *Example 1: compressible mixing layer*

The compressible mixing layer, introduced earlier, represents a generic flow configuration that can be observed, at least locally, in many technological and industrial applications. In our investigation we will focus on the unstable shear mode ($LM1$) and a specific mode from the acoustic branch ($LM4$) as depicted in figure 2 as well as on some selected parameter settings (see table 4 for details); we will discuss flexibility, accuracy, robustness and efficiency of our global stability solver employing three methods: (i) the (simple) implicitly restarted Arnoldi method (IRAM), (ii) its Cayley-transformed but unpreconditioned version (abbreviated as CIRAM) and (iii) its Cayley-transformed and ILU-preconditioned variant (abbreviated as PCIRAM). As parameters for the Arnoldi method we set $m = 80$, $k = 32$ and $tol_A = 10^{-4}$, and we choose $\epsilon_0 = 10^{-8}$ for the Jacobian-free implementation.

5.1.1 *Increasing flexibility: the Cayley-transformed IRAM*

We start by studying the Cayley-transformed implicitly restarted Arnoldi method (PCIRAM) as our proposed global stability algorithm (see section §4) and demonstrate its flexibility in computing specified regions of the global spectrum (related to shear modes or acoustic modes) by adjusting the Cayley parameters. For this purpose, the two configurations displayed in figure 3(b,c), the first for the Cayley parameters $\sigma = \text{Real}\{\omega_{LM1}\} + 5\text{i}$ and $\mu = \text{Real}\{\omega_{LM1}\} + 20\text{i}$

and the second applying $\sigma = \text{Real}\{\omega_{LM4}\} + 5\text{i}$ and $\mu = \text{Real}\{\omega_{LM4}\} + 20\text{i}$ have been chosen, and the global spectra (a) and associated global modes (b,c) are visualized by the disturbance pressure $\widetilde{p}(x, y)$ in figure 5. Guess values for the Cayley parameters have to be taken when no prior information or estimates of the flow behavior are available; an iterative adapting of these parameters is conceivable. The real part of each (normalized) mode is plotted using three periods in the periodic x-direction. A clear distinction between global modes with support in the areas of highest shear ($GM1$) and acoustic modes with non-zero amplitudes in the freestream ($GM4$) can be made. The successful extraction of these modes from the general spectrum demonstrates the increase in flexibility of the DNS-based global stability solver as the Cayley transformation is added. As expected, the two-dimensional global spectrum is far more complex due to a superposition of modes with multiple streamwise scales as a consequence of a discretization in the streamwise x-direction. Therefore, it should not come as a surprise that the Arnoldi method does not necessarily converge to the global acoustic mode shown in figure 2(c). Instead, the PCIRAM extracts the least-stable global modes with respect to the chosen Cayley parameters.

The possibility of the Cayley-transformed IRAM of exploring desired parts of the full global spectrum represents at the same time a significant drawback of the Arnoldi method without such a transformation which, applied to the same choice of flow parameters, converges to only the unstable mode and a random sample of other modes, such as fast-traveling acoustic modes (see figure 5a black dots). No influence over the convergence towards specific modes, however, can be exerted.

5.1.2 *Increasing accuracy: the influence of the parameter* ϵ_0

An important component of our global stability solver contains the replacement of the exact Jacobian matrix $\mathbf{J}(\boldsymbol{\phi}_0)$ by a first-order finite-difference approximation (see equation (3.5)). This approximation crucially depends on a user-defined parameter ϵ_0. In particular, we are interested in the influence of ϵ, computed via equation (3.6), on the accuracy of the Ritz values as well as the Ritz pairs.

For this analysis, we resort to the (simple) implicitly restarted Arnoldi method (IRAM) to delineate the effects of ϵ_0 from those introduced by the inexact Cayley transformation and by the preconditioner. The influence of ϵ_0 on our solution is measured by two quantities, namely, the relative error and the direct residual.

The first quantity, the relative error e_1, is defined as

$$e_1(\epsilon_0) = \frac{|\omega_{2D,DNS}(\epsilon_0) - \omega_{1D}|}{|\omega_{1D}|}, \tag{5.1}$$

where $\omega_{2D,DNS} \equiv \theta_1$ denotes the least-stable Ritz value of the global DNS-based calculation and ω_{1D} represents the least-stable eigenvalue of the one-dimensional eigenvalue problem obtained by direct means (as shown in table 5).

The second quantity, the direct residual $\|\mathbf{r}_1\|$ (see Lehoucq et al., 1998), provides a measure of the accuracy of the computed least-stable Ritz pair $(\widetilde{\mathbf{x}}_1, \theta_1)$; it is defined as

$$\|\mathbf{r}_1(\epsilon_0)\| = \frac{\|\mathbf{J}(\boldsymbol{\phi}_0)\widetilde{\mathbf{x}}_1 - \widetilde{\mathbf{x}}_1\theta_1\|}{|\theta_1|}. \tag{5.2}$$

To cover a range of parameters, the following four flow configurations have been investigated (see table 4 for details about Config I and III): (i) a low Mach-number case with a rather low resolution (Config I, $n_x = 16$, $n_y = 101$), (ii) the same low Mach-number case but with a higher resolution (Config I, $n_x = 32$, $n_y = 201$), (iii) a high-Mach number case with the previous high resolution (Config III, $n_x = 32$, $n_y = 201$) and, finally, (iv) a high-Mach number case with a low Reynolds number (Config III with $Re = 1000$, $n_x = 32$, $n_y = 201$). The results are summarized in figure 6 where the evolution of the relative error e_1 and the norm of the direct residual $\|\mathbf{r}_1\|$

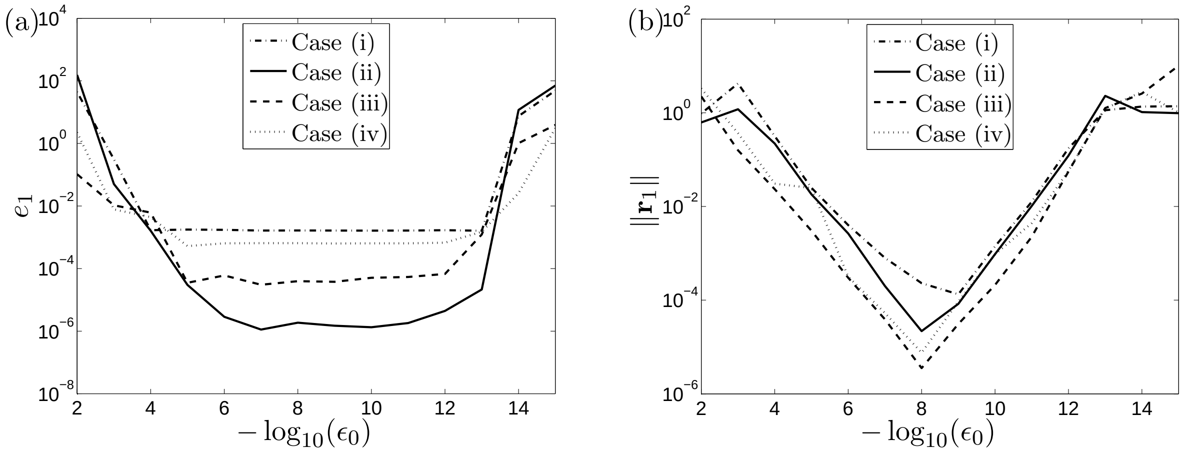

Figure 6. (a) Relative error e_1 and (b) direct residual $\|\mathbf{r}_1\|$ as a function of the user-specified parameter ϵ_0 for four selected flow configurations (i)–(iv); see text for details. The (simple) implicitly restarted Arnoldi method (IRAM) was applied.

are displayed versus ϵ_0 (with ϵ_0 ranging from 10^{-2} to 10^{-15} as a consequence of the double precision arithmetic).

In the case of the relative error e_1 (see figure 6a), the curves for each of the four cases show a similar shape: a rather small relative error plateau for a moderate range of ϵ_0 (10^{-6} to 10^{-11}) and a rapidly increasing relative error as we tend towards larger (10^{-2}) and smaller (10^{-15}) values of ϵ_0. The range of values where e_1 is nearly independent of the parameter ϵ_0, however, depends itself on the value of e_1; this means that the more accurate the least-stable Ritz value is determined — resulting in a smaller value of e_1, — the more narrow is its range of independence from ϵ_0.

Different results are found for the direct residual $\|\mathbf{r}_1\|$ (see figure 6b): instead of a plateau suggesting a range of optimal values for ϵ_0, a distinct choice of $\epsilon_0 \approx 10^{-8}$ yields the lowest residual norm; for values larger or smaller than this critical value, the residual norm increases substantially.

It is important to keep in mind, though, that for non-Hermitian matrices $\mathbf{A} \equiv \mathbf{J}(\boldsymbol{\phi}_0)$ a low direct residual does not necessarily imply an equivalent low error, and that the converged Ritz pair $(\underset{\sim}{\widetilde{\mathbf{x}}}, \theta)$ may not represent an accurate approximation of the corresponding eigenpair $(\mathbf{x}, \lambda) \equiv (\underset{\sim}{\boldsymbol{\phi}}, \omega)$. Direct residual and error are linked via the condition number of the system matrix $\mathbf{A}$, and an ill-conditioned system may yield inaccurate solutions. For precisely this reason do we observe a distinct plateau in the error (see figure 6a) but a lack thereof in the direct residual (see figure 6b). As far as the user is concerned the precise choice of ϵ_0 is not critical as long as it falls within the range of values defined by the plateau.

5.1.3 *Increasing robustness: an analysis of the growth rate and the direct residual*

The results of our investigation into robustness of the proposed methods are demonstrated and summarized in table 6. In it we compare findings obtained by applying (i) the simple untransformed, (ii) the Cayley-transformed but unpreconditioned and (iii) the Cayley-transformed and ILUT-preconditioned Arnoldi method. Only the convergence to the least-stable shear mode ω_1, with Real$\{\omega_1\} = 0$, and its dependence on a representative choice for the governing parameters are considered here. We observe that for the low-Mach number case (see table 4, Config I) the Cayley-transformed but unpreconditioned Arnoldi method failed to produce accurate results (see CIRAM in table 6). The ILUT-preconditioned version, on the other hand, converged towards the least-stable Ritz pair. With the exception of the failed computation employing the

Table 6. Growth rates Imag$\{\omega_1\}$ and associated direct residuals $\|\mathbf{r}_1\|$ applying the simple (IRAM), the Cayley-transformed but unpreconditioned (CIRAM) and the Cayley-transformed and ILUT-preconditioned Arnoldi method (PCIRAM) for the four flow configurations defined in table 4 and a resolution 32 × 201. For the inexact Cayley-transformation we set $\sigma = 5\text{i}$, $\mu = 20\text{i}$ and $tol_B = 10^{-5}$ and as preconditioner we used ILUT(10,10^{-2}).

	IRAM		CIRAM		PCIRAM	
Config #	Imag$\{\omega_1\}$	$\|\mathbf{r}_1\|$	Imag$\{\omega_1\}$	$\|\mathbf{r}_1\|$	Imag$\{\omega_1\}$	$\|\mathbf{r}_1\|$
I	0.187521	3.3e-5	(0.114675)	2.0e1	0.187520	7.5e-4
II	0.141167	5.1e-6	0.141167	4.4e-4	0.141165	6.3e-5
III	0.054723	2.6e-5	0.054723	1.1e-4	0.054723	5.4e-5
IV	0.127155	6.2e-6	0.127154	5.7e-5	0.127154	4.4e-5

(unpreconditioned) CIRAM for the low-Mach number case (Config I) the accuracy of the results listed in table 6 are satisfactory.

5.1.4 *Increasing efficiency: the performance of the proposed stability solver*

The application of a preconditioner $\mathbf{P}$ in the solution of equation (4.3) has proven imperative for the extraction of the least-stable mode for low-Mach numbers (see table 6). Even for converging cases the preconditioner plays a secondary role as it dramatically improves the efficiency of the Cayley-transformed Arnoldi method (see table 7). With this in mind, we compare the convergence behavior of our solver by applying various preconditioner matrices from the class of incomplete LU decomposition techniques denoted by ILUT(p,τ).

The results of our numerical experiments are shown in figure 7(a) displaying the relative residual $\|r\|/\|b\|$ as a function of the number of BiCGStab iterations. Best results are obtained — not surprisingly — by applying the complete LU-preconditioner, since no approximations (other than the low-accuracy discretization in $\mathbf{P}$) have been made, resulting in a true inverse of the linear system $\mathbf{P}_\sigma\widehat{\mathbf{p}} = \mathbf{p}$ (see section §4). To reach the same relative residual level of $\|r\|/\|b\| \leq tol_B = 10^{-5}$ the LU-preconditioned BiCGStab required 12 instead of 122 iterations (unpreconditioned). The impressive convergence acceleration, however, hides the fact that computing the full LU-decomposition as well as the solution of $\mathbf{P}_\sigma\widehat{\mathbf{p}} = \mathbf{p}$ is, due to the number of non-zero entries nnz of $\mathbf{P}_\sigma^{-1}$ (see table 7), excessively costly for general matrices and thus unattractive for our application. Preconditioners based on the incomplete LU-decomposition also show a dramatic increase in convergence speed but do not incur the cost of a full LU-decomposition; ILUT(10,10^{-2}) and ILUT(10,10^{-3}) require 21 and 24 iterations, respectively, to reach a relative residual level of $\|r\|/\|b\| \leq tol_B = 10^{-5}$. Therefore, ILUT-preconditioners represent a class of effective and efficient convergence acceleration techniques.

The size of the fill level p, at least for values within a range that still optimizes memory requirements, does not substantially influence the convergence behavior. Osei-Kuffuor and Saad (2007) report that "the rule of thumb is to take a large [p] value, and use [τ] to control the amount of fill-in. This generally yields good results without compromising memory efficiency." We have identified a fill level $p = 10$ as satisfying this requirement, and we found a drop tolerance $\tau = 0.01 - 0.005$ to be an optimal choice for ILUT(10,τ) in terms of cost-efficiency of our iterative linear solver. The reader is referred to the latter authors as well as to Benzi et al. (2000) for a discussion on tuning ILUT-type preconditioners and on enhancing their performance by using techniques such as reordering.

Results from numerical experiments for supersonic flow about a swept parabolic body (see figure 9) are presented in figure 7(b). As before, ILUT-based preconditioning is found to be capable of dramatically improving the speed of convergence for BiCGStab. The results indicate, however, that this time a larger value of the fill level p is required to obtain a robust

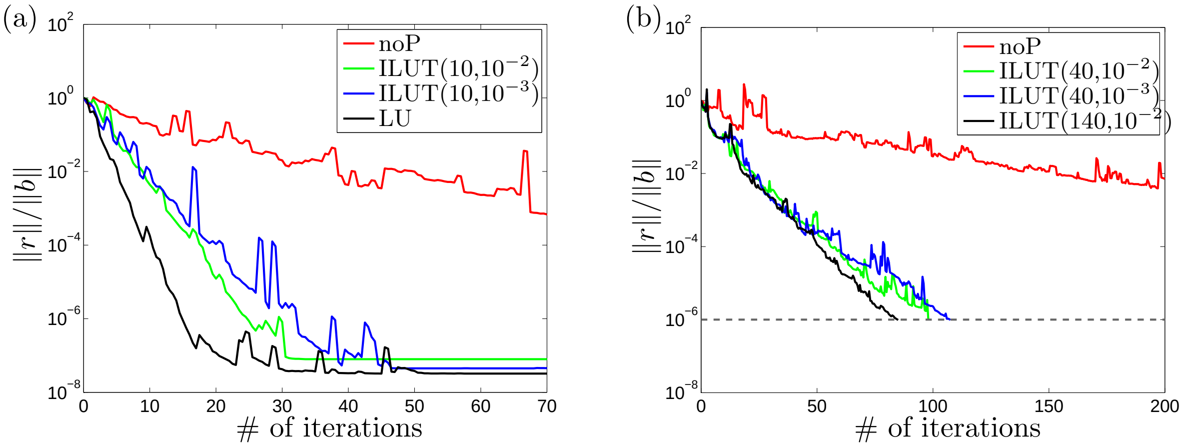

Figure 7. Relative residual as a function of the number of BiCGStab iterations for unpreconditioned (noP stands for "no preconditioner $\mathbf{P}$") and selected preconditioned computations: (a) Config IV with a resolution of 32×201 grid points and (b) convergence results for a more challenging flow case given by supersonic flow about a swept parabolic body (see section §5).

Table 7. Results from performance tests for the simple and the Cayley-preconditioned Arnoldi method showing the number of non-zero entries nnz of $\mathbf{P}_\sigma^{-1}$, the total number of required matrix-vector multiplications (# of matvec), the number of outer iterations of the Arnoldi method (# of outer iterations) and the CPU time; Config IV with a resolution of 32×201 grid points is used (see table 4). For the inexact Cayley-transformation we choose $\sigma = 5\mathrm{i}$, $\mu = 20\mathrm{i}$ and $tol_B = 10^{-5}$.

Method	Ptype	nnz	# of matvec	# of outer iterations	CPU time (h)
IRAM	-	-	338245	13548	13.28
CIRAM	-	-	6252	211	6.65
PCIRAM	ILUT(10,10^{-1})	159263	6909	218	4.10
PCIRAM	ILUT(10,10^{-2})	219977	5777	172	3.58
PCIRAM	ILUT(10,10^{-3})	331412	6286	192	3.89
PCIRAM	ILUK(0)	674532	5242	153	4.06
PCIRAM	ILUK(1)	1891106	5587	175	5.60

preconditioner; again, a drop tolerance $\tau = 0.01 - 0.005$ seems to be an appropriate choice.

In table 7 we provide details on the performance tests for the (simple) implicitly restarted Arnoldi method (IRAM) as well as variants of the Cayley-transformed IRAM. This table contains the number of non-zero entries nnz of $\mathbf{P}_\sigma^{-1}$, the total number of matrix-vector multiplications (# of matvec), the number of outer iterations of the Arnoldi method (# of outer iterations) and the CPU time. It is found that ILU-based preconditioning techniques can be successfully applied to increase the efficiency of the global stability solver and that PCIRAM with ILUT-based preconditioning performs best in terms of CPU time.

5.1.5 *Preconditioned spectra*

Finally, to judge the effectiveness of the applied preconditioners we extract the product of $\mathbf{P}_\sigma^{-1}$ and the high-order system matrix $\mathbf{A}$ using the finite difference approximation

$$\mathbf{M}(:,i) = \mathbf{A}\mathbf{P}_\sigma^{-1}\mathbf{e}_i \approx \frac{\mathbf{F}_{high}(\phi_0 + \epsilon\mathbf{P}_\sigma^{-1}\mathbf{e}_i) - \mathbf{F}_{high}(\phi_0)}{\epsilon} \qquad \text{with} \qquad i = 1, 2, \ldots, n, \tag{5.3}$$

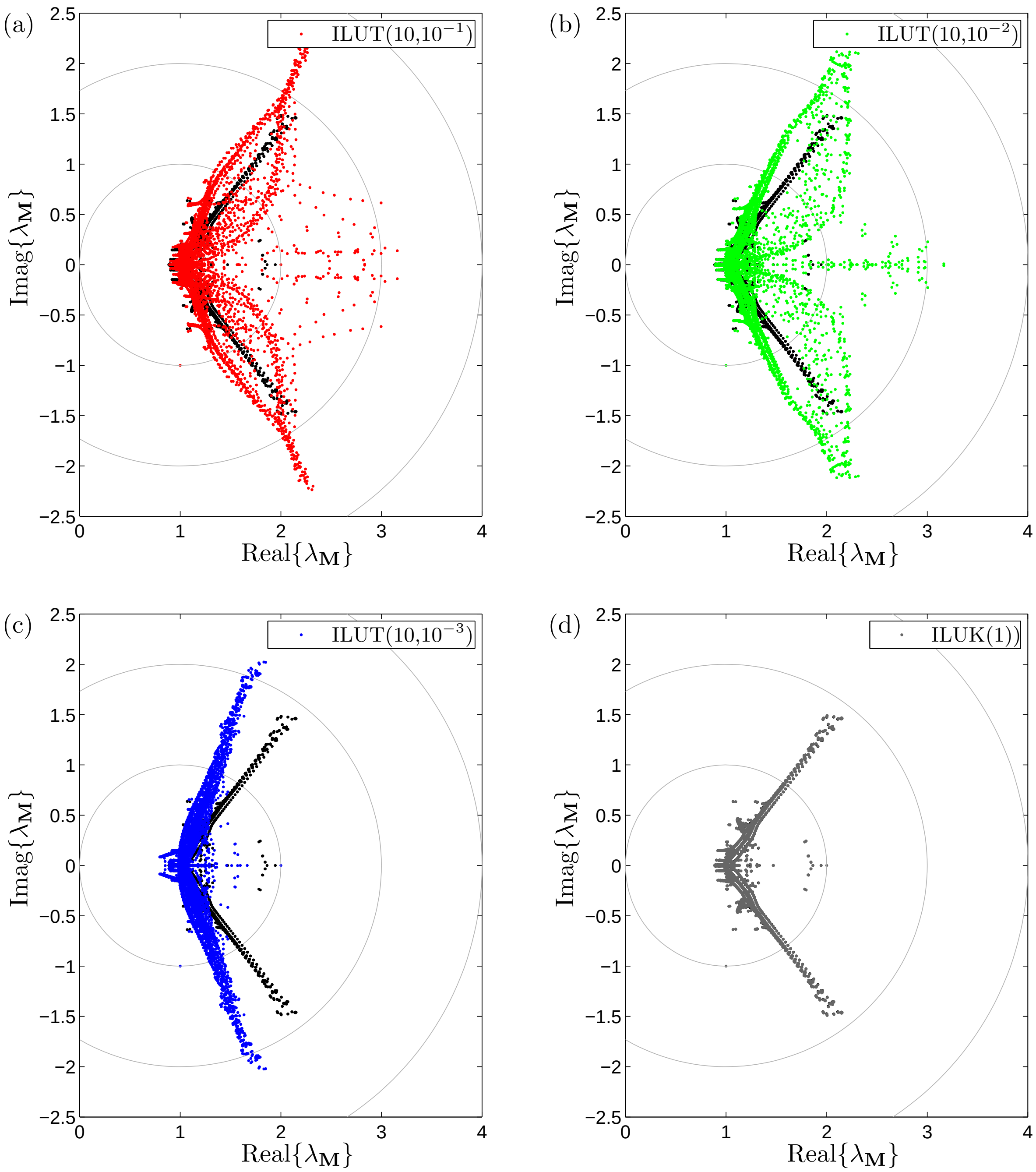

Figure 8. Spectra of $\mathbf{M}_\sigma$ for selected ILU-based preconditioning techniques. The spectrum in black denotes the LU-preconditioned case.

and compute the eigenvalues $\lambda_{\mathbf{M}}$ of $\mathbf{M}_\sigma = \mathbf{M} - \sigma \mathbf{P}_\sigma^{-1}$. The notation $\mathbf{M}(:, i)$ stands for the i-th column of the matrix $\mathbf{M} \in \mathbb{C}^{n \times n}$, and the above expression is analogous to equation (4.5). The asymptotic convergence behavior of the preconditioned system can then be deduced from how closely the eigenvalues of $\mathbf{M}_\sigma$ cluster about one — the ideal spectrum.

In figure 8 we present the spectra of $\mathbf{M}_\sigma$ for four preconditioners employed in the previous subsection (see table 7), where a parameter value of $\epsilon_0 = 10^{-8}$ and a shift parameter $\sigma = 5\mathrm{i}$ have been used. The resolution was decreased to 8×201 grid points in order to be able to perform a (complete) eigenvalue decomposition. The spectrum based on a complete LU decomposition (in black) is used as a reference to assess the quality of four ILU-based preconditioners. It is

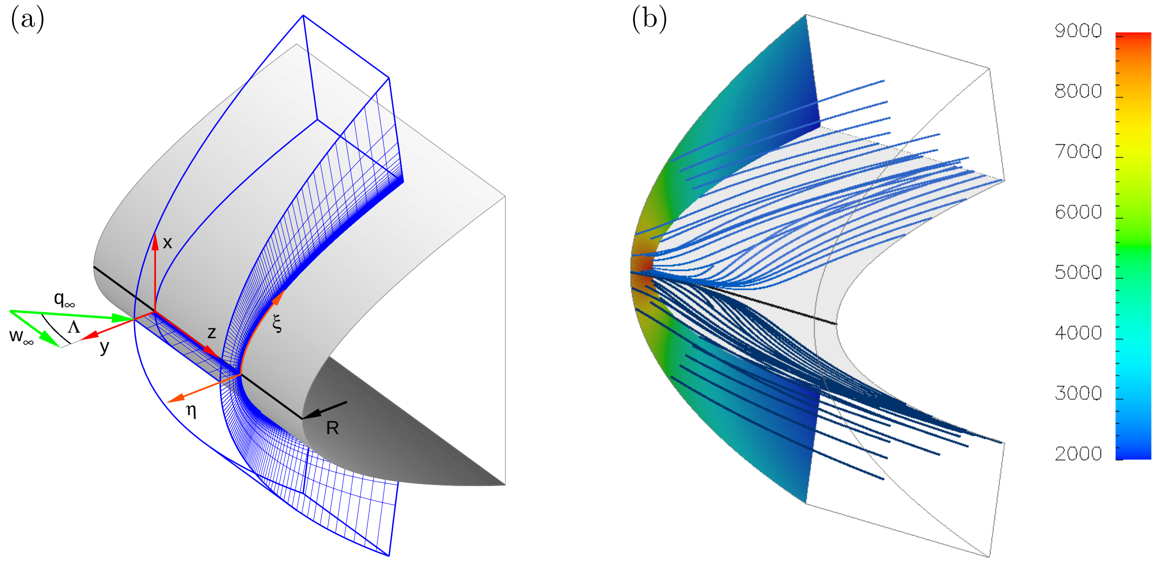

Figure 9. (a) Sketch of the three-dimensional flow configuration showing the relevant flow parameters, the used coordinate systems and the grid-point distribution. The quantities R, q_∞, Λ and w_∞ denote respectively the leading-edge radius of the parabolic body, the freestream velocity, the sweep angle and the resulting sweep velocity. (b) Streamlines (in blue) and pressure field in [Pa] of the computed steady base flow for a sweep Reynolds number $Re_s = w_\infty \delta/\nu_r = 800$ and a sweep Mach number $Ma_s = w_\infty/c_\infty = 1.25$. The resolution is 128×255 points in the normal η-direction and the chordwise ξ-direction. The spanwise z-direction is assumed periodic.

found that decreasing the drop tolerance in ILUT(p,τ) from $\tau = 10^{-1}$ to 10^{-3} (see figure 8a–c) leads to more spectral clustering about one and, as a consequence, to an increase in convergence speed of the preconditioned BiCGStab (see figure 7a). The configuration ILUK(1) displays the best spectral properties (see figure 8d). This preconditioning technique comes, however, at the expense of more floating-point operations (represented by a larger computational time) due to a larger number of non-zero entries nnz of $\mathbf{P}_\sigma^{-1}$ (see table 7).

5.2. *Example 2: supersonic flow about a swept parabolic body*

We will now turn our attention to the second example which describes supersonic flow about a swept parabolic body. In this configuration the flow impinges through a bow shock onto the body forming a local stagnation flow near the attachment line which further downstream turns into a three-dimensional curved boundary-layer flow. It thus should not come as a surprise that this flow comprises a multitude of instability features that will also be reflected in the full global spectrum. There exists an abundance of literature (e.g. Spalart, 1988; Balakumar and Malik, 1992; Joslin, 1995; Saric et al., 2003; Mack et al., 2008) that provides evidence for the following characteristic properties regarding the perturbation dynamics: (i) inside the boundary layer boundary-layer modes are present which can be divided into distinct structures near the stagnation line and a region further downstream; (ii) as a result of compressibility acoustic modes will appear; (iii) the interaction between the moving bow shock and the boundary layer might give rise to a special type of instabilities; (iv) finally, wave packet modes propagating near the edge of the boundary layer describe the convective nature of the flow. As we have previously seen for the compressible mixing layer, the mere existence of acoustic modes has put considerable strain on the global stability analysis which necessitated the use of additional tools such as a Cayley transformation and preconditioning to extract pertinent stability information from the direct numerical simulations (DNS). With its even more complex stability features, supersonic flow about a swept parabolic body requires to an even greater extent the incorporation of such tools into an effective, robust and efficient DNS-based global stability solver. Without these

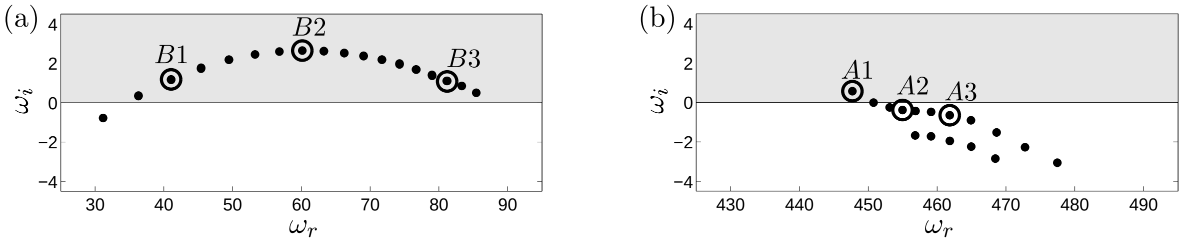

Figure 10. Subsets of the full global spectrum (for $\beta = 0.314$) computed with our proposed global stability solver ($m = 80$, $k = 32$, $tol_A = 10^{-4}$, $\epsilon_0 = 10^{-8}$; the linear solver tolerance was chosen as $tol_B = 10^{-5}$ and BiCGStab was preconditioned using ILUT(40,10^{-2})): (a) most unstable boundary-layer modes and (b) eigenvalues belonging to acoustic modes.

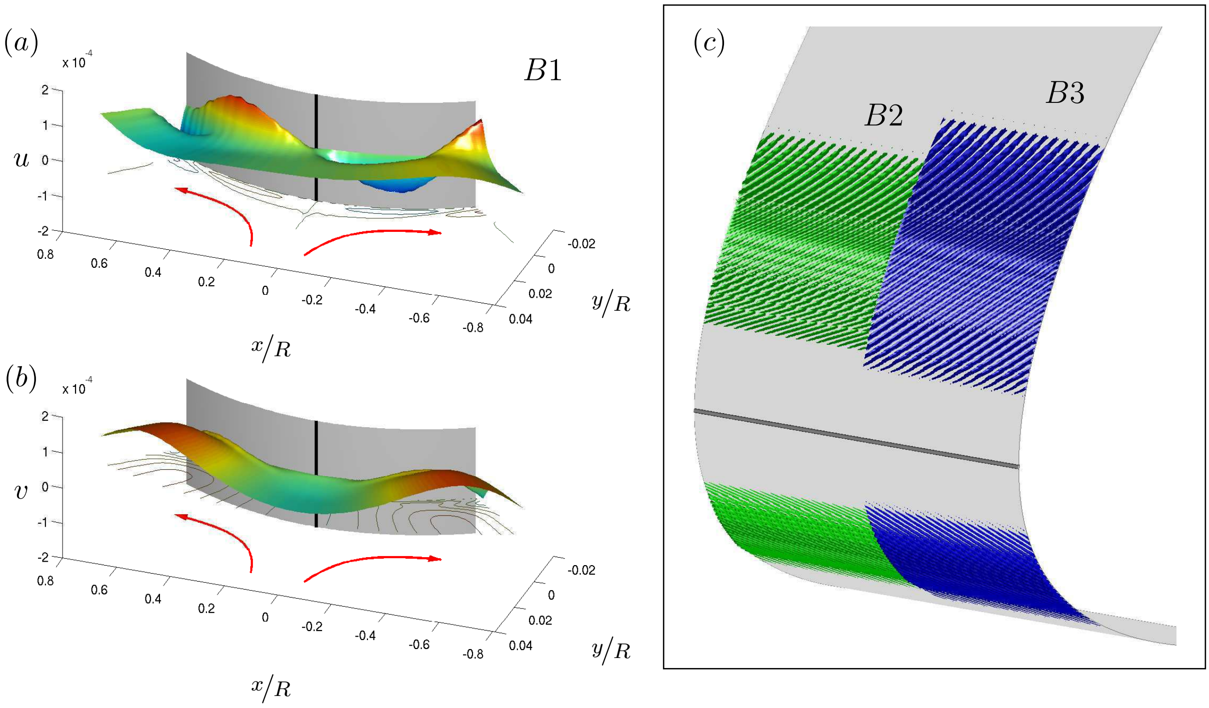

Figure 11. Spatial structure of a sample of associated global boundary-layer modes: (a,b) shape of the chordwise and the normal velocity component u and v, respectively, of a slow-moving boundary-layer mode ($B1$) in the x-y-plane near the attachment line; (c) shape of two faster-moving modes ($B2$, $B3$) displayed by iso-surfaces of the normal velocity v.

tools certain parts of the global spectrum will simply not be accessible, and a complete picture of the full perturbation dynamics of this flow would be out of reach.

Our direct numerical simulations are based on the same implementation as used before for the compressible mixing layer; in addition, a moving curvi-linear grid and shock-fitting techniques have been incorporated (for the details the reader is referred to, Mack et al., 2008). The geometric configuration, the computational grid and some of the relevant flow parameters (see caption) are displayed in figure 9(a); the computed base flow is illustrated in figure 9(b). This steady base flow $\boldsymbol{\phi}_0$ is used in equation (3.5) to compute the approximate action of the linearized operator onto a perturbation field $\boldsymbol{\phi}'$ within our Jacobian-free framework.

The results from a global linear stability analysis of the above-described flow are presented in figure 10. It shows two subsets of the global spectrum corresponding to (a) slow-moving boundary-layer modes ($30 \lesssim \omega_r \lesssim 90$) and to (b) fast-moving acoustic modes ($445 \lesssim \omega_r \lesssim 480$). The associated global modes displaying the spatial structure of the modal perturbation are shown

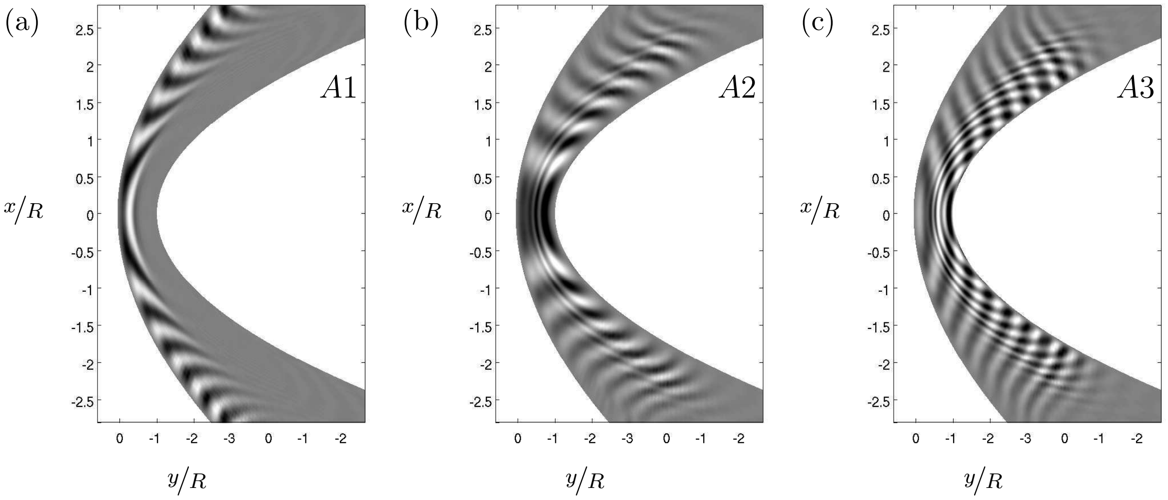

Figure 12. Spatial structure of a sample of associated global acoustic modes visualized by the pressure p in the x-y-plane: (a) unstable mode ($A1$) and (b) faster-moving stable modes ($A2$, $A3$).

in figure 11 and 12 for a representative sample of eigenvalues from each of the two instability mechanisms mentioned above. Global modes belonging to unstable boundary-layer modes are plotted in figure 11, and in (a,b) we display the spatial structure of a slow-moving boundary-layer mode near the attachment line. A typical polynomial dependence of the chordwise velocity u can clearly be detected in the vicinity of the attachment line, which agrees with results from local stability theory reported, e.g., in Theofilis et al. (2003) and Obrist and Schmid (2003). This initially two-dimensional mode gradually merges into a three-dimensional one until the vortical structures nearly align with the external streamlines resulting in co-rotating vortices (see figure 11c). Stable and unstable acoustic global modes are presented in figure 12. The unstable mode ($A1$) shows a dominant spatial structure downstream of the bow shock (a), while the more stable modes ($A2$, $A3$) exhibit smaller spatial structures which extend into the boundary layer (c).

These results clearly demonstrate that our DNS-based global stability solver is capable of producing hydrodynamic stability information for flow configurations as complicated as the above. It further instills confidence that similar findings can be obtained for flow situations that are dominated by a wide range of spatial and temporal scales as well as multi-physics phenomena.

6 Discussion and Conclusions

A DNS-based iterative stability solver has been developed and successfully applied to study the hydrodynamic global stability of a compressible mixing layer and a supersonic flow about a swept parabolic body. In general, this combination of modern iterative techniques such as the implicitly restarted Arnoldi method (IRAM) and direct numerical simulations (DNS) using a Jacobian-free formulation readily enables global stability analyses of complex flows for which the underlying computations faithfully and accurately capture the dominant physical processes. For flows that are characterized by multi-physics features or a wide range of temporal and spatial scales a mapping such as the Cayley transformation is required to access specific parts of the full global spectrum and to ensure the convergence of the global stability solver. Preconditioning is further mandatory to robustify the stability solver and to enhance its performance. Among the class of ILU-based techniques, ILUT was found to perform best.

For large-scale applications where a parallel computing approach is necessary or desirable the proposed global stability solver can be parallelized in a straightforward manner. For a successful application of a parallel version of the underlying DNS-code the reader is referred to Schulze et al. (2009); for a parallel implementation of the employed implicitly restarted Arnoldi method (IRAM), the publically available software package PARPACK (Maschhoff and Sorensen, 1996) provides parallelization details. Only the ILU-based preconditioning technique might be difficult to optimize for parallel environments.

Even though, the presented hydrodynamic global stability solver has been designed to treat complex stability problems it should be kept in mind that the interaction of multi-physical processes and numerical convergence behavior leads to a complicated dynamics which requires the careful adjustment of the governing parameters to obtain robust solutions. The appropriate choice of parameters has to be equally based on a physical understanding of the flow and a familiarity with the convergence behavior of the iterative methods. For this reason, each flow configuration under investigation has its inherent dynamical properties, and the question of proper parameter choices for a robust convergence of the global stability solver has to be answered anew.

Acknowledgments

Financial support from the Deutsche Forschungsgemeinschaft (DFG), the Studienstiftung des Deutschen Volkes, the Alexander-von-Humboldt Foundation and the ANR program “chaires d’excellence” is gratefully acknowledged. Olivier Marquet is thanked for his insightful comments on the manuscript.

References

Adams, N. A. and Shariff, K. (1996). A high-resolution hybrid compact-ENO scheme for shock-turbulence interaction problems. *J. Comput. Phys.*, 127:27–51.

Arbenz, P., Hetmaniuk, U. L., Lehoucq, R. B., and Tuminaro, R. S. (2005). A comparison of eigensolvers for large-scale 3D modal analysis using AMG-preconditioned iterative methods. *Int. J. Numer. Meth. Engng.*, 64:204–236.

Bai, Z. (1992). Progress in the numerical solution of the nonsymmetric eigenvalue problem. *Num. Lin. Alg. Appl.*, 2(3):219–234.

Balakumar, P. and Malik, M. R. (1992). Discrete modes and continuous spectra in supersonic boundary layers. *J. Fluid Mech.*, 239:631–656.

Benzi, M. (2002). Preconditioning Techniques for Large Linear Systems: A Survey. *J. Comput. Phys.*, 182:418–477.

Benzi, M., Haws, J. C., and Tůma, M. (2000). Preconditioning highly indefinite and nonsymmetric matrices. *SIAM J. Sci. Comput.*, 22:1333–1353.

Blumen, W. (1970). Shear layer instability of an inviscid compressible fluid. *J. Fluid Mech.*, 40(4):769–781.

Burroughs, E. A., Romero, L. A., Lehoucq, R. B., and Salinger, A. G. (2004). Linear stability of flow in a differentially heated cavity via large-scale eigenvalue calculations. *Int. Journal of Num. Meth. for Heat & Fluid Flow*, 14:803–822.

Crouch, J. D., Garbaruk, A., and Magidov, D. (2007). Predicting the onset of flow unsteadiness based on global instability. *J. Comput. Phys.*, 224(2):924–940.

Crouch, J. D., Garbaruk, A., Magidov, D., and Travin, A. (2009). Origin of transonic buffet on aerofoils. *J. Fluid Mech.*, 628:357–369.

Edwards, W. S., Tuckerman, L. S., Friesner, R. A., and Sorensen, D. C. (1994). Krylov methods for the incompressible Navier–Stokes equations. *J. Comput. Phys.*, 110:82–102.

Ericsson, T. and Ruhe, A. (1980). The spectral transformation Lánczos method for the numerical solution of large sparse generalized symmetric eigenvalue problems. *Math. Comp.*, 35(152):1251–1268.

Freund, R. W. (1993). A transpose-free quasi-minimal residual algorithm for non-Hermitian linear systems. *SIAM J. Sci. Comput.*, 14(2):470–482.

Füllenbach, T. and Stüben, K. (2002). Algebraic multigrid for selected PDE systems. In *Elliptic and Parabolic Problems*, pages 399–410.

Garratt, T. J., Moore, G., and Spence, A. (1993). A generalised Cayley transform for the numerical detection of Hopf bifurcations in large systems. In *Contributions in numerical mathematics*, volume 2 of *World Sci. Ser. Appl. Anal.*, pages 177–195. World Sci. Publishing.

Heeg, R. S. and Geurts, B. J. (1998). Spatial instabilities of the incompressible attachment-line flow using sparse matrix Jacobi–Davidson techniques. *Applied Scientific Research*, 59:315–329.

Joslin, R. D. (1995). Direct simulation of evolution and control of three-dimensional instabilities in attachment-line boundary layers. *J. Fluid Mech.*, 291:369–392.

Kitsios, V., Rodriguez, D., Theofilis, V., Ooi, A., and Soria, J. (2009). BiGlobal stability analysis in curvilinear coordinates of massively separated lifting bodies. *J. Comput. Phys.*, 228(19):7181–7196.

Knoll, D. A. and Keyes, D. E. (2004). Jacobian-free Newton–Krylov methods: a survey of approaches and applications. *J. Comput. Phys.*, 193(2):357–397.

Le Duc, A., Sesterhenn, J., and Friedrich, R. (2006). Instabilities in compressible attachment-line boundary layers. *Phys. Fluids*, 18(044102).

Lehoucq, R. B. and Meerbergen, K. (1998). Using generalized Cayley transformations within an inexact rational Krylov sequence method. *SIAM J. Matrix Anal. Appl.*, 20(1):131–148 (electronic).

Lehoucq, R. B. and Salinger, A. G. (2001). Large-scale eigenvalue calculations for stability analysis of steady flows on massively parallel computers. *Int. J. Numer. Meth. Fluids*, 36:309–327.

Lehoucq, R. B. and Scott, J. A. (1996). An evaluation of software for computing eigenvalues of sparse nonsymmetric matrices. *Preprint MCS-P547-1195, Argonne National Laboratory, Argonne, IL.*

Lehoucq, R. B., Sorensen, D. C., and Yang, C. (1998). *ARPACK Users' Guide.* Software, Environments, and Tools. Society for Industrial and Applied Mathematics (SIAM), Philadelphia, PA. Solution of Large-Scale Eigenvalue Problems with Implicitly Restarted Arnoldi Methods.

Lele, S. K. (1992). Compact finite difference schemes with spectral-like resolution. *J. Comput. Phys.*, 103:16–42.

Mack, C. J. and Schmid, P. J. (2009). Direct numerical simulations of hypersonic flow about a swept parabolic body. *Comput. Fluids.* submitted.

Mack, C. J., Schmid, P. J., and Sesterhenn, J. L. (2008). Global stability of swept flow around a parabolic body: connecting attachment-line and crossflow modes. *J. Fluid Mech.*, 611:205–214.

Maschhoff, K. J. and Sorensen, D. C. (1996). A portable implementation of ARPACK for distributed memory parallel architectures. In *Copper Mountain Conference on Iterative Methods*. SIAM.

Meerbergen, K. and Roose, D. (1997). The restarted Arnoldi method applied to iterative linear system solvers for the computation of rightmost eigenvalues. *SIAM J. Matrix Anal. Appl.*, 18(1):1–20.

Michalke, A. (1964). On the inviscid instability of the hyperbolic-tangent velocity profile. *J. Fluid Mech.*, 19:543–556.

Morgan, R. B. (1996). On restarting the Arnoldi method for large non-symmetric eigenvalue problems. *Math. Comp.*, 65(215):1213–1230.

Morzynski, M., Afanasiev, K., and Thiele, F. (1999). Solution of the eigenvalue problems resulting from global non-parallel flow stability analysis. *Comput. Methods Appl. Mech. Engrg.*, 169:161–176.

Nejat, A. and Ollivier-Gooch, C. (2008). Effect of discretization order on preconditioning and convergence of a high-order unstructured Newton-GMRES solver for the Euler equations. *J. Comput. Phys.*, 227:2366–2386.

Obrist, D. and Schmid, P. J. (2003). On the linear stability of swept attachment-line boundary layer flow. Part 1. Spectrum and asymptotic behaviour. *J. Fluid Mech.*, 493:1–29.

Osei-Kuffuor, D. and Saad, Y. (2007). A comparison of preconditioners for complex-valued matrices. Technical report, University of Minnesota Supercomputing Institute Research Report UMSI 2007/139.

Robinet, J.-C. (2007). Bifurcations in shock-wave/laminar-boundary layer interaction: global instability approach. *J. Fluid Mech.*, 579:85–112.

Saad, Y., editor (2003). *Iterative Methods for Sparse Linear Systems, Second Edition*. Society for Industrial and Applied Mathematics.

Saad, Y. and Schultz, M. H. (1986). GMRES: a generalized minimal residual algorithm for solving nonsymmetric linear systems. *SIAM J. Sci. Stat. Comput.*, 7(3):856–869.

Saric, W. S., Reed, H. L., and White, E. B. (2003). Stability and transition of three-dimensional boundary layers. *Annu. Rev. Fluid Mech.*, 35:413–440.

Schmid, P. J. and Henningson, D. S. (2001). *Stability and transition in shear flows*, volume 142 of *Applied Mathematical Sciences*. Springer.

Schulze, J., Schmid, P. J., and Sesterhenn, J. L. (2009). Exponential time integration using Krylov subspaces. *Int. J. Num. Meth. Fluids*, 60(6):591–609.

Sesterhenn, J. L. (2001). A characteristic-type formulation of the Navier–Stokes equations for high-order upwind schemes. *Comput. Fluids*, 30:37–67.

Sorensen, D. C. (1992). Implicit application of polynomial filters in a k-step Arnoldi method. *SIAM J. Matrix Anal. Appl.*, 13(1):357–385.

Sorensen, D. C. (2002). Numerical methods for large eigenvalue problems. *Acta Numer.*, 11:519–584.

Spalart, P. R. (1988). Direct numerical study of leading-edge contamination. In *AGARD-CP-438*, pages 5/1–5/13.

Theofilis, V. (2003). Advances in global linear instability analysis of nonparallel and three-dimensional flows. *Prog. Aero. Sci.*, 39:249–315.

Theofilis, V. and Colonius, T. (2004). Three-dimensional instabilities of compressible flow over open cavities: direct solution of the BiGlobal eigenvalue problem. *AIAA Paper*, 2004-2544.

Theofilis, V., Fedorov, A., Obrist, D., and Dallmann, U. C. (2003). The extended Görtler–Hämmerlin model for linear instability of three-dimensional incompressible swept attachment-line boundary layer flow. *J. Fluid Mech.*, 487:271–313.

Trottenberg, U., Oosterlee, C. W., and Schüller, A. (2000). *Multigrid.* Academic Press, London.

Tuckerman, L. S., Bertagnolio, F., Daube, O., LeQuéré, P., and Barkley, D. (2000). Stokes preconditioning for the inverse Arnoldi method. *Notes on Numerical Fluid Mechanics*, 74:241–255.

van der Vorst, H. A. (1992). Bi-CGSTAB: A fast and smoothly converging variant of Bi-CG for the solution of non-symmetric linear systems. *SIAM J. Sci. Statist. Comput.*, 13:631–644.

Zhang, J. (2000). Preconditioned Krylov subspace methods for solving nonsymmetric matrices from CFD applications. *Comput. Methods Appl. Mech. Engrg.*, 189:825–840.

Article 3

Global stability of swept flow around a parabolic body: connecting attachment-line and crossflow modes

By C. J. Mack[1,2], P. J. Schmid[2] and J. L. Sesterhenn[1]

[1]Department of Numerical Mathematics, Universität der Bundeswehr (UniBw),
D-85577 Munich, Germany

[2]Laboratoire d'Hydrodynamique (LadHyX), CNRS-École Polytechnique,
F-91128 Palaiseau, France

Published in *J. Fluid Mech.* (2008), **611**, pp. 205–214

The global linear stability of a three-dimensional compressible flow around a yawed parabolic body of infinite span is investigated using an iterative eigenvalue method in conjunction with direct numerical simulations. The computed global spectrum shows an unstable branch consisting of three-dimensional boundary layer modes whose amplitude distributions exhibit typical characteristics of both attachment-line and crossflow modes. In particular, global eigenfunctions with smaller phase velocities display a more pronounced structure near the stagnation line, reminiscent of attachment-line modes while still featuring strong crossflow vortices further downstream. This analysis establishes a link between the two prevailing instability mechanisms on a swept parabolic body which, so far, have only been studied separately and locally. A parameter study shows maximum modal growth for a spanwise wavenumber of $\beta = 0.213$, suggesting a preferred disturbance length scale in the sweep direction.

1 Introduction

The aerodynamic design of high-performance aircraft crucially depends on a sound understanding of the compressible flow around swept wings. The details of the transition process from laminar to turbulent fluid motion play a dominant role in the description of this flow. Two instability mechanisms have been suggested to trigger transition: the amplification of perturbations in the swept attachment-line boundary layer and of crossflow vortices in the three-dimensional boundary layer further downstream. These two instability mechanisms have been studied *separately*, despite a general acknowledgment that they coexist under realistic conditions. The subdivision of the flow configuration and the resulting separate treatment of these two instability mechanisms has been a necessary simplification of the complex flow problem in order to treat it with classical tools of hydrodynamic stability theory. Owing to the recent progress in computational resources and in global stability analysis, however, we are now able to address a more realistic configuration that covers *simultaneously* attachment-line and crossflow vortex instabilities. Note, however, that the notion of two independent instability mechanisms has more of an historical than a physical origin.

First evidence for the interaction of instabilities near the leading edge with the crossflow vortices further downstream came from the experiments of Gray (1952). He found that by increasing the sweep angle, the location where the onset of transition was observed moved toward the attachment line. In following decades a great number of experimental efforts addressed instability issues for both the attachment-line boundary layer and, even more so, the three-dimensional boundary layer (see Bippes 1999; Saric et al. 2003 for a recent review). Among this body of literature, Poll (1979) was the first to establish a distinction between crossflow-induced transition and transition initiated by leading-edge instabilities. His measurements on an immersed swept cylinder provided motivation for theoretical investigations.

A simplified model of the attachment-line boundary layer was studied by Hall et al. (1984) who demonstrated that this flow becomes linearly unstable to wave-like disturbances propagating along the attachment line. This model was based on swept Hiemenz flow, which represents a similarity solution of the incompressible three-dimensional Navier–Stokes equations for swept attachment-line flow, and the Görtler–Hämmerlin assumption, which takes the same linear x-dependence for the perturbation and the base flow. Subsequently, Lin and Malik (1996) discarded the restrictive Görtler–Hämmerlin assumption and uncovered additional linearly unstable modes. They extended their analysis to compressible flows (Lin and Malik, 1995) and also assessed the influence of the leading-edge curvature on flow stability (Lin and Malik, 1997). A recent overview of attachment-line instabilities is given in Le Duc et al. (2006).

Further downstream, the presence of sweep and curvature significantly modifies the flow. An imbalance between centrifugal forces and the streamwise pressure gradient induces curved streamlines throughout the boundary layer, and the resulting crossflow velocity gives rise to stationary or traveling crossflow vortices (Reed and Saric, 1989). In contrast to the attachment-line instability, the crossflow instability is of inviscid type caused by an inflection point in the three-dimensional base velocity profile. Numerous theoretical and numerical efforts have studied the stability of compressible crossflow vortices for planar geometries, based on the parabolized stability equations (e.g. Herbert, 1997) or direct numerical simulations (e.g. Joslin, 1995); for an overview of the relevant literature see Saric et al. (2003) and the references therein.

Despite many studies of each instability, little is known to date about a connection between the two. Starting from incompressible swept Hiemenz flow, Spalart (1988) obtained solutions off the attachment line that are strongly reminiscent of crossflow vortices and thus provide a first indication of a link between them. Bertolotti (1999), using the parabolized stability equations, furnishes strong evidence for a connection between attachment-line instabilities and crossflow vortices. By continuing an attachment-line mode significantly far downstream, he finds a close match – both in terms of growth rate and modal shape – with the least-stable crossflow mode. The structure of the entire mode connecting the attachment line and the crossflow neutral point, however, was not examined.

This lack of a connecting mode as well as the findings above strongly suggest a global treatment of the stability problem without limiting assumptions regarding the geometrical domain of interest. Such an investigation allows the simultaneous treatment of the attachment-line instability and crossflow vortices. Modern techniques such as iterative eigenvalue methods (Edwards et al., 1994) in conjunction with direct numerical simulations based on higher-order spatial discretization schemes provide the necessary tools to address the global stability problem. In this article, we present results from a global stability analysis of compressible flow around a swept parabolic body which demonstrate a connection between the two prevailing local instability mechanisms.

2 Flow configuration, governing parameters and numerical method

The flow configuration, as displayed in figure 1, consists of a parabolic body (in grey) about which a three-dimensional body-fitted grid (in blue) is mapped. The local Cartesian coordinate

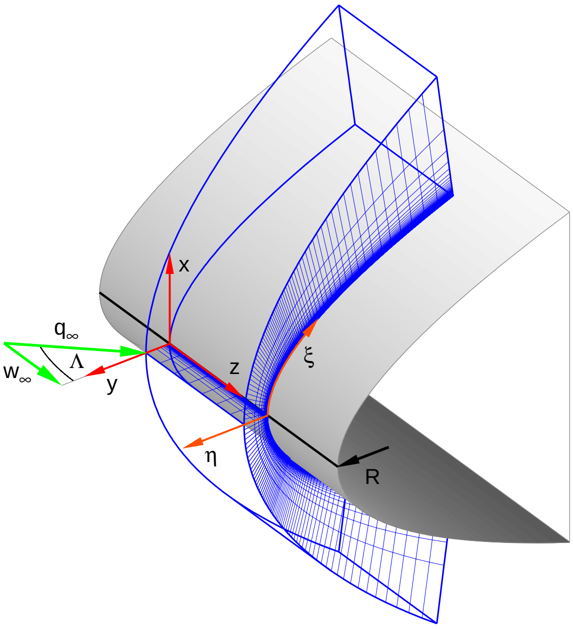

Figure 1. Sketch of the three-dimensional flow configuration showing the relevant flow parameters, the coordinate systems and the grid-point distribution.

system (in red) is given by the x-direction, the y-direction and the spanwise z-direction pointing along the attachment line (in black), and the local parabolic coordinate system (in orange) consists of the chordwise ξ-direction and the normal η-direction pointing along grid lines in the downstream direction and normal to the wall, respectively. The leading-edge radius of the parabolic body is denoted by R. The incoming flow impinges on the body with a velocity q_∞ and a sweep angle Λ yielding a sweep velocity w_∞ and a wall-normal velocity v_∞. The subscript $_\infty$ refers to the flow state downstream of a detached bow shock which acts as the inflow boundary.

We define a viscous length scale δ, a sweep Reynolds number Re_s and a sweep Mach number Ma_s as

$$\delta = \left(\frac{\nu_r}{S}\right)^{1/2}, \qquad Re_s = \frac{w_\infty \delta}{\nu_r}, \qquad Ma_s = \frac{w_\infty}{c_\infty}, \tag{2.1}$$

respectively, where ν_r denotes the kinematic viscosity evaluated at recovery temperature, S is the strain rate at the wall, at the attachment line ($x = 0$), and c_∞ is the speed of sound. Alternatively, the Reynolds number Re_s can be reformulated to display an explicit dependence on the leading-edge radius R and the sweep angle Λ. We obtain (in accordance with Lin and Malik, 1997, up to a scaling factor)

$$Re_s = \left(\frac{v_\infty R}{2\nu_r}\right)^{1/2} \tan\Lambda. \tag{2.2}$$

We consider the motion of a compressible fluid modeled as a perfect gas with constant specific heat ratio $\gamma = 1.4$ and constant Prandtl number $Pr = 0.71$. The compressible Navier–Stokes equations, the equation of state, Fourier's law for the thermal conductivity and Sutherland's law (at ambient conditions) for the viscosity fully describe the flow. The equations are formulated based on pressure p, Cartesian velocities (u, v, w) and entropy s and are solved on a time-dependent, curvilinear and non-uniformly distributed grid, with a clustering of the grid points towards the wall as well as in the leading-edge region, as shown in figure 1. The governing equations are discretized using fifth- and fourth-order compact difference schemes for the inviscid and viscous terms, respectively, and a resolution of 128 × 255 points was used to resolve the characteristic length scales of the eigenmodes with more than six points in the normal η-direction and approximately four points in the chordwise ξ-direction. The temporal discretization is accomplished by a fourth-order Runge–Kutta scheme (see Sesterhenn, 2001; Le Duc et al., 2006, for details).

In the wall-normal direction, the computational domain is limited by a detached unsteady bow shock which is incorporated through a shock-fitting mechanism (Fabre et al., 2001) and provides the inflow conditions via the Rankine–Hugoniot relations (see Oswatitsch, 1956). Along the surface of the body no-slip boundary conditions and adiabatic wall conditions are applied. At the chordwise edges of the computational domain, non-reflecting outflow boundary conditions are imposed and, under the assumption of infinite span, periodic boundary conditions are used in the z-direction.

3 Global stability analysis

The two-dimensional base flow $\phi_0(x,y)$ is stable to two-dimensional perturbations, which allows a simple time-integration toward a steady state and avoids more sophisticated methods such as Newton iteration, arclength continuation or selective filter techniques to compute the steady state. The obtained base flow forms the foundation for the subsequent global stability analysis and is displayed, in terms of streamlines and pressure field, in figure 2. The complexity of the base flow requires a global stability approach since the x- and y-coordinate directions can no longer be separated. For this reason, a three-dimensional small-amplitude perturbation $\phi'(x,y,z,t)$ is superimposed on the base flow, and the traveling-wave form

$$\phi'(x,y,z,t) = \widetilde{\phi}(x,y)\mathrm{e}^{\mathrm{i}(\beta z - \omega t)} \tag{3.3}$$

is assumed. In this expression, $\widetilde{\phi}(x,y)$ denotes the complex amplitude and β the real spanwise wavenumber of the perturbation. The temporal long-term evolution of this disturbance is characterized by ω whose real part describes the frequency ω_r with the imaginary part as the corresponding growth rate ω_i.

Under these assumptions, the global stability problem can formally be written as

$$\omega\ \widetilde{\phi} = \mathcal{J}(\phi_0)\ \widetilde{\phi}, \tag{3.4}$$

where $\mathcal{J}(\phi_0)$ represents the linear stability operator (the Jacobian), i.e. the Navier–Stokes equations linearized about the base state ϕ_0. The direct solution of this eigenvalue problem is prohibitively expensive, and iterative solution techniques have to be employed to extract pertinent stability information. To this end, an m-dimensional Krylov subspace sequence

$$\mathcal{K}_m\{\phi, \mathcal{J}(\phi_0)\} = \mathrm{span}\{\phi,\ \mathcal{J}(\phi_0)\phi,\ \mathcal{J}(\phi_0)^2\phi, \ldots, \mathcal{J}(\phi_0)^{m-1}\phi\}, \tag{3.5}$$

consisting of repeated applications of the Jacobian matrix to a given initial flow field ϕ is used in connection with the Arnoldi method (see Edwards et al. 1994 for applications of iterative techniques in fluid mechanics) to project the full stability problem onto a lower-dimensional system. The resulting lower-dimensional Hessenberg matrix together with an orthonormalized basis of the Krylov subspace $\mathcal{K}_m$ can then be used to approximate the spectrum of the linearized compressible Navier-Stokes equations.

The form of the Krylov sequence (3.5) indicates that the Jacobian matrix does not need to be formed explicitly; rather, only matrix–vector products are necessary to build the reduced system. Such products are readily obtained from direct numerical simulations via

$$\mathcal{J}(\phi_0)\phi \approx \frac{\mathcal{F}(\phi_0 + \epsilon\phi) - \mathcal{F}(\phi_0)}{\epsilon}, \tag{3.6}$$

where ϵ is a small parameter, chosen as $||\epsilon\phi||/||\phi_0|| = 10^{-8}$, and $\mathcal{F}$ represents the nonlinear Navier–Stokes equations. The independence of the results with respect to the choice of the

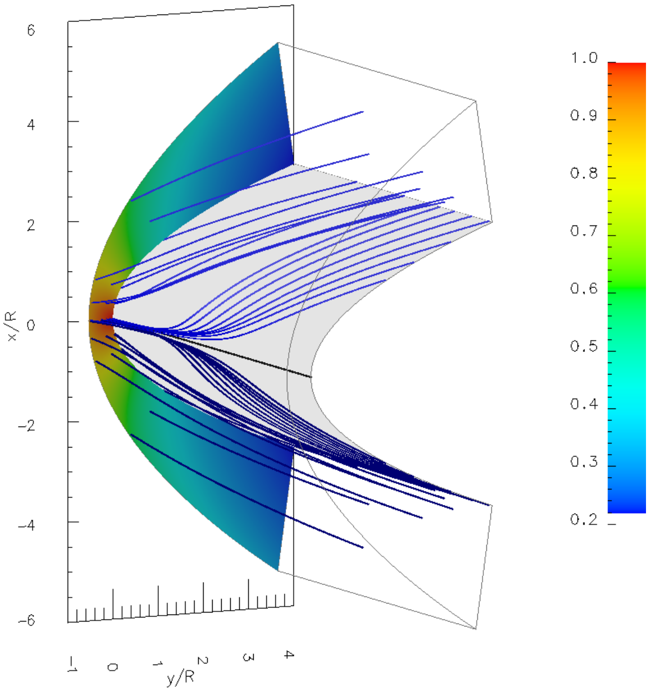

Figure 2. Streamlines (in blue) and pressure field of the computed steady base flow for $Re_s = 800$ and $Ma_s = 1.25$. The pressure has been non-dimensionalized by the stagnation pressure, and a leading-edge radius of $R = 0.1 = 508\delta$ has been used. The resolution is 128×255 points in the normal η-direction and the chordwise ξ-direction, respectively.

parameter ϵ has been corroborated over a range of many decades of the value of ϵ. This approximation allows a Jacobian-free framework where the direct numerical simulation provides the input for the iterative stability solver.

4 Results

The above iterative scheme is applied to simulations of the compressible flow about the parabolic body depicted in figure 1. As the Krylov subspace is augmented by subsequent calls to the direct simulation code, the Arnoldi method provides an approximate spectrum that consequently increases in complexity but also in accuracy.

4.1. *Spectrum and global modes*

The global spectrum reflects the richness of physical processes present in the flow configuration under investigation. It consists of acoustic branches that describe the presence of sound waves, of wavepacket modes that capture the dynamics of perturbations at the edge of the boundary layer, of continuous modes that represent disturbances in the freestream, of modes that account for the interaction of the bow shock with the body's leading-edge region, and of shear modes that express the flow characteristics in the boundary layer. These latter modes are the most unstable ones for the present flow configuration and are the focus of this study.

Concentrating on boundary layer modes, the global stability analysis reveals that, for our flow parameters ($Re_s = 800$, $Ma_s = 1.25$, $\beta = 0.314 = 2\pi/L_z$, with L_z as the fundamental length scale, non-dimensionalized by δ, in the spanwise z-direction), a three-dimensionally unstable discrete branch is present whose disturbance frequencies ω_r range from 41.1 to 81.2 (see figure 3c). The maximum growth rate $\omega_i = 2.64$ is achieved for a frequency $\omega_r = 60.1$. Though barely visible in the figure, the eigenvalues appear double – a consequence of the symmetry properties of the

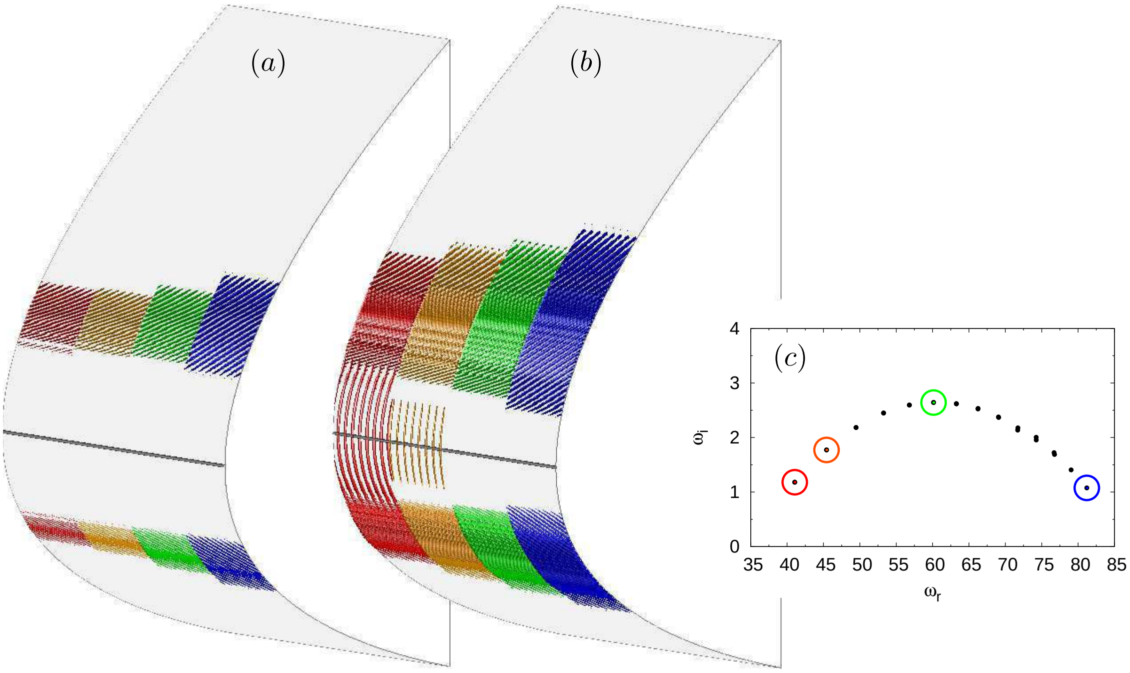

Figure 3. Global stability results of compressible swept flow around a parabolic body ($Re_s = 800$, $Ma_s = 1.25$, $\beta = 0.314 = 2\pi/L_z$): (c) most unstable branch of the temporal spectrum and (a,b) four associated global modes displaying the velocity distribution $v(x,y,z) = \mathrm{Real}\{\widetilde{v}(x,y)\,(\cos\beta z + \mathrm{i}\sin\beta z)\}$ of four eigenvalues depicted by circles in (c). The normalized eigenfunctions are plotted using iso-surfaces with a value of $10^{-2}\ v_{max}$ (a) and $5 \times 10^{-5}\ v_{max}$ (b), and eight wavelengths, stretched by a factor of two, in the spanwise direction are used to visualize each mode (attachment line in black). See text for color coding.

flow. The associated global eigenmodes divide into symmetric and antisymmetric functions with respect to the attachment line.

Figure 3(a,b) displays four global eigenmodes from this branch, visualized by iso-surfaces, with iso-values of $10^{-2}\ v_{max}$ (a) and $5 \times 10^{-5}\ v_{max}$ (b), of the normalized velocity $v(x,y,z) = \mathrm{Real}\{\widetilde{v}(x,y)\,(\cos\beta z + \mathrm{i}\sin\beta z)\}$. They belong to the slowest moving mode (in red), the second slowest moving mode (in orange), the most unstable mode (in green) and the fastest moving mode (in blue). The amplitude distribution of the slowest moving global mode clearly demonstrates a link between the attachment-line and the crossflow dynamics (figure 3b). It convincingly shows that the global modes of the branch depicted in figure 3(c) have typical attachment-line properties while still connecting to the familiar crossflow pattern further downstream from the stagnation line.

For faster moving global eigenfunctions (modes with a higher phase velocity ω_r) the crossflow component is more pronounced and the dominant part of the global mode lies further downstream from the leading edge. At the same time, owing to the increasing base velocity in the boundary layer, global modes with higher phase velocities prevail downstream from the attachment line.

Near the attachment line the global modes display the well-known and well-studied two-dimensional structure consisting of chordwise vortices with a specific spanwise scale. This structure is more pronounced for slower moving modes (see figure 3c). As an example, the spatial shape of the velocity component $v(x,y,z)$ of the slowest moving global mode (see figure 3b in red) is presented in figure 4(a). This mode travels along the attachment line without significant three-dimensional features. It is reminiscent of results from stability computations by Joslin (1995) (see figure 4b) who computed the spatial evolution of three-dimensional disturbances in an incompressible attachment-line boundary layer by direct numerical simulations for the Reynolds number $Re = 570$ and the disturbance frequency $\omega = 0.1249$. The same types of

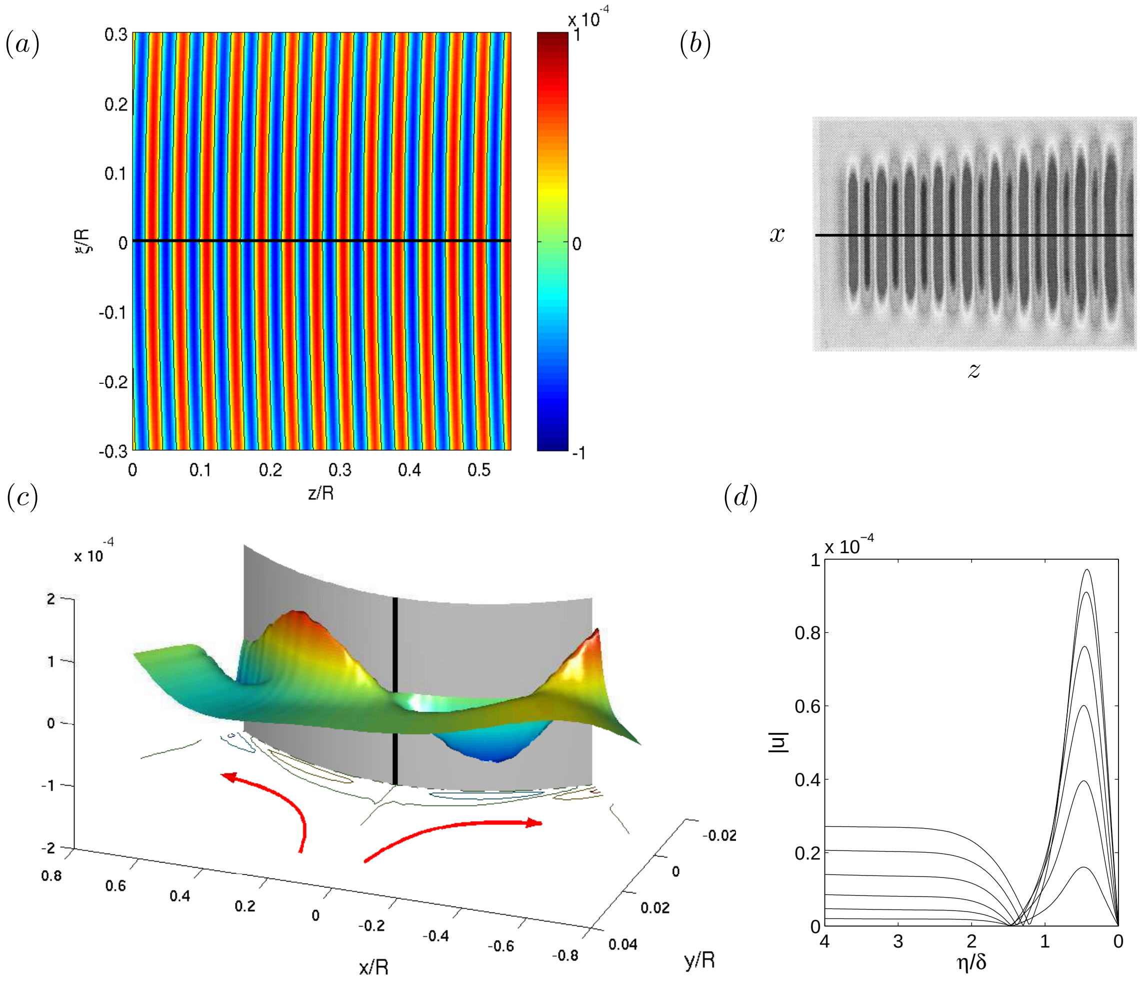

Figure 4. Spatial shape of the slowest moving global mode: (a) top view of the velocity component $v(\xi, \eta, z)$ near the attachment line in the chordwise ξ-direction at half the boundary-layer thickness ($R = 0.1 = 508\delta$); (b) top view of three-dimensional traveling mode $v(x, y, z)$ in an incompressible attachment-line boundary layer as presented by Joslin (1995) for $Re = 570$ and $\omega = 0.1249$ (attachment line in black, relabelled coordinate system). (c) Shape of the velocity component $u(x, y, z)$ in the (x, y)-plane near the attachment line and (d) equispaced cross-cut profiles of $u(\xi, \eta, z)$ at six selected positions in the positive ξ-direction.

structure has been determined by Guégan et al. (2006) in studies of optimal temporal disturbances in swept Hiemenz flow. However, the similarity between these two incompressible results and our compressible result is only of a qualitative nature. Further evidence linking the local behavior of the global mode near the stagnation line to a typical local attachment-line mode is given in figure 4(c) where the characteristic linear dependence in the chordwise direction of the velocity component $u(x, y, z)$ is visible over a significant range along the attachment line before it saturates to connect to the crossflow behavior further downstream. In addition, figure 4(d) displays equispaced cross-cut profiles of $u(\xi, \eta, z)$ at six selected positions in the positive ξ-direction, which closely resemble the corresponding eigenfunction shapes from a solution of a modal stability problem for swept Hiemenz flow.

Further downstream in the chordwise direction, the initially two-dimensional structure of the global mode near the attachment line (see figure 4a) gradually merges into a three-dimensional one (see figure 5a) until the vortical structures nearly align with the external streamlines, resulting in co-rotating vortices (see figure 5b), a feature that is specific to crossflow vortices as described by Reed and Saric (1989).

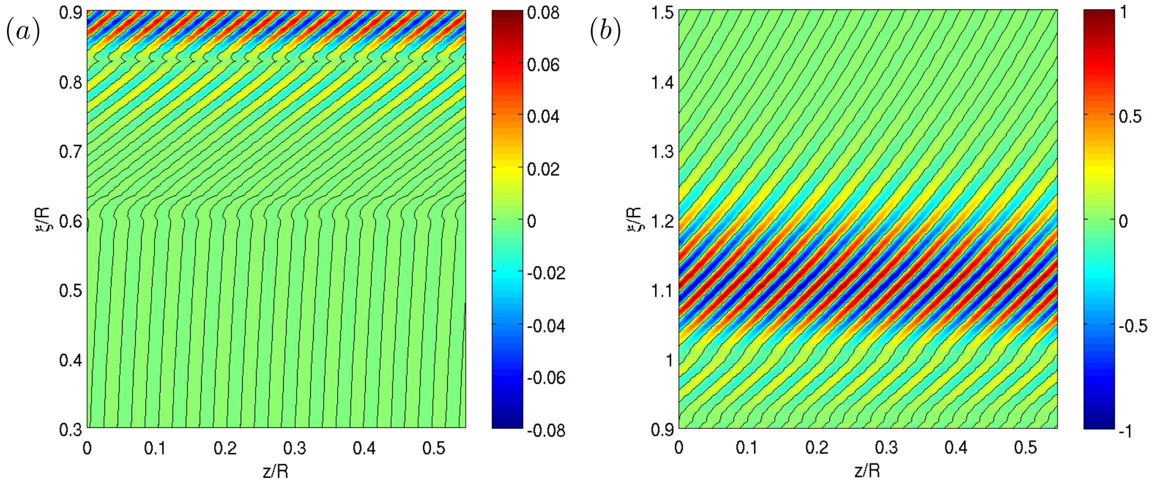

Figure 5. Spatial shape of the velocity component $v(\xi, \eta, z)$ of the slowest moving global mode in a body-fitted cut at half the boundary-layer thickness: (a) structure in the connection region and (b) structure further downstream in the positive ξ-direction (iso-contour lines of zero amplitude in black).

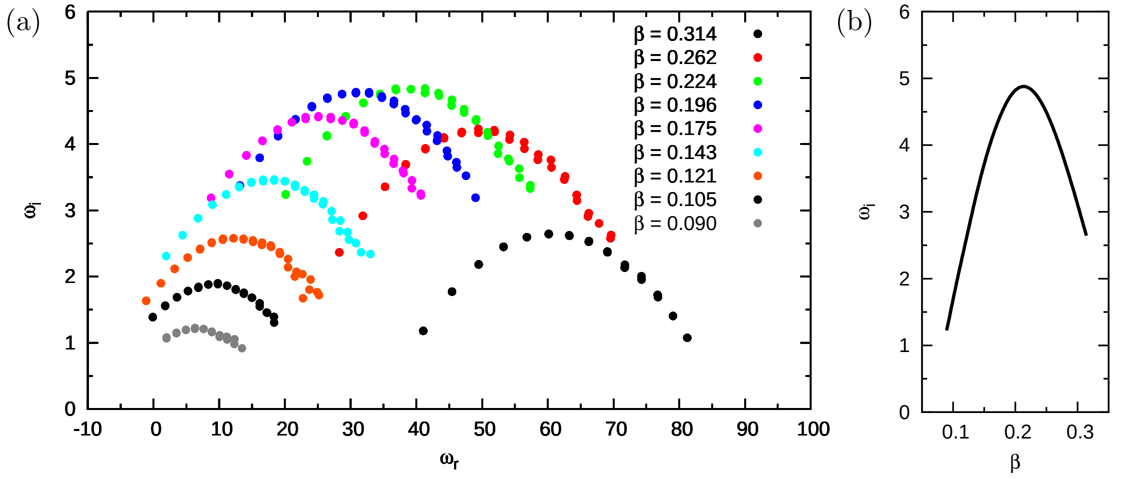

Figure 6. (a) Temporal spectra from global stability calculations for selected spanwise disturbance wavenumbers β; (b) temporal growth rate ω_i as a function of β.

As detailed above, the compressible flow around a swept parabolic body is governed by a large number of parameters describing various flow quantities, fluid properties and geometric characteristics. Even though the above observations are expected to hold for a wide range of parameters, we chose to present a parametric study of the global stability properties with respect to the spanwise wavenumber β. The computed temporal global spectrum consisting of growth rate ω_i and frequency ω_r is shown in figure 6(a) for selected spanwise wavenumbers ranging from 0.090 to 0.314. The typical parabolic shapes of the unstable boundary layer branch are clearly visible where smaller phase velocities are observed for smaller spanwise wavenumbers. The growth rates ω_i appear to grow steadily up to a specific spanwise wavenumber before decaying again. The spanwise wavenumber at which a maximum modal growth is observed has been determined to be $\beta = 0.213$ (see figure 6b), thereby pointing toward a preferred disturbance length scale (or scale selection mechanism) in the spanwise direction.

Parenthetically, one can see more clearly in figure 6(a) that the boundary layer branch consists of double eigenvalues. For some parameter combinations, the eigenvalue pairs at the edge of the parabola separate slightly, which is a typical aliasing phenomenon caused by a marginal numerical resolution of the corresponding global eigenfunctions.

5 Discussion and conclusions

A global stability analysis of compressible flow around a yawed parabolic body has numerically established a link between attachment-line modes and crossflow modes. Though for the parameters studied in this article the crossflow vortices represent the largest amplitude component of the global boundary layer mode, eigenfunctions from the slower part of the unstable branch displayed the characteristic two-dimensionality and linear chordwise dependence (in the chordwise velocity) of a typical attachment-line mode. We thus conclude that the global spectrum of flow around a swept parabolic body contains combination modes that display typical features of both local crossflow vortices and local attachment-line instabilities. In this sense, the study of attachment-line or crossflow instabilities in a separate and local setting is simply the respective local approximation of one of these global combination modes. Consequently, this investigation adds to the previous study by Bertolotti (1999) in establishing a link between attachment-line and crossflow modes. In addition, it provides numerical evidence for the experimental observations of Gray (1952). A most preferred spanwise scale has been found; since it is given by global modes with a dominant crossflow component, it is expected that the crossflow vortices will imprint their favored spanwise length scale onto the entire flow.

Besides the stability characteristics of the attachment-line and crossflow modes presented in this article, the receptivity of the global modes to external excitations or wall roughness distributions is important for industrial applications. An analysis of this type (which is beyond the scope of this investigation) will reveal the mechanisms that excite dominant structures in the flow about a blunt body, be it by direct excitation of the crossflow modes or by forcing of structures near the attachment line that, in turn, initiate the growth of crossflow vortices via the connection demonstrated in this study.

On a more methodological point, the combination of iterative eigenvalue algorithms and direct numerical simulations has proved to be an effective tool in addressing complex stability problems in their entirety instead of via piecewise local approximations. Many more flow configurations of academic or technological interest await analysis in the manner described in this article.

Acknowledgments

Financial support from the Deutsche Forschungsgemeinschaft (DFG), the Studienstiftung des Deutschen Volkes and the Alexander-von-Humboldt Foundation is gratefully acknowledged. Patrick Huerre is warmly thanked for his insightful comments on the manuscript.

References

Bertolotti, F. P. (1999). On the connection between cross-flow vortices and attachment-line instabilities. In *IUTAM Symp. on Laminar-Turbulent Transition*, pages 625–630, Sedona, USA.

Bippes, H. (1999). Basic experiments on transition in three-dimensional boundary layers dominated by crossflow instability. *Prog. Aero. Sci.*, 35:363–412.

Edwards, W. S., Tuckerman, L. S., Friesner, R. A., and Sorensen, D. C. (1994). Krylov methods for the incompressible Navier–Stokes equations. *J. Comput. Phys.*, 110:82–102.

Fabre, D., Jacquin, L., and Sesterhenn, J. (2001). Linear interaction of a cylindrical entropy spot with a shock. *Phys. Fluids*, 13(8):2403–2422.

Gray, W. E. (1952). The effect of wing sweep on laminar flow. Technical Report RAE TM Aero 255, British Royal Aircraft Establishment.

Guégan, A., Schmid, P. J., and Huerre, P. (2006). Optimal energy growth and optimal control in swept Hiemenz flow. *J. Fluid Mech.*, 566:11–45.

Hall, P., Malik, M., and Poll, D. I. A. (1984). On the stability of an infinite swept attachment-line boundary layer. *Proc. R. Soc. Lond.*, A 395:229–245.

Herbert, T. (1997). Parabolized stability equations. *Annu. Rev. Fluid Mech.*, 29:245–283.

Joslin, R. D. (1995). Direct simulation of evolution and control of three-dimensional instabilities in attachment-line boundary layers. *J. Fluid Mech.*, 291:369–392.

Le Duc, A., Sesterhenn, J., and Friedrich, R. (2006). Instabilities in compressible attachment-line boundary layers. *Phys. Fluids*, 18:044102.

Lin, R. S. and Malik, M. R. (1995). Stability and transition in compressible attachment-line boundary-layer flow. Technical Report 952041, SAE.

Lin, R. S. and Malik, M. R. (1996). On the stability of attachment-line boundary layers. Part 1. The incompressible swept Hiemenz flow. *J. Fluid Mech.*, 311:239–255.

Lin, R. S. and Malik, M. R. (1997). On the stability of attachment-line boundary layers. Part 2. The effect of leading edge curvature. *J. Fluid Mech.*, 333:125–137.

Oswatitsch, K. (1956). *Gas Dynamics*. Academic.

Poll, D. I. A. (1979). Transition in the infinite swept attachment-line boundary layer. *Aero. Q.*, 30:607–628.

Reed, H. L. and Saric, W. S. (1989). Stability of three-dimensional boundary layers. *Annu. Rev. Fluid Mech.*, 21:235–284.

Saric, W. S., Reed, H. L., and White, E. B. (2003). Stability and transition of three-dimensional boundary layers. *Annu. Rev. Fluid Mech.*, 35:413–440.

Sesterhenn, J. (2001). A characteristic-type formulation of the Navier–Stokes equations for high-order upwind schemes. *Comput. Fluids*, 30:37–67.

Spalart, P. R. (1988). Direct numerical study of leading-edge contamination. In *AGARD-CP-438*, pages 5/1–5/13.

Article 4

Global stability of swept flow around a parabolic body: features of the global spectrum

By C. J. Mack[1,2] and P. J. Schmid[1]

[1]Laboratoire d'Hydrodynamique (LadHyX), CNRS-École Polytechnique,
F-91128 Palaiseau, France

[2]Department of Numerical Mathematics, Universität der Bundeswehr (UniBw),
D-85577 Munich, Germany

Published in *J. Fluid Mech.* (2009), submitted

The global temporal stability of three-dimensional compressible flow about a yawed parabolic body of infinite span is investigated using an iterative eigenvalue technique in combination with direct numerical simulations. The computed global spectrum provides a comprehensive picture of the temporal perturbation dynamics of the flow, and a wide and rich variety of modes has been uncovered for the investigated parameter choices: stable and unstable boundary-layer modes, different types of stable and unstable acoustic modes and stable wave packet modes have been found. A parameter study varying the spanwise perturbation wavenumber and the sweep Reynolds number reproduced a preferred spanwise length-scale and a critical Reynolds number for a boundary-layer or acoustic instability. Convex leading-edge curvature has been found to have a strongly stabilizing effect on boundary-layer modes but only a weakly stabilizing effect on acoustic modes. Furthermore, for certain parameter choices, the acoustic modes have been found to dominate the boundary-layer modes.

1 Introduction

Soon after the invention of the aircraft in the beginning of the twentieth century it was realized that the aerodynamic design of high-performance aircraft crucially depends on a profound understanding of compressible flow around wings. In particular, the details of the transition process from laminar to turbulent fluid motion, yielding increased drag and a loss of flight performance, play a dominant role in the description of this flow. Two-dimensional hydrodynamic instabilities of the Tollmien–Schlichting type have been found to trigger this transition process and to initiate the breakdown into turbulence further downstream for unswept wings.

With the advent of high-speed aircraft in the 1940s, for instance, the jet-engined Messerschmitt ME 262, the introduction of swept wings became necessary in order to overcome serious design problems emanating from compressibility effects, notably the shock stall phenomenon. The immediately following theoretical and experimental investigations on swept wings suggested that the presence of sweep does not affect the stability of the flow. However, in later flight tests on swept wing aircraft, Gray (1952) found that beyond a critical freestream velocity q_∞, the transition front moved towards the attachment line of the wing; this phenomenon could not be explained by existing two-dimensional arguments. He further observed that this critical freestream velocity depends on the sweep angle Λ as well as the leading-edge radius R of the wing.

The theoretical and experimental investigations that followed revealed a new type of instability, the crossflow instability, which is due to a velocity component inside the boundary layer that is transverse to external streamlines (Bippes, 1999). The presence of sweep (and curvature) leads to a highly three-dimensional boundary-layer flow in the leading-edge region of a swept wing and, thus, fundamentally alters its inherent stability properties; the initially two-dimensional boundary-layer flow along the attachment line gradually develops into a three-dimensional boundary-layer flow downstream of the stagnation line (see, e.g., Bippes, 1999; Saric et al., 2003, for a detailed description of the flow). The crossflow instability exhibits coherent co-rotating vortices whose axes are aligned with the streamlines of the external flow. As an example, Poll (1978) reported their presence in form of oil-film streaks in his wind-tunnel experiments; the same characteristic pattern has been observed in flight tests by Gray (1952). The prevalence of crossflow vortices led to the hypothesis of a crossflow-vortex induced transition, and experiments have been designed to eliminate the vortices by suction and thus render the flow in the vicinity of the leading edge laminar (see, e.g., Pfenninger, 1977).

New experiments revealed once more a lack of understanding of swept leading-edge flow, since they demonstrated that leading-edge transition — in particular, the phenomenon of leading-edge contamination caused by turbulent flow propagating along the leading edge — cannot be explained by the crossflow instability mechanism alone. Based on wind-tunnel experiments on a swept wing model with a circular leading edge, Poll (1979) concluded that the flow is also susceptible to instabilities right at the attachment line. This general finding has become known as attachment-line instability. The above experimental results as well as the need to fully understand the flow, in particular, in the leading-edge region, have fueled a substantial effort to investigate the flow behavior governed by the two identified mechanisms. These investigations, however, have been based on local flow models for either instability mechanism: (i) the swept Hiemenz flow model has been generally accepted as an approximation for the incompressible flow near the attachment line, and the studies of, among others, Hall et al. (1984); Spalart (1988); Kazakov (1990); Joslin (1995, 1996); Lin and Malik (1996, 1997, 1995) have established a remarkable body of literature discussing the properties of the attachment-line instability and its dependence on curvature, compressibility and wall temperature; (ii) crossflow instabilities, which have been experimentally observed further downstream of the stagnation line, have been studied using a local flow model based on a three-dimensional boundary layer. For an overview of the current state-of-the-art the reader is referred to, e.g., Saric et al. (2003); Bonfigli and Kloker (2007) and references therein.

Up until about a decade ago, the two instability mechanisms have been investigated in isolation of each other. Despite hints from experimental efforts that a link between the two instability mechanisms may exist, the technical and numerical tools to investigate the two instabilities together were not available at that time. One attempt to establish a link between the two mechanisms has been undertaken by Bertolotti (1999) who continued, in the chordwise direction, higher attachment-line modes using the parabolized stability equations. He found that the continued attachment-line modes closely resemble the features and scales of crossflow instabilities downstream of the attachment line. A recent global stability analysis, focusing on boundary-layer instabilities, of compressible flow about a swept parabolic body established a more definite connection between (local) attachment-line instabilities and (local) crossflow vortices (see Mack et al., 2008).

The same flow model, which includes both local models, will be used in the present study to compute the global spectrum and to obtain a more complete picture of the temporal flow dynamics. In particular, we expect, besides boundary-layer modes, additional instability mechanisms due to compressibility effects (see, e.g., Mack, 1984) as well as continuous branches (Grosch and Salwen, 1978; Balakumar and Malik, 1992).

Our goal is the comprehensive study of the stability behavior of compressible flow near the leading-edge of a swept blunt body using global stability theory. First attempts in global stability analysis date back to Jackson (1987) and Zebib (1987) who were among the first researchers to apply global linear theory to study the flow past variously-shaped bodies and circular cylinders, respectively. Over the following years, global stability analysis evolved into a widely used approach to investigate moderately complex flows such as, for example, the periodic wake of a circular cylinder (Barkley and Henderson, 1996), the three-dimensional flow over a backward-facing step (Barkley et al., 2002) or the fully three-dimensional flow of a jet-in-crossflow (Bagheri et al., 2009). Recently, numerous results and applications of global stability analysis have been summarized in the review of Theofilis (2003).

A significant advance in global stability analysis occurred when direct methods, used in the early studies, to compute the spectrum have been replaced by powerful iterative techniques such as the Arnoldi method (Sorensen, 1992). Even though these techniques originated in large-scale matrix algebra, their successful combination with numerical simulation techniques allowed a considerable step towards a global stability analysis of complex flows with multiple scales and multiple physical phenomena which where until then out of reach. Today, the accessible level of complexity for global stability analysis crucially depends on (i) the availability of high-performance computers, (ii) the efficiency and robustness of iterative algorithms and (iii) the quality of numerical simulations that provide the flow fields to the iterative algorithms. The concept of DNS-based global stability analysis, as used in the present study, is one of many examples where the combination of high-performance computing and fast iterative algorithms enables us to gain more insight into the dynamic behavior of complex fluid flow.

The present article is organized as follows. In the next section §2 we present the three-dimensional flow model including the governing parameters, the governing equations and details of the direct numerical simulation (DNS). In section §3 we briefly introduce the concept of DNS-based global stability analysis and its implementation. This is followed by the results in section §4 where features of the global spectrum are discussed; concluding remarks are offered in section §5.

2 Flow configuration, governing parameters and numerical method

The flow configuration, as displayed in figure 1(b), consists of a parabolic body (in grey) about which a three-dimensional body-fitted grid (in blue) is mapped. The local Cartesian coordinate system (in red) is given by the x-, y- and spanwise z-direction pointing along the attachment line (in black), and the local parabolic coordinate system (in orange) consists of the chordwise ξ- and the normal η-direction pointing along grid lines in the downstream direction and along grid lines normal to the wall, respectively. The surface of the parabolic body is given by

$$x(y) = \frac{1}{2R} y^2, \tag{2.1}$$

where R denotes its leading-edge radius. We consider flow situations where the oncoming flow is supersonic

$$M_1 = M_\infty \cos \Lambda > 1, \tag{2.2}$$

where M_∞ and M_1 denote the freestream Mach number and its component normal to the shock, and Λ is the freestream angle (see figure 1a); thus, the computational domain is limited by a detached unsteady bow shock in the wall-normal direction, and this shock, assumed to be an infinitely-thin moving discontinuity, acts as the inflow boundary.

The supersonic flow state upstream of the detached bow shock, denoted by the subscript $_\infty$, is given by the freestream Mach number M_∞ and the freestream angle Λ, and a total temperature

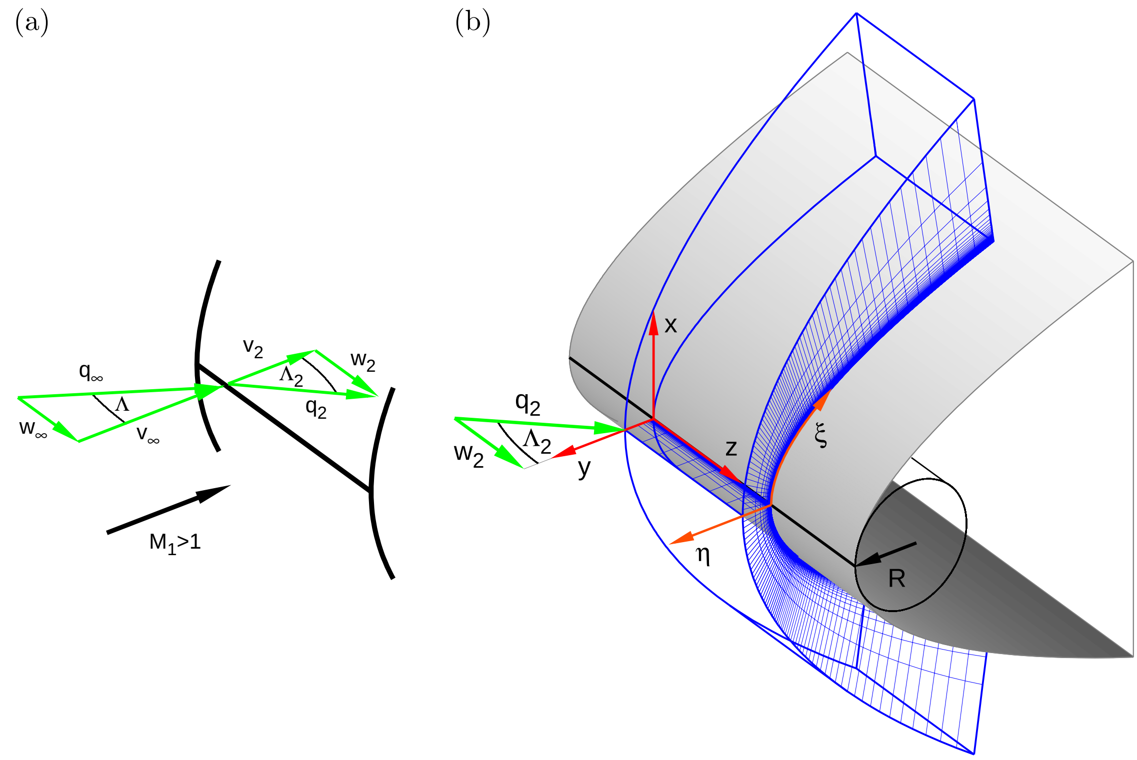

Figure 1. (a) Schematic of a detached bow shock (in black) and the relevant flow parameters upstream and downstream of the shock. (b) Sketch of the three-dimensional flow configuration.

$T_0 = 728$ [K] and total pressure $p_0 = 1.55 \cdot 10^6$ [Pa] are used as a reference state. From these quantities and the Rankine–Hugoniot relations, the flow state downstream of the shock, denoted by the subscript $_2$, is obtained (see figure 1a). Consequently, the incoming flow impinges on the body with a velocity q_2 and a sweep angle Λ_2 yielding a sweep velocity w_2 and a normal velocity v_2. The latter quantities will be used in what follows to define the governing parameters.

2.1. *Governing parameters*

The flow configuration under investigation is characterized by two distinct length scales, the leading-edge radius R and a viscous length scale δ, which respectively describe the outer flow and the flow inside the boundary layer. We define this viscous length scale as

$$\delta = \left(\frac{\nu_r}{S}\right)^{1/2} \qquad \text{with} \qquad S = \left(\frac{\partial u}{\partial x}\right)_w = \frac{2v_2}{R}, \tag{2.3}$$

where S is the strain rate at the wall, at the attachment line, which follows from the chordwise derivative of the potential solution of flow around a circular cylinder with radius R, chosen as $R = 0.1$ [m], evaluated at the stagnation point. The size of the length scale δ is depicted in figure 3(c) for a selected parameter choice.

We further define a sweep Reynolds number Re_s, a leading-edge Reynolds number Re_R, a sweep Mach number Ma_s and a wall temperature ratio θ_w as

$$Re_s = \frac{w_2\delta}{\nu_r}, \qquad Re_R = \frac{v_2 R}{\nu_r}, \qquad Ma_s = \frac{w_2}{c_2}, \qquad \theta_w = \frac{T_w}{T_r}, \tag{2.4}$$

where v_2 and w_2 are the wall-normal and sweep velocity downstream of the bow shock, c_2 stands for the speed of sound, and ν_r denotes the kinematic viscosity evaluated at recovery temperature

T_r and stagnation pressure p_s. In the present work we consider an adiabatic wall, and thus the ratio of the temperature T_w at the wall and T_r is $\theta_w = 1$.

Alternatively, the sweep Reynolds number Re_s can be reformulated to display an explicit dependence on the leading-edge Reynolds number Re_R and the sweep angle Λ_2 as well as the leading-edge radius R.

$$Re_s = \left(\frac{Re_R}{2}\right)^{1/2} \tan\Lambda_2 = \frac{R}{2\delta}\tan\Lambda_2 \tag{2.5}$$

As we can see from (2.5), the sweep Reynolds number describes the influence of sweep as well as leading-edge curvature.

2.2. *Freestream dependence*

The governing parameters have been defined using the flow quantities downstream of the bow shock (see section §2), and thus these parameters depend on the freestream conditions in a nonlinear manner. As an example, using the definition of the sweep Mach number in (2.4), the thermodynamic relation for the speed of sound for a perfect gas $c^2 = \gamma RT$ as well as the Rankine–Hugoniot relation for the temperature ratio T_2/T_1, the sweep Mach number can be computed via

$$Ma_s = \frac{\gamma+1}{2} M_1^2 \tan\Lambda \left(\frac{1-\gamma}{2} + \gamma M_1^2\right)^{-1/2} \left(1 + \frac{\gamma-1}{2} M_1^2\right)^{-1/2}; \tag{2.6}$$

for the shock-free configuration, this relation reads

$$Ma_s = M_1 \tan\Lambda \left(1 + \frac{\gamma-1}{2} M_1^2\right)^{-1/2}. \tag{2.7}$$

Both equations, (2.6) and (2.7), reveal a nonlinear dependence of Ma_s on the freestream conditions, and this dependence is given in figure 2. In figure 2(a), we show Ma_s as a function of M_1 and Λ, where the solid and the dashed lines represent constant values of Λ and M_∞, respectively. For instance, in this article, we study a freestream Mach number $M_\infty = 8.15$ and a freestream angle $\Lambda = 30\,^\circ$, yielding a shock-normal Mach number $M_1 = 7.06$, which results in a sweep Mach number $Ma_s = 1.25$. Furthermore, figure 2(b) demonstrates that, since the sweep Reynolds number Re_s is a function of the sweep angle Λ_2 (2.5), it also depends in a nonlinear manner on the freestream conditions.

2.3. *Numerical method*

We consider the motion of a compressible fluid modeled as a perfect gas with constant specific heat ratio $\gamma = 1.4$ and constant Prandtl number $Pr = 0.71$. The compressible Navier–Stokes equations, the equation of state, Fourier's law for the thermal conductivity and Sutherland's law (at ambient conditions) for the viscosity fully describe the flow. The equations are formulated based on pressure p, Cartesian velocities (u, v, w) and entropy s and are solved on a time-dependent, curvilinear and non-uniformly distributed grid, with a clustering of the grid points towards the wall as well as in the leading-edge region, as shown in figure 1(b). For the direct numerical simulations (DNS) in this article the computational domain is limited by a detached unsteady bow shock, assumed to be an infinitely-thin moving discontinuity, in the wall-normal direction. This discontinuity is incorporated through a shock-fitting technique (Moretti, 1987) and provides the inflow conditions via the Rankine–Hugoniot relations. Along the surface of the

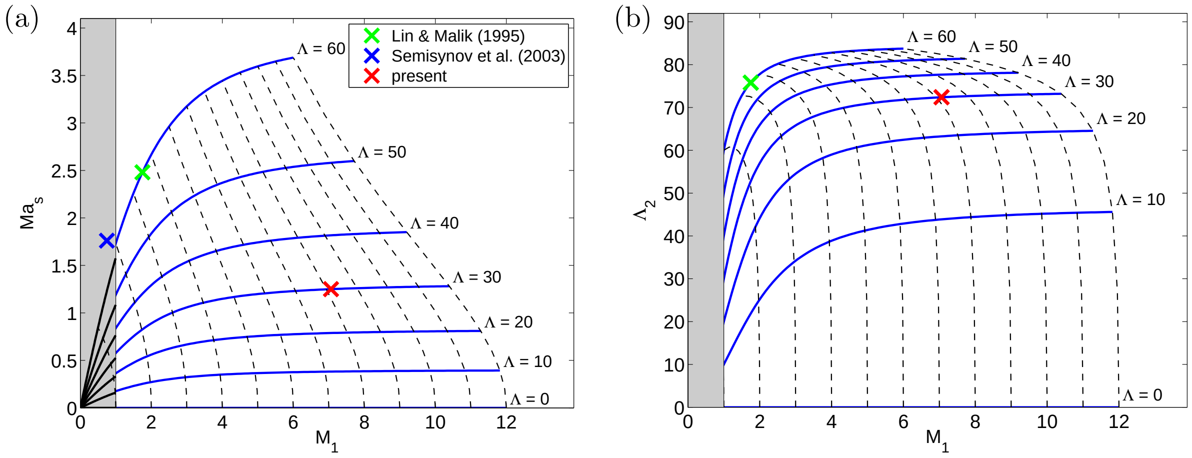

Figure 2. (a) Sweep Mach number Ma_s and (b) sweep angle Λ_2 as a function of the shock-normal Mach number $M_1 = M_\infty \cos\Lambda$ and the freestream angle Λ. The region in grey denotes the case where the oncoming flow is subsonic, i.e., $M_1 < 1$ (note that in this case $\Lambda_2 = \Lambda$), and the blue lines represent constant values of Λ while the dashed black lines depict constant values of M_∞. The red cross marks the freestream conditions of the present study, and the green and blue cross represent the flow conditions which have been used in previous linear stability analyses.

body no-slip boundary conditions and adiabatic wall conditions are applied. At the chordwise edges of the computational domain, non-reflecting outflow boundary conditions are imposed and, under the assumption of infinite span, periodic boundary conditions are used in the z-direction. For details on the implementation of the numerical procedure such as the spatial, where compact finite-difference schemes are employed, and the temporal discretization we refer the reader to Mack and Schmid (2009). The homogeneity in the spanwise z-direction allows us to Fourier transform this direction, and the remaining inhomogeneous η- and ξ-coordinate directions are discretized using 128×255 grid points, respectively.

3 Global stability analysis

Information about the disturbance behavior for complex geometries and/or complex flow physics relies on the formulation of a global stability problem when limiting assumptions such as locally-parallel flow, multiple homogeneous coordinate directions or a low-Mach number approximation are undesirable or impossible. For a comprehensive understanding of the perturbation dynamics for our flow configuration (see figure 1) neither of the above-mentioned limiting assumptions should be made; rather, a global formulation of the stability problem has to be attempted. For this reason, we assume a three-dimensional perturbation field $\phi' = (p', u', v', w', s')^T$ superimposed on a (steady) base flow ϕ_0 according to

$$\phi(x, y, z, t) = \phi_0(x, y, z) + \epsilon\phi'(x, y, z, t) \qquad \epsilon \ll 1. \tag{3.1}$$

We proceed by computing a base flow as a steady solution of the nonlinear compressible Navier–Stokes equations, and a subsequent linearization about this base flow yields the linearized Navier–Stokes equations for the perturbations ϕ' which can formally be written as

$$\frac{\partial \phi'}{\partial t} = \mathcal{J}(\phi_0)\phi' \tag{3.2}$$

with $\mathcal{J}(\phi_0)$ denoting the linear stability operator (the Jacobian).

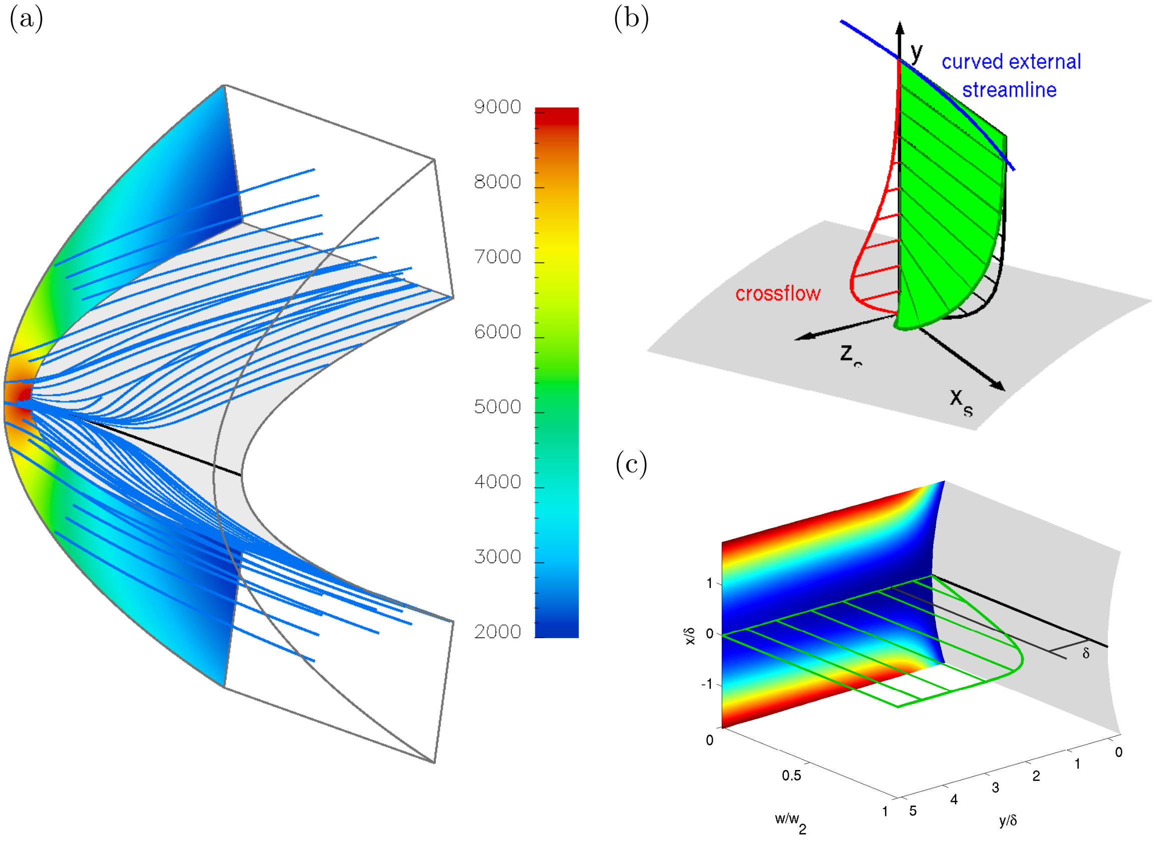

Figure 3. (a) Streamlines (in blue) and pressure field [in Pa] of the computed steady base flow for $Re_s = 800$, $Re_R = 129136$, $Ma_s = 1.25$ and $\theta_w = 1$; attachment line in black. (b) Schematic of the three-dimensional boundary layer at a selected position downstream of the attachment line (adapted from Bippes, 1999). (c) Normalized w-velocity profile, stretched by a factor of 100 in η, along the attachment line; the normal velocity v is shown in the back $\delta = 1.968 \cdot 10^{-4}$ [m] for the present parameter choice.

3.1. *Base flow*

The assumption of infinite span permits us to eliminate the z-dependence, but not the w-component, from the base flow $\phi_0(x, y, z)$ and to reduce the computations to a problem with only two independent variables x and y. From the solution of a long-time integration the full three-dimensional base flow can be recovered. This procedure is possible since the flow is stable with respect to two-dimensional perturbations thus allowing a simple time-integration toward a steady state. As a consequence, more sophisticated techniques such as Newton-type methods, (Jacobian-free) Newton–Krylov techniques (Knoll and Keyes, 2004) or selective frequency damping (Åkervik et al., 2006) can be avoided.

An initial two-dimensional flow field has thus been integrated in time until a steady state has been reached to within a sufficiently high accuracy. For a detailed discussion of the required quality of this steady base flow and the distinction between base and mean flow for global stability problems the reader is referred to Theofilis (2003) and Sipp and Lebedev (2007). The converged three-dimensional base flow is visualized, in terms of streamlines and pressure field, in figure 3(a). In addition, the local and nearly two-dimensional flow field in the vicinity of the leading edge is depicted in figure 3(c) shown by the normal and streamwise velocity. The three-dimensional base velocity profile further downstream from the attachment line is illustrated in figure 3(b). It represents a typical profile of a three-dimensional boundary layer consisting of twisted velocity vectors inside the boundary layer which eventually align with the curved streamlines of the inviscid outer flow.

3.2. *DNS-based global stability solver*

This three-dimensional base flow forms the starting point for our DNS-based global stability analysis. The details of this stability solver are given in Mack and Schmid (2010), but for the sake of completeness we briefly outline and discuss its main features.

Assuming a disturbance field, see equation (3.1), of a traveling-wave form

$$\phi'(x,y,z,t) = \widetilde{\phi}(x,y)\mathrm{e}^{\mathrm{i}(\beta z-\omega t)}, \tag{3.3}$$

where $\widetilde{\phi}(x,y)$ denotes the complex amplitude and β the real spanwise wavenumber of the perturbation; the temporal long-term evolution of the disturbance is characterized by ω whose real part ω_r describes the frequency and whose imaginary part ω_i represents the growth rate. Upon substitution of expression (3.2) into the linearized compressible Navier–Stokes equations (3.2) and subsequent discretization in the remaining coordinate directions, we can formally write the global discrete stability problem as

$$\omega\ \widetilde{\boldsymbol{\phi}} = \mathbf{J}(\boldsymbol{\phi}_0)\ \widetilde{\boldsymbol{\phi}}. \tag{3.4}$$

Herein, the matrix $\mathbf{J}(\boldsymbol{\phi}_0)$ represents the linear stability matrix (the Jacobian). The direct solution of the resulting discrete $n \times n$ eigenvalue problem, where $n = 5n_\xi n_\eta$ (with n_ξ and n_η as the number of grid points in the chordwise and normal direction) denotes the size of $\mathbf{J}(\boldsymbol{\phi}_0)$ and typically is of the order $\mathcal{O}(10^6 - 10^7)$, is prohibitively expensive. For this reason iterative solution techniques have to be employed to extract pertinent stability information.

The algorithm to accomplish this task is the implicitly restarted Arnoldi method (IRAM), a Krylov subspace technique presented by Sorensen (1992) which is publicly available and described in Lehoucq et al. (1998). This class of techniques only requires the action of the Jacobian matrix $\mathbf{J}(\boldsymbol{\phi}_0)$ onto a given velocity field $\boldsymbol{\phi}'$. These matrix-vector products can readily be obtained from direct numerical simulations via

$$\mathbf{J}(\boldsymbol{\phi}_0)\boldsymbol{\phi}' \approx \frac{\mathbf{F}(\boldsymbol{\phi}_0 + \epsilon\boldsymbol{\phi}') - \mathbf{F}(\boldsymbol{\phi}_0)}{\epsilon} = \left.\frac{\partial \mathbf{F}(\boldsymbol{\phi})}{\partial \boldsymbol{\phi}}\right|_{\boldsymbol{\phi}=\boldsymbol{\phi}_0} \boldsymbol{\phi}' + \mathcal{O}(\epsilon), \tag{3.5}$$

where ϵ is a user-specified parameter, chosen as $||\epsilon\boldsymbol{\phi}'||/||\boldsymbol{\phi}_0|| = \epsilon_0 = 10^{-8}$, and $\mathbf{F}$ represents the right-hand side of the nonlinear Navier–Stokes equations. This approximation avoids the explicit formulation and storage of the Jacobian matrix and thus allows a Jacobian-free framework where direct numerical simulations (DNS) provide the input for the iterative stability solver. For a discussion on the choice of the parameter ϵ_0 see Mack and Schmid (2010). In the same reference it was further demonstrated that a spectral transformation such as the Cayley transformation is necessary to accelerate and control the convergence of the iterative eigensolver by judiciously deforming the complex plane. In addition, this same spectral transformation adds to the robustness of the solver and allows the Krylov subspace method to converge toward specific parts of the complex global spectrum. The Cayley transformation consists of a two-parameter conformal mapping defined as

$$\mathbf{T}_C(\sigma,\mu) \equiv (\mathbf{J}(\boldsymbol{\phi}_0) - \sigma\mathbf{I})^{-1}(\mathbf{J}(\boldsymbol{\phi}_0) - \mu\mathbf{I}), \qquad \omega = \frac{\sigma\lambda - \mu}{\lambda - 1}, \tag{3.6}$$

where σ and μ denote the mapping parameters, and $\mathbf{I}$ is the mass matrix, in our case the identity matrix. The computed region of the full global spectrum depends on the choice of these parameters, most notably on the choice of the shift parameter σ. The desired eigenvalues ω of $\mathbf{J}(\boldsymbol{\phi}_0)$ can straightforwardly be recovered from the eigenvalues λ of the transformed problem. The advantages of using the transformation (3.6), however, comes at the expense of solving a linear system which, in keeping with the overall iterative nature of our global stability method, has to be done iteratively by a Krylov subspace technique, in our case the BiCGStab method (van der Vorst, 1992) with an ILU-type preconditioner (Saad, 2003). Details can be found in Mack and Schmid (2010).

4 Results

The iterative algorithm outlined in section §3 is applied to simulations of compressible flow around a swept parabolic body as depicted in figure 1. As the Krylov subspace is augmented by subsequent calls to the direct numerical simulation (DNS) code, the ILU-preconditioned Cayley-transformed Arnoldi method provides an approximate spectrum that consequently increases in complexity but also in accuracy.

4.1. *Global spectrum*

The iteratively computed global spectrum is shown in figure 4. This global spectrum reflects the richness of physical processes present in the flow configuration under investigation. It consists of (mostly unstable) discrete shear modes (region I, in red) that express the flow characteristics inside the boundary layer, of acoustic modes that describe the presence of (stable and unstable) sound waves (region I, II and III, in blue) and of (stable) wave packet modes (region IV, in green) that represent the dynamics of general perturbations outside the boundary layer; the latter type of modes is complemented by the partial spectrum (region IV, in grey) obtained by directly solving for the eigenvalues of the Jacobian matrix for an embedded and significantly smaller sub-domain located near the attachment line. For the current parameter choice — i.e., a sweep Reynolds number of $Re_s = 800$, a leading-edge Reynolds number of $Re_R = 129136$, a sweep Mach number of $Ma_s = 1.25$, an adiabatic wall ($\theta_w = 1$) and a disturbance wavenumber $\beta = 0.314 = 2\pi/L_z$ (with L_z as the fundamental length scale of the perturbations, nondimensionalized by the viscous length scale δ, in the spanwise z-direction) —, the discrete boundary-layer branch (in red) features the most unstable global modes.

The global spectrum (see figure 4) also shows that the physical processes described by different types of global modes exhibit a distinct but characteristic frequency ω_r. The boundary-layer modes (in red), for instance, prevail inside the boundary layer, and the displayed modes travel with a phase speed of approximately 12% to 37% of the (mean) velocity $w_{mean} \approx w_2$ in the spanwise z-direction ($\omega_{r,mean} = w_2\beta/(S\delta)$ with $w_2 = 583.1$ [m/s], $\delta = 1.968 \cdot 10^{-4}$ [m] and $S = 3704$ [1/s]). The acoustic modes (in blue), on the other hand, travel downstream and upstream in z with $w_2 \pm c_2$, where c_2 stands for the speed of sound in the freestream. This speed of $w_2 \pm c_2$ corresponds to Mach numbers $Ma_s = (w_2 \pm c_2)/c_2$ of 2.25 and 0.25 (see figure 4). The wave packet modes (in green) move with approximately the (mean) velocity w_2 since they mainly capture the dynamics of perturbations in the freestream.

4.1.1 *Boundary-layer modes*

Concentrating on boundary-layer modes (in red, see region I in figure 4), the employed global stability solver identified, for our flow parameters, an eigenvalue branch of typical parabolic shape. This branch consists of stable and unstable discrete modes whose frequency ω_r ranges from 31.1 to 92.8 (see figure 5e); the maximum growth rate $\omega_i = 2.64$ is achieved for $\omega_r = 60.1$. Owing to the inherent symmetry properties of the flow the eigenvalues appear double at closer inspection, and the associated modes exhibit characteristic symmetry properties with respect to the attachment-line.

Two representative global modes, labeled $B1$,$B2$ and indicated by black circles in figure 5(e), are visualized by iso-surfaces of the normal velocity v in figure 5(a). The slower-moving mode $B1$ displays typical features of both attachment-line instabilities and crossflow vortices, as previously reported by Mack et al. (2008). The faster-moving mode $B2$ shows a substantially stronger component of the crossflow instability, and its maximum amplitude is located further downstream from the attachment line. This property is more evident in figure 5(b) where we present a body-fitted cross-cut at a distance of half the boundary-layer thickness from the wall. The same figure demonstrates again the two-dimensional character of the global modes near the attachment line (see mode $B1$). Further downstream both modes display the typical curved

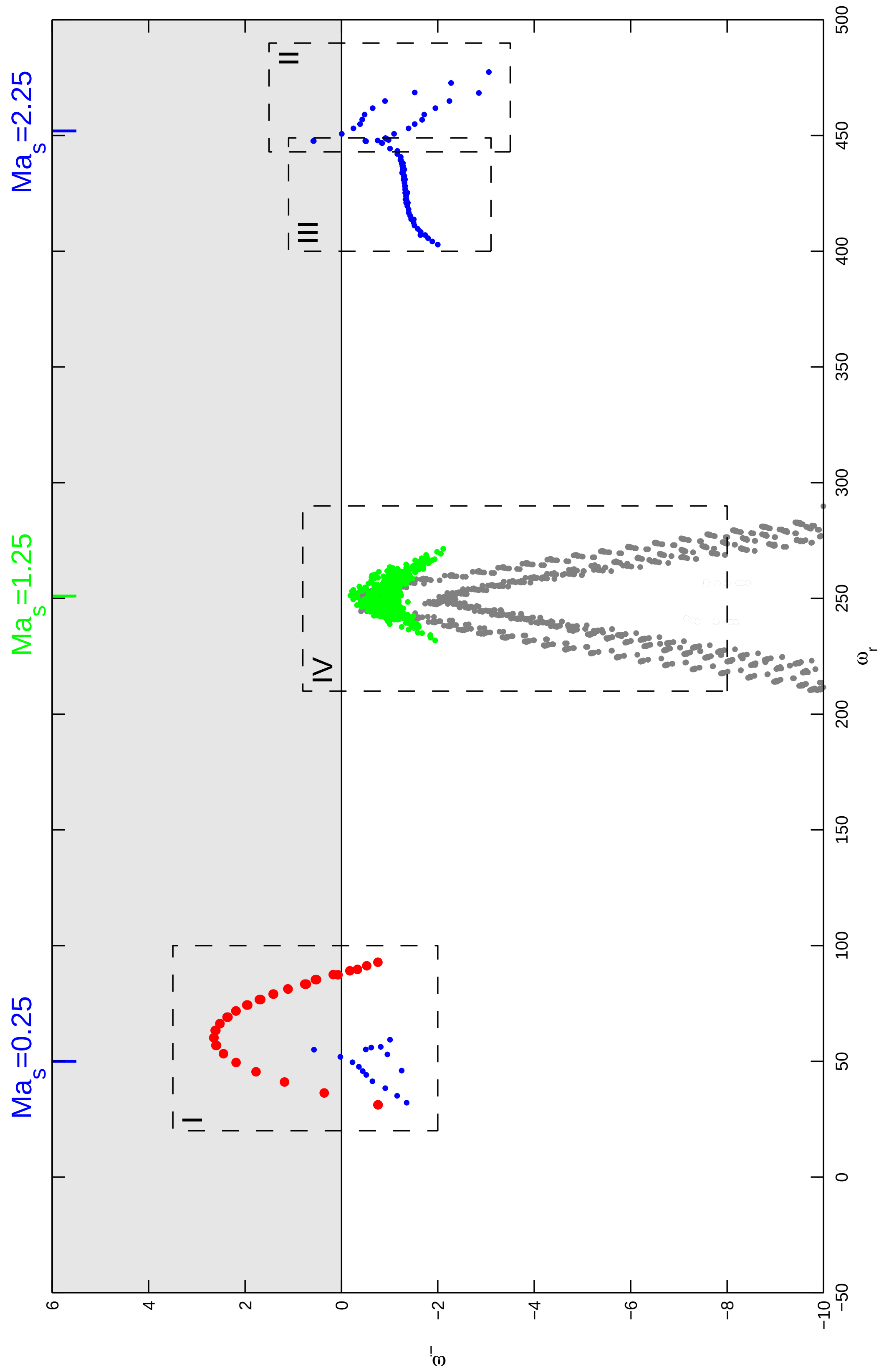

Figure 4. Global spectrum showing the frequency ω_r and the corresponding growth rate ω_i of the iteratively computed modal structures ($Re_s = 800$, $Re_R = 129136$, $Ma_s = 1.25$, $\theta_w = 1$ and $\beta = 0.314$); the eigenvalues ω have been nondimensionalized using the strain rate S. Each region shows the least-stable eigenvalues belonging to boundary-layer modes (region I), acoustic modes (region I, II and III), and wave packet modes (region IV); unstable-half plane in grey. The most unstable modes in region I were presented in Mack et al. (2008).

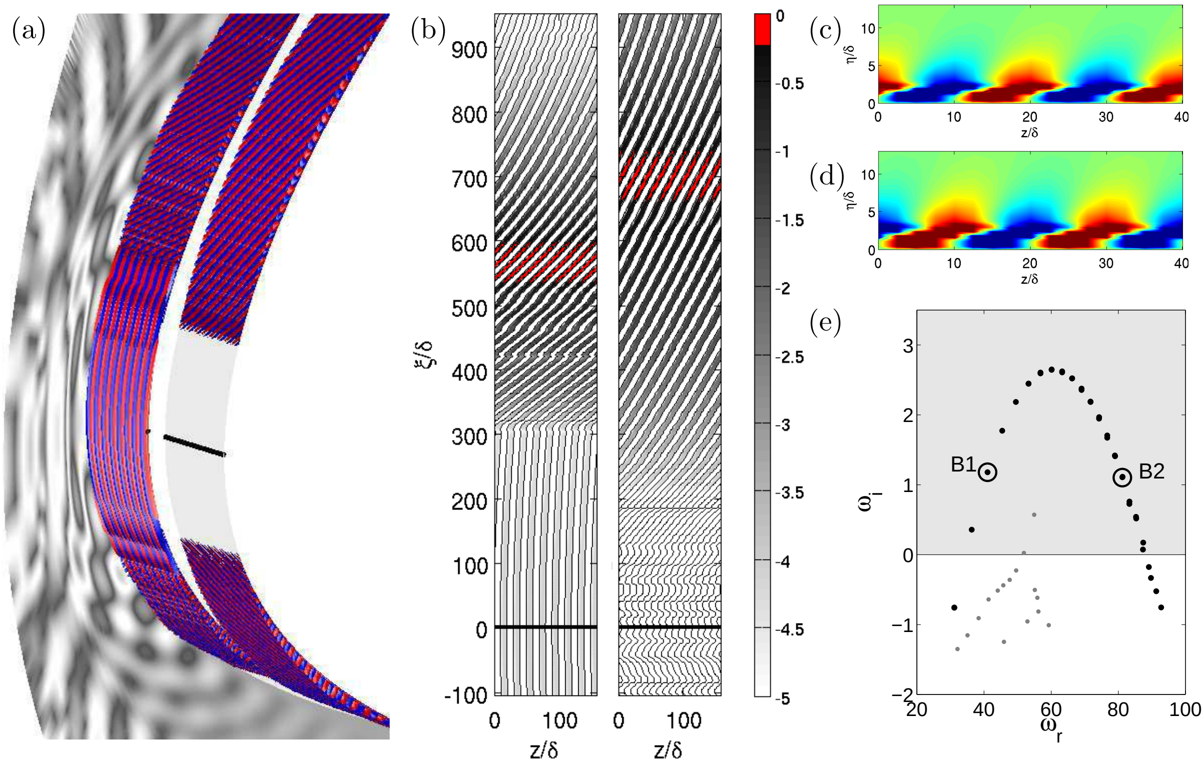

Figure 5. (a) Two representative global modes from the boundary-layer branch visualized by iso-surfaces (positive values in red, negative values in blue) of the normal velocity $v(x, y, z) = \mathrm{Real}\{\widetilde{v}(x, y)\,(\cos\beta z + \mathrm{i}\sin\beta z)\}$; eight periods in z are shown. The left and right mode correspond respectively to the two eigenvalues $B1$ and $B2$ depicted by circles in (e); contours of the associated pressure field are shown in the background; attachment line in black. (b) Top view of v in the ξ-z-plane at approximately half the boundary-layer thickness; a log-scale is used to visualize the positive values of v. (c,d) Chordwise cross-cuts of v at $\xi/\delta \approx 400$ and $\xi/\delta \approx 580$. (e) Region I of the global spectrum shown in figure 4.

shape of crossflow instabilities. With the spanwise wavenumber $\beta = 2\pi/L_z$ held constant for both modes, the clearly visible difference in the spatial orientation of the crossflow vortices is a consequence of a corresponding difference in the equivalent "local chordwise wavenumber". This same "local chordwise wavenumber" parameterizes the parabolic eigenvalue branch of the associated global boundary-layer modes in figure 5(e). An equivalent parabolic shape would be obtained in *local* stability analyses as the least-stable eigenvalue is traced as a function of the chordwise wavenumber. Figure 5(c,d) depict two chordwise cross-cuts of the normal velocity v at two selected positions, (c) at $\xi/\delta \approx 400$ and (d) at the location of the maximum amplitude of $B1$.

The compressible nature of the flow is expressed in the existence of an associated weak pressure field which reflects the acoustic footprint of a global shear mode. This phenomenon is visualized in the ξ-η-plane by contours of the pressure for the boundary-layer mode $B1$ (see figure 5a).

4.1.2 *Acoustic modes (type A)*

Due to the presence of compressibility, the global spectrum also features distinct sets of slow- and fast-moving acoustic global modes (see blue dots in region I and II in figure 4) which describe the presence of sound waves. These modes travel with approximately $w_2 \pm c_2$ in the spanwise z-direction as already discussed in section §4. In figure 6(a), we display region II of the global spectrum (see figure 4) which contains the fast-moving set of acoustic modes. It is found that these modes can be divided into symmetric S-modes — the spatial distribution of all disturbance quantities except for the chordwise velocity u is symmetric with respect to the attachment line

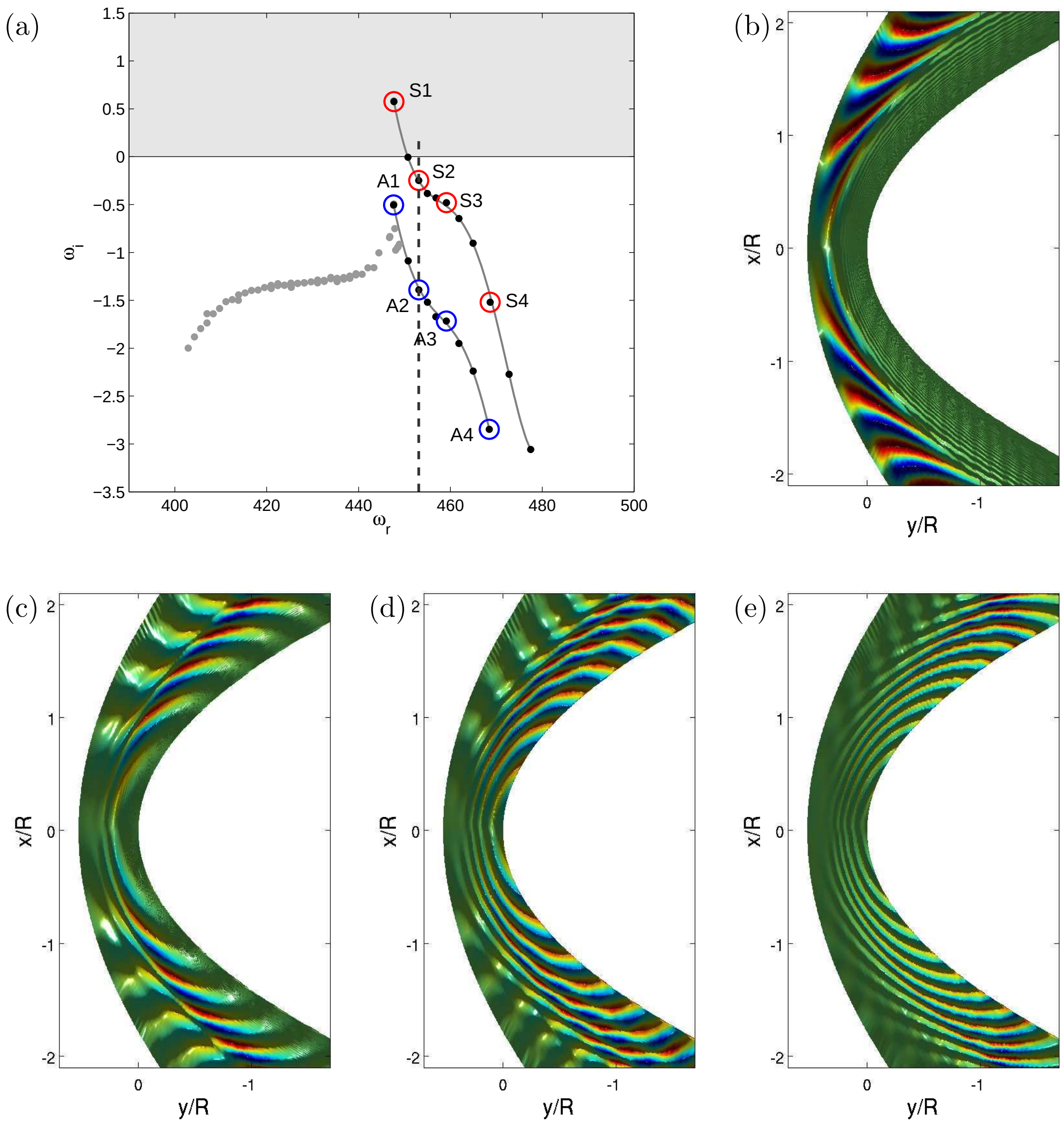

Figure 6. (a) Computed region of the global spectrum containing the fast-moving set of acoustic modes (see region II and III in figure 4). (b–e) Spatial structure of a sample of associated global acoustic modes belonging to the eigenvalues $S1$, $S2$, $S3$ and $S4$ from the S-branch depicted by red circles in (a). The modes are visualized by the chordwise velocity $u(x, y, z)$ in the x-y-plane. The green hue corresponds to vanishing amplitudes (larger amplitudes in red); $R = 0.1 = 508\delta$.

— and antisymmetric A-modes. Furthermore, each S-mode is found to pair with an A-mode at the same frequency ω_r, e.g., $\omega_{r,S2} = \omega_{r,A2}$ (see dashed line in figure 6a). Moreover, either type of modes describes a distinct branch in the eigenvalue spectrum, indicated by the grey line in figure 6(a), where the modes on the A-branch are always more stable than the modes on the S-branch.

The spatial structure of a representative sample of acoustic modes from the S-branch is presented in figure 6(b–e); the corresponding eigenvalues of these modes are circled in red in figure 6(a) and denoted by $S1$–$S4$, respectively. All modes are visualized by the amplitude distribution of the chordwise velocity u in the x-y-plane. The unstable ($S1$) and the marginally stable mode ($S2$) reveal a dominant spatial structure downstream of the detached bow shock, and this structure decays toward the surface of the body; the bow shock acts as a flexible "wall"

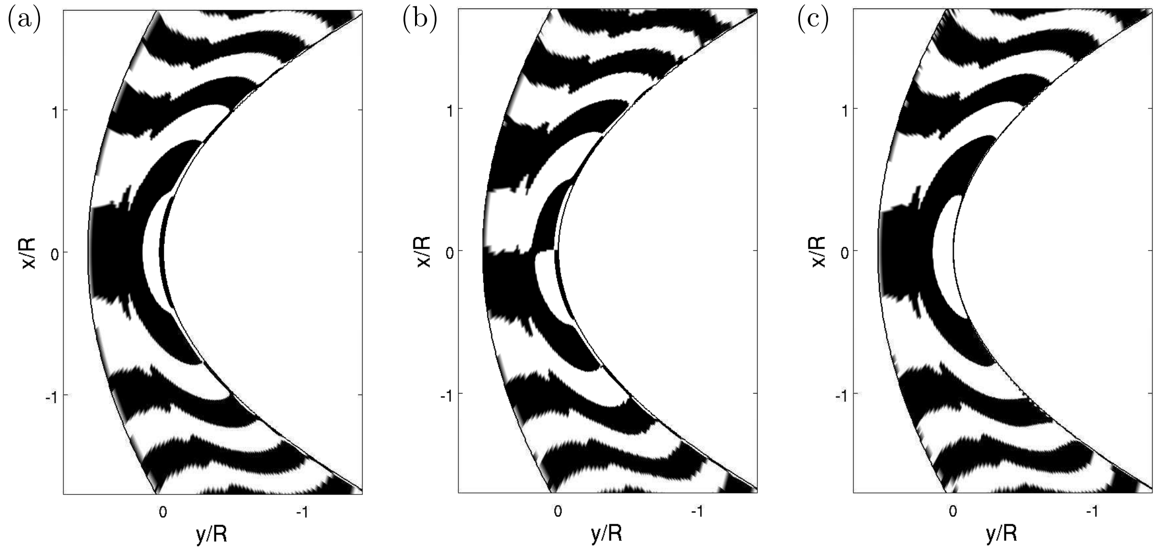

Figure 7. Sign of the pressure distribution sign(p) of selected global acoustic modes in the x-y-plane: (a) S-mode ($S2$) and (b) A-mode ($A2$) from the fast-moving set of acoustic modes (see figure 6a); (c) mode corresponding to $S2$, from the slow-moving set of acoustic modes denoted by $\bar{S}2$ (see blue dots in region I in figure 4).

which prevents sound waves from traveling upstream of the shock. More stable modes ($S3$ and $S4$) are more pronounced in the half of the physical domain which is adjacent to the body, and they exhibit smaller spatial structures as they are increasingly tilted and damped; the smaller spatial structures are the result of this obliqueness of the waves.

The smaller the spatial structures, the larger is the chordwise "wavenumber" α and thus the propagation angle of the acoustic waves. The unstable mode $S1$ exhibits a small value of α and thus displays an approximately two-dimensional wave traveling in the spanwise z-direction. This mode further shows no strong interaction with the shock; rather, the bow shock reacts to the structure of the mode by adjusting its spatial shape. However, for larger values of α, the oblique traveling acoustic waves strongly interact with the bow shock resulting in a small energy loss ($S2$). Finally, for even larger α structures close to the parabolic body prevail ($S3$ and $S4$).

In figure 7, we present a comparison of three acoustic global modes belonging to the S- and A-branch of the fast-moving set of acoustic modes (see region II in figure 4) as well as an acoustic mode from the corresponding slow-moving symmetric branch (marked by blue dots in region I in figure 4). As an example we concentrate on the mode $S2$ and its associated mode $A2$ (see dashed line in figure 6a). From the slow-moving set of acoustic modes we choose the image mode (denoted by $\bar{S}2$) to $S2$, i.e., the mode with the identical decay rate ω_i as $S2$ but with a frequency of approximately $\omega_r \approx w_2 - c_2$. Regarding the spatial shape of these three modes it is found that the sign of the pressure distribution sign(p) is nearly identical (see figure 7). Besides the above-mentioned chordwise symmetric/anti-symmetric structure of these modes the two fast-moving modes exhibit a characteristic wall layer that decreases as we proceed downstream from the attachment line (figure 7a,b); this feature is absent for the slow-moving mode $\bar{S}2$ (figure 7c).

4.1.3 *Acoustic modes (type B)*

In addition to the acoustic modes presented in section §4, another type of global acoustic modes exists. The dominant part of these modes lies in the freestream, and they display a characteristic structure in a local region between the detached bow shock and the attachment line (see figure 8). Starting with the global mode in figure 8(a), which represents the first mode

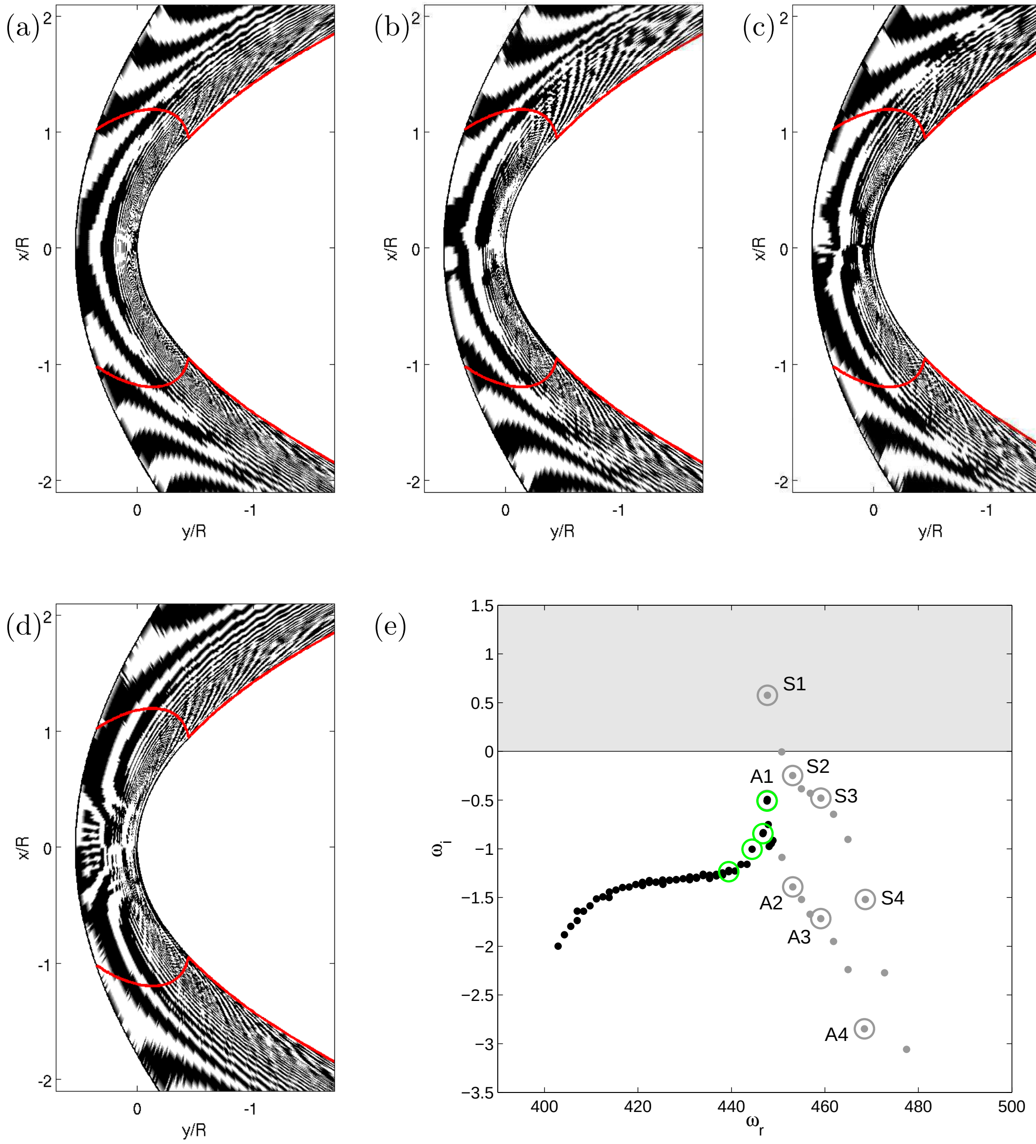

Figure 8. (a)–(d) Sample of a further type of global acoustic modes visualized by the sign of the chordwise velocity, sign(u), in the x-y-plane; sonic line, i.e., $Ma = (u^2 + v^2)^{1/2}/c = 1$, in red. (e) The black dots display the corresponding eigenvalues in the global spectrum (see region III in figure 4); the eigenvalues circled in green belong to the global modes (a)–(d).

$A1$ of the A-branch shown in the previous section §4, we again observe a symmetric spatial distribution for the chordwise velocity component u in the freestream (visualized by the sign of u). As we proceed along the eigenvalue branch marked in black in figure 8(e), an interesting behavior emerges. It appears that a localized region between the bow shock and the attachment line decouples itself — in terms of distinct spatial scales — from the regions downstream from the attachment line. This decoupling is already visible, even though barely, in figure 8(a) directly behind the bow shock at $x = 0$. Progressing farther along the eigenvalue branch this feature becomes more pronounced as the localized region further extends in a semi-circular fashion from its point of origin towards the body, and as the structure within shows increasingly finer scales (see figure 8b–d). It appears that the symmetry properties of the structures inside and outside the localized region are uninfluenced by each other. The range of scales, on the other hand, indicates a link between the two regions: generally speaking, the smaller the scales inside the

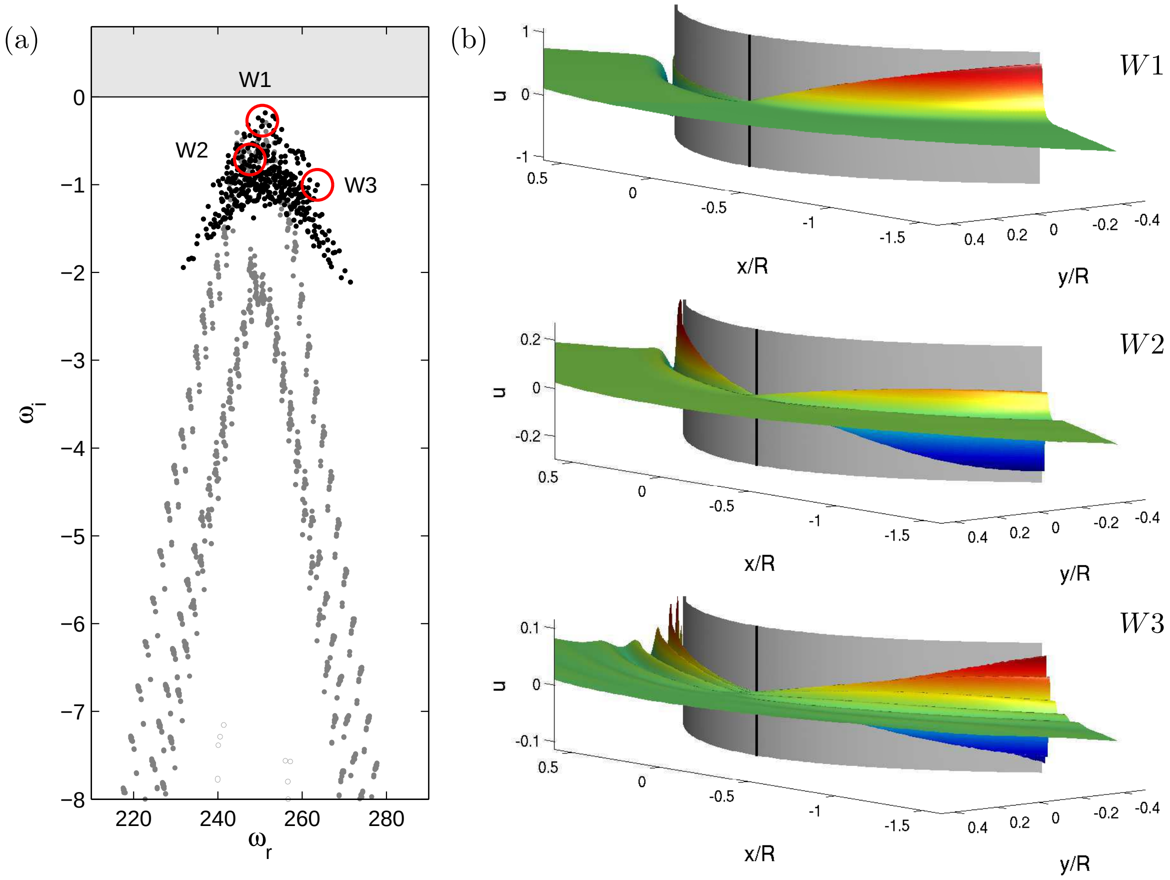

Figure 9. (a) Computed region of the global spectrum containing the eigenvalues belonging to wave packet modes (see region IV in figure 4). (b) Three representative wave packet modes ($W1$, $W2$ and $W3$) are visualized by the (normalized) chordwise velocity u; attachment line in black.

localized region, the coarser the structures on the outside (see figure 8d).

This type of modes is believed to account for the interaction of a moving flexible shock and a rigid curved surface, and these modes are reminiscent of localized standing waves. The increasingly finer spatial scales of the higher-order modes are linked to higher damping rates. The localized spatial shape of the modes is also influenced by the different reflective behavior (impedance) of acoustic waves by the curved solid surface (perfect reflection) and the curved flexible shock (imperfect reflection).

4.1.4 *Wave packet modes*

Returning to the global spectrum in figure 4 a distinct set of eigenvalues centered around the mean spanwise velocity is clearly visible. This region IV is again plotted in figure 9(a), and it shows a dense clustering of damped eigenvalues confined to a triangular-shaped region. The exact location of individual eigenvalues within this region is highly sensitive to numerical details. For this reason, it can be assumed, and will be later argued, that this part of the spectrum consists of an area which is progressively filled by the discrete eigenvalues as the numerical parameters (resolution, starting vector, Cayley parameters, convergence tolerances, etc.) but not the physical parameters are varied.

The location and distribution of the eigenvalues in region IV suggest a link to the continuous spectrum, familiar from boundary layers (Grosch and Salwen, 1978; Balakumar and Malik, 1992) and other semi-infinite and bi-infinite viscous shear flows. In the boundary-layer case, the continuous spectrum can be determined by a constant coefficient Orr–Sommerfeld equation for the freestream. Its solutions are given by bounded exponential and trigonometric functions; the

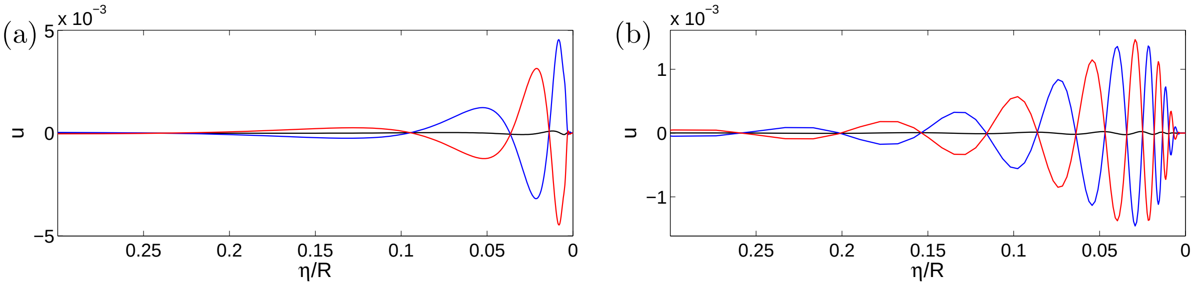

Figure 10. Amplitude distribution of two wave packet modes shown in figure 9: (a) $W2$ and (b) $W3$. The modes are visualized using cross-cut profiles at the attachment line (in black) and at selected positions near the attachment line.

location of the spectrum is defined by a line parameterized by a wall-normal wavenumber.

In contrast, our governing equations evaluated in the freestream still retain a dependence on the wall-normal coordinate via the non-uniform base velocity. As a consequence, the solutions in the freestream are no longer wave trains (as, for instance, in the boundary layer) but rather localized wave packets. As an example, three representative modes ($W1$, $W2$ and $W3$) from region IV are displayed in figure 9(b) which show the spatial distribution of u in the normal direction in form of a wave packet; this property is even more visible in figure 10 where we present cross-cut profiles of $W2$ and $W3$ in the normal direction near the attachment line. These cross-cuts also demonstrate, even though barely visible, that the wave packet modes extend into the boundary layer and thus establish a connection between boundary-layer and exterior perturbation dynamics. They are thus certain to play a critical role in the receptivity of boundary-layer instabilities to the external disturbance environment.

A consequence of the wave packet shape is its parameterization by *two* variables, a wall-normal local wavenumber and the location of the wave packet peak (Trefethen, 2005; Obrist and Schmid, 2009). For this reason, the associated continuous spectrum is area-filling as the continuous spectrum for the boundary layer was line-filling due to only *one* variable, the wall-normal local wavenumber.

4.2. *Parameter studies*

Compressible flow around a swept parabolic body is governed by a large number of parameters describing various flow quantities, fluid properties and geometric characteristics of the flow configuration. For a particular choice of parameters, i.e., $Re_s = 800$, $Re_R = 129136$, $Ma_s = 1.25$, $\theta_w = 1$ and $\beta = 0.314$, the global spectrum (see figure 4) revealed that the only temporal instabilities arise from boundary-layer and/or acoustic modes. To gain further insight into the global stability properties of both types of instabilities, we present a parametric study of their stability behavior by varying the spanwise disturbance wavenumber $\beta = 2\pi/L_z$ and the leading-edge Reynolds number Re_R. In particular, we focus on the stability of the global modes in region I and II in figure 4.

The first parametric study allows us to investigate the linear stability of a computed base flow with respect to spanwise-propagating perturbations with a fundamental length scale L_z. The second parametric study assesses the influence of the leading-edge Reynolds number Re_R, via the leading-edge radius R, on the stability of the flow. This influence is particularly important for the global stability of the boundary-layer modes. Such a study requires, for each value of Re_R, the computation of a steady base flow, even though the freestream conditions remain fixed. For all other types of parameter studies, for example, the influence of the sweep Reynolds number $Re_s = Re_s(M_1, \Lambda)$ or the sweep Mach number $Ma_s = Ma_s(M_1, \Lambda)$, the nonlinear dependence

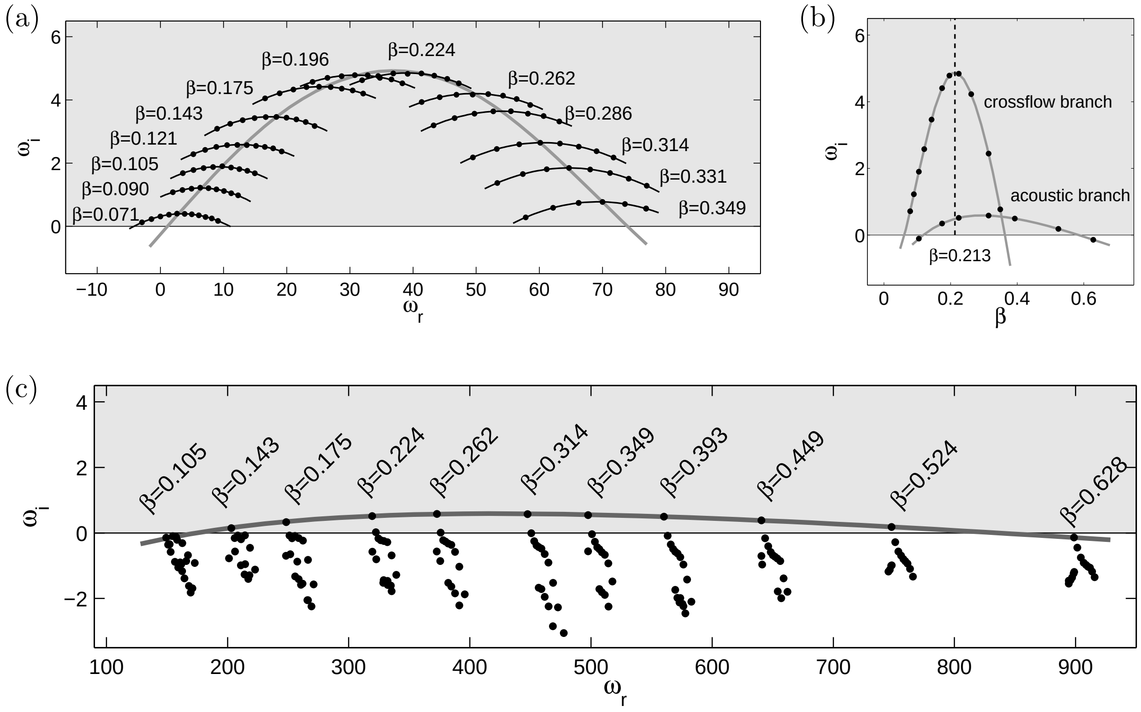

Figure 11. Influence of the spanwise disturbance wavenumber β on the stability of the flow: (a) temporal spectra of the least-stable boundary-layer modes for selected values of β; unstable half-plane in grey. The solid line in dark grey describes the evolution of the maximum temporal growth rate $\omega_{i,max}$, and the evolution of $\omega_{i,max}$, denoted by crossflow branch, as a function of β is shown in (b); (c) Temporal spectra and evolution of the maximum temporal growth rate $\omega_{i,max}$ of the least-stable acoustic modes; the corresponding acoustic branch is displayed in (b).

between the governing parameters (see section §2) requires a substantial effort for a systematic exploration of the four-dimensional parameter space.

4.2.1 *Influence of the spanwise disturbance wavenumber* β

The influence of the spanwise disturbance wavenumber on the boundary-layer modes was already discussed in Mack et al. (2008) for $0.090 \leq \beta \leq 0.314$ where they found a maximum modal growth for $\beta = 0.213$. For a more comprehensive parameter study the application of the Cayley-transformed Arnoldi method, as employed in this article, was found to be mandatory for accessing selected parts of the global spectrum and to investigate a larger range of spanwise wavenumbers β. The computed temporal spectra of the (most unstable) boundary-layer modes are shown in figure 11(a) for $0.071 \leq \beta \leq 0.349$. For a given value of β, the frequency ω_r and its corresponding growth rate ω_i reveal an unstable discrete branch as discussed in section §4. Each branch displays a maximum value of the growth rate ω_i, and this value appears to grow steadily up to a specific wavenumber β before decaying again (see crossflow branch in figure 11b). The same figure 11(b) indicates that the boundary-layer modes are unstable for $0.061 \leq \beta \leq 0.363$.

By adjusting the parameters in the Cayley transformation (3.6), we are also able to focus on the computation of fast-moving acoustic modes (see region II in figure 4). In figure 11(c), we present the influence of β on the stability of these modes. We observe clusters of discrete acoustic eigenvalues where the least-stable mode belongs to the S-branch. This mode is, similar to the most unstable boundary-layer mode, unstable for a specific range of spanwise wavenumbers $0.118 \leq \beta \leq 0.585$ (see acoustic branch in figure 11b). It is furthermore evident from the same figure that the overall prevailing instability can come from either branch depending on the spanwise scale of the perturbation.

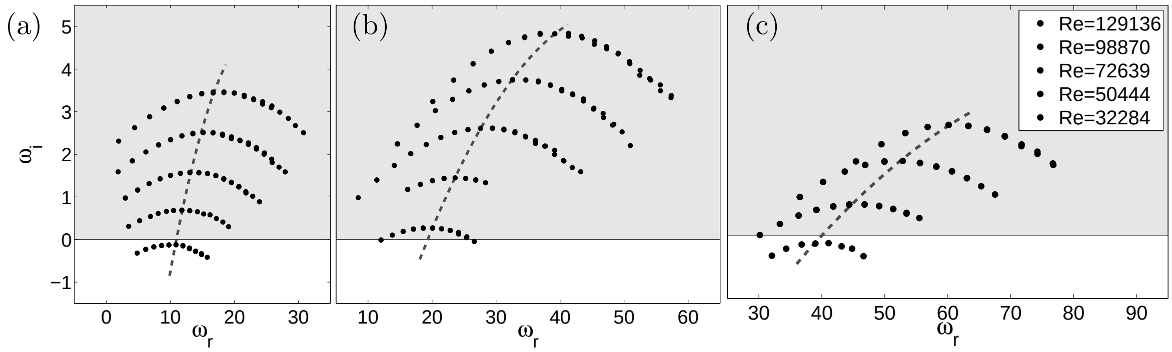

Figure 12. Influence of the leading-edge Reynolds number Re_R on the stability of the flow: (a) $\beta = 0.143$, (b) $\beta = 0.224$ and (c) $\beta = 0.314$. Re_R ranges from 129136 to 32284 (Re_s decreases from 800 to 400 with a step size of 100) from the top to the bottom. The dashed lines indicate the evolution of the maximum growth rate $\omega_{i,max}$.

4.2.2 *Influence of the leading-edge Reynolds number* Re_R

The influence of the leading-edge Reynolds number Re_R on the global stability of the flow is demonstrated in figure 12. As mentioned in section §2 variations in the leading-edge Reynolds number Re_R cause a proportional change in the sweep Reynolds number Re_s (see equ. (2.5)). Three spanwise wavenumbers, located near the peak of the crossflow branch in figure 11(b) with $\beta = 0.224$ and from either side of the peak with $\beta = 0.143$ and 0.314, have been selected for this parameter study. As expected, a stabilizing effect due to a convex curvature parameterized by the leading-edge radius R has been found as Re_R is decreased from 129136 to 32284 (and consequently Re_s changes from 800 to 400). This observation is in accordance with wind-tunnel experiments on a swept wing as reported in Bippes (1999) and with theoretical studies on the effect of leading-edge curvature using local models of the attachment-line boundary layer (Lin and Malik, 1997). Our results also indicate that, for the selected values of β, the frequency ω_r of the computed unstable global boundary-layer modes decreases as Re_R is decreased (see dashed lines in figure 12).

5 Summary and Conclusions

The flow about yawed blunt bodies constitutes a configuration with many applications, not only in aeronautics (such as swept wings) but also in general vehicle engineering. A profound understanding of all aspects of this flow, in particular its stability characteristics, is hence important for the geometric design and analysis of any blunt body that is subject to an obliquely impinging flow.

Historically, the flow about swept bodies has been broken down into two local flow models that describe the flow in the neighborhood of the attachment line (stagnation-point flow) and in the region further downstream (three-dimensional boundary-layer flow). Growth rates and modal structures for each of these models have been studied, and deviations from the most common assumptions, among them nonlinearities, curvature and compressibility, have been incorporated, mostly in a perturbative manner. The resulting body of literature still forms the basis for any current design process, despite the fact that discrepancies between the two local models exist. Efforts to connect the dominant structures of these two models have recently been reported (Bertolotti, 1999; Mack et al., 2008); but a first comprehensive study of the *full* global problem has been attempted in the present work. This is possible owing to a DNS-based global stability solver which is based on iterative algorithms and a spectral transformation of the complex eigenvalue plane (Mack and Schmid, 2010).

Due to the complex nature of the flow, which includes curved geometry and compressibility effects, the global spectrum is accordingly rich and intricate. Nevertheless, distinct modal structures could be identified and catalogued. Boundary-layer modes, describing the perturbation dynamics close to the wall, are dominated by structures reminiscent of cross-flow vortices which connect to associated attachment-line modes. For specific parameter combinations, modes from this boundary-layer branch become unstable. Acoustic modes have been observed to fall into two categories: common wave-like structures that progagate at approximately the respective characteristic velocities, i.e., the mean spanwise velocity plus or minus the speed of sound, and acoustic standing waves communicating between the flexible bow shock and the attachment-line region of the solid body. Symmetry properties and a hierarchy of increasingly finer spatial scales parameterize both types of acoustic modes. Wave packet modes complete the global spectrum and describe the perturbation dynamics between the edge of the boundary layer and the bow shock. They represent the equivalent of what is known in semi- and bi-infinite flows as the continuous spectrum. Evidence supports the fact that for our flow case this continuous spectrum covers an area of the complex plane, rather than a curve as is the case, e.g., for classical flat-plate boundary layers.

In general, advanced numerical techniques — both for providing highly-resolved flow fields and for processing them by modern iterative algorithms — are capable of tackling the global stability problem of complex flows without the need to resort to local models or simplifying assumptions. Such a type of stability analysis, employed in this study for compressible flow about a swept parabolic body, gives a more complete and encompassing picture of the flow behavior, and the challenge of interpreting the spectral features of the flow far outweighs the insight one gains into the global perturbation dynamics.

Acknowledgments

Financial support from the Deutsche Forschungsgemeinschaft (DFG), the Studienstiftung des Deutschen Volkes, the Alexander-von-Humboldt Foundation and the ANR program “Chaires d’excellence” is gratefully acknowledged.

References

Åkervik, E., Brandt, L., Henningson, D. S., Hœpfner, J., Marxen, O., and Schlatter, P. (2006). Steady solutions of the Navier–Stokes equations by selective frequency damping. *Phys. Fluids*, 18(068102).

Bagheri, S., Schlatter, P., Schmid, P., and Henningson, D. (2009). Global stability of a jet in crossflow. *J. Fluid Mech.*, 624:33–44.

Balakumar, P. and Malik, M. R. (1992). Discrete modes and continuous spectra in supersonic boundary layers. *J. Fluid Mech.*, 239:631–656.

Barkley, D., Gomes, M. G. M., and Henderson, R. D. (2002). Three-dimensional instability in flow over a backward-facing step. *J. Fluid Mech.*, 473:167–190.

Barkley, D. and Henderson, R. D. (1996). Three-dimensional Floquet stability analysis of the wake of a circular cylinder. *J. Fluid Mech.*, 322:215–241.

Bertolotti, F. P. (1999). On the connection between cross-flow vortices and attachment-line instabilities. In *IUTAM Symposium on Laminar-Turbulent Transition*, pages 625–630, Sedona, USA.

Bippes, H. (1999). Basic experiments on transition in three-dimensional boundary layers dominated by crossflow instability. *Prog. Aero. Sci.*, 35:363–412.

Bonfigli, G. and Kloker, M. (2007). Secondary instability of crossflow vortices: validation of the stability theory by direct numerical simulation. *J. Fluid Mech.*, 583:229–272.

Gray, W. E. (1952). The effect of wing sweep on laminar flow. Technical Report RAE TM Aero 255, British Royal Aircraft Establishment.

Grosch, C. E. and Salwen, H. (1978). The continuous spectrum of the Orr–Sommerfeld equation. Part I. The spectrum and the eigenfunctions. *J. Fluid Mech.*, 87:33–54.

Hall, P., Malik, M., and Poll, D. I. A. (1984). On the stability of an infinite swept attachment-line boundary layer. *Proc. R. Soc. Lond.*, A(395):229–245.

Jackson, C. P. (1987). A finite-element study of the onset of vortex shedding in flow past variously shaped bodies. *J. Fluid Mech.*, 182:23–45.

Joslin, R. D. (1995). Direct simulation of evolution and control of three-dimensional instabilities in attachment-line boundary layers. *J. Fluid Mech.*, 291:369–392.

Joslin, R. D. (1996). Simulation of nonlinear instabilities in an attachment-line boundary layer. *Fluid Dyn. Res.*, 18:81–97.

Kazakov, A. V. (1990). Effect of surface temperature on the stability of swept attachment line boundary layer. *Fluid Dyn.*, 25(6):875–878.

Knoll, D. A. and Keyes, D. E. (2004). Jacobian-free Newton–Krylov methods: a survey of approaches and applications. *J. Comput. Phys.*, 193(2):357–397.

Lehoucq, R. B., Sorensen, D. C., and Yang, C. (1998). *ARPACK Users' Guide.* Software, Environments, and Tools. Society for Industrial and Applied Mathematics (SIAM), Philadelphia, PA. Solution of Large-Scale Eigenvalue Problems with Implicitly Restarted Arnoldi Methods.

Lin, R. S. and Malik, M. R. (1995). Stability and transition in compressible attachment-line boundary-layer flow. Technical Report 952041, SAE.

Lin, R. S. and Malik, M. R. (1996). On the stability of attachment-line boundary layers. Part 1. The incompressible swept Hiemenz flow. *J. Fluid Mech.*, 311:239–255.

Lin, R. S. and Malik, M. R. (1997). On the stability of attachment-line boundary layers. Part 2. The effect of leading edge curvature. *J. Fluid Mech.*, 333:125–137.

Mack, C. J. and Schmid, P. J. (2009). Direct numerical simulations of hypersonic flow about a swept parabolic body. *Comput. Fluids.* submitted.

Mack, C. J. and Schmid, P. J. (2010). A preconditioned Krylov technique for global hydrodynamic stability analysis of large-scale compressible flows. *J. Comput. Phys.*, 229(3):541–560.

Mack, C. J., Schmid, P. J., and Sesterhenn, J. L. (2008). Global stability of swept flow around a parabolic body: connecting attachment-line and crossflow modes. *J. Fluid Mech.*, 611:205–214.

Mack, L. M. (1984). Boundary layer linear stability theory. Technical Report 709, AGARD.

Moretti, G. (1987). Computations of flows with shocks. *Annu. Rev. Fluid Mech.*, 19:313–337.

Obrist, D. and Schmid, P. J. (2009). Algebraically decaying modes and wave packet pseudomodes in swept Hiemenz flow. *J. Fluid Mech.* in press.

Pfenninger, W. (1977). Laminar flow control – Laminarization. Special course on concepts for drag reduction. Technical Report 654, AGARD.

Poll, D. I. A. (1978). Some aspects of the flow near a swept attachment line with particular reference to boundary layer transition. Technical Report CoA 7805, Cranfield Institute of Technology.

Poll, D. I. A. (1979). Transition in the infinite swept attachment-line boundary layer. *Aero. Q.*, 30:607–628.

Saad, Y., editor (2003). *Iterative Methods for Sparse Linear Systems, Second Edition.* Society for Industrial and Applied Mathematics.

Saric, W. S., Reed, H. L., and White, E. B. (2003). Stability and transition of three-dimensional boundary layers. *Annu. Rev. Fluid Mech.*, 35:413–440.

Semisynov, A. I., Fedorov, A. V., Novikov, V. E., Semionov, N. V., and Kosinov, A. D. (2003). Stability and transition on a swept cylinder in a supersonic flow. *Journal of Applied Mechanics and Technical Physics*, 44:212–220.

Sipp, D. and Lebedev, A. (2007). Global stability of base and mean flows: a general approach and its applications to cylinder and open cavity flows. *J. Fluid Mech.*, 593:333–358.

Sorensen, D. C. (1992). Implicit application of polynomial filters in a k-step Arnoldi method. *SIAM J. Matrix Anal. Appl.*, 13(1):357–385.

Spalart, P. R. (1988). Direct numerical study of leading-edge contamination. In *AGARD-CP-438*, pages 5/1–5/13.

Theofilis, V. (2003). Advances in global linear instability analysis of nonparallel and three-dimensional flows. *Prog. Aero. Sci.*, 39:249–315.

Trefethen, L. N. (2005). Wave packet pseudomodes of variable coefficient differential operator. *Proc. Roy. Soc. A*, 461(2062):3099–3122.

van der Vorst, H. A. (1992). Bi-CGStab: A fast and smoothly converging variant of Bi-CG for the solution of non-symmetric linear systems. *SIAM J. Sci. Statist. Comput.*, 13:631–644.

Zebib, A. (1987). Stability of viscous flow past a circular cylinder. *J. Eng. Math.*, 21:155–165.

Article 5

Global stability of swept flow around a parabolic body: the neutral curve

By C. J. Mack[1,2] and P. J. Schmid[1]

[1]Laboratoire d'Hydrodynamique (LadHyX), CNRS-École Polytechnique,
F-91128 Palaiseau, France

[2]Department of Numerical Mathematics, Universität der Bundeswehr (UniBw),
D-85577 Munich, Germany

Published in *J. Fluid Mech.* (2009), to be submitted

The onset of transition in the leading-edge region of a swept blunt body depends on the stability characteristics of the flow. Modeling this flow configuration by swept flow around a parabolic body a global approach is taken to extract pertinent stability information via a DNS-based iterative eigenvalue solver. Global modes combining features from boundary-layer and acoustic instabilities are presented. A parameter study, varying the spanwise disturbance wavenumber and the sweep Reynolds number, showed the existence of unstable boundary-layer and acoustic modes. The corresponding neutral curve displays two overlapping regions of exponential growth and two critical Reynolds numbers, one for boundary-layer instabilities and one for acoustic instabilities. The employed global approach is expected to shed more light on the rich perturbation dynamics of swept leading-edge flow, particularly, in the subcritical regime.

1 Introduction

Since the early fifties the problem of transition in the leading-edge region of *swept* wings has been central to a great deal of investigations concerning the design of high-performance aircraft. This problem was first observed in early flight tests on swept wing aircraft, where Gray (1952) found that beyond a critical freestream velocity the transition front moved toward the attachment line of the wing, a feature that could not be explained by existing two-dimensional arguments. Furthermore, the employed flow visualization technique showed a series of closely-spaced streaky structures almost aligned with the external streamlines of the flow. Subsequent investigations confirmed these streaky structures as a consequence of crossflow instabilities.

In an attempt to gather further information on leading-edge transition, Pfenninger conducted a series of flight tests on a swept X-21 wing in 1963, where he observed that *unexpectedly* high suction rates had to be applied to eliminate the crossflow vortices and to thus achieve laminar flow over the outer part of the wing. This strong suction was required particularly in the wing's leading-edge region which indicated that rather strong disturbances had to be present in the laminar boundary layer originating near the upstream part of the wing. Evaluating his database (Pfenninger, 1965), he was able to establish a criterion for the existence of spanwise contamination along the wing's leading edge in the presence of an initially turbulent attachment-line boundary layer emanating from the wing-body junction. He further realized that maintaining a full-chord laminar flow on an X-21 wing critically depended on the existence of an undisturbed laminar attachment-line boundary layer, thus stressing the importance of flow instabilities in the vicinity of the attachment line. Pfenninger's criterion is expressed as a critical sweep Reynolds number of $\bar{R} \approx 245$, which corresponds to a Reynolds number of $R_\theta \approx 100$ (based on the momentum thickness), to avoid leading-edge contamination, and this value to this day still guides state-of-the-art design efforts for swept wings.

The observed prevalence of crossflow vortices in the experiments of, among others, Pfenninger (1965) and Poll (1979) led, in the beginning, to the hypothesis of a leading-edge transition that is based on crossflow vortices; however, doubts remained as to their singular role. In wind-tunnel experiments on a swept wing configuration with a semi-circular leading edge, Poll (1979) reported that the flow is also susceptible to instabilities close to the attachment line and established attachment-line instabilities as a viable alternative governing the stability of leading-edge flow. Summarizing his investigations of incompressible swept attachment-line boundary-layer flow he confirmed Pfenninger's critical Reynolds numbers of $\bar{R} \approx 245$ for finite-amplitude disturbances and furthermore established a critical Reynolds number of $\bar{R}_{crit} \approx 570$ for small-amplitude perturbations. The discrepancy between these two critical Reynolds numbers indicates the subcritical nature of leading-edge transition, and an interplay between linear and nonlinear mechanisms is expected in this parameter range (see, e.g., Joslin, 1996). Investigations into the subsonic, supersonic and hypersonic flow regime have been undertaken by many scientists, and a comprehensive summary of their results is given in Poll (1983) and Gaillard et al. (1999). Adopting a reference temperature concept, a unique critical Reynolds number of $\bar{R}^* \approx 245$ has been determined for a finite-amplitude disturbance environment (Poll, 1983). For infinitesimal perturbations a critical Reynolds number of $\bar{R}^*_{crit} \approx 650$ has been found (see, e.g., Gaillard et al., 1999). In both cases, the critical Reynolds numbers appear to be independent of the sweep Mach number Ma_s up to a value of $Ma_s \approx 5$.

The experimental results as well as the need to fully understand swept leading-edge flow have fueled a substantial effort (see, e.g., Hall et al., 1984; Hall and Malik, 1986; Spalart, 1988; Joslin, 1995; Lin and Malik, 1996; Semisynov et al., 2003) to investigate the flow behavior governed by the two identified mechanisms, i.e., attachment-line instabilities and crossflow vortices. These investigations, however, have been based on local flow models for either instability mechanism which was a necessary step to apply classical tools of hydrodynamic stability theory. Despite remarkable theoretical and numerical efforts based on these local models our understanding of the mechanisms behind the perturbation dynamics in the subcritical range still remains incomplete, even though limited success, such as approximating the critical Reynolds number for attachment-line instabilities (Hall et al., 1984; Lin and Malik, 1996), has been achieved.

The shortcomings of the local flow models have been discussed by a number of scientists, and the potential of a global stability approach based on a comprehensive flow model is unquestionable. Such an approach will yield a more complete understanding of swept leading-edge flow and help answer questions such as the connection between attachment-line instabilities and crossflow vortices. An approach of this type has already been alluded to by Lin and Malik (1996) who stated that "... By choosing a computational domain large enough in the [chordwise] direction to cover both the attachment-line instability and crossflow instability regions, and by using an appropriate spatial resolution, the two-dimensional eigenvalue approach can provide us with a means to explore this connection ...". Based on such a global approach this connection has been established in Mack et al. (2008), and the same line of analysis will be further pursued in this article to explore the parameter dependence of swept flow around a parabolic body.

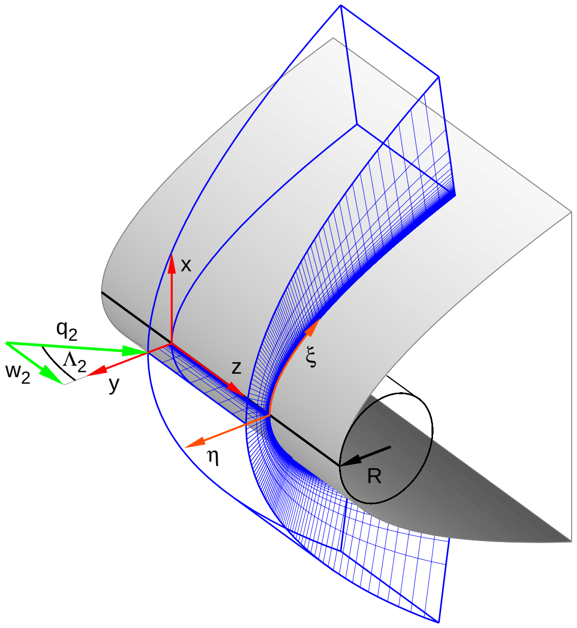

Figure 1. Sketch of supersonic flow about a swept parabolic body.

2 Flow model, governing parameters and numerical method

Our model consists of supersonic flow about a swept parabolic body displayed (in grey) in figure 1. The same figure introduces the used three-dimensional body-fitted grid (in blue), and two coordinate systems: a local (x, y, z) Cartesian coordinate system (in red) and a local parabolic (ξ, η, z) coordinate system (in orange). The attachment line (in black) coincides with the spanwise z-direction. The surface of the parabolic body is given by $y(x) = -1/(2R)x^2$, where R denotes its leading-edge radius. We consider flow situations where the oncoming flow is supersonic $M_1 = M_\infty \cos\Lambda > 1$, with M_∞ and M_1 respectively denoting the freestream Mach number and its normal component; Λ stands for the freestream angle. The computational domain is limited by a detached unsteady bow shock in the wall-normal direction, and this shock, assumed to be an infinitely thin, moving discontinuity, acts as the inflow boundary. The supersonic flow state upstream of the detached bow shock is given by the Mach number M_∞, the freestream angle Λ as well as the pressure p_∞ and temperature T_∞. Via the Rankine–Hugoniot relations, the flow state downstream of the shock, denoted by the subscript $_2$, is obtained. As a result, the incoming flow impinges on the body with a velocity q_2 and a sweep angle Λ_2 yielding a sweep velocity w_2 and a normal velocity v_2 (see figure 1).

This flow configuration is characterized by two distinct length scales, the leading-edge radius R and a viscous length scale δ, which describe the outer flow and the flow inside the boundary layer, respectively. We define the viscous length scale as

$$\delta = \left(\frac{\nu_r}{S}\right)^{1/2} \qquad \text{with} \qquad S = \left(\frac{\partial u}{\partial x}\right)_w = \frac{2v_2}{R}, \tag{2.1}$$

where S is the strain rate at the wall, evaluated at the attachment line. Its value is approximated using the potential solution of flow around a circular cylinder with radius R. Based on these two length scales we define a sweep Reynolds number Re_s and a leading-edge Reynolds number Re_R as

$$Re_s = \frac{w_2\delta}{\nu_r}, \qquad Re_R = \frac{v_2 R}{\nu_r}, \tag{2.2}$$

where ν_r denotes the kinematic viscosity evaluated at recovery temperature T_r and stagnation pressure p_s. We further consider a supersonic sweep Mach number of $Ma_s = w_2/c_2 = 1.25$ and assume an adiabatic wall, i.e., the ratio of the temperature T_w at the wall and T_r is $\theta_w = T_w/T_r = 1$.

It is instructive to demonstrate an explicit dependence of the sweep Reynolds number Re_s on the sweep angle Λ_2 and the leading-edge radius R as well as the leading-edge Reynolds number Re_R according to

$$Re_s = \left(\frac{q_2 R}{\nu_r}\frac{\sin\Lambda_2 \tan\Lambda_2}{2}\right)^{1/2} = \left(\frac{Re_R}{2}\right)^{1/2}\tan\Lambda_2 = \frac{R}{2\delta}\tan\Lambda_2. \tag{2.3}$$

The definition in (2.3) was used by Poll (1979) for incompressible flow over a swept cylinder. For compressible flow it was extended using a reference temperature concept (see Poll, 1984) where the kinematic viscosity ν^* in the sweep Reynolds number $\bar{R}^*$ is evaluated at a reference temperature T^* given by $T^* = T_e + 0.1(T_w - T_e) + 0.6(T_r - T_e)$; the temperature T_e is computed at the boundary-layer edge.

The governing compressible Navier–Stokes equations are solved on a curvi-linear, moving and body-fitted mesh using high-order compact finite-difference schemes and high-order time stepping. Shock-fitting techniques, a characteristic-type formulation and standard non-reflecting outflow boundary conditions are used, and further details about the direct numerical simulation (DNS) are given in Mack and Schmid (2009a). To properly resolve small-scale features inside the boundary layer as well as near the attachment line a highly non-uniform grid distribution is employed, as indicated in figure 1.

3 Global stability analysis

It should be evident that stability studies of flow about a blunt body such as a swept wing no longer allows the standard simplifying assumptions of multiple homogeneous coordinate directions or a low-Mach number approximation. Rather, a global approach has to be adopted to extract pertinent stability information about the flow. An approach of such type has already been amply motivated in the introduction where we concluded that further advances in our understanding of leading-edge contamination critically relies on the formulation of a global stability problem.

We therefore assume a three-dimensional perturbation field, which in our case consists of the pressure, velocity components and entropy, i.e., $\phi' = (p', u', v', w', s')^T$, superimposed on a steady base flow ϕ_0 according to

$$\phi(x,y,z,t) = \phi_0(x,y,z) + \epsilon\phi'(x,y,z,t) \qquad \epsilon \ll 1. \tag{3.1}$$

The base flow ϕ_0 is computed as a steady solution of the nonlinear compressible Navier–Stokes equations by time marching the direct numerical simulation (DNS) code.

Despite the complexity of our flow model we can still take advantage of the homogeneous spanwise z-direction in form of a Fourier transform in z introducing a spanwise wavenumber β. Physically, this corresponds to a swept parabolic body of infinite span. Assuming exponential behavior in time, we take the perturbation in (3.1) in the form of traveling waves according to

$$\phi'(x,y,z,t) = \widetilde{\phi}(x,y)\mathrm{e}^{\mathrm{i}(\beta z - \omega t)}. \tag{3.2}$$

In this expression, $\widetilde{\phi}(x,y)$ denotes the complex amplitude of the disturbance, and its temporal long-term evolution is given by ω whose real part ω_r describes the frequency and whose imaginary part ω_i represents the corresponding growth rate.

Characteristic information about the stability behavior of compressible flow about a swept parabolic body is contained in the global modes $\widetilde{\phi}(x,y)$, which present the spatial shape of the

Re_s	Re_R	R_δ	δ in 10^{-4} [m]	$\bar{R}^*$
800	129136	508	1.968	840
600	72639	381	2.624	630
400	32284	254	3.935	420

Table 8. Values of the Reynolds numbers, as defined in section §2, of the investigated parameter choices.

instabilities, and the corresponding global eigenvalues ω, which describe the associated temporal dynamics. This information is extract by a applying a DNS-based iterative global stability solver which consists of the implicitly restarted Arnoldi method (see Lehoucq et al., 1998) combined with a conformal map (Cayley transformation) of the complex eigenvalue plane. By implementing a Jacobian-free framework, flow fields computed by the direct numerical simulations (DNS) provide the required input for the Arnoldi method, and a shift parameter σ in the Cayley transformation allows us to manipulate the computed flow fields and direct the convergence of the Arnoldi method toward specific global modes. In this manner, we are able to scan the physically relevant regions of the full global stability spectrum. For more details about the DNS-based global stability solver the reader is referred to Mack and Schmid (2010).

4 Results

Compressible flow around a swept parabolic body (see figure 1b) exhibits a complex perturbation dynamics and thus features a wide and rich variety of global modes. This fact has already been discussed in Mack and Schmid (2009b) where several types of global modes have been uncovered for $Re_s = 800$, $Re_R = 129136$, $Ma_s = 1.25$, $\theta_w = 1$ and $\beta = 0.314$: stable and unstable boundary-layer modes, different types of stable and unstable acoustic modes and stable wave packet modes have been found. Furthermore, the present flow configuration is governed by a large number of parameters describing various flow quantities, fluid properties and geometric characteristics of the flow. Among these parameters, the influence of the spanwise wavenumber β and the leading-edge Reynolds number Re_R on the global stability of the flow has been briefly addressed in Mack and Schmid (2009b). A more comprehensive study including the neutral curve will be presented in what follows.

4.1. *Spectrum and global modes*

Boundary-layer instabilities have been found in previous studies (Mack and Schmid, 2009b) to play a dominant role in the transition process. For this reason we start by presenting results from the global spectrum which is displayed in figure 2(a) for a sweep Reynolds number of $Re_s = 800$ and a spanwise wavenumber of $\beta = 0.314$. It shows (in blue) a characteristic parabolic shape of discrete global modes which are unstable for a frequency range of $36 \lesssim \omega_r \lesssim 93$. The most unstable modes from this branch for $Re_s = 800$, 600 and 400 are shown in figure 2(b); this time the spanwise disturbance wavenumber was chosen as $\beta = 0.224$ which is close to 0.213, the value for the most amplified perturbations (see Mack and Schmid, 2009b). Figure 2(b) further shows that decreasing Re_s — which is equivalent to decreasing the leading-edge Reynolds number Re_R and thus the leading-edge radius R (see table 8) — has a stabilizing effect on boundary-layer modes.

In figure 3, we present the spatial distribution of three global boundary-layer modes each belonging to the most unstable eigenvalue (depicted by a circle) of the three eigenvalue branches in figure 2. The modes are visualized by iso-surfaces of the normal velocity v, and 8 periods in the spanwise z-direction are used; furthermore, contours of the associated pressure field of each mode

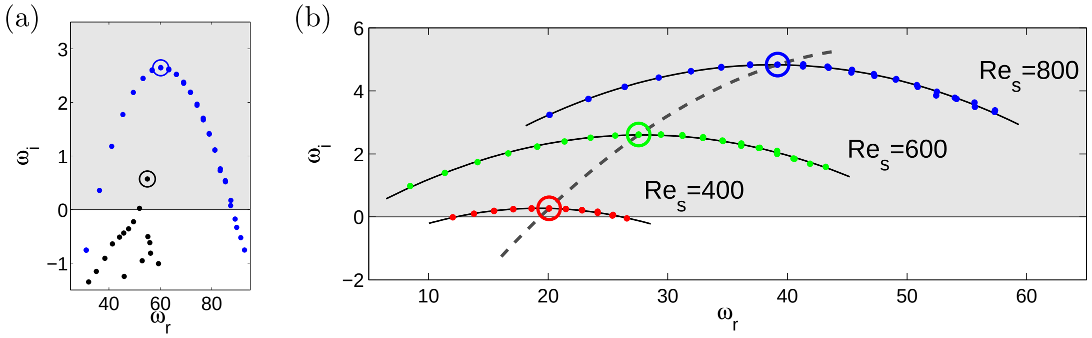

Figure 2. (a) Part of the full global spectrum showing the least-stable boundary-layer modes (in blue) and the slow-moving set of acoustic modes (in black) as presented in Mack and Schmid (2009b); unstable half-plane in light grey. (b) Least-stable eigenvalues, belonging to global boundary-layer modes, of the global spectrum for selected sweep Reynolds numbers Re_s ($Ma_s = 1.25$, $\theta_w = 1$ and $\beta = 0.224$). The dashed line indicates the evolution of the maximum growth rate.

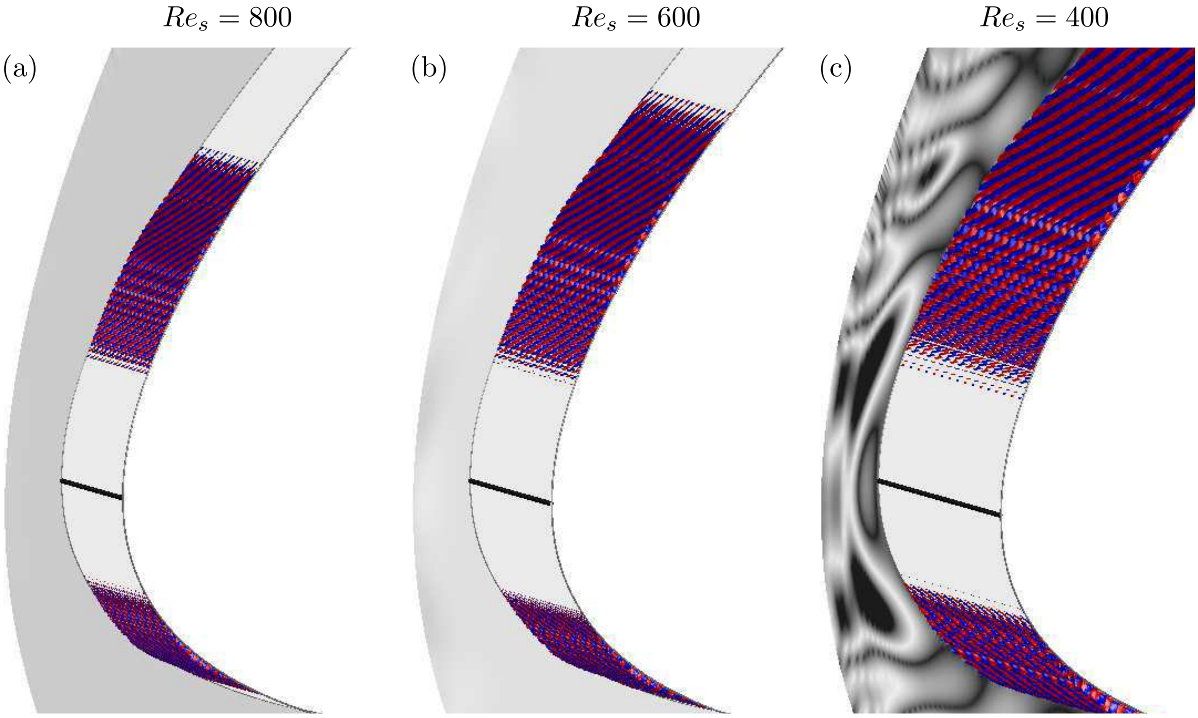

Figure 3. Spatial structure of a the most unstable boundary-layer modes (depicted by circles in figure 2a) visualized by iso-surfaces (positive values in red, negative values in blue) of the normal velocity $v(x, y, z) = \text{Real}\{\tilde{v}(x, y)\,(\cos\beta z + \mathrm{i}\sin\beta z)\}$; eight periods in z are shown; attachment line in black: (a) $Re_s = 800$, (b) $Re_s = 600$ and (c) $Re_s = 400$. Contours of the associated pressure field of each mode are displayed in the background.

are plotted in a wall-normal cross plane at $z = 0$. The noticeably different size of the domain in z, for a fixed wavenumber β, is the consequence of our definition of the spanwise length scale $L_z = (2\pi/\beta)\cdot\delta$, where the viscous length scale δ depends on the sweep Reynolds number Re_s (see table 8). The disturbance wave length thus scales with the length scale δ and the thickness of the boundary layer $\delta_{99} \approx 2.38\delta$. Regarding the structure of the global modes in figure 3 we identify typical features of crossflow instabilities: co-rotating vortices that almost align with the external streamlines. Closer inspection of their spatial distribution, as Re_s is decreased from 800 to 400 (see figure 3a–c), reveals, as we proceed downstream from the attachment

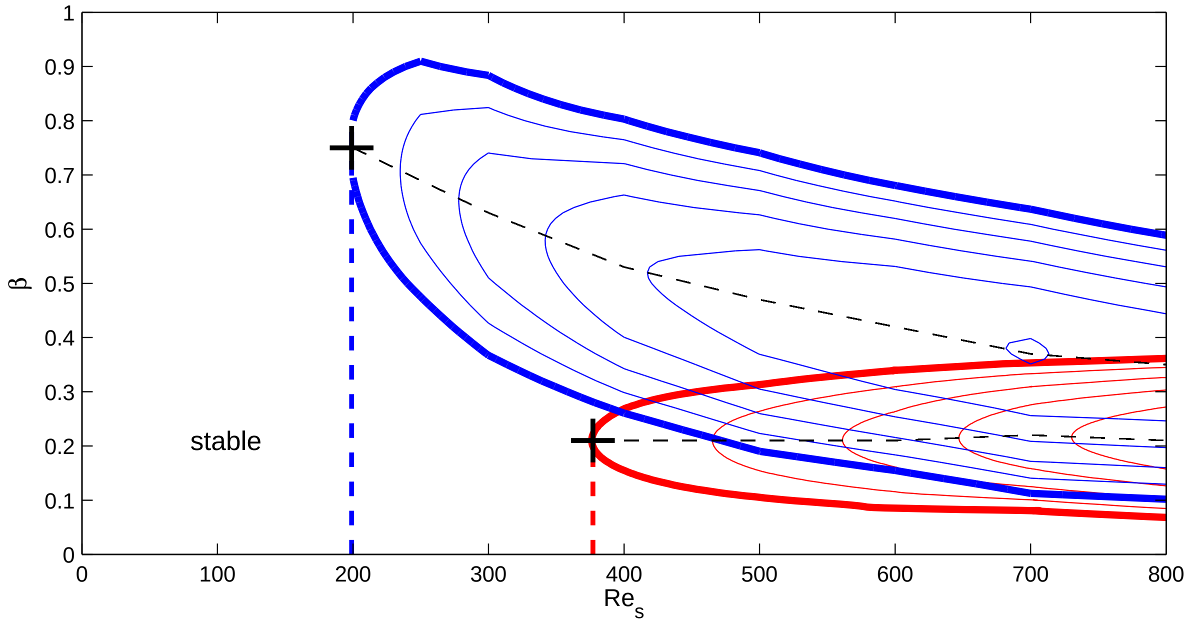

Figure 4. Neutral curve for supersonic flow about a swept parabolic body for a sweep Mach number $Ma_s = 1.25$ and an adiabatic wall (boundary-layer modes in red, acoustic modes in blue); contour spacing for the boundary-layer modes $\Delta\omega_i = 1$, contour spacing for the acoustic modes $\Delta\omega_i = 0.1$. The dashed lines indicate the evolution of the maximum value of the growth rate.

line, (i) a weaker spatial exponential growth, causing (ii) a shift of the maximum amplitude in the chordwise direction, followed by (iii) a weaker exponential decay further downstream. A consequence of this behavior is, on one hand, a more compact spatial distribution closer to the attachment line of more unstable global modes at higher Reynolds numbers and, on the other hand, a substantially more elongated spatial distribution farther downstream from the attachment line of less unstable global modes. It is these latter modes that are capable of describing the dynamics in the entire leading-edge region and, at same time, of establishing a possible link to Tollmien–Schlichting-type instabilities even further downstream.

Regarding the associated pressure field of the global modes in figure 3 an interesting feature is observed. While the global modes in figure 3(a,b) do not display any pronounced pressure field, the global mode in figure 3(c) adopts a pressure distribution which is known from the least-stable acoustic mode of the slow-moving acoustic modes (see figure 2a, marked by a black circle). This is a consequence of the coalescence of two eigenvalues, the least-stable eigenvalues of the respective types, for the particular parameter choice $Re_s = 400$ and $\beta = 0.224$, which results in a composite mode (showing typical features of boundary-layer modes and the least-stable acoustic mode).

4.2. *Neutral curve*

The neutral curve for supersonic flow about a swept parabolic body is presented in figure 4. In this figure, we display contours of constant growth rate ω_i for the boundary-layer modes (in red) and the acoustic modes (in blue). The presence of unstable global modes of boundary-layer as well as acoustic type yields a composite neutral stability curve delineating parameter regimes across which either boundary-layer or acoustic modes change from stable to unstable. Boundary-layer instabilities prevail for small spanwise wavenumbers β and cease to exist below a critical Reynolds number of $Re_{s,crit} \approx 377$ (for $\beta = 0.213$). For rather large values of the spanwise disturbance wavenumber β acoustic instabilities dominate the linear stability of the flow even

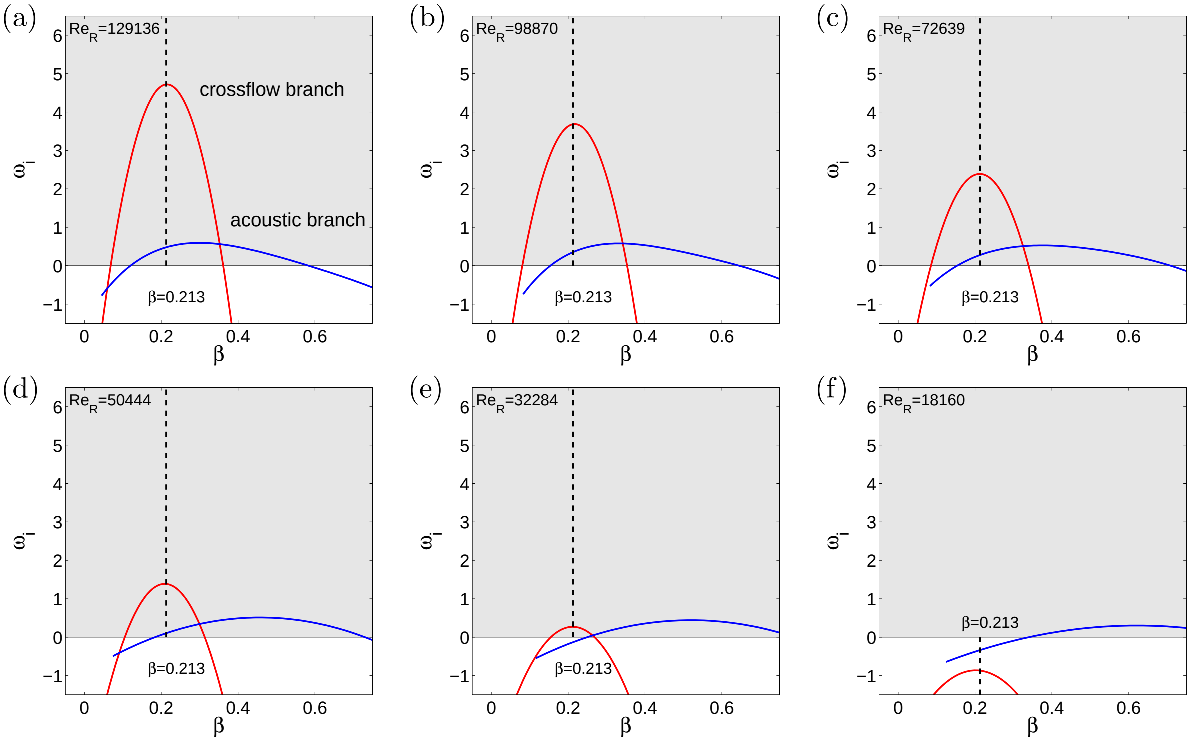

Figure 5. Cross-cuts of the neutral curve in figure 4 showing the influence of β on ω_i for selected values of Re_s; unstable half-plane in light grey.

for sweep Reynolds numbers $Re_{s,crit} < 377$. However, for $Re_s < 195$ acoustic instabilities cease to exist as well.

For more detailed information, cross-cut profiles of the neutral curve for selected values of Re_s are presented in figure 5. The cross-cuts (as well as the neutral curve) show that the boundary-layer modes (denoted by crossflow branch) exhibit significantly larger growth rates ω_i than the acoustic modes for large values of Re_s. These growth rates decay linearly with Re_s; the maximum growth rate is always found at a critical spanwise wavenumber of $\beta = 0.213$. The acoustic modes, on the other hand, show rather weak growth rates, do not scale linearly with Re_s and do not show a Reynolds number independent critical value of β.

The neutral curve displayed in figure 4 represents a two-dimensional cut through a high-dimensional parameter space. The immediate choice of varying parameters consists of the spanwise wavenumber β (based on a one-time computed base flow) and the sweep Reynolds number Re_s (requiring the computation of a new base flow for each value of Re_s). While for these two parameter studies the freestream conditions remain unchanged, investigating the influence of additional parameters (sweep angle, sweep Mach number, wall temperature ratio, etc.) requires a substantial effort owing to the added complication of a nonlinear dependence of these parameters on the freestream conditions (see Mack and Schmid, 2009b, for details).

5 Discussion and Conclusions

The stability of supersonic flow around a swept parabolic body has been studied using a global approach based on a inclusive flow model which incorporates attachment-line instabilities and crossflow vortices. These two instabilities have been identified as the dominant mechanisms for the onset of transition in swept leading-edge boundary-layer flow. Global boundary-layer and acoustic modes have been found to become unstable for specific parameter combinations, and a neutral stability curve for these two types of modes has been presented as a function of the spanwise disturbance wavenumber and the sweep Reynolds number. Two critical Reynolds numbers, based on a boundary-layer or an acoustic instability, have been determined.

Central to our analysis is the global stability approach and consequently the realization that the computed global modes are of composite type combining features from boundary-layer and acoustic instabilities. Even though the global boundary-layer modes show characteristics that are known from the stability analysis of local flow models (for the attachment-line and the flow further downstream), our approach treats the coherent dynamic structures of the flow as one entity. Consequently, stability information obtained from a local approach, which constitutes our current theoretical understanding of swept leading-edge flow, is expected to not coincide with results from a global approach.

The need to venture beyond local investigations together with the observations that provided evidence for a link between attachment-line instabilities and crossflow vortices brought up thoughts about a possible interplay between both instability mechanisms and their combined role in swept leading-edge transition. Motivated by results from direct numerical simulations (DNS) (Spalart, 1989) alluding to a possible link between both instabilities, Bertolotti (1999), starting with a local attachment-line mode and marching in the chordwise direction using the parabolized stability equations (PSE), eventually obtained stability features reminiscent of crossflow vortices. This phenomenological link was later quantified by a global stability analysis (Mack et al., 2008) which lead to a definite connection between attachment-line instabilities and crossflow vortices.

In conclusion, a stability analysis based on a global point of view — avoiding the limitations of local flow models — constitutes a novel approach for swept leading-edge flow, promises new insight into the inherent instability mechanisms and has the potential to uncover a wealth of stability behavior as stated by Joslin (1996). In particular, for the subcritical regime the global stability approach taken in this article is expected to give new results which will help answer some of the remaining questions regarding the onset of transition for swept leading-edge flow.

Acknowledgments

Financial support from the Deutsche Forschungsgemeinschaft (DFG), the Studienstiftung des Deutschen Volkes, the Alexander-von-Humboldt Foundation and the ANR program "Chaires d'excellence" is gratefully acknowledged.

References

Bertolotti, F. P. (1999). On the connection between cross-flow vortices and attachment-line instabilities. In *IUTAM Symposium on Laminar-Turbulent Transition*, pages 625–630, Sedona, USA.

Gaillard, L., Benard, E., and Alziary de Roquefort, T. (1999). Smooth leading edge transition in hypersonic flow. *Experiments in Fluids*, 26:169–176.

Gray, W. E. (1952). The effect of wing sweep on laminar flow. Technical Report RAE TM Aero 255, British Royal Aircraft Establishment.

Hall, P. and Malik, M. (1986). On the instability of a three-dimensional attachment-line boundary layer: weakly nonlinear theory and a numerical approach. *J. Fluid Mech.*, 163:257–282.

Hall, P., Malik, M., and Poll, D. I. A. (1984). On the stability of an infinite swept attachment-line boundary layer. *Proc. R. Soc. Lond.*, A(395):229–245.

Joslin, R. D. (1995). Direct simulation of evolution and control of three-dimensional instabilities in attachment-line boundary layers. *J. Fluid Mech.*, 291:369–392.

Joslin, R. D. (1996). Simulation of three-dimensional symmetric and asymmetric instabilities in attachment-line. *AIAA J.*, 34(11):2432–2434.

Lehoucq, R. B., Sorensen, D. C., and Yang, C. (1998). *ARPACK Users' Guide.* Software, Environments, and Tools. Society for Industrial and Applied Mathematics (SIAM), Philadelphia, PA. Solution of Large-Scale Eigenvalue Problems with Implicitly Restarted Arnoldi Methods.

Lin, R. S. and Malik, M. R. (1996). On the stability of attachment-line boundary layers. Part 1. The incompressible swept Hiemenz flow. *J. Fluid Mech.*, 311:239–255.

Mack, C. J. and Schmid, P. J. (2009a). Direct numerical simulations of hypersonic flow about a swept parabolic body. *Comput. Fluids.* submitted.

Mack, C. J. and Schmid, P. J. (2009b). Global stability of swept flow around a parabolic body: features of the global spectrum. *J. Fluid Mech.* submitted.

Mack, C. J. and Schmid, P. J. (2010). A preconditioned Krylov technique for global hydrodynamic stability analysis of large-scale compressible flows. *J. Comput. Phys.*, 229(3):541–560.

Mack, C. J., Schmid, P. J., and Sesterhenn, J. S. (2008). Global stability of swept flow around a parabolic body: connecting attachment-line and crossflow modes. *J. Fluid Mech.*, 611:205–214.

Pfenninger, W. (1965). Some results form the X-21 programm. Part I - Flow phenomena at the leading edge of swept wings. Technical Report 97, AGARDograph.

Poll, D. I. A. (1979). Transition in the infinite swept attachment-line boundary layer. *Aero. Q.*, 30:607–628.

Poll, D. I. A. (1983). The development of intermittent turbulence on a swept attachment line including the effects of compressibility. *Aero. Q.*, XXXIV:1–23.

Poll, D. I. A. (1984). Transition description and prediction in three-dimensional flows. In *Special Course on Stability and Transition of laminar Flow*, pages 5/1–5/23. AGARD.

Semisynov, A. I., Fedorov, A. V., Novikov, V. E., Semionov, N. V., and Kosinov, A. D. (2003). Stability and transition on a swept cylinder in a supersonic flow. *Journal of Applied Mechanics and Technical Physics*, 44:212–220.

Spalart, P. R. (1988). Direct numerical study of leading-edge contamination. In *AGARD-CP-438*, pages 5/1–5/13.

Spalart, P. R. (1989). Direct numerical study of crossflow instability. In *IUTAM Laminar-Turbulent Symposium III*, pages 621–630.

Abstract

The present thesis is concerned with the global stability of compressible flow in the leading-edge region of a swept blunt body, a flow situation which can be found in many engineering applications. It is the goal of the present study to investigate a more comprehensive model and to thus gain new insight into the complex stability characteristics of this flow. To this end, two objectives have been pursued: (i) a powerful DNS-based global stability solver has been developed and (ii) this stability algorithm has then been employed to extract stability information from our flow model. The former objective has been accomplished by combining direct numerical simulations (DNS) and Krylov methods using a matrix-free implementation; furthermore, a Cayley transformation as well as preconditioning techniques are used to add, on the one hand, flexibility and, on the other hand, robustness and efficiency to our algorithm. The developed stability algorithm has then been employed to study the global stability of compressible flow about a swept parabolic body. The computed spectrum provides a comprehensive picture of the temporal perturbation dynamics of this flow and, as a result, a wide and rich variety of global modes has been uncovered: boundary-layer modes, different types of acoustic modes and wave packet modes have been found. Furthermore, boundary-layer modes connecting attachment-line and crossflow instabilities as well as composite global modes featuring both the structure of boundary-layer and acoustic instabilities have been computed. Moreover, the neutral curve for boundary-layer and acoustic modes has been presented.

Keywords: global stability, compressible leading-edge flow, direct numerical simulation, Krylov subspace methods, matrix-free implementation, Cayley transformation

Résumé

L'objet de cette thèse est l'étude d'un écoulement compressible, impactant un bord d'attaque en flèche par une méthode de stabilité globale. Cette méthode, très générale, permet une meilleure compréhension de la stabilité de cet écoulement. La démarche suivie consiste en deux étapes : (i) le développement d'un solveur de stabilité globale basé sur une simulation numérique directe, et (ii) l'application de ce solveur à notre cas d'étude. Concernant le premier point, nous avons utilisé une méthode combinant des simulations numériques directes et des méthodes de type Krylov ne nécessitant pas la construction explicite de la matrice de stabilité ("matrix-free implementation"). La flexibilité de l'algorithme a été accrue par l'utilisation d'une transformation de Cayley et sa robustesse améliorée par des techniques de préconditionement. La méthode ainsi développée, a été appliquée à l'étude de la stabilité globale de l'écoulement compressible autour d'un cylindre de section parabolique. La dynamique temporelle des perturbations est caractérisée par le spectre de cet écoulement. Une grande variété de modes globaux a été decouverte : des modes de couche limite, différents types de modes acoustiques et des modes représentant des paquets d'ondes. En particulier, nous avons établi une connection spatiale entre les instabilités de type "attachment-line" et "crossflow" dans les modes de couche limite. De même, quelques modes globaux représentant à la fois des structures dans la couche limite et des instabilités acoustique ont été trouvés. Finalement, nous avons présenté la courbe de stabilité marginale des modes de couche limite et des modes acoustiques.

Mots-clefs: stabilité globale, écoulement compressible, simulation numérique directe, méthodes de type Krylov, matrix-free implementation, transformation de Cayley